Optical chirped pulse generation and its applications for distributed optical fiber sensing

by

Yuan Wang

Thesis submitted to the
University of Ottawa
in partial Fulfillment of the requirements for the
Doctor of Philosophy
in
Electrical and Computer Engineering

School of Electrical Engineering and Computer Science
Faculty of Engineering
University of Ottawa

To my late grandmother.

Abstract

Distributed optical fiber sensors offer unprecedented advantages, and the most remarkable one is the ability to continuously measure physical or chemical parameters along the entire optical fiber, which is attached to the device, structure and system. As the most recently investigated distributed optical fiber sensors, phase-sensitive optical time domain reflectometry (φ-OTDR), Brillouin optical time domain analysis (BOTDA) and Brillouin dynamic grating-optical time domain reflectometry (BDG-OTDR) techniques have been given tremendous attention on the advantage of quantitative measurements ability over high sensitivity and absolute measurement with long sensing distance, respectively. However, the accompanying limitations in terms of static measurement range, acquisition rate, laser frequency drifting noise, and spatial resolution limitations in these techniques hinder their performance in practical applications. This thesis pays particular attention to the above three distributed sensing techniques to explore the fundamental limitations of the theoretical model and improve the sensing performance. Before presenting the novel sensing scheme with improved sensing performance, an introduction about distributed fiber optical sensing, including three main light scattering mechanisms in optical fiber, the recent advancements in distributed sensing and key parameters of Rayleigh scattering- and Brillouin scattering-based sensing systems. After that, a study on the theoretical analysis of large chirping rate pulse generation and the theoretical model of using chirped pulse as interrogation signal in φ-OTDR, BOTDA and BDG-OTDR systems are given.

In the disruptive experimental implementations, the sensing performance has been improved in different aspects. By using a random fiber grating array as the distributed sensor, a high-precision distributed time delay measurement in a CP φ-OTDR system is proposed thanks to the enhanced in-homogeneity and reflectivity. In addition, a simple and effective method that utilizes the reference random fiber grating to monitor the laser frequency drifting noise is demonstrated. Dynamic strain measurement with a standard deviation of 66 nε over the vibration amplitude of 30 $\mu\varepsilon$ is achieved. To solve the limited static measurement range issue, a multi-frequency database demodulation (MFDD) method is proposed to release the large strain variation induced time domain trace distortion by tuning the laser initial frequency. The maximum measurable strain variation of about 12.5 $\mu\varepsilon$ represents a factor of 3 improvements.

By using the optimized chirped pulse φ-OTDR system, a practical application of monitoring the impact load response in an I-steel beam is demonstrated, in which the static and distributed strain variation is successfully reconstructed. To obtain an enhanced static measurement range without a complicated database acquisition process, a photonic approach for generating low-frequency drifting noise, arbitrary and large frequency chirping rate (FCR) optical pulses based on the Kerr effect in the nonlinear optical fiber is theoretically analyzed and experimentally demonstrated by using both fixed-frequency pump and chirped pump. Due to the Kerr effect-induced sinusoidal phase modulation in the nonlinear fiber, high order Kerr pulse with a large chirping rate is generated. Thus the static measurement range of higher order Kerr pulse is significantly improved.

Chirped pulse BOTDA based on non-uniform fiber is also analyzed, showing a high acquisition rate that is only limited by the sensor length and averaging times due to the relative Brillouin frequency shift (BFS) changes are directly extracted through the local time delays between adjacent Brillouin traces from two single-shot measurement without frequency sweep process. BFS measurement resolution of 0.42 MHz with 4.5 m

spatial resolution is demonstrated over a 5 km non-uniform fiber. A hybrid simultaneous temperature/strain sensing system is also demonstrated, showing a strain uncertainty of 4.3 $\mu\varepsilon$ and temperature uncertainty of 0.32 °C in a 5 km non-uniform fiber.

Besides, the chirped pulse is also utilized as a probe signal in the Brillouin dynamic grating (BDG) detection along the PM fiber for distributed birefringence variations sensing. The strict phase-matching condition only enables part of the frequency components within the chirped probe pulse to be reflected by BDG, giving an adjustable spatial resolution without photo lifetime limitation. The spatial resolution is determined by the frequency chirping rate of the probe pulse.

Acknowledgements

I would like to express my gratitude to all those who offered great help for my thesis.

First and foremost, my deepest gratitude goes to my supervisor Professor Xiaoyi Bao, for her encouragement and guidance in scientific research. Her painstaking teaching and valuable advice have profoundly contributed to completing the present thesis. Her perseverance and dedication toward real physics are astounding, and she will always be regarded as an inspiring model in my future research career.

I would also like to thank Professor Liang Chen for his abundant suggestions and priceless criticisms of my research during the last four years. His profound knowledge in physics and mathematics helps and inspires me to have a better understating on the experimental results. I would like to thank Dr. Pedro Tovar Braga for his valuable suggestions and instructive discussions in my research and thesis writing. He is more than an instructor and Postdoc to me but a big brother and close friend.

I am thankful to Dr. Liang Zhang for his insightful suggestions and constant encouragement during my early PhD career. He helped me understand the basic concept of phonics and the working principle of the typical experimental setup in distributed fiber-optic sensing. Many thanks to Dr. Ping Lu and Dr. Stephen Mihailov in the National Research Council for providing me with random fiber grating samples and helping me understand the fabrication process and working principle of random fiber gratings. I also express my gratitude to Mr. Ole Krarup, Dr. Chams Baker, Mr. Zichao Zhou, Mr. Haiyang Wang, Mr. Chen Chen, who were always there to help and happy

to discuss about all the interesting phenomena we witnessed. My thanks also go to the current and previous group members as well as the guest students: Dr. Yanping Xu, Mr. Bhavaye Saxena. Dr. Song Gao, Dr. Benoit Vanus, Dr. Huibo Fan, Dr. Lijuan Gu, Dr. Wei Cai, Mr. Zhuo Wang, Mr. Robert Chutu Li, Ms. Wenwen Ma (and many other friends whom I must apologize for not mentioning).

Special thanks go to my family, especially my parents. I am deeply indebted to my wife, Bingxin Xu, for her unconditional love and support. Also It's impossible to finish my PhD study without her encouragement and understanding. I also want to thank my daughter Mia, who brings me a lot of happiness.

Thank you all again!

Table of Contents

List of Tables

List of Figures

Abbreviations

AOM Acousto-optic Modulator 32

BFS Brillouin frequency shift 15

BGS Brillouin gain spectrum 18, 45

BOTDA Brillouin optical time domain analyzer 43

BOTDR Brillouin optical time domain reflectometry 41

DOFSs Distributed optical fiber sensors 2

EDFA Erbium Doped Fiber Amplifier 46

EOM Electro-Optic Modulator 36

FBG Fiber Bragg grating 47, 221

FCR Frequency chirping rate 5

fs Femtosecond 227

FTTM Frequency-to-time mapping 65

FWM four-wave mixing 151

MZI Mach-Zehnder interferometer 32

NA Numerical aperture 18

OFDR Optical frequency domain reflectometry 49

OFSs optical fiber sensors 2

OSC Oscilloscope 34

OTDR optical time domain reflectometry 25

PD Photo-detector 46

PMD Polarization mode dispersion 27

PMF Polarization maintaining fiber 18

PZT Piezoelectric transducer 33

RFGA Random fiber grating array 234

SBS Stimulated Brillouin scattering 15

SMF Single mode fiber 1

SNR Signal-to-noise ratio 34

SOP State of polarization 18, 27

SpBS spontaneous Brillouin scattering 12

SpRS Spontaneous Raman scattering 211

SRS Stimulated Raman scattering 214

UV Ultraviolet 221

Chapter 1

Introduction

This chapter primarily introduces the background and motivation, contributions, and the outline of research works. Section 1.1 gives a brief introduction to the motivation and the background of the research conducted in this thesis, focusing on the study and development of high-performance distributed OTDR sensing systems by using chirped pulse based on Rayleigh/Brillouin scattering mechanisms. Section 1.2 summarizes the contributions of our work to the Rayleigh/Brillouin scattering-based distributed sensing. Section 1.3 gives the outline of the thesis.

1.1 Background and Motivation

Standard Single mode fiber (SMF) was invented in the early 1960's as a higher-capacity transmission medium (with low attenuation and dispersion) to be utilized in high-speed and broadband optical fiber communications, which is the cornerstone of modern internet technology and keeps changing our daily lives. Apart from high-speed communications, in which optical fiber plays a crucial role as the transmission media. Optical fiber can also be used as distributed sensors. The fiber act as the disturbance information provider (sensing element), enabling the measurement of environmental parameters, such as temperature, static and dynamic strain and stress, sound and

vibrations, electrical and magnetic fields, presence and concentration of chemical species and biological reagents, ionizing radiation and more from any point along an optical fiber through light scattering.

Nowadays, optical fiber sensors (OFSs) play an important role in the safety monitoring applications for buildings, bridges, highways, tunnels, power plants, industrial facilities, and pipelines that are critical to the day-to-day lives of people around the world. The concept of distributed optical fiber sensing was initially inspired by active sonar and radar, which locates a target with a continuous reading of the propagating medium between the central radar station and the target [1]. Distributed optical fiber sensing is a cost-effective technique that offers continuous reading along a single fiber, and it is able to spatially resolve one or more measurands by using only one interrogator unit. In this sensing scheme, local external disturbance information from thousands of or even millions of locations could be obtained. Based on different light scattering mechanisms including, Rayleigh scattering, Brillouin scattering and Raman scattering in the fiber, various Distributed optical fiber sensors (DOFSs) have been researched and demonstrated for quantitative external disturbance sensing, such as Rayleigh scattering based sensing system: phase-sensitive optical frequency domain reflectometry (φ-OTDRs) [2] [3] [4] and optical frequency domain reflectometry (OFDRs) [5]; Brillouin scattering based sensing system: Brillouin optical time domain reflectometry (BOTDR) [6] [7], Brillouin optical time domain analysis (BOTDA) [8] [9],Brillouin dynamic grating-optical time domain reflectometry (BDG-OTDR) [10] [11]; and Raman scattering based sensing system: Raman optical time domain reflectometry (Raman-OTDR) [12]. In this thesis, we mainly focus on the φ-OTDR, BOTDA and BDG-OTDR systems.

DOFSs support a thriving research community and a growing industrial market, offering many advantages when compared to conventional electronic-based sensors, including high sensitivity, immunity to electromagnetic interference, compact size, light-

weight, robustness, flexibility, and the ability to provide multiplexed or distributed sensing. Thanks to the advances in research and development of DOFS over several decades, there are currently found in a large number of applications, such as the oil and gas industry [13] [14]; power industry for power transmission [15] [16]; structure monitoring [17] [18]; transportation industry [19] [20], and security monitoring [21] [22]. As distributed fiber optic sensors become more cost-effective and technology advances, we expect to see a growth in demand for these sensors in the energy, medical, and industrial markets. In recent years, many interesting types of research related to distributed sensing or intruder detection based on telecom networks have been carried out, validating the efficiency in detecting disturbances near a transmission line such as traffic, construction, or even seismic monitoring [23] [24]. A review of recent developments in distributed fiber-optic sensing can be found in Chapter 3.

Since the DOFSs have broad applications in our daily lives, it is significant to explore their underlying physics and improve their performance. Probably the two most adopted solutions for DOFSs are φ-OTDR and BOTDA systems. These have been intensely studied over the past ten years, with current state-of-art techniques using single-frequency pulses from a narrow linewidth laser as the interrogation signal. In φ-OTDR, the phase recovery process requires a coherent detection scheme in which the backscattering signal is mixed with the local oscillator. Such implementation brings several issues: (1) Highly coherent source with ultra-narrow linewidth laser increases the system cost; (2) intensity and polarization fading problem; (3) in-homogeneity induced non-linear response; (4) phase noise accumulation problem; and (5) the weak reflection of Rayleigh scattering gives a low signal-noise-ratio (SNR) in long sensing distance. Recently, the chirped pulse φ-OTDR has been proposed aiming to overcome these problems, and it has the following advantages: (1) single-shot measurement without the requirement of coherent detection, in which the amplitude of external disturbance is measured by local time delays in Rayleigh traces. The direct measurement

in the electrical domain without an optical interferometer structure shows good sensing accuracy. (2) A broadband DFB laser (MHz range) is used as a laser source, leading to a system free of the fading problem and a cost reduction; (3) The frequency scanning (chirp) with a single transmission pulse enables the development of a system with high acquisition rate, resulting in the capacity of high-frequency vibration detection. However, this technique still has some problems that need to be solved, such as static measurement range limitation, laser frequency drifting noises, and accumulation errors in the integration of differential measurement (detailed in Section 4.2). Thus, the first motivation of this thesis is to solve, with the support of theoretical analysis and experimental demonstration, the limitations in φ-OTDR to optimize the sensing performance in terms of SNR, measurement accuracy, and static measurement range.

Secondly, the static measurement range in chirped pulse φ-OTDR is limited by the frequency chirping range of the interrogation pulse (Section 4.2.1). To achieve both high spatial resolution and large static measurement range, a narrow pulse with a large frequency chirping range (or high chirping rate) is generally required. Thus, our second motivation is finding a method to generate ns pulses with high-frequency chirping rates. In addition, the pursue of high chirping rate pulses is not only important for fiber sensing applications but for multiple other fields, such as radar [25], ultra-wideband sensing [26], bio-medical imaging [27], and non-contact healthcare monitoring [28].

Apart from φ-OTDR, we also focus on improving BOTDA technique, which is a typically Brillouin scattering-based sensing technique, providing a high spatial resolution over long sensing ranges, and it has found many applications in structural health monitoring of bridges, dams, pipelines, and railways over the past decades. The current challenges in the traditional BOTDA system include (1) a low acquisition rate due to the slow frequency sweep process; (2) intensity fading problems in Brillouin traces; and (3) phonon lifetime limited spatial resolution. Therefore, our third motivation is to solve these limitations and propose an optimized BOTDA sensing system.

Finally, a novel birefringence measurement enabled by Brillouin dynamic grating (BDG) detection is also investigated at the end of this thesis. The distributed temperature/strain measurement based on local birefringence variation has the advantage of high sensitivity, which is a hundred times larger than that in BOTDA systems. Beyond that, the different strain/temperature sensitives in chirped pulse BOTDA and Chirped pulse BDG-OTDR also potentially solve the cross-sensitive problem between strain and temperature. It's noted that the Brillouin trace in BOTDA and BDG reflected traces could be collected in one system by simply using frequency diversity detection, with negligible increase in the system complexity.

1.2 Thesis contributions

This thesis is focused on the generation of optical chirped pulses in ns regime for applications in distributed fiber-optic sensing systems, including chirped pulse phase-sensitive optical time domain reflectometry (CP φ-OTDR), chirped pulse Brillouin optical time domain analyzer (CP-BOTDA), and chirped pulse Brillouin dynamic grating optical time domain reflectometry (CP BDG-OTDR) which enables fast quantitative measurements with high accuracy and spatial resolution on different measurands without time-consuming frequency sweep process. Below are the main contributions of this thesis:

(1) We investigated and demonstrated the extension of the frequency chirping range of a chirped laser pulse by all-optical means via the Kerr effect to improve the Chirped Pulse φ-OTDR measurement range. Benefiting from the use of a single laser source and large Frequency chirping rate (FCR) Kerr pulse, the system exhibits a 3.9 $\mu\varepsilon$ static strain measurable range with 8 times enhancement and 0.24 $\mu\varepsilon$ measurement uncertainty by using the -4^{th} order Kerr pulse that has a frequency chirping rate of up to 0.8 GHz/ns [29].

(2) We proposed a high-precision distributed time delay measurement in a CP φ-OTDR system based on a random fiber grating array. As the distributed sensor, a random fiber grating array gives unique localized speckle patterns at different locations. These patterns change with temperature so that the backscattering spectral response will change accordingly. Unlike a conventional φ-OTDR sensing system which measures a distributed phase change along the fiber using an ultra-narrow linewidth laser, the distributed time delay is directly measured in real-time, achieving a minimum detectable temperature variation of about 0.028 °C [30].

(3) We first proposed a multi-frequency database demodulation (MFDD) method for strain variation measurement in CP φ-OTDR, which enables a larger measurement range for both static and dynamic strain sensing. Furthermore, a random fiber grating made with embedded large random refractive index changes along the single-mode fiber provides a stable reflection with a wide reflection spectrum range. Such a structure successfully improves the time delay measurement precision and achieves a large tuning range as demonstrated by the database demodulation method. Ultimately, a dynamic strain with the peak-to-peak value of 12.5 $\mu\varepsilon$ at a vibration frequency of 50 Hz is accurately reconstructed when the pulse repetition rate is 1 kHz, which was not detected using a conventional chirped pulse φ-OTDR [31].

(4) After solving the static measurement range limitation in CP φ-OTDR systems, significant laser frequency drifting (LFD) becomes a major limitation for detecting dynamic strain events over a frequency range from 0.01 to 20 Hz. Therefore, we propose a simple and effective method that utilizes the random fiber grating reflection as a stale reference to monitor the variation of the laser frequency. A minimum detectable frequency drifting of 7.28 MHz could be achieved over the optical frequency of 2^{14} Hz, which is later shown to be compensated, resulting in a light source with reduced frequency drifts [32]. By using the fully optimized CP φ-OTDR system, we demonstrate a real-time monitoring system to detect the responses of an I-beam from the impact of

a free-falling load, including acoustic wave, damped harmonics oscillations, and static strain measurement [33].

(5) For the application of chirped pulse in the Brillouin scattering-based sensing system, we first proposed and demonstrated a novel method by using a chirped pulse as a pump signal to extract the relative Brillouin frequency shift (BFS) changes through the real-time delays between two adjacent Brillouin traces without need of Brillouin gain spectrum recovery. Thanks to the single-shot measurement, the system has a high acquisition rate that is only limited by the sensor length without averaging and is immune to the polarization fading problem thanks to electrical delay time measurement. In the experiments, BFS measurement resolution of 0.42 MHz with 4.5 m spatial resolution is demonstrated over a 5 km non-uniform fiber. To solve the temperature strain cross-sensitive problem, we propose a real-time simultaneous temperature and strain sensing system by combining the CP-BOTDA and CP]φ-OTDR together, achieving 4.5m spatial resolution with strain uncertainty of 4.3 $\mu\varepsilon$ and temperature uncertainty of 0.32 °C in a 5 km non-uniform fiber [34].

(6) Finally, we investigate the distributed four-wave mixing (FWM) mismatching due to the randomly varied birefringence along a PM fiber by Chirped pulse BDG-OTDR system. Most importantly, there is phonon lifetime-related spatial resolution limitation imposed by weak Brillouin spectrum in such a technique, and the spatial resolution (effective pulse width) is limited by the combination of non-uniformity of fiber birefringence and the chirped frequency rate rather than the pulse width of interrogation pulse. In the experiment, a high spatial resolution of up to 10 cm (equivalent to 1 ns pulse width) is achieved by using 20 ns interrogation chirped pulses with a chirping rate of 93.5 MHz/ns, resulting in a sensing accuracy of up to 370 $n\varepsilon$ for strain and 38 mK for temperature.

1.3 Thesis outline

The thesis is structured as follows:

Chapter 1 contextualizes the work presented in this thesis, describing the main motivations of the research, objectives, main contributions, and also the outline of the thesis.

Chapter 2 introduces the fundamentals of light scattering mechanisms, including Rayleigh scattering and Brillouin scattering.

Chapter 3 gives a comprehensive review of recent advancements in distributed fiber-optic sensing. The working principle and detailed developments of different Rayleigh/Brillouin scattering-based sensing systems are presented. This chapter is important for the work as a parallel with distributed sensing system is traced along the thesis, contributing to a full understating of theoretical and experimental results in the rest of the thesis. Finally, four key parameters are discussed, including sensing distance, SNR, spatial resolution, and acquisition rate (sampling rate).

Chapter 4 starts by showing the theoretical analysis of the generation process of high chirping rate pulses. Next, it addresses the fundamentals of two particular DOFS systems: chirped pulse φ-OTDR and chirped pulse BOTDA, including theoretical models of the two systems, their limitations of static measurement range and acquisition rate in chirped pulse φ-OTDR, and also the chirped rate dependence spatial resolution in chirped pulse BOTDA.

Chapter 5 investigates the random fiber grating array (RFGA) based high-performance chirped pulse φ-OTDR system. Firstly, the enhanced backscattering of RFGA gives an optimized signal-noise ratio of Rayleigh traces, thus lowering the measurement uncertainty. Secondly, the limitation of maximum measurable strain or temperature variation introduced by the large time delay estimation (TDE) error is mitigated using the multi-frequency database demodulation method. Finally, the last section studies a simple but effective method to compensate for the laser frequency drifting noises.

Chapter 6 describes the experimental results of using a high chirping rate Kerr pulse as the interrogation signal in the φ-OTDR system to improve the static measurement range. Two types of implementations are investigated and compared in this chapter. The difference is that one uses a fixed-frequency pump, and the other uses an opposite-chirped pump.

Chapter 7 studies one application of our optimized chirped pulse φ-OTDR system in structural health monitoring fields. A distributed impact load measurement is demonstrated.

Chapter 8 proposes a novel chirped pulse BOTDA sensing system, and the results of distributed dynamic measurement along the non-uniform fiber are presented. The non-uniformity of the core size enables a fast time-varied profile in Brillouin traces, which gives a high accuracy of time delay measurement.

Chapter 9 explores the BDG detection in a PM fiber with chirped pulses as the probe signal. It has been found that the temperature/strain-induced local birefringence variation could be directly measured by the local time delay in BDG reflected traces. The experimental results of static temperature and dynamic strain measurements are involved.

The final chapter summarizes the main results of this thesis and suggests possible directions for future research.

Chapter 2

Light scattering mechanisms in optical fiber

2.1 Introduction

To better understand and further improve the performance of Rayleigh and Brillouin scattering-based DOFS, it is important to study the fundamentals of light scattering mechanisms. Light scattering phenomena are physical processes involving light-matter interactions. When a light wave propagates along an optical fiber, it interacts with the atoms and molecules inside the medium. The electric field will then introduce a time-dependent polarization dipole. When the optical wavelength of incident light is far from the medium resonance, the polarization dipole generates secondary electromagnetic waves, resulting in a small portion of forward-traveling light being re-directed into random directions. Due to different physical mechanisms, including mechanical and optical properties of the materials, the scattering process is classified into elastic or inelastic scattering. The former scattering phenomenon is a linear process, which means the power of back-scattering light is linearly proportional to the incident power and without energy exchange. Therefore, the frequency of scattered light does not have a frequency shift compared with the incident light.

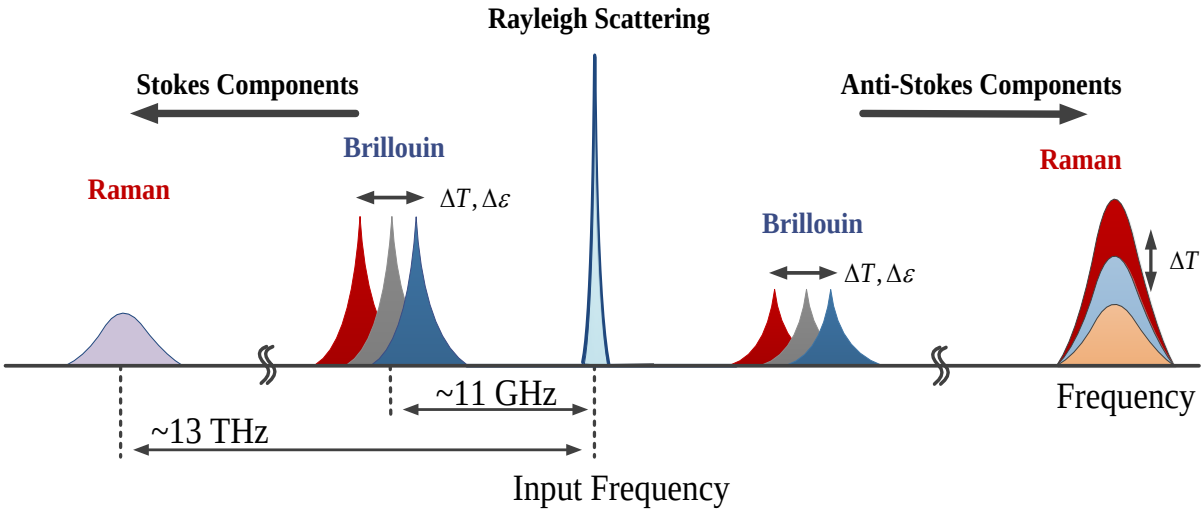

Figure 2.1: The spectrum of three types of back-scattered light in optical fibers.

On the other hand, inelastic scattering processes are regarded as those with energy exchange, i.e, the energy between the incident and scattered photons is not conserved since the energy and momentum of incident photons are partially transferred to the medium. Based on the interaction between the incident photon and microscopic vibrations, the inelastic scattering process includes Brillouin and Raman scattering. Basically, the Brillouin scattering is initially generated by the thermal-excited acoustic wave, resulting in material density variations manifesting in the optical domain in the form of variations in the refractive index. Thus acoustic-like vibrations among the entire molecule chain are generated. The energy and momentum are transferred from the optical photon to the acoustic phonon with low energy but high momentum, resulting in a relatively small frequency shift of about 11 GHz with a typical linewidth of 30 MHz, as shown in Figure 2.1. Another optical branch of inelastic scattering is Raman scattering, in which the light interacts with optical-like vibrations that come from the molecular chain's oscillatory motion. This optical-like vibration will introduce a periodic modulation of local polarizability corresponding to the molecular vibrational frequency. In this process, the energy is transferred from the optical photon to the optical phonon with high energy and low momentum, giving a Stokes light with a frequency

of 13 THz apart from the frequency of incident light and with a typical linewidth of 6 THz. In inelastic scatterings, a stimulated interaction exists and gives rise to the dynamic coupling between all waves participating in this process.

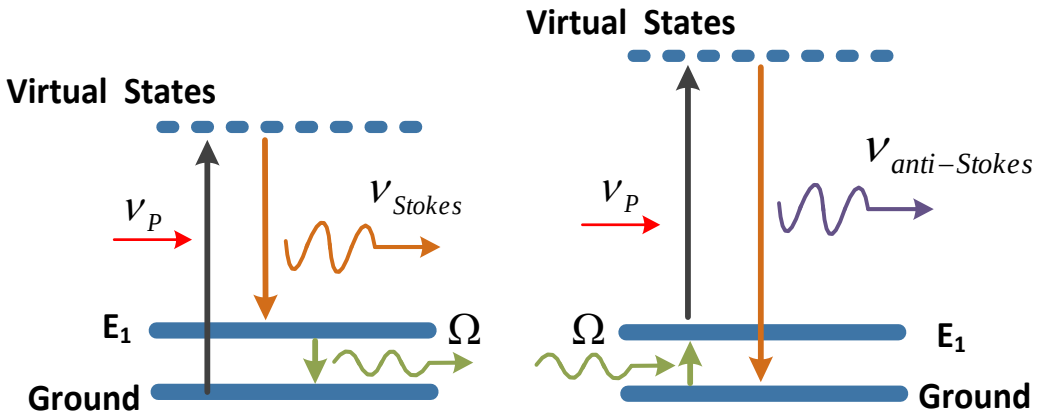

Figure 2.2: The energy diagram of the generation of Stokes and anti-Stokes light.

As shown in Figure 2.2, both Brillouin scattering and Raman scattering have Stokes and anti-Stokes components, which are presented by the back-scattered light spectral component showing a lower and a higher frequency than the incident light, respectively. For Stokes scattering, when a stream of photons with a frequency ν_p interacts with excited particles (electrons), a photon with reduced optical frequency ν_{Stokes} is emitted accompanied by a phonon (acoustic or optical) with frequency $\Omega = \nu_p - \nu_{Stokes}$. In the anti- Stokes process, a phonon must be available in the medium so that when an incident photon is absorbed, a photon with higher energy is emitted with a frequency (energy) higher than the incident photon, of $\nu_{anti-Stokes} = \nu_p + \Omega$.

2.2 Brillouin scattering

2.2.1 Spontaneous Brillouin scattering

In the spontaneous Brillouin scattering (SpBS), the scattering process occurs as the interaction between incident optical waves and thermally excited acoustic waves

propagate at sound speed. Due to the elastic properties of the medium, it is equivalent to the density waves inside the medium. Therefore, the density variations of the medium introduce refractive index changes due to the photo-elastic effect. The physical reason behind this is that the polarization field increases with a denser medium, resulting in a higher electric susceptibility (χ) and thus a higher effective refractive index (n_{eff}), which is given by:

$$n_{\text{eff}} = \sqrt{1+\chi}. \tag{2.1}$$

The heat in the medium is held in the form of lattice vibrations (acoustic waves) that usually occur at the hyper-sonic frequency range (10-30 GHz), a much lower range compared with Raman scattering. Thus, there is an energy exchange between incident light and dielectric medium, and the resulting new spectral features on both sides are known as Stokes and anti-Stokes light lines with typical narrow bandwidth.

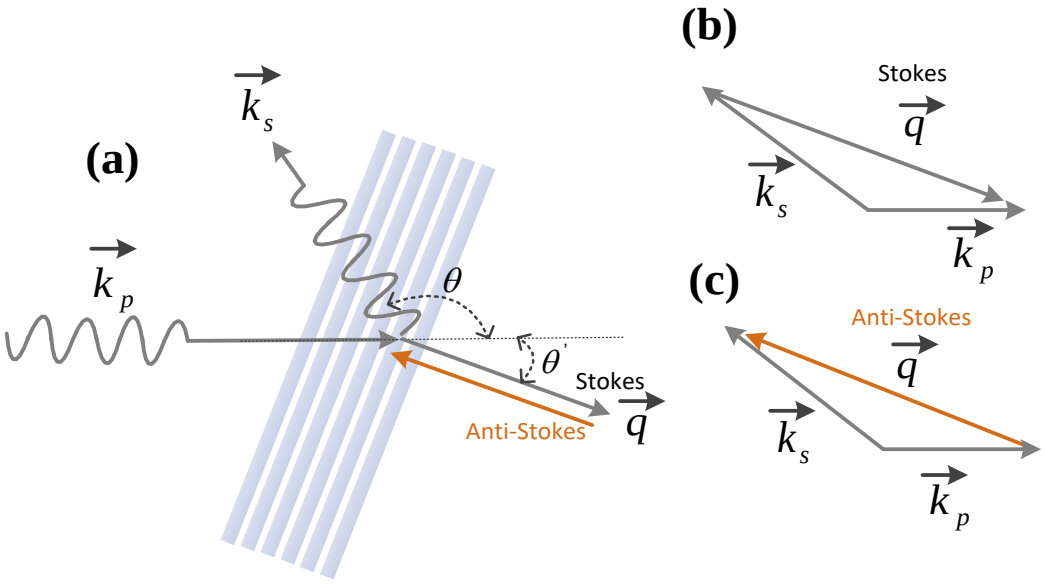

Figure 2.3: Wavevector diagram of Brillouin scattering.

As discussed above, the Brillouin scattering could be regarded as the interaction between the pump light (incident light) and the acoustic phonons initially generated thermally. Unlike the Raman scattering process in which the optical phonons vibrate at a very high frequency with a vanishing momentum, the acoustic phonons in Brillouin

scattering carry the momentum that increases with acoustic frequency. The proportional factor is determined by the acoustic velocity V_a. As shown in Figure 2.3 (a), the thermally excited acoustic wave with a frequency Ω and wavevector $\overrightarrow{q}$ will introduce local refractive index modulation and then diffract the incident wave with a frequency ν and wavevector $\overrightarrow{k_p}$, generated a scattered light wave with frequency ν_s and wavevector $\overrightarrow{k_s}$. During the interaction between these three waves, including incident optical wave, scattered optical wave, and acoustic wave. The energy and momentum must be conserved. The conservation condition of large momentum is translated into a strict phase-matching condition, resulting in a narrow Brillouin gain bandwidth. The momentum and energy conservation conditions are given by:

$$h\nu = h\nu_s + h\Omega, \tag{2.2}$$

$$\hbar\overrightarrow{k_p} = \hbar\overrightarrow{k_s} + \hbar\overrightarrow{q}. \tag{2.3}$$

And the coupled equations between the wavevectors, and the scattering angle θ and θ' for Stokes and anti-Stokes waves, respectively, as shown in Figure 2.3 (b), are given by:

$$\begin{cases} \overrightarrow{k_s}\sin\theta = \overrightarrow{q}\sin\theta', \\ \overrightarrow{k_p} = \overrightarrow{k_s}\cos\theta + \overrightarrow{q}\cos\theta', \end{cases} \tag{2.4}$$

where θ is the angle between $\overrightarrow{k_p}$ and $\overrightarrow{k_s}$, and θ' the angle between $\overrightarrow{k_p}$ and $\overrightarrow{q}$. After squaring and summing these equations, the magnitude of the acoustic wavevector can be expressed as [35]:

$$|q|^2 = |k_p|^2 + |k_s|^2 - 2|k_p|\,|k_s|\cos\theta. \tag{2.5}$$

By using the relationship between frequency and wavevector, i.e., $\nu = k_p c/2\pi, \nu_s = k_s c/2\pi, \Omega = qV_\mathrm{a}/2\pi$, and considering the fact that V_a ($\sim$ 5900 m/s) is much smaller than light velocity c in the silica ($\sim$ 200,000,000 m/s) and ν is much larger than Ω,

then the frequency of the acoustic wave is given by [36]:

$$\Omega = 2\frac{V_{\mathrm{a}}}{c}\nu \sin\frac{\theta}{2}. \tag{2.6}$$

On the other hand, the energy is transferred from the acoustic phonons to the incident photos for the scattered anti-Stokes wave generation. The wavevector of anti-Stokes light is given by $k_s = k_p + q$ [37]. Using the same derivations from (2.4) to (2.6), the frequency shift of anti-Stokes wave will be:

$$\Omega_{AS} = 2\frac{V_{\mathrm{a}}}{c}\nu \sin\frac{\theta}{2}. \tag{2.7}$$

Hence, in the single-mode fiber, the frequency shifts of the Stokes and anti-Stokes waves are the same. Equation (2.6) and (2.7) show that the frequencies of scattered Stokes and anti-Stokes waves depend on the scattering angle θ. In the optical fibers, only forward ($\theta = 0$) and backward ($\theta = \pi$) propagation directions are supported. The frequency shift is 0 with a scattering angle of 0, indicating no scattering in the forward direction. The frequency shifts become maximum when the scattering angle is equal to π, and the backward Brillouin frequency shift (BFS) is expressed as:

$$\nu_B(\theta = \pi) = 2\frac{V_{\mathrm{a}}}{c}\nu. \tag{2.8}$$

In materials that support shear stress, such as glasses, Brillouin scattering exists with both longitudinal acoustic (LA) pressure waves and transverse acoustic (TA) shear waves [38], with TA waves being substantially slower than LA waves. In real applications, the LA waves are used almost exclusively in distributed sensing, primarily because only back-scattered light is considered for sensing. In contrast, scattering from TA phonons is weaker than that from LA phonons.

2.2.2 Stimulated Brillouin scattering

The concept of high-frequency phonon generation via the interaction of matter with intense laser light was first introduced by Townes in [39] and led to the first Stimulated

Brillouin scattering (SBS) demonstration in liquids. Once the power of the launched incident light wave exceeds the threshold, the Brillouin scattering becomes a stimulated process, in which the interference wave generated from the intensity beating between the incident and scattered waves will strengthen the acoustic wave through electrostriction (or radiation pressure). In the SBS process, when the incident lightwave interacts with the weak Stokes lightwave or a probe light with a frequency matching the Brillouin frequency, then their interference will introduce a local electrical field intensity variation. Thus, an acoustic wave with the same frequency as this intensity-interference wave is excited due to the electrostriction effect. Electrostriction introduces density variation in the material through the electrostrictive pressure (Δp), which is given by:

$$\Delta p = -\frac{1}{2}\varepsilon_0 \gamma_e E^2, \tag{2.9}$$

where ε_0 is the permittivity in vacuum, E is the electric field, $\gamma_e = \rho(\partial\varepsilon/\partial\rho)$ is the electrostrictive constant, and ρ is the material density. Thus, the density change of the material is expressed as:

$$\Delta\rho = -\left(\frac{-\partial\rho}{\partial p}\right)\Delta p = \frac{1}{2}\varepsilon_0 \rho C \gamma_e E^2, \tag{2.10}$$

where $C = \rho^{-1}(\partial\rho/\partial p)$ is the compressibility of the material. The equations above indicate that a strong electromagnetic field translates into higher variations in material density, which ends up increasing the refractive index due to the photo-elastic effect as shown in Figure 2.4 [40]. Hence the electromagnetic energy density in the medium also increases since the intensity is proportional to the refractive index: $I = n\left|E_0\right|^2/2\eta_0$ [41]. The grown refractive index modulation causes the light from the pump to be diffracted more towards the Stokes lightwave, reinforcing the signal so that the acoustic and Stokes waves mutually reinforce each other.

In the SBS process, the energy is transferred from the incident lightwave to the Stokes lightwave. It should be noted that stimulated scattering only occurs for Stokes scattering, i.e., that coupling only occurs from the higher frequency wave towards the

lower frequency wave, as only in this way the idler acoustic wave is enhanced and thus the coupling reinforced. The anti-Stokes process annihilates a phonon, and the stimulated interaction rapidly quenches the acoustic wave [42].

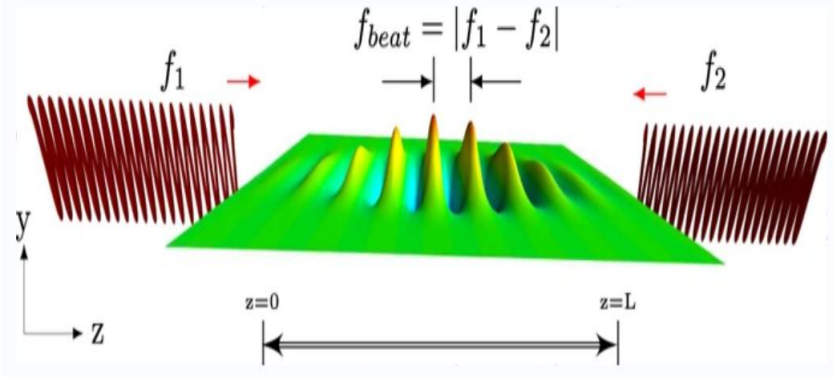

Figure 2.4: Conceptual picture illustrating stimulated Brillouin scattering [40]. The two fields are incident from left and right at frequencies f_1 and f_2, respectively. In the center, the waves in the medium represent the density variations (acoustic waves). L is the total interaction length in the sample.

Considering the stimulated Brillouin scattering as the interaction between three waves, incident pump wave ($E_p(z,t)$), scattered Stokes wave ($E_s(z,t)$), and the acoustic wave ($E_a(z,t)$), the set of equations coupling the amplitude of these three interacting waves can be expressed as [35] [43]:

$$\begin{cases} \frac{\partial E_p}{\partial z} - \frac{n_f}{c}\frac{\partial E_p}{\partial t} = E_a E_s, \\ \frac{\partial E_s}{\partial z} + \frac{n_f}{c}\frac{\partial E_s}{\partial t} = E_a^* E_p, \\ \frac{\partial E_a}{\partial z} + \Gamma E_a = \frac{1}{2}\Gamma_B g_B E_p E_a^*, \\ \Gamma = \Gamma_B + i\Gamma_2, \end{cases} \tag{2.11}$$

where n_f is the refractive index of fiber, c is the velocity of the light in the vacuum, and g_B is the Brillouin gain factor. Γ is the damping constant of the acoustic wave, Γ_B^{-1} is the damping time of the phonon, Γ_2 is the detuning angular frequency that is given by $\Gamma_2 = 2\pi\delta\nu_B$, and $\delta\nu_B$ is the detuning factor, i.e. the difference between the Brillouin shift of the material and the actual value of the frequency difference between

Stokes and pump waves. In the SBS process, the Brillouin gain bandwidth is related to the phonon lifetime ($T_B = \Gamma_B^{-1}$), and it is much narrower ($\sim$ 10 MHz) than the Raman gain spectrum bandwidth. The acoustic wave decay as $\exp(\Gamma_B t)$, resulting in Brillouin gain spectrum with a Lorentzian shape [36] [35]:

$$g_B(\nu) = \frac{g_p \left(\Gamma_B/4\pi\right)^2}{\left(\nu - \nu_B\right)^2 + \left(\Gamma_B/4\pi\right)^2}, \tag{2.12}$$

where ν is the beat frequency between the pump and Stokes lightwaves, and ν_B is the Brillouin frequency shift. The g_p is the peak value of Brillouin gain at the $\nu = \nu_B$, and it is given by [36]:

$$g_p \equiv g_B\left(\nu_B\right) = \frac{4\pi^2 \gamma_e^2 n_f^7 P_p K_P}{c\lambda_p^2 \rho_0 V_A \Gamma_B}, \tag{2.13}$$

where γ_e^2= 0.902 is the electrostrictive constant of silica; ρ_0= 2210 kg/m^3 is the material density; P_p is the pump power; K_P is the State of polarization (SOP) related coefficient. For instance, K_P=1 when the pump and Stokes waves propagate along with the same polarization axis in a Polarization maintaining fiber (PMF). The full width at half maximum of the Brillouin gain spectrum (BGS) is related to the Γ_B and is given by $\Delta\nu_B = \Gamma_B/2\pi$.

2.2.3 Spectral width

The phonon lifetime is temperature and frequency-dependent. For example, the phonon lifetime is $\sim$ 10 ns, and the BGS bandwidth ($\Delta\nu_B$) is about 17 MHz when the pump wavelength is 1550 nm [44]. Another factor that can affect the BGS bandwidth is the waveguide geometric, in which the increase of Numerical aperture (NA) makes the bandwidth broader since more light is captured by the waveguide from different angles [45]. The inhomogeneous SBS bandwidth can be calculated by:

$$\Delta\nu_B(\mathrm{NA}) = \sqrt{\Delta\nu_B(0)^2 + \nu_B^2 \frac{\mathrm{NA}^4}{4n_1^4}}, \tag{2.14}$$

where $\Delta\nu_B(0)$ is the homogeneous width of the Brillouin spectrum. ν_B is the BFS at $\theta = \pi$.

2.3 Rayleigh scattering

When a monochromatic wave propagates through the optical fiber (dielectric medium), it interacts with the medium particles by forcing the atomic electrons to oscillate, generating electric dipoles. Then the dipoles will radiate and generate an electric field, resulting in light scattering. When the medium is perfectly homogeneous, the phase relationship of the emitted waves only allows the forward scattered beam due to the destructive interference in other directions.

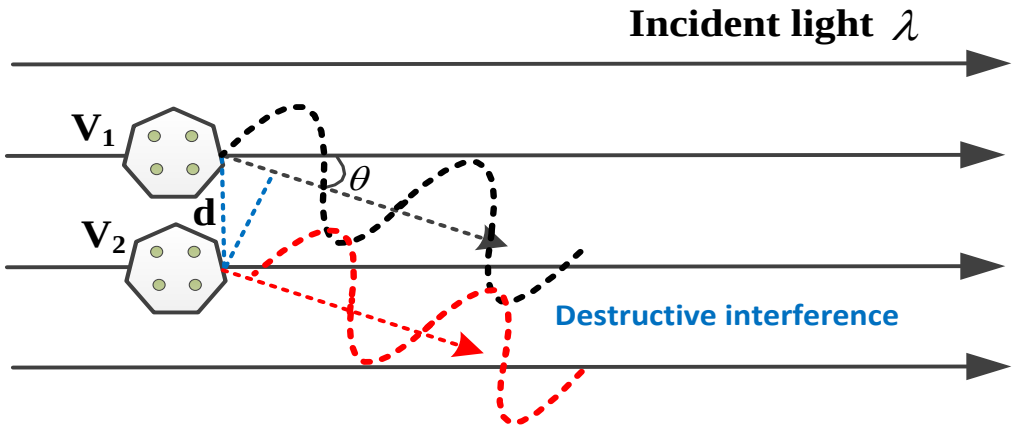

Figure 2.5: Rayleigh scattering in dense and homogeneous materials [35].

As shown in Figure 2.5, the total scattering centers within the volume V_1 give a scattering angle of θ. Since the scattering center is much smaller than the wavelength (λ) and each volume has the same number of scattering centers in homogeneous materials, there is always another volume V_2=V_1 whose scattered field will destructively interfere with light scattered from V_1. This is always valid when the following condition is satisfied: $2d \sin\theta = \lambda$ ($\theta \neq 0$).

The medium can then be considered continuous, and the scattered lights are coherently added. Thus random scattering (except in the forward direction) cannot occur in a completely homogeneous medium. However, optical fiber is an inhomogeneous medium due to the random order of small size particles in nano-meter scale (typical

lees than $\lambda/15$) resulting from the presence of flaws and impurities [46], which causes non-propagating (localized) variations in density [35]. Therefore refractive index fluctuations along the fiber. As a result, the inhomogeneity of the medium disturbs the interference condition of radiation, leading to light scattering.

A macroscopic approach is preferred to analyze the strength of the scattered light from the scattering centers in the dense medium. On a small spatial scale, one would observe fluctuations in local temperature or strain values under incident light on material. This EM field $\mathbf{E}$ would reorient the originally incoherent random fluctuating molecular clouds to tend to respond collectively the same way on a small spatial scale covering the wavelengths of the EM field. Such collective tendency to respond to an EM field would result in macroscopic polarization that is proportional to the external electric field $\mathbf{E}$. The macroscopic polarization ($\mathbf{P}$) is expressed as:

$$\mathbf{P} = \epsilon_0 \chi \mathbf{E}, \tag{2.15}$$

where ϵ_0 is the electric permittivity of free space and χ is the electric susceptibility. Assuming simple linearity of the polarization for a non-magnetic material like the fiber, we write the electric displacement field vector [22]:

$$\boldsymbol{D} = \boldsymbol{\epsilon E} = \epsilon_0 \boldsymbol{E} + \mathbf{P} = \epsilon_0 (1 + \chi) \boldsymbol{E} = (\varepsilon + \Delta \boldsymbol{\epsilon}) \boldsymbol{E}, \tag{2.16}$$

where ε is a constant, and the second term $\Delta\epsilon$ is the fluctuation dielectric tensor that describes the locally fluctuating physical mechanism contributing to the scattering process. It can be re-written as [42]:

$$\Delta \boldsymbol{\epsilon} = \Delta \epsilon \mathbf{I} + \Delta \epsilon^t. \tag{2.17}$$

The first term ($\Delta\epsilon$) indicates the thermodynamic quantities fluctuations, such as pressure, density, temperature and entropy, resulting in two scalar light scattering phenomena: Rayleigh and Brillouin scatterings. While the second term ($\Delta\epsilon^t$) results in the Rayleigh-wing and Raman scatterings.

2.3.1 Rayleigh Scattering coefficient

From the above analysis, the forward propagating light will be scattered in the non-uniform optical fiber due to the spatially and time-varied permittivity (dielectric constant fluctuations). These fluctuations are themselves the result of fluctuations in thermodynamic variables, such as the material density (ρ) and temperature (T) [35]. In order to obtain the scattering coefficient in the Rayleigh scattering process, a macroscopic analysis approach is used, in which light is assumed to be scattered from a small volume V containing a group of molecules, and not that it is scattered by each atom. A common interpretation for this approach is that all atoms within the volume V radiate essentially in phase and in the same direction. If we consider a plane-wave incident electric field [47]:

$$\mathbf{E}_{in}(\mathbf{R},t) = \mathbf{E_{in}} \exp\left[i\left(\boldsymbol{\beta_{in}} \cdot \mathbf{R} - \omega_{\mathbf{1}} t\right)\right], \tag{2.18}$$

where E_{in} is the amplitude of the incident light, $\beta_{\mathbf{in}}$ is the propagation constant vector, and ω_1 is the frequency of the sinusoidal travelling wave. $\mathbf{R}$ is the position of interest in the xyz coordinated system. The component of the scattering electric field at a large distance R from the smaller scattering volume V with electric susceptibility fluctuation $\Delta\chi$ is given by:

$$\begin{aligned}\mathbf{E}_s(\mathbf{R},t) =& \boldsymbol{\beta}_{\mathrm{s}} \times \left(\boldsymbol{\beta}_{\mathrm{s}} \times \mathbf{E}_{in}\right) \frac{\exp\left[i\left(\beta_{\mathrm{s}} R - \omega_1 t\right)\right]}{4\pi R} \\ & \times \int_v \Delta\chi_e\left(\mathbf{r}', t\right) \exp\left[i\left(\boldsymbol{\beta}_{\mathrm{in}} - \boldsymbol{\beta}_{\mathrm{s}}\right) \cdot \mathbf{r}'\right] d\mathbf{r}',\end{aligned} \tag{2.19}$$

where $\beta_{\mathbf{s}}$ is the propagation constant vector of scattered light. Since $\boldsymbol{\epsilon} = \epsilon_0(1+\chi)$, the fluctuation in the electric susceptibility is then given by $\Delta\chi = \Delta\epsilon/\epsilon_0$. Considering the propagation constant $\beta = \omega/c$, it leads to the scattered electric fields:

$$\begin{aligned}\mathbf{E}_s(\mathbf{R},t) =& E_{in} \frac{\omega^2 sin\varphi}{c^2\epsilon_0^2} \frac{\exp\left[i\left(\beta_{\mathrm{s}} R - \omega_1 t\right)\right]}{4\pi R} \\ & \times \int_v \Delta\epsilon\left(\mathbf{r}', t\right) \exp\left[i\left(\boldsymbol{\beta}_{\mathrm{in}} - \boldsymbol{\beta}_{\mathrm{s}}\right) \cdot \mathbf{r}'\right] d\mathbf{r}',\end{aligned} \tag{2.20}$$

where c is the light speed in vacuum, $\beta_s = |\boldsymbol{\beta_s}|$, $R = |\mathbf{R}|$. From the Equation (2.20), the scattering electric field is inversely proportional to the distance R. In addition,

the integral part for the phase component represents the interference between different lightwaves scattered within the volume V. Lastly, the equation reveals that the fluctuation of permittivity causes the Rayleigh scattering and there is no Rayleigh scattering if $\Delta\epsilon\left(\mathbf{r}', t\right) = 0$.

The intensity of scattered light corresponds to the flow of power crossing a unit area along the direction of propagation, which should be identified with the time-averaged value of $\langle \mathbf{E}_\mathrm{s} \cdot \mathbf{E}_\mathrm{s}^* \rangle$:

$$I_\mathrm{s} = \frac{1}{2}(\epsilon/\mu)^{1/2} \left\langle \mathbf{E}_\mathrm{s} \cdot \mathbf{E}_\mathrm{s}^* \right\rangle, \tag{2.21}$$

where μ is the magnetic permeability, and the factor of $1/2$ is induced as the scattered electric fields are taken as complex. By introducing Equation (2.20) into Equation (2.21) we obtain:

$$I_\mathrm{s} = I_\mathrm{in} \frac{\omega^4}{c^4} \frac{\sin^2\varphi}{\epsilon_0^2 (4\pi R)^2} \int_V \int_V \left\langle \Delta\epsilon\left(\boldsymbol{r}_1', t\right) \Delta\epsilon\left(\boldsymbol{r}_2', t\right) \right\rangle exp[i\left(\boldsymbol{\beta}_\mathrm{in} - \boldsymbol{\beta}_\mathrm{s}\right)\left(\boldsymbol{r}_1' - \boldsymbol{r}_2'\right)] \mathrm{d}\boldsymbol{r}_1' \mathrm{d}\boldsymbol{r}_2', \tag{2.22}$$

where $I_\mathrm{in} = \frac{1}{2}(\epsilon/\mu)^{1/2} E_{in}^2$. Considering that each scattering center within a small volume V, with V much smaller than the wavelength of the incident light, radiates in phase at the direction of φ, then the phase component of the integral at the right of the Equation (2.22) can be written as 1. The fluctuation of the electric permittivity within the volume V is approximated to be constant, and given by $\Delta\epsilon$. Therefore, the intensity of the scattered light emitted by the volume V can be expressed by:

$$I_\mathrm{s} = I_\mathrm{in} \frac{\omega^4}{c^4} \frac{\sin^2\varphi V^2 \left\langle \Delta\epsilon^2 \right\rangle}{\epsilon_0^2 (4\pi R)^2}. \tag{2.23}$$

Based on the above equation, the intensity of scattered light is related to the direction φ, and there is no light scattering when $\varphi = 0$, indicating the intensity of scattered light in the direction orthogonal to the incident light propagation is zero.

2.3.2 Thermodynamic variables theory in Rayleigh scattering

The parameter χ is a randomly fluctuating term in the medium with $\Delta\epsilon(t, z)$, which is the fundamental reason for Rayleigh scattering. These permittivity fluctuations are themselves the result of fluctuations in thermodynamic variables, such as the material density (ρ) and temperature T:

$$\Delta\epsilon = \left(\frac{\partial\epsilon}{\partial\rho}\right)_T \Delta\rho + \left(\frac{\partial\epsilon}{\partial T}\right)_\rho \Delta T. \tag{2.24}$$

In the silica fibers, the contribution of temperature to $\Delta\epsilon$ is lees than 2 % [48], so we only need to consider the density fluctuation of the material:

$$\left\langle \Delta\epsilon^2 \right\rangle = \gamma_e^2 \frac{\langle \Delta\rho^2 \rangle}{\rho_0^2}, \tag{2.25}$$

where ρ_0 denotes the mean density of the material, and γ_e^2 is the electrostrictive constant, which is defined by:

$$\gamma_e = \left(\rho\frac{\partial\epsilon}{\partial\rho}\right)_{\rho=\rho_0}. \tag{2.26}$$

In Equation (2.25), the term $\frac{\langle \Delta\rho^2 \rangle}{\rho_0^2}$ can be calculated using the laws of statistical mechanics [49]:

$$\frac{\langle \Delta\rho^2 \rangle}{\rho_0^2} = \frac{kTC_T}{V'}, \tag{2.27}$$

where k is the Boltzmann constant and C_T is the isothermal compressibility coefficient. By introducing Equation (2.27) and Equation (2.25) into Equation (2.23), the scattered intensity can be rewritten as:

$$I_\mathrm{s} = I_\mathrm{in}\frac{\omega^4}{c^4}\frac{\sin^2\varphi V\gamma_e^2 kTC_T}{\epsilon_0^2(4\pi R)^2}. \tag{2.28}$$

So, the scattering coefficient is thus given by:

$$R = \frac{\omega^4}{16\pi^2 c^4}\gamma_e^2 C_T kT\sin^2\varphi. \tag{2.29}$$

The above equation indicates that Rayleigh scattering is an elastic scattering process, i.e., no energy is transferred from the incident photons to the material; therefore,

the incident and scattered lights frequencies are equal. Also, Rayleigh scattering is the principal cause of transmission losses in SMF at 1550 nm [50], which comes from frozen density fluctuations in fused silica during the manufacturing process. According to Equation (2.23), the intensity of scattered light is proportional to the ω^4, thus inversely proportional to λ^4. So the intrinsic loss coefficient as a result of Rayleigh scattering is:

$$\alpha_R = \frac{A}{\lambda^4}, \tag{2.30}$$

where A is a constant with typical value of in range 0.7-0.9 ($\mathrm{dB} \cdot \mathrm{km}^{-1} \cdot \mu\mathrm{m}^{-4}$).

Rayleigh scattering and material absorption are the two main mechanisms for fiber losses. The total attenuation coefficient is denoted as α (with units of km^{-1}). In the wavelength of 1550 nm, commonly used in optical communication, the attenuation coefficient is about 0.2 dB/km in standard single-mode fibers. The scattering coefficient in the range of 0.12-0.16 dB/km shows that Rayleigh scattering is the dominant loss near that wavelength. It provides a way to estimate fiber attenuation by monitoring the Rayleigh.

Chapter 3

Recent advancements in distributed fiber-optic sensing

3.1 Rayleigh scattering-based distributed sensing techniques

3.1.1 Conventional OTDR

Rayleigh scattering is caused by the in-homogeneity property of the optical fiber and is actually a source of noise and transmission loss, which is a detrimental phenomenon in optical communication. However, it could be used to achieve distributed measurement since the ongoing optical signal is continuously backscattered along with the fiber and the sensing system allows the determination of the spatial distribution of the key parameters. As a well-known technique, Rayleigh scattering based optical time domain reflectometry (OTDR) is first proposed in 1976 [51] and initially developed to detect attenuating or reflective faults or imperfections in optical transmission lines. In the OTDR scheme, as shown in Figure 3.1, a series of optical pulses from a broadband laser is probed into a section of optical fiber through an optical circulator, and the reflected optical power is detected at the input end by a photo-detector (PD)

that converts the optical power to electrical current. When the broadband optical pulse propagates along the fiber, the Rayleigh scatters due to the material density fluctuation will re-direct a small portion of forward-propagating light into all directions. Finally, the backscattered light within the acceptance angle is captured by the fiber core and propagates back to the input end. Rayleigh traces at a different location, as shown in the right hand of the Figure 3.1, is mapped through the time of flight, and the spatial resolution is determined by the duration of the optical pulse (approximate 10 cm/ns). At some strong reflection points, such as fiber break, optical connectors or a splice spot, a larger fraction of the probe light will be reflected at the fiber region due to large refractive index variations (Fresnel effect), which could be employed for detecting the defects, measuring the fiber length or checking the performance of connectors [1].

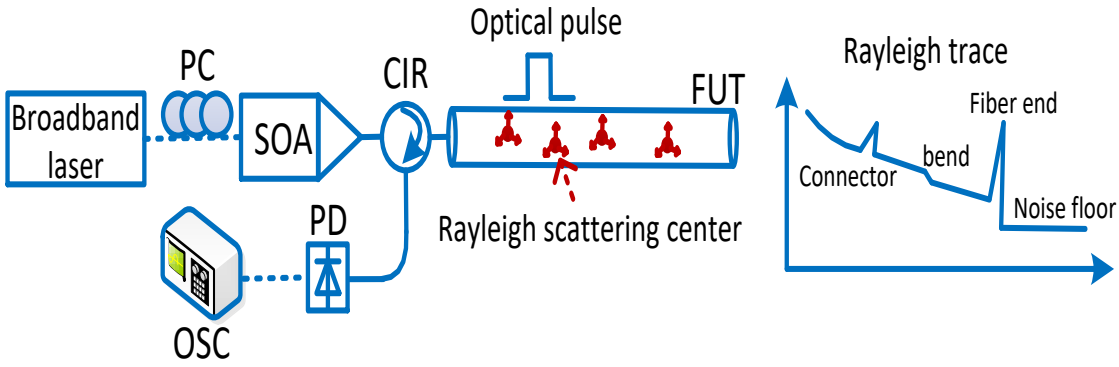

Figure 3.1: Schematic diagram of an OTDR system and the typical back-scattered Rayleigh traces in time domain.SOA: semiconductor optical amplifier; FUT: fiber under test; PD: photo-detector; OSC: oscilloscope; CIR: circulator; PC: polarization controller.

The transmission attenuation could be spatially monitored by Rayleigh scattering-based OTDR system, which is a direct way to achieve distributed sensing. One source of power loss is micro-bending loss [52], which increases local attenuation in single-mode fiber. Based on that, A high-sensitivity fiber-optic micro-bend strain sensor for detecting the bending of large mechanical structures has been constructed [53] [54]. In

addition, lateral pressure measurement on optical fiber has been developed [55] that places a fiber inside a spiral sheath that induces micro-bending in the fiber when a lateral force is applied. Moreover, a liquid hydrocarbon sensor is designed such that liquid swelling polymers transducer their swelling into a micro-bend force on optical fiber when exposed to hydrocarbon fuels [56]. The first demonstration to measure the change of scattering intensity due to the local temperature change was in 1983 [57] by using a fiber with liquid-core as a sensor. However, the major problem of using attenuation detection for achieving distributed sensing is that the larger attenuation coefficient makes the available optical power for downstream interrogating locations very low after the high-loss sensing point.

3.1.2 Polarization-OTDR

To achieve long-distance distributed measurement with a larger number of sensing points, the measurand under test is required not to affect the attenuation of the fiber too much. In 1980, the polarization-OTDR (POTDR) was proposed by Alan Rogers [58] by using the basic concept that the backscattered light maintains the SOP in the Rayleigh scattering. The typical setup of POTDR system is shown in Figure 3.2. Unlike the conventional OTDR system, the generated optical pulse passes through a polarizer 1 and is completely polarized. It is noted that the light source used here has a narrower linewidth of about 0.1 nm rather than 10-20 nm in conventional OTDR, to avoid light depolarization. Given the fact that the SOP of the probe light keeps changing along with the single-mode fiber, the backscattered light will preserve the incoming polarization states. After that, the Rayleigh backscattered light is detected with a periodically variations after passing through another polarizer 2. In other words, the SOP variation of the probe light is measured by optical intensity as it propagates along the fiber, which indicates the information about the distributed polarization properties of the fiber, such as Polarization mode dispersion (PMD) and birefringence. So, the

distributed measurement could be achieved by monitoring the intensity profile change since the SOP of light is sensitive to external disturbances, such as PMD [59], Faraday effect [60] [61] [62], fiber bending [63] [64] and lateral pressure [65].

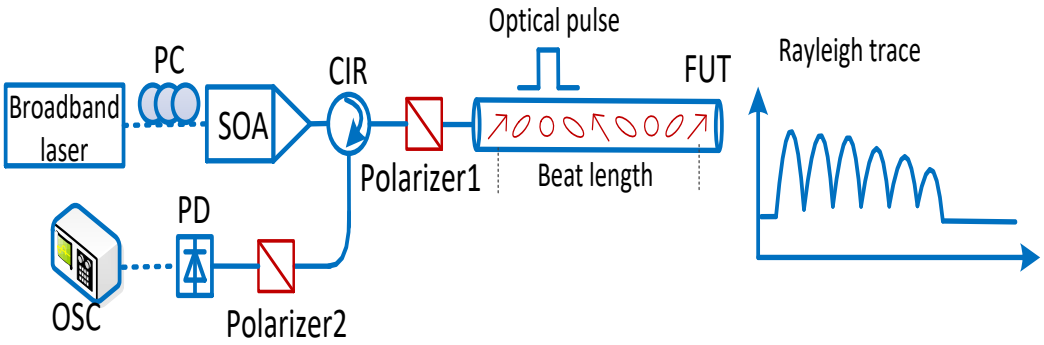

Figure 3.2: Schematic diagram of a polarization-OTDR system and the typical back-scattered Rayleigh traces in time domain.

POTDR has advantages in applications requiring fast response and high positioning accuracy. The reason is that the SOP of the light at a specific location is also related to the locations before it. Thus, SOP changes in one location will make the following Rayleigh signals after the perturbation point change together, which detects the external disturbance quickly and accurately locates the perturbation point. However, this mechanism also has some problems. Firstly, in conventional fibers, the SOP is affected simultaneously by many potential measurands, and it is problematic to apply this technology to sense just one measurand reliably [1]. Secondly, due to the downstream perturbations will be hidden by the disturbance at upstream locations, the multiple events at different locations are hard to be demodulated simultaneously [66].

Thus some solutions have been proposed to overcome this issue and achieve multiple events detection. A novel image processing and an automatic-clustering algorithm are proposed to achieve multi-point disturbance detection based on the identifiable temporal-spatial evolving information of the multiple individual events [67].In [68], authors propose a distributed vibration sensor with a 2 km sensing length and 10 m spatial

resolution in which 5 kHz vibration frequency and double events were detected using frequency spectrum analyzing method. More importantly, two simultaneous disturbances with the same frequency can be successfully identified by plotting the magnitude of a specific frequency component from an FFT spectrum along the fiber position. Another proposed method to detect two events with identical frequencies is that FFT obtains the phase of the vibration signal along the fiber. Therefore, two vibration events with the same frequency could be distinguished effectively using the phase distribution pattern.

3.1.3 Phase-sensitive OTDR

Rayleigh scattering-based DOFS in OTDR scheme could be mainly divided into three categories: OTDR, Polarization OTDR, phase-sensitive OTDR ($\varphi-$OTDR) [69] [4] [70]. Polarization OTDR has been demonstrated for extracting the vibration frequency in distributed dynamic sensing, but only the phase-sensitive OTDR could extract not only the frequency but also the amplitude of the perturbations. A major difference between $\varphi-$OTDR and the other two types of schemes is the laser source. The linewidth of the laser source used in $\varphi-$OTDR is much narrow, which ensures the backscattered light within the pulse width is coherent. Recall the Rayleigh scattering is due to the localized in-homogeneity of the refractive index of the medium, and the re-emitted light from the polarized dipoles has a fixed relationship with incident light. Because the narrow linewidth laser has a longer coherent length, the propagating pulse shines the light with a consistent phase over the coherent length covering the fiber section corresponding to half pulse width, resulting in the re-radiated light consists a collection of electric fields with fixed phase relation and a random phase term depends on its random disposition. As shown in Figure 3.3, the intensity of the reflected light at the input end is the sum of the interference between any two re-radiated lights within the pulse width. The random fluctuation of the Rayleigh traces (backscattered light) shows a static speckle pattern fundamentally determined by the in-homogeneity

property of the fiber.

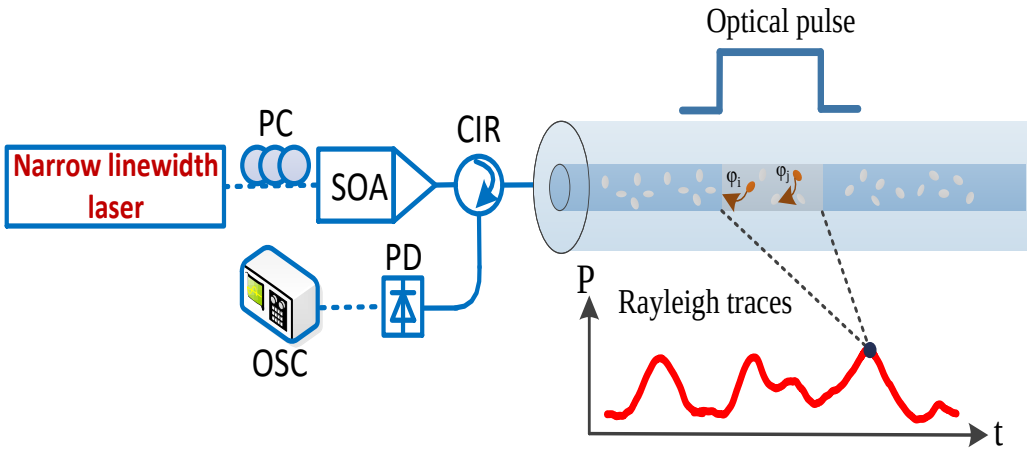

Figure 3.3: Schematic diagram of an polarization-OTDR system and the typical back-scattered Rayleigh traces in time domain.

The Rayleigh traces profile is pretty much constant if no perturbation is applied to the fiber. While in the presence of external perturbation, the optical path length between any two scattering centers within the perturbed fiber section is altered, resulting in a local fluctuation intensity of the Rayleigh traces. In 1993, Taylor and Lee first proposed an intrusion detection system base on this concept in a patent application [2]. Benefiting from the single-shot measurement and direct intensity-based demodulation, this demodulation method is a good candidate for high-frequency dynamic strain sensing by simply monitoring the intensity changes between adjacent Rayleigh traces. [71] [4] [72]. In [72], Authors demonstrate a high-frequency vibration sensing system merging a Mach–Zehnder interferometer and $\varphi-$OTDR, in which the frequency information is obtained by demodulating the interference signal, and vibration points are located by $\varphi-$ OTDR system, resulting in the combined benefits of MZI, and $\varphi-$OTDR allow this new scheme for high-frequency responses up to 3 MHz with satisfied spatial resolution about 5 m. However, the relationship between the magnitude of a distributed applied disturbance and the change in the intensity of the back-scattered Rayleigh traces is not linear. Thus conventional amplitude demodulation cannot be

used in $\varphi - \mathrm{OTDR}$ to measure the magnitude of the disturbance.

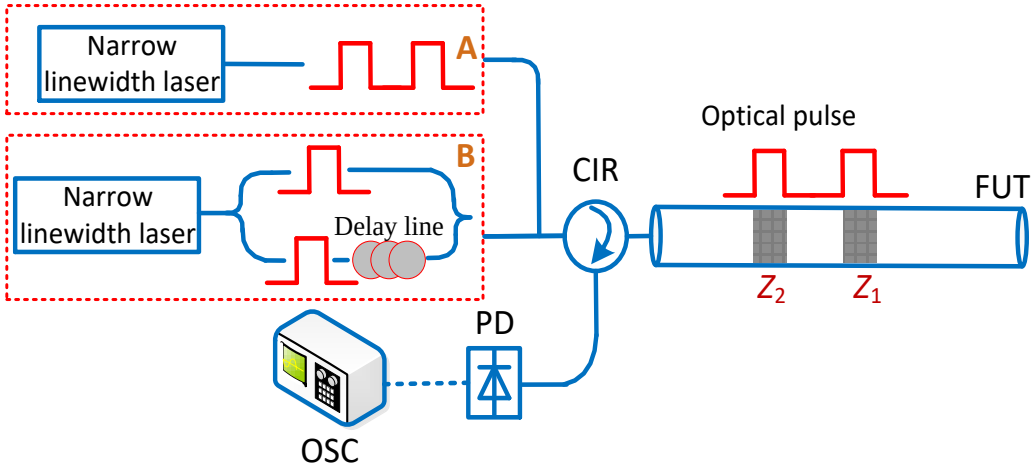

Figure 3.4: Two schematic diagrams of dual pulse phase sensitive OTDRs. A: Two pulse cascaded with time separation; B: Two pulses connected in parallel with delay line in one branch.

To quantify the amplitude of external perturbation, the phase information of Rayleigh backscattered light should be extracted since the phase difference between the backscattered light from two ends of the perturbed fiber section is linearly proportional to the optical path length change (related to the effective refractive index and physical distance). For this purpose, several techniques for phase demodulation for quantitive measurement have been proposed:

(1) *Dual pulse system*: a pair of pulses with different optical frequencies is injected into the fiber under test with time separation related to the desired spatial resolution. As shown in Figure 3.4, due to the fixed time interval between two pulses, the backscattered Rayleigh signals from these two pulse regions will arrive at the detection end at the same time. The mixed term is directly related to the fiber section between two scattering zones (Z_1 and Z_2) and its phase is determined by the optical path length between two scattering zones. Therefore, the phase of the beat signal at each position along with the fiber has a linear relationship with applied external disturbance on that fiber section, such as strain and temperature variations. This configuration is

initially proposed by Dakin and Lamb [73]. One drawback of this method is that the laser frequency drifting noise between the generation of two pulses will affect the mixed Rayleigh signal. To eliminate this potential noise, an optimized scheme is proposed in [74], as shown in Figure 3.4. The output of the narrow linewidth laser is split into two paths, each of which encounters an Acousto-optic Modulator (AOM) that creates a pulse with frequency shifts. In the bottom arm, a delay line adjusts the time separation between two pulses. In 2014 [75], by controlling the phase of the second half of the probe pulse signal after the intensity modulation, the single pulse rather than the pulse pair is launched into the fiber for phase recovery. The first and second half within the single pulse could be regarded as a pulse pair, similar to the dual-pulse scheme, but with a fixed spatial resolution of half the distance occupied by the pulse. In addition, the same group also modulates the phase of dual pulses rather than frequency, showing that this sensing technique can measure 230 Hz periodic perturbations along a 2 km long sensing fiber with a spatial resolution of 5 m.

(2) *Interferometric phase recovery*: In 2000, a novel setup for measuring the relative phase between two sections of fiber based on Mach-Zehnder interferometer (MZI) was first proposed by Posey ea al [3], as shown in Figure 3.5. In 2013, Masoudi et al. used the same interferometric phase recovery principle and demonstrated a dynamic strain sensor with a spatial resolution of 2 m and a frequency range of 500–5000 Hz [76]. The minimum detectable strain perturbation of the sensor was measured to be 80 nano-strain. In this technique, the single pulse is launched into an imbalanced MZI having a different path due to the delay line in the receive path to compare the phase of backscattering light return from separate parts of the fiber (Z_1, Z_2). The imbalanced MZI includes a 2×2 coupler and a 3×3 coupler, and the mixed backscattering light after delays is then sent to the 3×3 coupler to provide a 120 degree phase difference between each of the three outputs. Finally, the relative phase difference at one fiber section could be extracted based on the intensity information from the Rayleigh time-domain

traces. The intensity of three outputs of the 3×3 coupler that with 120 degree phase shift is given by [77]:

$$\begin{aligned} I_1 &= I_0[M + N\cos(\varphi)], \\ I_2 &= I_0\left[M + N\cos\left(\varphi + \frac{2\pi}{3}\right)\right], \\ I_3 &= I_0\left[M + N\cos\left(\varphi - \frac{2\pi}{3}\right)\right], \end{aligned} \tag{3.1}$$

where M and N are constant, φ is the phase difference of the light returning through the two arms of the MZI, and I_0 is the intensity of the input signal. The dynamic extension between the fiber section Z_1 and Z_2 will alter the differential phase, which is spatial resolved along the fiber.

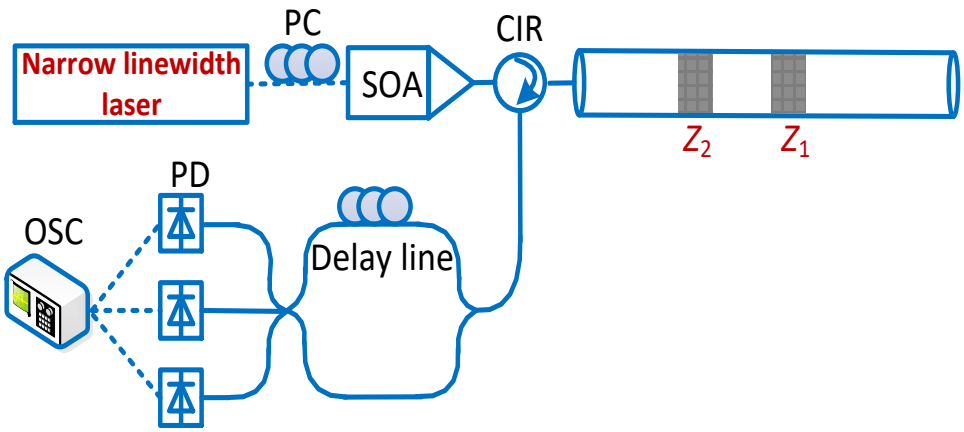

Figure 3.5: Two schematic diagrams of interferometric phase recovery-based phase sensitive OTDRs.

Besides, another interferometric phase recovery technique in φ-OTDR based on an unbalanced Michelson configuration is also studied [78] [79]. By using Faraday rotation mirrors, the problem of the relative alignment of the polarisation state of the interfering light is solved. Moreover, the Phase-generated carrier method is recently proposed and carried out as an interferometric phase recovery technique to recover the phase information by Fang et al. [80]. In the experiments, a phase modulator driven by Piezoelectric transducer (PZT) is added into one interferometer arm for generating

specific tones in the detected signal, clearly showing the feasibility of single frequency vibration event detection over 10 km fiber length with a spatial resolution of 6 m and the Signal-to-noise ratio (SNR) of 30.45 dB.

One drawback of these techniques is the SNR. Since several couplers are used and thus attenuate the reflected Rayleigh signal, the longer pulse width is required to improve the optical power at the detention end, which limits the spatial resolution to a few meters. In addition, high thermal and mechanical stabilization is usually required for MZI based scheme since the interferometer is a highly sensitive sensor to external environmental noises. This fact, together with the demand for a precise coupler and three identical photo-detectors, hinders its application beyond tests under laboratory conditions [81].

(3) *Coherent detection*, which is originally from the optical communication community and has the capacity to perform phase recovery, is based on optical and electrical mixing of the backscattered signal with a local oscillator (LO) in optical and electrical domain [82]. Unlike the previous technique, the phase information in coherent detection is carried out from the electrical domain rather than directly from the optical domain [83]. Among coherent detection scheme in φ-OTDR, the optical frequency of optical local oscillator could be same ((homodyne [84] [85]) or different (heterodyne [83] [86] [87] [88]) with the frequency of Rayleigh backscattering signals. As Shown in Figure 3.6 (a), highly coherent light emitted from a narrow linewidth laser is split into two branches; one path is frequency and intensity modulated by an AOM with frequency shifts of Δf. A circulator is used to launch the pulses into the sensing fiber and to direct the backscattered Rayleigh signals to the balanced receiver via a further coupler that mixes the backscattered signals with the reference signal from the narrow linewidth laser. Finally, the mixed electrical signals with a typical frequency of Δf is collected by Oscilloscope (OSC) for the phase demodulation. The phase of the backscattered light is measured via the down-shifted mixing signals that retain

that phase information and yet are at a frequency that can be handled in the electronics. In-phase/Quadrature (IQ) phase demodulation [89] [85] and Hilbert-transform phase demodulation [90] [91]are two main techniques used in coherent detection based φ-OTDR schemes.

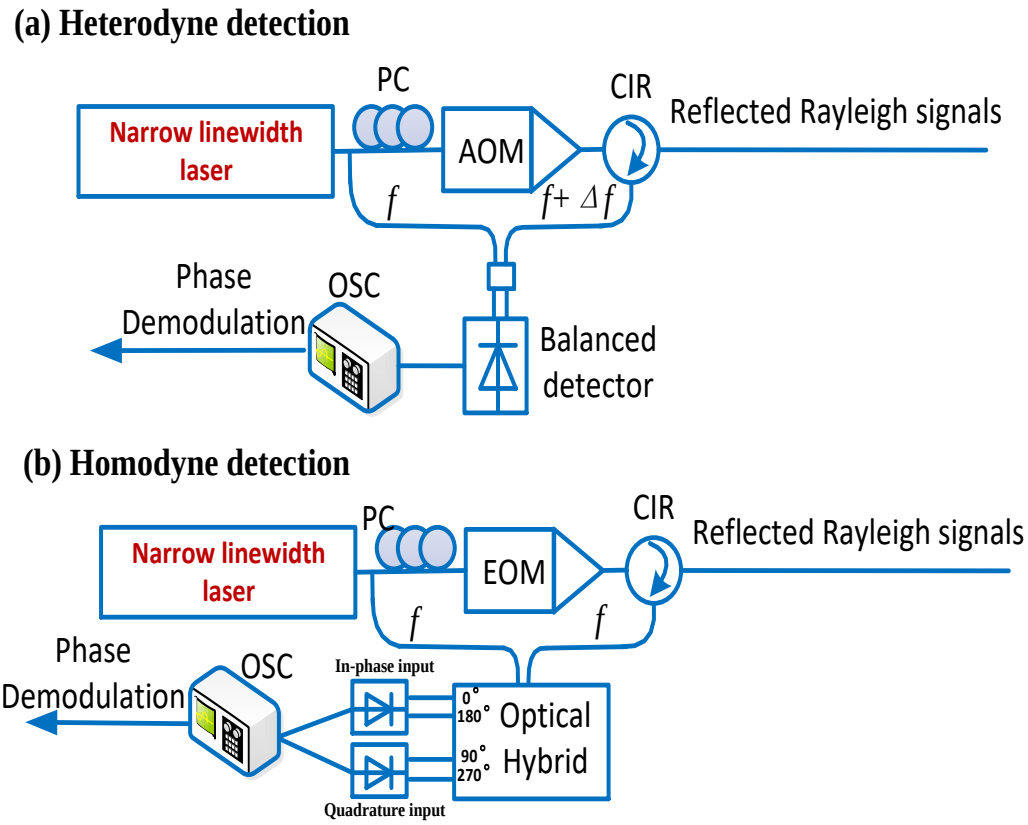

Figure 3.6: Two schematic diagrams of coherent detection-based phase sensitive OTDRs. (a) Heterodyne detection; (b) Homodyne detection.

In IQ demodulation, The heterodyne signal output by a detector is mixed with the two parts of the local signal with a frequency of Δf. The local signal should be split into two parts; one part is applied with $\pi/2$ phase shift, and another one keeps the initial phase. Then the In-phase and Quadrature components could be obtained after sending the two outputs of the hybrid signals to the low pass filters to remove the

high-frequency components, which could be expressed as [89]:

$$\begin{aligned} I(t) &= \frac{1}{2} I_S(t) I_{\mathrm{LO}} \sin[\varphi(t)], \\ Q(t) &= \frac{1}{2} I_S(t) I_{\mathrm{LO}} \cos[\varphi(t)], \end{aligned} \tag{3.2}$$

where $I_S(t)$ is the amplitude of the heterodyne signal, and I_{LO} is the amplitude of the local signal. φ is the difference between the initial phases of the local signal and the heterodyne signal. Then, the amplitude and phase of the Rayleigh scattered light are given by:

$$\begin{aligned} I_S &\propto \sqrt{I^2(t) + Q^2(t)}, \\ \varphi(t) &= \arctan(I(t)/Q(t)) + m\pi, \end{aligned} \tag{3.3}$$

where $m\pi$ is used to unwrap the arc-tan function, and m is an integer number so that the range of the demodulated phase changes from negative infinite to positive infinite [86]. The heterodyne signals could also be Hilbert-transformed first. The transformed and the original heterodyne signal are used as the I and Q components in the I/Q demodulation process to extract the phase information [91].

Another potential arrangement of coherent detection is Homodyne detection based φ-OTDR [92], in which the interrogation signal is only intensity modulated by the Electro-Optic Modulator (EOM) without optical frequency shifts, resulting in the same frequency between an optical local oscillator (OLO) and the Rayleigh backscattered signal. Thus the mixed signal is in the baseband, and only low-speed ADC is sufficient for detection, allowing the phase difference to be unwrapped and tracked in slow time. It is noted that the phase information measured here is the phase difference between the Rayleigh backscattered signal and the OLO, so the phase difference will continuously increase along with the fiber. A valid approach in a real application is to calculate the phase difference across a certain fiber length determined by spatial resolution by simply subtraction for quantifying the external perturbations.

The coherent detection technique has some advantages: Firstly, the power of the mixed signal at the detector end depends on the Rayleigh backscattered signal and

OLO power. Thus the noise could be highly suppressed by setting a sufficient strong OLO signal, and the low SNR due to the inherent attenuation of the fiber would not be a problem. In addition, the balanced detection can further reduce the DC noise and increase the SNR significantly. The sensitivity of the detected signal can reach a shot-noise limit. Secondly, the signal's dynamic range is improved compared with the single-shot technique without beating with OLO. Since the power of OLO remains constant, making the mixed signal drop more slowly.

However, coherent detection also has some drawbacks: The first is the requirement for a highly coherent laser source, substantially increasing the system cost. And the coherent detection needs the mixing between OLO and Rayleigh signal from fiber, which limits the sensing distance up to the coherent length.

The second one is the fading problems, including intensity fading and polarization fading. Due to the usage of a highly coherent laser source, the backscattered light waves within the half pulse width (spatial resolution cell) are easily destructive interference, giving a super low intensity at the detection end even blow than the noise floor. The polarization fading problem is mainly from the cohere detection scheme, in which the SNR degradation and even complete loss of signal will occur when the SOP of the OLO and Rayleigh backscattered signal are mismatched. To solve this problem, one approach [93] [94] by using multiple interrogation pulses with different wavelengths is proposed to obtain the independently Rayleigh profile and then combine these traces to eliminate the intensity fading problem. The polarization fading problem could be effectively mitigated by the polarization diversity scheme [95].

The third limitation of the φ-OTDR sensing technique is the linearity of its responses. In the demodulation, the perturbations within each spatial resolution cell are reconstructed by the relative phase difference between the two ends of that cell. Thus, the intrinsic phases of the two ends are important for the linearity of the response. And any perturbation in the distribution of inhomogeneities at the two ends results in a

non-linear response between the strain and the measured phase [96].

The last one is the phase noise accumulation problem [87]. It is crucial to notice that variations in the phase accumulate from the point of occurrence until the end of the fiber. Hence, a differentiation process on the recovered phase trace is generally required. This process further increases the detrimental effect of phase noise [81].

3.1.4 Frequency-swept phase sensitive-OTDR

In φ-OTDR, The phase difference between any two scattering centers is proportional to the product of optical path length and the carrier frequency of the interrogation optical pulse. Thus, the external perturbations induced optical path length changes could not only be measured by demodulating the exact phase, but also could be obtained through frequency/wavelength shifts. In the other word, the changes in optical path difference between the scattering centers induced by a uniform refractive index (Δn) and distance (ΔL) change can be compensated by a shift of the pulse frequency Δv, which allows the recovery of the original Rayleigh patterns. Based on the phase matching conditions, the relationship between Overall, the optical frequency change of incident optical pulse to compensate for the strain and temperature variations is given approximately by: [97]:

$$\begin{aligned} \frac{\Delta f_T}{f_0} &= -0.78 \times \Delta\varepsilon, \\ \frac{\Delta f_\varepsilon}{f_0} &= -(6.92 \times 10^{-6}) \times \Delta T, \end{aligned} \tag{3.4}$$

where the Δf_T and Δf_ϵ are the strain/temperature changes induced frequency shifts; f_0 is the carrier frequency of the interrogation pulses. Detailed derivation could be found in Section 10.2.

This technique is firstly proposed in [97], and then has attracted much attention for different applications such as temperature/strain sensing [70], pressure sensing [98] [99], salinity sensor [100]. The sensing principle of the frequency-swept φ-OTDR is shown in Figure 3.7, a pulse train comprising a variety of interrogation pulses with a certain

frequency tuning step is launched into the fiber, and the time interval between pulses should be larger than the round trip time of the pulse to avoid the Rayleigh traces overlapping. Combining the jagged Rayleigh traces from different frequencies, the 2-D intensity map could be reconstructed to show the local spectral response at each given position, as shown in Figure 3.7 (b). This 2-D intensity map is supposed to be unchanged when the fiber is stable without disturbance, which is then unitized as a reference. Once the fiber is subjected to any strain or temperature change, the perturbations-induced frequency shifts could be extracted by performing a cross-correlation calculation between local spectral responses at a given position.

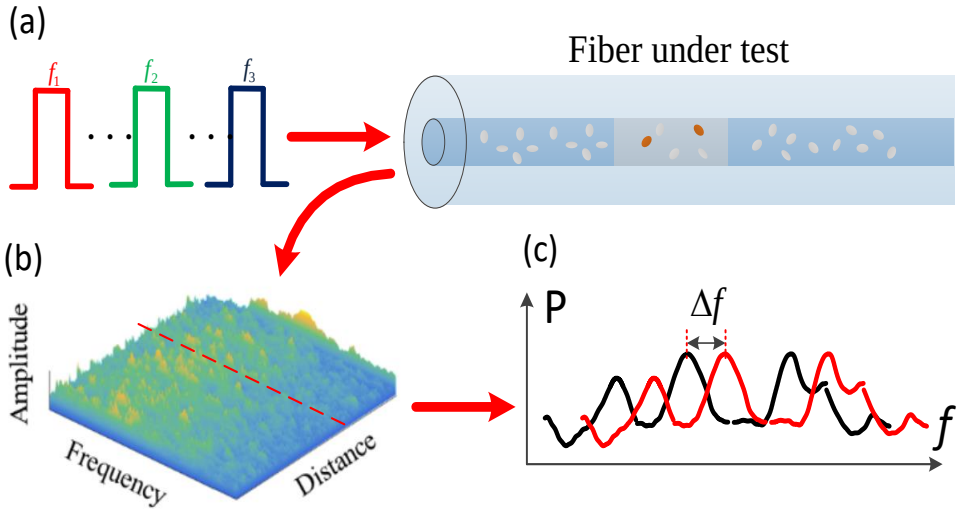

Figure 3.7: Principle of the frequency-swept φ-OTDR. (a) Different frequency pulses are sent into the fiber; (b) Rayleigh scattering spectra along with the fiber and (c) the cross-correlation between local spectrum at a given position before (reference) and after (live measurement) perturbations variation applied.

This technique does not require a coherent detection scheme and a narrow linewidth laser source. However, One drawback of this technique is that the frequency scanning process takes a long time, lowering the acquisition rate of the system.

3.1.5 Chirped pulse phase sensitive-OTDR

To avoid these coherent detection method-induced limitations, including the requirement of a stale interferometer and the intensity/polarization fading, a novel technique using a single pulse with linear frequency chirp without requiring the time-consuming frequency sweep is proposed in 2016 [101]. The change of the Rayleigh patterns due to external perturbations can be calculated by correlation in shifted frequency which is proportional to local optical path length changes, as shown in Figure 3.8. The local time shifts within the selected time window among two different traces can be determined along the fiber by calculating a local correlation of the trace segments obtained for the two consecutive measurements. Rayleigh OTDR gives relative measurement for temperature or strain change compared with reference temperate or strain. Due to its simple arrange and good repeatability, Chirped pulse φ-OTDR has attached increased attentions, and has been employed in many applications, such as temperature [30], dynamic strain sensing [102] [31], birefringence measurement in SMF [103] and PMF [104],Seismic monitoring [105] and sound measurement [106].

Since this technique is highly relevant to the thesis, the detailed theoretical derivation and limitations of this technique are discussed in another chapter, which can be found in Section 4.2.

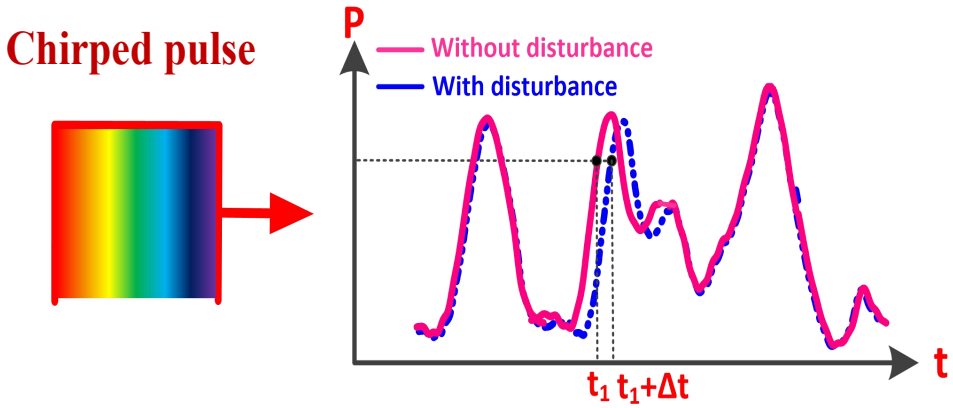

Figure 3.8: Principle of the Chirped pulse φ-OTDR.

3.2 Brillouin scattering-based distributed sensing techniques

Brillouin scattering is an inelastic process by which incident light waves are scattered by acoustic phonons. The interaction between the photos and phonon in the process must satisfy the phase-matching condition and thus appear as a narrow spectral resonance, which makes the scattering process very sensitive to temperature or strain changes. Compared to the Rayleigh scattering or Raman scattering-based distributed temperature sensors, Brillouin scattering-based distributed sensors provide a high spatial resolution over long sensing ranges due to the high SBS gain from narrow linewidth (MHz) and low power requirement for the high gain amplification [107].

Distributed Brillouin scattering sensing was first proposed and demonstrated by Horiguchi and Tateda as a method for measuring the attenuation of optical fibers in 1989 [9]. After that, due to the advantages of high scattering efficiency and high sensitivity to temperate and strain changes, Brillouin scattering has been widely used for distributed sensing applications. The Brillouin frequency shift in fiber is decided by two main factors, including the velocity of sound in the medium as well as the index of refraction. In the time domain-based Brillouin scattering sensing systems, the spatially resolved temperature/strain measurement is achieved by sending a narrow optical pulse as the probe signal to interrogate the acoustic wave in the optical fiber, and the location is mapped through the flight time of the pulse from the source to the fiber location.

3.2.1 BOTDR

Brillouin optical time domain reflectometry (BOTDR) is similar to the Rayleigh OTDR system, except the physical mechanism behind it is the spontaneous Brillouin scattering. Figure 3.9 shows the typical setup for the BOTDR system, in which an intense interrogation pulse with high peak power is sent into a fiber to acquire the

distributed time-varied spontaneous Brillouin scattering lightwave. The backscattered Brillouin signal is then optically mixed with an intense local oscillator from the laser source. Finally, the temperature or strain changes-induced Brillouin frequency shifts could be obtained by analyzing the electrical spectrum of the beating signal on the ESA. Such a coherent detection process could also enhance the sensitivity of the system [6]. In addition, the single-end access is attractive for the field test, especially when the sensing fiber is broken.

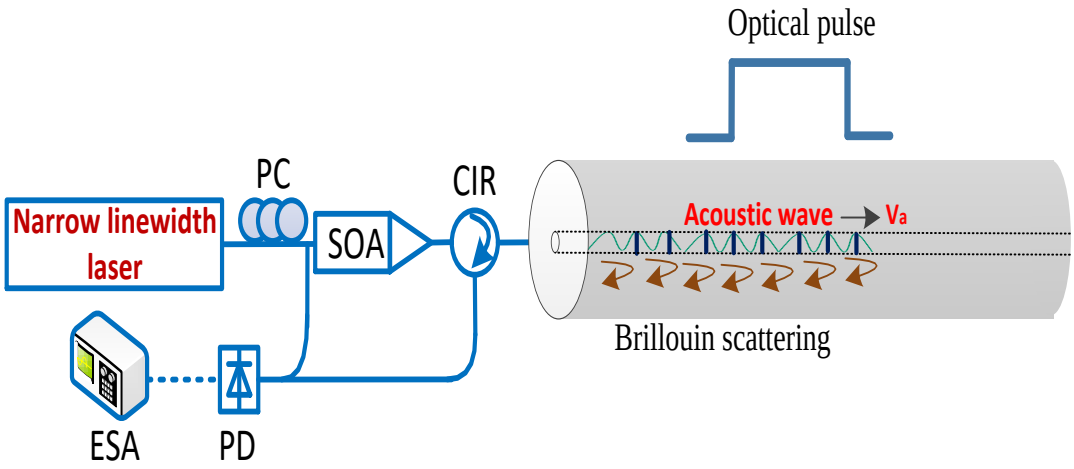

Figure 3.9: The generic layout of a Brillouin optical time domain reflectometry (BOTDR) setup. ESA: Electrical Spectrum Analyzer; SOA: semiconductor optical amplifier; PD: photo-detector; CIR: circulator; PC: polarization controller.

However, the BOTDR detection requires a substantial number of averaging for time domain traces to reach the acceptable SNR. Besides, the reconstruction of Brillouin gain by using a microwave detector is a slow process. These two factors make BOTDR hard to be used for high-frequency dynamic measurement. In [108], authors demonstrate a distributed vibration sensor, in which the vibration of fiber can be continuously monitored based on the principle of the POTDR, and the applied strain on the fiber is measured based on the principle of the BOTDR. Experimental results show a detection of 11 Hz vibration over 4 km fiber with 10m spatial resolution. Another approach to improve the acquisition rate by converting the Brillouin frequency shifts into the in-

tensity changes through an imbalanced MZI is demonstrated [76]. The results show an acquisition rate of 2 Hz with a strain sensitivity of 50 $\mu\epsilon$ over 2 km of sensing fiber with a spatial resolution of 1.3 m, and a maximum detectable frequency of up to 1 Hz.

3.2.2 BOTDA

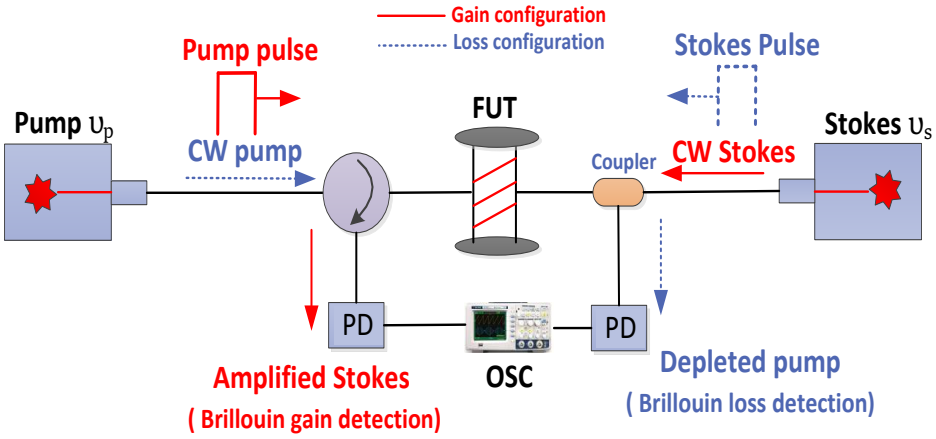

Figure 3.10: The generic layout of a Brillouin optical time domain analysis (BOTDA) setup. Red solid line is Brillouin gain detection, and the blue dashed line represents the Brillouin loss configuration.

Brillouin optical time domain analyzer (BOTDA) is a two-ends access interrogation system, relying on the stimulated version of Brillouin scattering. This technique is based on the pump-probe configuration, in which two light waves are launched from both ends of a single fiber: one of the optical signals is continuous, and the other is pulsed. As shown in Figure 3.10, in the Brillouin gain scheme, the intense pump pulse signal will generate a moving density grating (acoustic wave) in the fiber core via the electrostriction effect. Once the frequency deviation between the pump and probe light is around the BFS of the optical fiber, the dynamic grating will be further enhanced due to the nonlinear interaction. Therefore, more pump light will be scattered by the dynamic grating, resulting in an increase in the probe power. So the counter-propagating probe light and acoustic wave mutually reinforce the intensity of each

other. Due to the usage of pulsed pump light, the local information could be spatially resolved. One significant drawback of this configuration is that the energy of the short pump pulse is continuously transferred to the CW probe light. Thus the power of the pump signal will be depleted quickly due to the energy conversion, namely non-local effect [109] [110] [111]. This problem could be released by Brillouin loss detection configuration [112]. In this Brillouin loss configuration, as shown in the blue dashed lines ofFigure 3.10, the roles of the pump wave and Stokes wave are reversed. The Stokes wave is now pulsed, and the pump wave is CW and is the waveform detected at the output. Thus, the energy in the pump wave is much larger, and loss to the Stokes wave will not result in significant depletion [113]. The advantage of this technique is that much longer sensing lengths become possible.

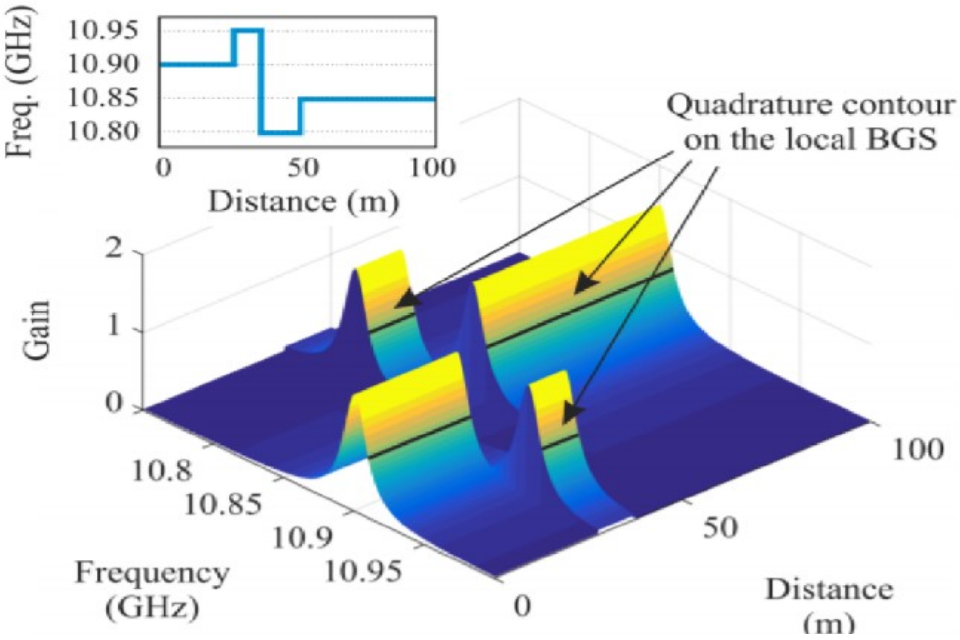

Figure 3.11: The principle of extracting the local Brillouin frequency shifts [114].

The BOTDA measurement usually requires a frequency sweep over a certain range to obtain the potential local BFS that alters with absolute valuer of external strain [115] and temperature [116]. In the demodulation process, as shown in Figure 3.11, by scanning the frequency deviation between pump and probe light wave step-by-step, the

local Brillouin gain along the fiber is measured by the intensity of the probe wave at a given pump-probe frequency difference. On the other hand, the local BGS could be obtained by analyzing the gain distribution within the frequency scanning range. The local BFS is calculated by fitting the BGS and picking the peak value. Such a fitting process can help to remove the system noise-induced error in peaking frequency determination [117].

Different from the Rayleigh scattering-based OTDR system, the local gain not only depends on the pump-probe frequency deviation and local BFS but also on the relative SOP of the pump and probe light. The SOP effect could be minimized by scrambling the polarisation states of pump light to randomize their interaction. Another challenge to reconstructing the BGS is that the frequency difference between the two independent pumps and the probe laser source is supposed to be well controlled for the precise frequency scanning process. One effective way is to lock the frequency deviation of two DFB lasers at the Brillouin frequency by a hardware proportional-integral-derivative (PID) controller, namely, offset locking technique [118]. Besides, the requirement of high suitability of frequency difference scanning is also could be achieved by using a single laser and EOM [119], in which the single laser source is frequency modulated by an EOM that is driven by a microwave signal at a desired electrical frequency to generate modulation sidebands at a different optical frequency around carrier light wave. Thus, the modulation sideband with lower frequency/high frequency could be used as a probe signal in the gain/loss detection-based BOTDA system. The frequency spacing between the pump and probe is determined by the microwave frequency that has high stability, and the frequency drifting of the laser source has no impact.

3.3 Four key parameters in distributed Rayleigh/Brillouin fiber-optic sensing.

3.3.1 Sensing distance and SNR

The sensing distance of the sensor is defined by the maximum length of sensing fiber that can be measured [1]. In an OTDR-based sensing system, sensing distance is limited by the maximum pulse repetition rate of the interrogation pulse since a too-high repetition rate would make the backscattering signals from the fiber overlapped, resulting in location ambiguity. Beyond that, the fiber attenuation that makes the power of the signal decay exponentially is a major limitation for achieving long-haul measurements. In an OTDR-based system, the maximum length of sensing fiber is weighed by the dynamic range:

$$R = \frac{1}{2}\left[10\log\left(\frac{P_0 - S}{P_{\mathrm{D}}}\right)\right], \tag{3.5}$$

where P_0 is the power of Rayleigh scattering light at the far end of the fiber; P_D is the minimum detectable power by Photo-detector (PD); S is the transmission loss. Thus, a longer sensing distance could be achieved by either improving the signal power, which is related to pulse energy, Rayleigh reflection and transmission loss or lowering the system's noise level. Erbium Doped Fiber Amplifier (EDFA) could increase the power of the pulse signal to extend the sensing distance, but further enhancement is limited by the nonlinear effect, such as Modulation Instability (MI) and Brillouin scattering, especially for narrow pulse scenarios. In 2009, the first-order Raman amplification was first reported to increase the pulse power and then improve the sensing distance by suppressing the nonlinear effect [120]. Using the bidirectional scheme with even amplification, sensing distance up to 62 km in φ-OTDR is achieved. The gain coefficient of SBS is larger than that of stimulated Raman scattering (SRS) by about three orders

of magnitude, which allows the use of much lower pump powers. The major concern of using the Raman application is that the Relative intensity noises (RIN) of the Raman pump will be transferred in the signal, lowering the SNR [121]. One solution to remove the RIN is achieved by creating an ultra-long Raman fiber laser cavity in the sensing fiber, then the RIN noise is completely eliminated by implementing a suitable balanced detection, which achieves a sensing distance of 125 km and an average SNR of 8 dB in φ-OTDR [122]. Brillouin scattering is firstly utilized to amplify the pulse signal, and 124 km sensing distance is achieved based on heterodyne detection [123]. However, one disadvantage of using the Brillouin amplification is that the temperature-sensitive gain will cause instability of the system. In the same year, using the combination of co-pumping second-order Raman amplification based on random fiber lasing, counter-pumping first-order Raman amplification, and counter-pumping Brillouin amplification, a sensing distance of 175 km with 20 m spatial resolution in φ-OTDR is achieved [124]. The CW portion of the pump pulse signal related to extinction ratio will introduce a noise floor from coherent Rayleigh scattering along the entire sensing fiber. Thus, in [125], a vibration event at 26.5 km is successfully detected by using high extinction ratio pulse up to 100 dB with a spatial resolution of 2 m. Other methods to compensate for the power losses have been proposed recently, including bidirectional EDFA (B-EDFA) [126], optical repeaters (two EDFAs and one Raman amplifier) [127], cascaded AOMs [128].

SNR is a crucial factor in determining the sensing length, sensitivity, and accuracy. To avoid the interference fading noise, a phase-shifted pulse pair is used to gain an SNR of more than 20 dB [129]. Pulse coding [130] [131] and pulse compression [132] are utilized to achieve better SNR but a more complex computation process. Furthermore, by using ultra week Fiber Bragg grating (FBG) array [133] or enhanced backscattering fiber [134], the intensity of the Rayleigh backscattering light could be raised to improve the SNR, and the enhancement is up to 15.8 dB. To suppress the polarization-related

noise, a system based on an all-polarization-maintaining configuration is proposed to eliminate polarization-induced signal fading and noises in 2011 [135]. In 2006, a polarization diversity detection method was proposed and demonstrated to release the impact of fading noise, and the SNR was improved by about 10.9 dB.

In Brillouin scattering-based sensing system, the increase of pump pules and CW probe powers to enhance the sensing distance is also constrained by nonlinear effects, such as Kerr effect [136], Modulation instability [137], and non-local effect [138]. The Kerr effect will give rise to a pulse spectrum broadening anomalous and normal dispersion fibers, which could deteriorate the system performance and reduce the sensing length. Modulation instability becomes a big issue when a square pulse is used in anomalous fiber. And it will cause discrete spectral broadening by inducing additional discrete spectral lines [139], which could be significantly suppressed in a normal dispersion fiber [136]. The non-local effect is mainly caused by the pump pulse depletion or probe pulse excessive amplification, resulting in distorted Brillouin gain spectra and systematic measurement errors. Several technologies have been proposed to achieve longer sensing distance in Brillouin scattering-based sensors:(1) Time-division multiplexing [140]: Both pump and probe signals are pulsed, and the interrogation length is determined by the probe pulse width rather than the entire fiber length. Then, the entire fiber length is measured by changing the relative time delays between the pump and probe pulse. Increasing the power of the probe pulse, SNR could be improved without non-local effect, giving a 100 km sensing length with 2 m spatial resolution. (2) Frequency-division multiplexing [141]: Multiple sections of sensing fiber with different BFSs are used so that the interaction fiber length is restricted to each BFS section, reducing the non-local effect. (3) Distributed Raman [142] or Brillouin [143] amplifier for compensating pump attenuation along the fiber for 100 km sensing range. (4) Pulse coding technique [144] could effectively improve the SNR and thus extend the sensing distance by scarifying the sensing speed and increasing the system computation

complexity. And (5) Optimizing image denoising method [145].

3.3.2 Spatial Resolution

In an OTDR-based sensing system, the spatial resolution is determined by the pulse width. For spatial resolution improvement in φ-OTDR, In 2010 [4], Lu et al. proposed a moving average and moving difference algorithm method based on the heterodyne detection, achieving 5 m spatial resolution. In 2013 [146], Zhu et demonstrated a two-dimensional edge detection method to reduce the spatial resolution from 5 m to 3 m by using a 50 ns pulse over a 1 km sensing length. Optical frequency domain reflectometry (OFDR) is a well-known technique based on Rayleigh scattering offering mm range spatial resolution. The spatial resolution is given by:

$$\delta z = \frac{v_g}{2 \cdot \Delta f}, \tag{3.6}$$

where v_g is the group velocity of the light; Δf is the frequency scanning range. Thus the spatial resolution is given by the range of frequency in the probe sweep. Although this technique offers an ultra-high spatial resolution, a long sensing distance that requires a good coherence of light and sweeps linearity is still a big challenge. Since it suffers from laser phase noise when it comes to long distances, the extracted phase term becomes inaccurate during the sweep process over a large range. To overcome this issue, a time-gated digital OFDR (TGD-OFDR) technique is proposed [147], in which the probe is chirped within a narrow time window with good linearity and low phase noises, achieving long sensing distance up to 110 km with a good spatial resolution of 1.64 m. By using a $LiNbO_3$ intensity modulator with e large modulation bandwidth in the same system, a higher spatial resolution of 0.8 m is achieved [148]. In 2015, Zou et al. proposed an optical pulse compression technique based on the concept of frequency-modulated pulse compression in microwave radar, showing a spatial resolution of 47 cm for detecting Fresnel reflection at the end of the fiber over 5.4 km [149]. This

technique uses linear frequency modulation (LFM) optical pulse with a relatively long pulse duration to achieve long sensing distance. Then the pulse compression technique is used by applying matched filter at the receiving end to achieve high spatial resolution. The spatial resolution is determined by the frequency sweep range rather than the pulse width. Later, this technique was used in φ-OTDR system to demonstrate high spatial resolution up to 30 cm over 19.8 km sensing length [132]. By the same author, a new scheme with a high linearly frequency swept low-frequency RF source is used to guarantee the frequency modulation linearity, achieving 0.95 m spatial resolution over 75 km sensing length [150].

The spatial resolution in Brillouin scattering-based sensing system is limited to 1 m. The reason is that the spectrum of the backscattered signal is attributed to the convolution of the pulse spectrum and natural Brillouin gain spectrum, and the measurement contrast and accuracy get worse when the pulse spectrum width increases, especially when it is larger than the natural Brillouin gain spectrum. To solve this problem, several techniques are proposed, including the dark-pulse technique, pulse pre-pump (PPP) technique, differential pulse-width pair (DPP) technique, and Brillouin echo technique.

The dark-pulse technique was proposed by Brown et al in 2005 [152]. This method is employed in the Brillouin loss scheme. The pump signal, as shown in Figure 3.12 (a) and CW anti-Stokes probe signal, are injected into the two ends of the fiber. The CW portion of the pump experiences amplification since the energy is transferred from the probe signal to the pump, while the pump does not have Brillouin gain when switched off during the dark-pulse duration. Since the pulse duration is much shorter than the CW portion in the pump signal, the Brillouin gain spectrum will keep its natural linewidth but gives a high spatial resolution of up to 5 cm over 100 m fiber. In 1999, Bao et al. found a way to achieve a sub-meter spatial resolution method by pre-excitation the acoustic wave to keep the Brillouin gain spectrum maintain its

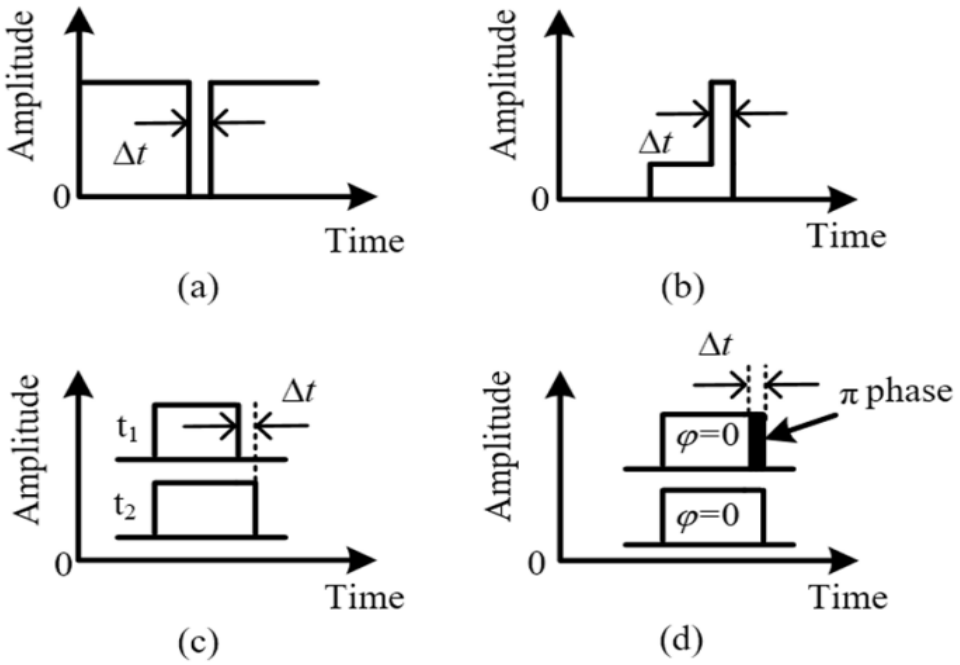

Figure 3.12: Four high spatial resolution techniques in BOTDA. (a) Dark pulse; (b) PPP technique;(c) DPP technique; and (d) Brillouin echo technique [151].

natural value [153]. In 2005, the pulse pre-pump method was proposed [154] as shown in Figure 3.12 (b), in which a pre-pump pulse is introduced to pre-excite the acoustic wave before the bright pulse comes in. The bright pulse interacts with the probe signal and gives high spatial resolution and a narrow Brillouin spectrum. By using this technique with a 13 ns pre-pump pulse and a 1 ns pump pulse, 10 cm spatial resolution is achieved [154]. In 2008, a novel technique called differential pulse-width pair (DPP) BOTDA was proposed. Two long-duration pulses with slightly different pulse widths are utilized for two measurements, and the differential Brillouin signal is obtained by simply making a subtraction [155]. The Brillouin spectrum is determined by the longer pulse, while the spatial resolution is decided by the pulse width difference between two pulses as shown in Figure 3.12 (c). The improved DPP-BOTDA was demonstrated in 2012 with better SNR, achieving 2 cm spatial resolution over a 2 km sensing length. Later on, by combining a novel scanning process with a larger sensing range, a 1 cm spatial resolution with a 10 km sensing distance is achieve in 2017 [156]. In 2008, the

Brillouin echo technique was proposed for high spatial resolution BOTDA sensor [157], and the pump pulse is shown in Figure 3.12 (d). The acoustic wave is well pre-excited by the non-phase shift portion of the pump pulse and then experiences a decrease when the π phase shift portion is injected into the fiber. The spatial resolution is determined by the π phase shift pulse, achieving a spatial resolution of 10 cm. And a higher spatial resolution was demonstrated up to 5 cm in 2010 [158]. A summarized proposed BOTDA scheme for obtaining higher spatial resolution, sensing accuracy and longer sensing range is shown in Table 1.

Table 3.1: Comparison of the proposed high performance BOTDA schemes

	Spatial resolution	Sensing accuracy	Sensing distance
Compound spectrum			
analysis (1998) [159]	50 cm	40 $\mu\epsilon$	100 m
Dark pulse (2005) [152]	5 cm	40 $\mu\epsilon$	100 m
PPP technique (2005) [154]	10 cm	25 $\mu\epsilon$	km
DPP technique (2008) [155]	10 cm	16 $\mu\epsilon$	12 km
Brillouin echo technique (2008) [157]	5 cm	60 $\mu\epsilon$	5 km
Tailored compensation (2017) [160]	20 cm	29 $\mu\epsilon$	51.2 km
Image Denoising methods (2018) [145]	2 m	20 $\mu\epsilon$	100 km

3.3.3 Acquisition rate

In an OTDR-based sensing system, the acquisition rate (sampling rate) is defined by the repetition rate of the probe pulses, which is restricted by the fiber length. The acquisition rate directly determines the highest measurable dynamic frequency. Due to the Nyquist sampling law, the highest measurable frequency is given by:

$$f_{\max} = \frac{1}{2T_{\min}} = \frac{v_g}{4L}, \tag{3.7}$$

where v_g is the group velocity of the light, and L is the fiber length. $T_{\min}$ is the minimum period of the probe pulses. To increase the highest measurable vibration frequency, a method by combining φ-OTDR and MZI is proposed [72], in which the wide pulse could be treated as continuous light and used in the MZI, while a narrow pulse is employed in the φ-OTDR system to obtain the high spatial resolution. A spatial resolution of 5 m and a maximum frequency response of about 3 MHz are achieved in a 1064 m fiber link when the narrow pulse width is 50 ns. In this method, the major limitation is the cross-talk between the Rayleigh backscattering light induced by the low-intensity pulse light and the location signal, which lowers the SNR and accuracy. To solve the cross-talk problem, time division multiplexing (TDM) [161] and wavelength division multiplexing (WDM) [162] [163] [164] based techniques are proposed to achieve measurable vibration frequency up to 6.3 MHz. Instead of using single-frequency pulses, a novel method by employing a multi-frequency pulse sequence with time sequence in φ-OTDR was demonstrated in 2015 to extend the frequency response range. In the experiments, 30 kHz vibration is detected over 3024 m sensing distance [165]. Similarly, frequency division multiplexed φOTDR (FDM-φOTDR) that can detect the entire distribution of a high-frequency vibration was demonstrated in 2017. The technique is to modify the frequency encoding for high-speed phase monitoring with control software parameters, achieving 80 kHz vibration frequency detection over a 5 km sensing distance [166]. In 2020, An orthogonal frequency division multiplexing (OFDM) method was proposed to multiplex multiple probe pulses into one interrogating period, and the measurement of 25 kHz vibration frequency over 51 km sensing length is achieved [167].

In Brillouin scattering-based sensing system. There are three main factors that limit the acquisition rate of the sensing system: (a) The time of flight, also called round-trip time $T_{\text{round}} = 2nL/c$;(b)The number of averaging N_{avg} to achieve the required SNR; (c) The number of scanning step, N_{freq}, to recovery the BGS. Thus, The overall time

required for a complete BGS spectrum is given by:

$$T_{BGS} = (N_{avg} T_{\text{round}} + T_{switch}) N_{\text{freq}} , \tag{3.8}$$

where T_{switch}, which is the frequency-switching time of the microwave generator.

Recently, many ultra-fast BOTDA systems have been studied to save sweeping time for high-frequency dynamic strain measurement. In the optical frequency comb (OFC) scheme [168], the OFC wave is utilized as the probe signal to obtain the Brillouin gain spectrum (BGS) in the frequency domain, in which the Brillouin beating signal will be amplified by the single-frequency pump pulse via the SBS effect when the frequency deviation span covers the BGS. Then the distributed BGS could be reconstructed by computing the fast Fourier transform of the Brillouin beating signal. However, the frequency interval of OFC limits the spatial resolution to several tens of meters. In a slope-assisted scheme [169], the BGS scanning process is skipped by taking advantage of the linearity at the edge of the BFS to convert the BFS to the amplitude variation so that a single-frequency pump pulse can demodulate the distributed BFS along the fiber. However, the Lorentz shape of the BGS has a limited linear range at the slope edge, resulting in a limited measurement range. In the fast-frequency sweeping scheme [170] [171], T_{switch}, has been significantly reduced. The high-speed reconstruction of the BGS is achieved by fast switching an arbitrary waveform generator instead of synthesizer-based electronic sweeping, in which only a single-shot measurement is required to obtain the BGS in the temporal (spatial) domain. However, the asymmetrical BGS should be reshaped through an algorithm to reduce demodulation errors, making the data process more complicated. Recently, a frequency-sweep fast BOTDA was implemented to achieve fast dynamic measurement in a 10 km fiber [172]. However, the entire distribution acquisition rate is limited by the number of measurement points along a fiber because repeated pulse launching is needed until the whole completed distribution is obtained.

Chapter 4

Theory of Optical chirped pulse generation and sensing

4.1 Introduction

Chirped pulses, known as frequency-swept pulses have been widely used in radar technologies [25], spread-spectrum communication system [173], chirped pulse microwave computed tomography [27] and also other applications covering military and civilian systems such as communications, surveillance, countermeasures, navigation and imaging equipment [174]. Most radar applications make use of long chirped pulses with wide bandwidth, or pulses with a high time-bandwidth product (TBWP), allowing the detection of targets at long distances with improved range resolution. High TBWP chirped pulses could be generated by many photonic approaches, including space-to-time mapping (STM) [175], frequency-to-time mapping (FTM) [176] and Self-Heterodyne Technique [174] [177] [178]. FTM methods attract more attention thanks to their simplicity and low cost. Such technique is enabled by sending a short optical pulse with large frequency bandwidth from mode-locked laser with a fixed repetition rate through a dispersive element (e.g. chirped fiber Bragg grating), so that the accumulated quadratic spectral phase impresses a large linear chirp on the resulting time-domain waveform.

For distributed optical fiber sensing, optical chirped pulses have increasingly gained the attention of researchers, as they can be used as interrogation signals for quantitatively detecting the environmental disturbance along the sensing fiber, without requiring the frequency sweep process. As a novel technique for distributed sensing, it has been widely used for temperature [179], dynamic strain [180] and seismic [181] sensing, based on chirped pulse ϕ-OTDR (CP-ϕ-OTDR) or chirped pulse BOTDA (CP-BOTDA) [182]. Although long duration chirped microwave pulses are required for radar applications, short duration chirped optical pulses are key for fiber-sensing applications. In most chirped pulse based systems, the spatial resolution is limited by the pulse width. An exception is the combination of chirped pulse with non-matched filter [183], but it requires an ultra-high coherent laser source, such that conventional techniques with narrow optical pulses are still of great interest. Therefore, optical chirped pulses with large frequency chirping range and small pulse width, i.e. with large FCR, are required to achieve large static measurement range (Section 4.2) with high spatial resolution. Due to limitations of electrical devices, the optical chirped pulses generated by arbitrary waveform generator (AWG) combined with frequency shifter (FS) usually have small chirping range and wide pulse width, resulting in limited chirping rates up to several tens of MHz per nanosecond. An alternative method to generate optical chirped pulses is by direct modulation of the DFB laser current, since the emitted optical frequency of a DFB laser varies with the injected current [179] [184]. However, the limited modulation speed and linear variation range increase the complexity to arbitrarily enhance the chirping rate [178]. FTM method, which is usually used for chirped microwave generation, is a good candidate for optical chirped generation by using one dispersive device to stretch the ultra-short pulses. However, the ultra-short pulses usually have a fixed repetition rate and because dispersive devices are passive elements, the FTM method is not suitable for the generation of optical chirped pulses with tunable parameters, such as repetition rate, chirping rate, and center frequency.

In this Chapter, we first introduce the conventional method to generate chirped pulse by directly modulating the drive current of the DFB laser, which is described in section 4.1.1. Based on that, section 4.1.2 gives a theoretical analysis for producing a high chirping rate pulse based on the Kerr effect. Section 4.2 and 4.3 gives a theoretical model to analyze chirped pulse φ-OTDR and chirped pulse BOTDA system, respectively.

4.1.1 Direct modulation on DFB laser for chirped pulse generation

Two main effects correspond to the drive current-induced laser frequency change, including carrier density modulation and temperature modulation. The relationship between carrier density/temperature change and optical frequency is given by [185]:

$$\begin{aligned} \Delta F_C/f_0 &= \left(C_{BB}+C_{FC}\right)\left(\Gamma_y/\bar{n}\right)\int \Delta N_e(x)|\epsilon(x)|^2dx, \\ \Delta F_t/f_0 &= -\left(\alpha_L+\alpha_n\right)\int \Delta T_a(x)|\epsilon(x)|^2dx, \end{aligned} \tag{4.1}$$

where $\Delta F_C/\Delta F_t$ is the carrier density effect/temperature effect related optical frequency changes. Coefficients C_{FC} and C_{BB}, relating the carrier density change to the refractive-index change, represent the free carrier plasma dispersion effect and the anomalous dispersion effect due to band-to-band transition. Γ_y is the mode confinement factor. $\bar{n}$ is the average value of the refractive index. α_L and α_n are the thermo-expansion and thermo-optic coefficients. $\Delta N_e(x)$ and $\Delta T_a(x)$ are the distribution of carrier density/temperature modulation. $\epsilon(x)$ is the normalized optical lasing field.

After applying a linearly varied current signal, the output optical frequency of the DFB experiences a periodic modulation, including blue and red shifts, as shown in Figure 4.1 (b). Note that, despite the application of a linearly varied input current as shown in Figure 4.1 (a), the output frequency change of the DFB laser is not linear across the rising or falling edge. The change of the drive current will introduce a different increasing or decreasing frequency chirping depending on the modulation

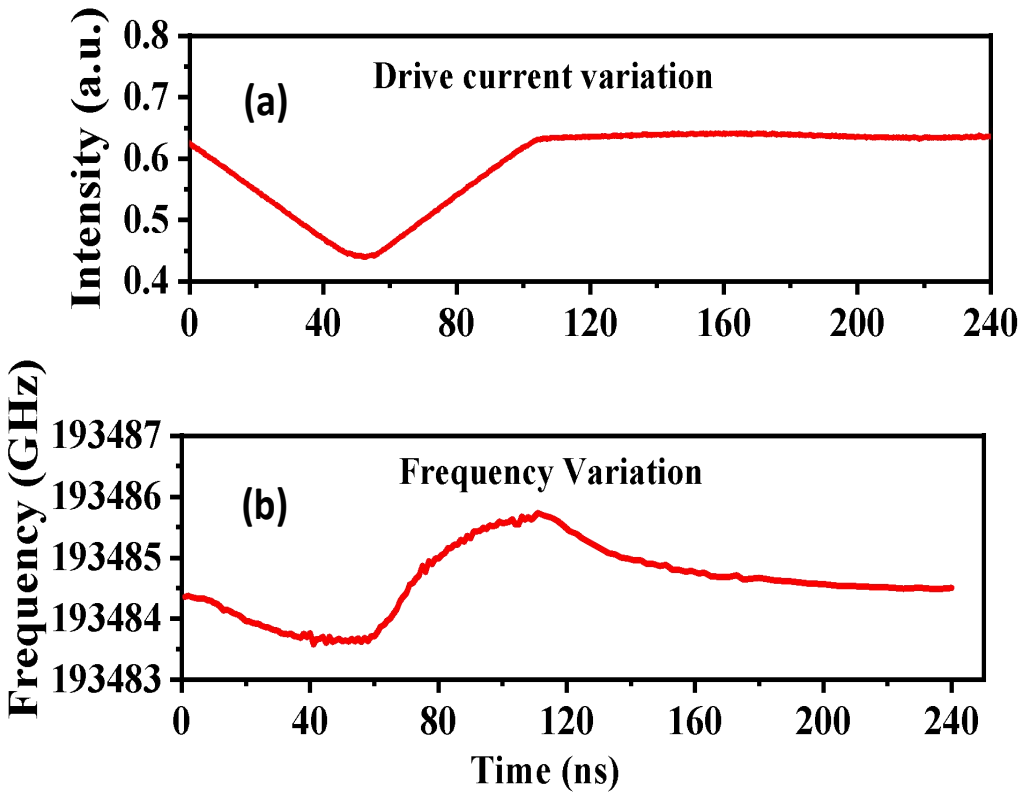

Figure 4.1: (a) Drive current induced output intensity variations.(b) Output frequency variations of the DFB laser.

frequency. The laser frequency is highly dependent on thermal effects for low-frequency modulation currents, with higher currents corresponding to lower frequencies. On the other hand, the carrier density effect governs laser frequency under high-frequency current modulation (>MHz) with an opposite frequency chirp, a fast increase (decrease) in current producing a fast increase (decrease) in frequency. Thus, it could be used to explain the reason why the laser frequency is firstly decreased when a decreasing drive current is applied.

After applying a linearly varied current signal, the overall output frequency change during 50 ns is not linear. The blue shift of the laser source is shown in Figure 4.2 (a). However, a linear portion could still be found as shown in the Figure 4.2 (b) and Figure 4.2 (c) below. The frequency chirping range is limited, reducing the measurable static strain range.

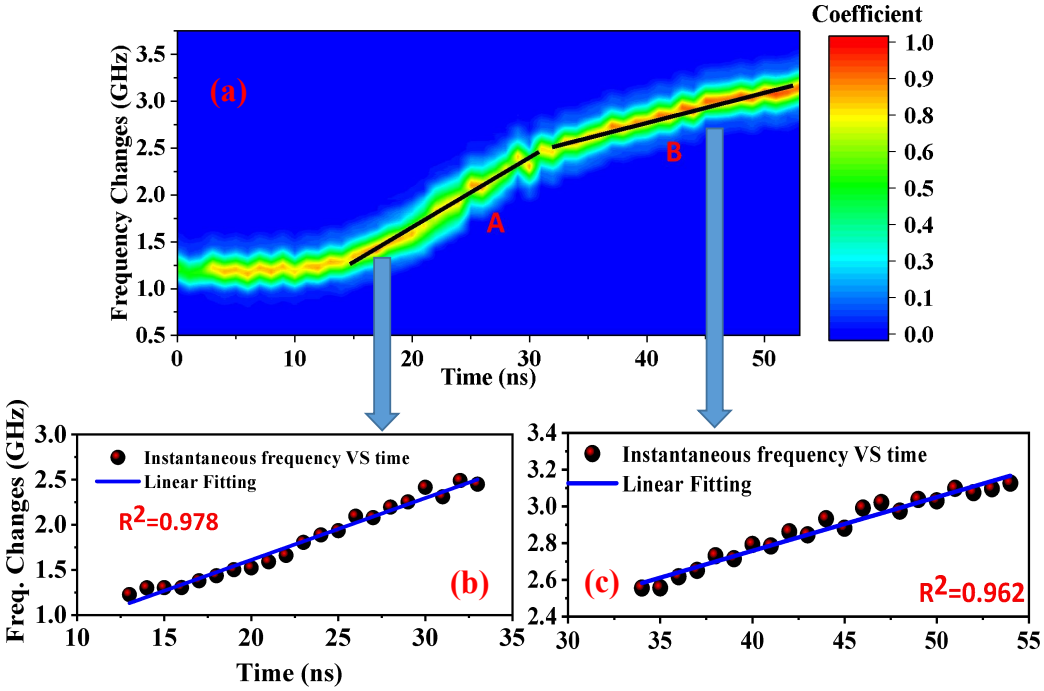

Figure 4.2: (a) Linear frequency chirping section with blue shift, and its close up views (b) and (c).

4.1.2 Theoretical analysis of large chirping rate optical chirped pulse generation based on Kerr effect

When optical waves propagate in dielectric media with molecular inversion symmetry, such as optical fiber, changes in the effective refractive index are induced and governed by the third-order susceptibility, $\chi^{(3)}$. The higher the optical wave intensity, the greater the changes in the refractive index, a phenomenon known as the Kerr effect. Media with high $\chi^{(3)}$, or high nonlinear parameter, exhibit higher index changes even for low powers and are hereafter referred to as Kerr media. As a result of the optical Kerr effect, two laser lights with different frequencies undergo self-phase modulation (SPM), and cross-phase modulation (XPM) along a Kerr medium [186]. Assuming that the angular frequencies of two light waves entering a Kerr medium are ω_p and ω_c, with optical electric fields E_p and E_c, respectively, and $\omega_p < \omega_c$, then the total input electric field is $E_{in} = E_p + E_c$, introducing a slowly varying envelope modulation in the

intensity profile with modulation frequency $\omega_d = \omega_c - \omega_p$. Therefore the amplitude of the slowly varying electrical field and its optical power at the input end of the Kerr medium are given by:

$$A_{in} = \eta \sqrt{2P} \cos(\omega_d t/2), \tag{4.2}$$

$$P_{in} = \eta^2 P(1 + \cos(\omega_d t)), \tag{4.3}$$

where P is half of the optical power of the total electric field, and η is the SOP efficiency of the coherent mixing. In the following derivations, we assume η to be 1 for simplicity, indicating that E_p and E_c enter the Kerr medium with polarizations aligned. Due to the Kerr effect, the overall effective refractive index is a linear function of the optical intensity, $I = P/A$, which is expressed by [41]:

$$n(I) = n + n_2 I, \tag{4.4}$$

where n_2 (in unit of cm^2/W) is the optical Kerr coefficient of the medium, with $n_2 = \frac{3\eta_0}{n^2\epsilon_0}\chi^{(3)}$, where η_0 is the vacuum impedance, ϵ_0 is vacuum permittivity, n is the refractive index, and A is the cross-section of the Kerr medium. So the amplitude of the slowly varying optical field at the output of the Kerr medium is given by [187]:

$$A_{out} = \sqrt{2P} \cos(\omega_d t/2) \exp(i\phi_{\mathrm{NL}}), \tag{4.5}$$

where $\phi_{NL} = (P + P\cos\omega_d t) n_2 k_0 L/A$ is the sinusoidal phase-modulation as a result of the Kerr effect induced by the field components, and L is the length of the Kerr medium. In the following, the exponential factor $\exp(in_2 k_0 LP/A)$ is neglected as it does not affect the output frequency if the input powers remain constant. Solving this equation for the field at the output of the Kerr medium with the Jacobi-Anger expansion, $\exp[iz\cos Bt] = \sum_{m=-\infty}^{\infty} i^m J_m(z) \exp(imBt)$, thereby expressing the results as an infinite sum of frequency sidebands spaced ω_d apart, the amplitude of the m^{th}

order sideband electrical field at the output end of the Kerr medium is expressed by:

$$A_m = \sqrt{2P}\cos(\omega_d t/2)(i)^m J_m(Pn_2k_0L/A)\exp(im\omega_d t), \tag{4.6}$$

where J_m indicates the m^{th} order Bessel function of the first kind. The above analysis mainly focus on the Kerr effect-induced phase modulation.

Equation (4.6) shows that the m^{th} order sideband generated by the Kerr effect is m times ω_d apart from ω_p. Also, since sidebands are generated at both sides of ω_p, but J only assume non-negative orders, we will hereafter refer to lower frequency sidebands as negative orders. Still, the positive value should be used for the Bessel function calculation, i.e. $J_{|m|}$. By modulating one of the laser lights with chirped pulses, say ω_c, after propagation through the Kerr medium, the chirping range of the m^{th} sideband would also be enhanced m times after propagation through the Kerr medium as predicted by Eq.(5). Figure 4.3 (a) shows a schematic spectral diagram of the fixed-frequency and chirped pulse configuration, where chirped pulses with spectral content $\Delta\nu$ and pulse width $(T_1 - T_0)$ are injected into a highly nonlinear fiber (Kerr medium). Considering the output spectrum at the end of the fiber, the starting frequency component

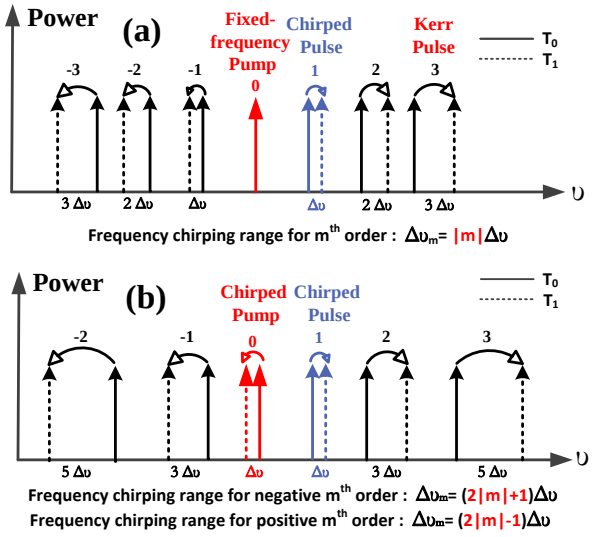

Figure 4.3: Schematic diagram of normalized spectrum for generated sidebands from Kerr effect for (a) fixed-frequency pump and (b) chirped pump.

of chirped pulses signal at time T_0 (solid line) will interact with pump signal yielding numerous sidebands that will be $\omega_m = m\omega_d = m(\omega_c - \omega_p)$ away from ω_p, while the ending frequency component at time T_1 (dashed line) of chirped pulses will generate sidebands that will be $\omega_m = m(\omega_d + \Delta v) = m(\omega_c + \Delta v - \omega_p)$ away from ω_p. Note that $m = 0$ corresponds to the output sideband located at the frequency of the input pump, ω_p, while $m = 1$ corresponds to the output sideband located at the same frequency as the input chirped pulses. In addition, the input pulse intensity profile is square-shaped, and higher-order sidebands do not alter the intensity profile or duration of the output pulse. Therefore, for the m^{th} order sideband Kerr pluses, the frequency chirping range is improved from Δv to $m\Delta v$, but with the same pulse duration W that equals to $(T_1 - T_0)$. It is noted that the generated Kerr pulses on the left side experience a decrease in optical frequency (redshift). In contrast, the right side Kerr chirped pulses undergo an increase in optical frequency (blue shift).

To further improve the frequency chirping rate $(\Delta v/W)$ without changing the pulse width W, an anti-chirped pump signal from the same laser source, i.e. with chirping content $-\Delta\nu$, is utilized to extend the frequency chirping range. This new optimized method is shown in Figure 4.3 (b). Since the chirped pump and original chirped pulses are synchronized in the time domain, the interaction between starting frequency components (at time T_0) of a chirped pulse (solid blue line) and chirped pump (red solid pump) generates sidebands with frequency $\omega_m = m\omega_d = m(\omega_c - \omega_p)$ apart from ω_p. On the other hand, the two ending frequency components (at time T_1) from the chirped pump and chirped pulse will interact with each other and yield negative sidebands that will be $\omega_m = m(\omega_d + 2\Delta v) = m(\omega_c + 2\Delta v - \omega_p)$ apart from $\omega_p - \Delta v$. Note that the ending frequency of negative order Kerr pulse at time T_1 is generated from the chirped pump signal at a frequency of $\omega_p - \Delta v$ since the blue shifts occur within the pulse duration from T_0 to T_1, resulting an additional frequency chirping extension of Δv. The frequency chirping range for negative sidebands is extended from Δv to $(2m + 1)\Delta v$

with the same pulse duration. Thus, the chirping rate enhancement factor is $(2m+1)$ for the negative $-m^{\text{th}}$ order sideband Kerr pulses. Similarly, the positive sidebands will experience a chirping rate enhancement factor of $(2m\text{-}1)$ since the first positive sideband is considered as the original chirped pulse, shown in Figure 4.3 (b).

4.2 Theoretic analysis of CP φ-OTDR

Now, we analyze the principle of the φ-OTDR system by using the chirped pulse generated in the last section as the interrogation (probe) signal. Assume that the pulse width and the optical frequency content of the probe pulse are W and Δv_c, respectively. t = 0 is the moment of the rising edge of the chirped pulse. The instantaneous frequency profile of the chirped pulse is then expressed as:

$$v(t) = \left(v_0 + \frac{\Delta v_c}{W} \cdot t\right) \text{Rect}(t/W), \tag{4.7}$$

where v_0 is the starting frequency of the chirped pulse, *Rect* is the rectangular function, r(Z) is the reflection coefficient. At given time t, the arrival back-scattered electrical field with the collision section (half pulse width length fiber) could be expressed as:

$$E(t) = \int_{(t-W)c/2n}^{tc/2n} E_0 e^{-2\alpha Z} r(Z) e^{i2\pi\varphi} dZ, \tag{4.8}$$

where n is the refractive index's average value, c is the velocity of light in a vacuum, and α is the average attenuation of the unit-length fiber. Since the optical frequency of the laser is linear swept, so the phase of the light scattered by the scattering center Z is given by:

$$\varphi = \int f dt = \int v_0 + \frac{\Delta v_c}{W}\left(t - \frac{2nZ}{c}\right) d\left(t - \frac{2nZ}{c}\right) + \phi_0. \tag{4.9}$$

To simplify the analysis, let's consider the two scattering center Z_i and Z_j within the pulse width $(t - T < 2nZ/c < t)$, the optical power P(t) is calculated by $E^{Z_i}(t)$ and $E^{Z_j}(t)$, leading to:

$$P(t) = P_0 \int_{(t-W)c/2n}^{tc/2n} \int_{(t-W)c/2n}^{tc/2n} e^{-2\alpha(Z_i+Z_j)} r\left(Z_i\right) \cdot r\left(Z_j\right) \cdot e^{i[\Delta\varphi_{ij}(t)]} \mathrm{d}Z_i \, \mathrm{d}Z_j, \tag{4.10}$$

where P_0 is the input power of the light; Z_i and Z_j are the fiber length between the input end of the fiber and i^{th} or j^{th} spot; and r(Z_i) and r(Z_i) are the reflection coefficient i^{th} and j^{th} scattered spots, respectively. Then, based on the Equation (4.9) the phase difference of any two scattered spots within the pulse width is expressed as:

$$\begin{aligned}\Delta\varphi_{ij} = &\left[v_0\left(t-\frac{2nZ_i}{c}\right)+\frac{\Delta v_c}{2W}\left(t-\frac{2nZ_i}{c}\right)^2\right] \\ &-\left[v_0\left(t-\frac{2nZ_j}{c}\right)+\frac{\Delta v_c}{2W}\left(t-\frac{2nZ_j}{c}\right)^2\right],\end{aligned} \tag{4.11}$$

it gives:

$$\Delta\varphi_{ij} = \frac{2n(Z_j-Z_i)}{c}\left[v_0+\frac{\Delta v_c}{W}\left(t-\frac{n(Z_j+Z_i)}{c}\right)\right] \tag{4.12}$$

It shows that the phase difference between the two scattered lightwaves from Z_i and Z_j is associated with optical path length ($L_{ij} = 2n(Z_j - Z_i)$) and the frequency of the scattered lightwave. Since an optical frequency chirped pulse is utilized as an interrogation signal, the frequency of scattered lightwave at scattering center Z_i and Z_j is linearly changed within the pulse profile at different given time t. This time-dependent phase difference allows us to compensate for the external disturbance-induced optical path length change by measuring the back-scattering with a time delay of Δt. Specifically, if there is a temperature/strain variation, the optical path length will change accordingly due to the thermo-optic, photo-elastic, therm-expansion and Poisson effect. The equal intensity point in the two Rayleigh traces with and without disturbance will arise at a different given time, leading to $\Delta\varphi(t,0) = \Delta\varphi(t+\Delta t, \Delta K + \Delta\varepsilon)$:

$$\begin{aligned}&\frac{L_{ij}}{c}\left[v_0+\frac{\Delta v_c}{W}\left(t-\frac{n(Z_j+Z_i)}{c}\right)\right] \\ &=\frac{(L_{ij}+\Delta L)}{c}\left[v_0+\frac{\Delta v_c}{W}\left((t+\Delta t)-\frac{n(Z_j+Z_i)}{c}\right)\right],\end{aligned} \tag{4.13}$$

where left-hand term represents the phase difference of any two scattered light wave by i^{th} and j^{th} scattering centers without temperature and strain variations, while the right-hand term represents the phase difference under certain temperature/strain changes (ΔK and $\Delta\varepsilon$). $L_{ij} = 2n(Z_j - Z_i)$ is the optical path length, and ΔL is the temperature

and strain changes induced optical path length changes. It is noted that the refractive index and physical location changes give a time delay based on the last term in each side ($(n(Z_i + Z_j))/C$), but it is very small compared the time delays Δt and could be neglected. Thus we assume $f_1 = \left[v_0 + \frac{\Delta v_c}{W}\left(t - \frac{n(Z_j+Z_i)}{c}\right)\right]$, and it is unchanged, giving the relation between time delays (Δt) and optical path length change (ΔL):

$$L_{ij} f_1 = (L_{ij} + \Delta L)\left(f_1 - \frac{\Delta v_c}{W}\Delta t\right), \tag{4.14}$$

so, the temperature and strain variations gives the time delay (Δt), which could be expressed by:

$$\frac{\Delta L}{L} = \frac{\Delta v_c \Delta t / W}{v_0} = C_T \cdot \Delta K + C_\varepsilon \cdot \Delta\varepsilon, \tag{4.15}$$

where C_T is the temperature variations related frequency shifts coefficient, C_ε is the strain variations related frequency shifts coefficient.

$$\Delta t = \frac{v_0 W}{\Delta v_c}(C_T \cdot \Delta K + C_\varepsilon \cdot \Delta\varepsilon). \tag{4.16}$$

Based on Equation (10.23), the typical value of $C_T = \Delta f/\Delta K$ and $C_\varepsilon = \Delta f/\Delta\varepsilon$ can be calculate at wavelength of 1550 nm. Therefore, the strain/temperature related time delays coefficients are expressed as:

$$\begin{aligned} \Delta t_K &= \frac{\Delta t}{\Delta K} = \frac{W}{\Delta v_c} \cdot 1.32\text{GHz}/K = \frac{1.32\text{GHz}/K}{R\cdot}, \\ \Delta t_\varepsilon &= \frac{\Delta t}{\Delta \varepsilon} = \frac{W}{\Delta v_c} \cdot 150.9\text{MHz}/\varepsilon = \frac{150.9\text{MHz}/\mu\varepsilon}{R}, \end{aligned} \tag{4.17}$$

where $R = \Delta v_c / W$ is the frequency chirping rate. We could know that the temperature/strain-related time delays coefficient is inversely proportional to the frequency chirping rate R.

The principle of this Frequency-to-time mapping (FTTM) method by using chirped pulse for real-time measurement is illustrated in Figure 4.4. A chirped pulse serving as a probe signal is sent to the sensor section, and then a jagged reflection interference pattern is detected by a photo-detector (PD). By sending the probe pulse a second time with a certain repetition rate, we obtain two-time domain traces (solid red line and blue

dashed line) representing different temperature/strain variations. The Rayleigh traces from that strain/temperature applied fiber section will show significant longitudinal time shift, attributed to the phase difference change compensation via time-dependent optical frequency variation within the pulse width, as shown in Equation (4.14). Therefore, the phase difference of the scattered lightwave from any of two i^{th} and j^{th} scattering centers at a given time t without strain/temperature changes equals that at a given time $t+\Delta t$ with disturbance. The longitudinal time delay between the two encoded time domain traces is linearly proportional to the external disturbance-induced frequency shifts and the corresponding local time delays (based on Equation (4.17)) are then calculated by using trace-to-trace correlation over a specific time window.

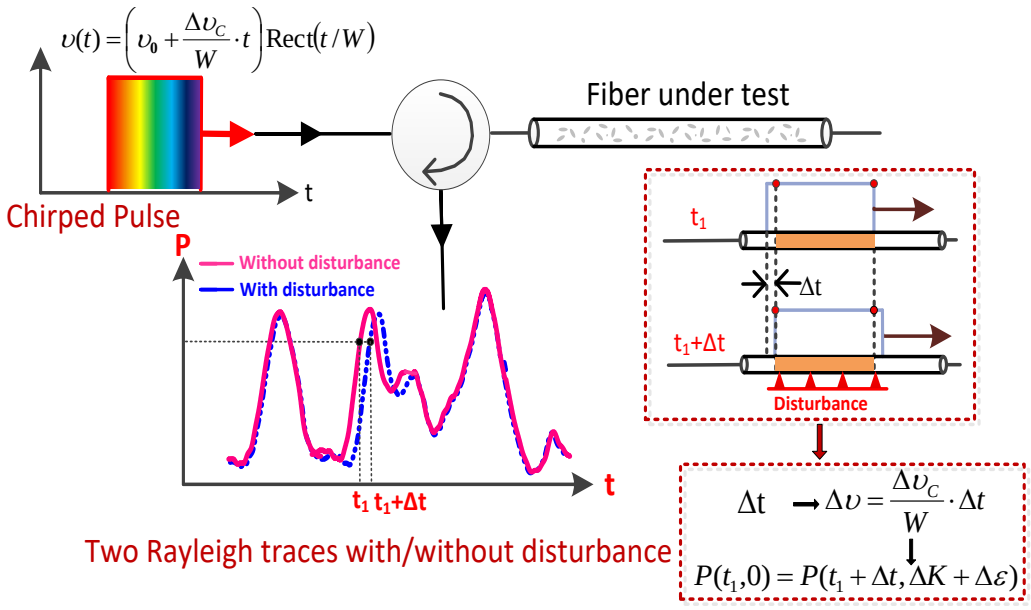

Figure 4.4: Working principle of Chirped pulse φ-OTDR system. υ_0: Starting frequency of the chirped pulse; $\Delta\upsilon_c$: Frequency chirping range; Rect: Rectangular function; W: Pulse width; P: Optical power at receive end; $\Delta K/\Delta\varepsilon$: Temperature/Strain changes; Δt: Time delays between two adjacent traces within in time window.

To obtain the local time delays of the jagged Rayleigh traces, a more precise method is to use cross-correlation calculation rather than the conventional peak wavelength inspection methods typically used in FBG sensors. The cross-correlation $R_{xy}(n)$ is

obtained by performing the cross-correlation calculation for the two reflected Rayleigh traces using the following equation:

$$R_{xy}(n) = \frac{1}{N}\sum_{k=0}^{N-1} x(k) \cdot y(n+k), \tag{4.18}$$

where N is the total data points of the collected Rayleigh signal, $n = -(N-1)..0..N-1$, and $x(n)$, $y(n)$ are two collected Rayleigh traces before and after applying the strain/temperature variation.

4.2.1 Static strain limitations in CP φ-OTDR

In chirped pulse φ-OTDR, by using a frequency chirped pulse, the local external disturbance(strain/temperature variation) could be directly measured by the local time delays within the selected time window in Rayleigh traces. However, there is an important assumption to make this method rigorous and feasible. As shown in Figure 4.5, the chirped pulse locates at a different position at two different given time t and $t+\Delta t$. We need to assume that the main contribution of the chirped pulse to form the optical intensity detected at the input end is the common part (a grey area), which is section AB at given time t_1 and CD at the bottom. Then, any two scattering center within the grey section will reflect the lightwave with different optical frequencies relating to time delays Δt, giving a phase difference change to compensate for the strain/temperature variation induced optical path length changes. As shown in Figure 4.5 (b), the two Rayleigh traces collected under different strain/temperature variations showing a significantly longitudinal shifts with a high cross-correlation coefficient up to 0.934.

However, too large strain/temperature changes between consecutive traces may result in a cross-correlation originating from partially different scatterers. Instead of a unique correlation peak, such cross-correlations may exhibit a few peaks of fairly close magnitudes and the likelihood of producing an anomalous estimate of Δt, so-called outlier, becomes too high [101]. Figure 4.5 (c) shows the two Rayleigh traces before and

after applying relatively larger strain/temperature variations resulting in time delays exceeding 10% of the pulse width, which gives a lower cross-correlation coefficient of about 0.505.

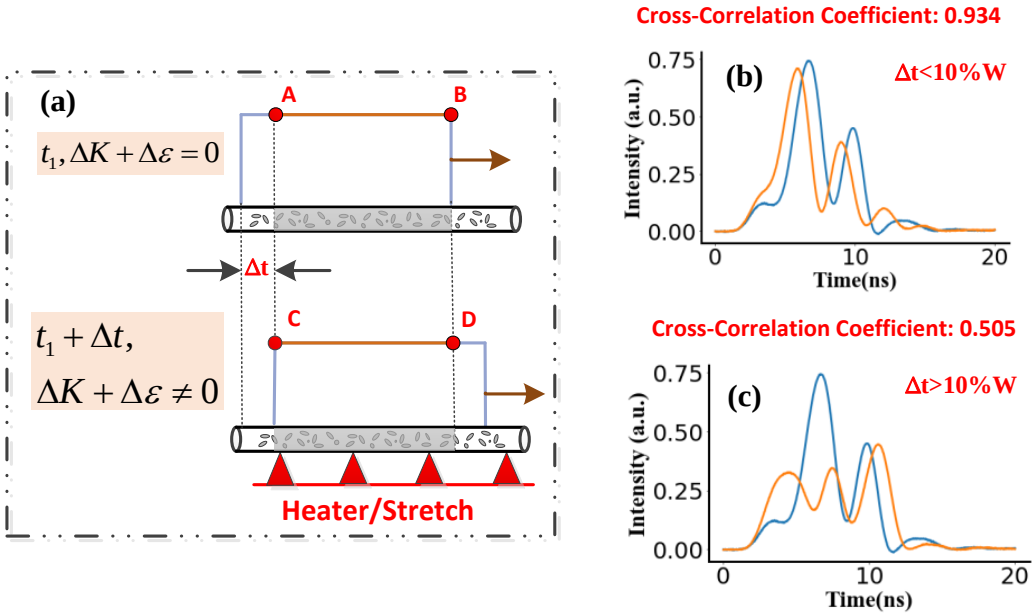

Figure 4.5: Static temperature/strain measurement range limitation in the chirped pulse φ-OTDR. Time delays Δt: strain/temperature variations induced longitudinal time shifts between Rayleigh traces (Equation (4.17)). (a) Chirped pulse location on the fiber at different given time t and $t + \Delta t$ (b) Two Rayleigh traces with and without strain/temperature variations applied (corresponding time delays (Δ) <10% of pulse width (W) (b) Two Rayleigh traces with and without strain/temperature variations applied (corresponding time delays (Δt) >10% of pulse width (W).

In order to investigate the impact of the "partially different scatterers" effect on the time delay determination, we measured the error possibility of the measurement when different strain/temperature variations were applied. With the increase of strain/temperature variations, the time delays between two Rayleigh traces will increase accordingly, leading to the "partially different scatterers" effect being more serious. The error possibility is the number of measurements that appear as outliers divided by the total number of

measurements.

As shown in Figure 4.6, if we set the 10% error possibility as the threshold, it shows that the corresponding maximum measurable time delays are around 10% of the pulse width, regardless of the pulse width of the chirped pulses that were used. When the measured time delay (frequency shifts) is less than 10% of the pulse width (total frequency scan range), the high correlation coefficient ensured a very low probability of appearing outliers due to external disturbance, which enabled high strain or temperature accuracy and repeatability. Hence, the "partially different scatterers" problem is the major factor in reducing the static strain measurement range in the chirped pulse φ-OTDR system. According to Equation (4.17), since the $\Delta t/W$ should be smaller than 10%, so the measurable range is finally limited by the frequency chirping range.

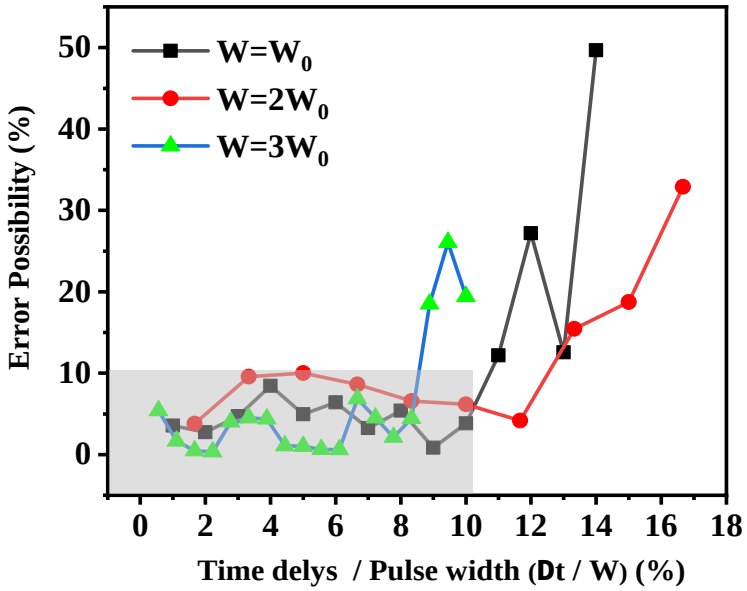

Figure 4.6: The relationship between measurement error possibility and time delays-pulse width ratio. The pulse width W in three tests are W_0, $2W_0$ and $3W_0$, respectively. The frequency chirping rate in three tests are the same.

4.2.2 Dynamic measurement with limited static range

So far, the quantitative relative strain/temperature variations measurement and its static measurable range in chirped pulse φ-OTDR is illustrated in the above section. It is capable of distributed and single-shot measurement of strain and temperature perturbations with good precision and robustness, without the requirement of phase demodulation. When the strain/temperature variations are sufficiently large, and out of the static measurement range, the strain variation could be measured by the differential strain from two adjacent Rayleigh traces. Then the whole strain variation is calculated by integration over time as following equations:

$$\varepsilon\left(t=\frac{n}{\text{Sample Rate}}\right)=\sum_{i=1}^{n}\Delta\varepsilon_i. \tag{4.19}$$

This method requires a high pulse repetition rate due to the limited static measurable range ($\Delta\varepsilon_i$) for dynamic strain/temperature measurement. In principle, the highest recoverable frequency of vibration is limited by the maximum detectable strain change of two single-shot measurements when the repetition rate of the interrogation pulse is fixed [188]. The maximum detectable vibration frequency ($f_{\text{vibration}}$) is defined by:

$$f_{\text{vibration}}=\frac{\Delta\varepsilon_{\text{shot-to-shot}}\cdot f_{\text{repetition}}}{\Delta\varepsilon_{\text{total}}\cdot 2}, \tag{4.20}$$

where $\Delta\varepsilon_{\text{shot-to-shot}}$ is the static measurement range, $f_{\text{repetition}}$ is the pulse repetition rate and $\Delta\varepsilon_{\text{total}}$ is the peak-to-peak strain variations, and 2 represents the Nyquist frequency is half of the sampling rate. Thus, for the fixed repetition of pulse and peak-to-peak strain change of perturbation signal, Higher detectable vibration frequency could be achieved by improving the static measurement range between two single-shot measurements.

4.3 Theoretic analysis of CP-BOTDA

In the traditional BOTDA system, two single-frequency counter-propagating optical waves (pump and Stokes light) are injected from two ends of the fiber. Due to the electrostriction effect, a moving density grating will be generated to scatter the pump light when the high peak power pulse propagates along the fiber. The backward scattered pump light will reach maximum once the frequency difference between the pump and Stokes light equals the local BFS. Since the pump pulse reinforces the power of Stokes light (probe signal) differently with different frequency deviations, the Brillouin gain spectrum (BGS) could be obtained through laser frequency sweeping for strain or temperature sensing. The frequency sweeping process usually takes several seconds to several minutes, which lowers the acquisition rate of the system, leading to a limited measurable frequency range of dynamic strain.

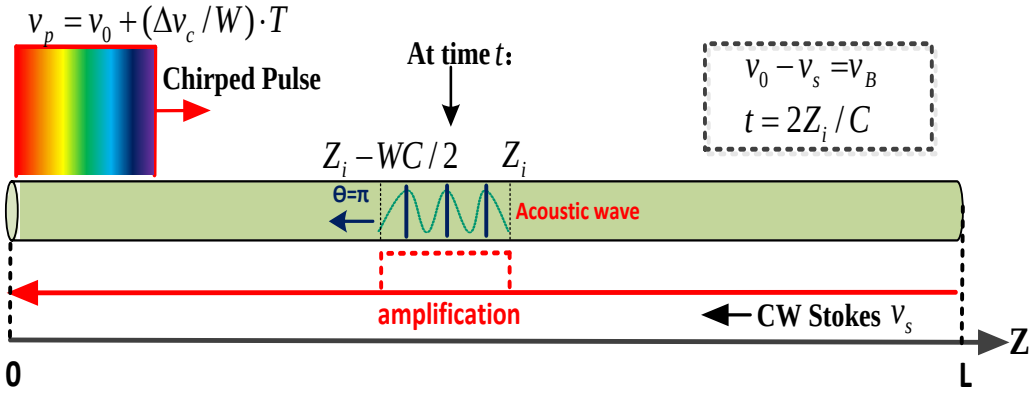

Figure 4.7: The working principle of chirped pulse BOTDA system. v_B is the local Brillouin frequency shift, C is the velocity of the pump and probe light, and v_s is the frequency of Stokes light.

Here, we thus propose a novel chirped pulse BOTDA system by using chirped pulse as a pump signal without the requirement of frequency sweeping and Brillouin gain spectrum recovery process. Let us consider a chirped pulse with a frequency profile of $v_p = v_0 + (\Delta v_c / W)T$ utilized as the pump signal, as shown in Figure 4.7, where v_0 is the

initial optical frequency of the laser source, Δv_c is the frequency chirping range, v_s is the frequency of Stokes light, and W is the effective pulse width. Suppose the chirped pulse is launched at t=0 with the energy of $E_p(tC/2)$ and propagates to $+Z$ direction, where C is the speed for both pump and Stokes lights. CW Stokes light is launched at $Z = L$ with the energy of $E_{cw}(tC/2)$ and propagates to $L - Z$ direction. At given time t, Brillouin interaction in the region of $[Z_i - WC/2, Z_i]$ will arrive at $Z = 0$; here Z_i is the distance between the input end and the front end of the interaction range. Thus, the energy of the CW stokes is given by [8]:

$$E_{cw}(t) = P_{cw}(L)\exp\left(-\alpha_{cw}L\right)dt + (g/A)\cdot E_p(z)\cdot(dz)\cdot P_{cw}(L)\exp\left(-\alpha_{cw}L\right), \quad (4.21)$$

where g is the Brillouin gain coefficient, $\alpha_c w$ is the attenuation coefficient, and A is the effective cross-section of the fiber. Then, the power of the CW Stokes light that experiences the attenuation and amplification at the input end is then given by:

$$\begin{aligned} P_{cw}(t) =& E_{cw}(t)/dt = P_{cw}(L)\exp\left(-\alpha_{cw}L\right) + (g/A), \\ & \cdot E_p\left(\frac{tC}{2}\right)\cdot\frac{WC}{2}/dt\cdot P_{cw}(L)\exp\left(-\alpha_{cw}L\right). \end{aligned} \quad (4.22)$$

Ignoring the contribution of spontaneous Brillouin emission, the pulse energy $E_p(tC/2)$ satisfies the following equation:

$$\begin{aligned} \frac{dE_p(tC/2)}{d(tC/2)} &= -\left[\alpha_p + (g/A)P_{cw}(tC/2)\right]E_p(tC/2), \\ P_{cw}(tC/2) &= P_{cw}(L)\exp\left[-\alpha_{cw}(L - tC/2)\right], \end{aligned} \quad (4.23)$$

where α_p is the attenuation coefficient for a chirped pump pulse, the first equation in Equation (4.23) represents the pump pulse lost power due to the attenuation and the energy transfer between the pump pulse and CW Stokes light. While the second equation shows the CW stokes light experiences attenuation at a given position. To simplify the calculation, when the total fiber length (L) is smaller than 60 km, the non-local effect could be neglected. So the pulse energy could be then expressed as:

$$E_p(tC/2) = E_p(0)\cdot\exp\left(-\alpha_p\cdot tC/2\right), \quad (4.24)$$

by substituting the Equation (4.24) to the Equation (4.22), the optical power of CW Stokes light at fixed receiving time t is given by:

$$P_{cw}(t) = P_{dc} + (g/A) \cdot \frac{WC}{2} \cdot P_p(0) \cdot \exp(-\alpha_p \cdot tC/2) \cdot P_{dc},$$

where

$$P_{dc} = P_{cw}(L) \exp(-\alpha_{cw} L), \tag{4.25}$$

where P_{dc} represents the CW Stokes light that arrives at Z= 0 without interacting with the pump pulse signal, $P_p(0)$ is the optical power of the pump pulse signal at the input end.

$$g(\Omega) = \frac{g_p (\Delta\omega_B/2)^2}{4\pi^2 (\Omega - v_B)^2 + (\Delta\omega_B/2)^2}, \tag{4.26}$$

where g_p is the peak value of the Brillouin gain coefficient, $\Omega = v_p - v_s$ and $\Delta\omega_B$ is the Brillouin gain bandwidth. If we consider the pump signal is non-chirped and the local v_B within the collision section is unchanged, the Brillouin gain (g) is almost uniform. However, in our chirped pump pulse-based scheme, the local Brillouin gain within the pulse width keeps changing and should be calculated by the integral within the interaction region $[Z_i - WC/2, Z_i]$. The Brillouin gain spectrum should be the integration within the pulse width, leading to:

$$(g/A) \cdot \frac{WC}{2} \propto \frac{Cg_p}{2A} \int_{t-2Z_i/C}^{t-(2Z_i/C-W)} \frac{(\Delta\omega_B/2)^2}{4\pi^2 \left(v_0 + \frac{\Delta v_c}{W} \cdot t - v_s - v_B\right)^2 + (\Delta\omega_B/2)^2} dt. \tag{4.27}$$

Then, the power of Stokes light $P_cw(t)$ could be expressed as:

$$\begin{aligned} P_{cw}(t) &\propto P_{dc} + P_p(0, v_p) \cdot \exp(-\alpha_p \cdot tC/2) \cdot P_{dc} \\ &\cdot \frac{Cg_p}{2A} \int_{t-2Z_i/C}^{t-(2Z_i/C-W)} \frac{(\Delta v_B/2)^2}{\left(v_0 + \frac{\Delta v_c}{W} t - v_s - v_B\right)^2 + (\Delta v_B/2)^2} \, \mathrm{d}t. \end{aligned} \tag{4.28}$$

By using the $P_{peak,BGS}$ to represent the peak value of the amplified Stokes light, the power of the amplified Stokes light at the detection end is further simplified, leading to:

$$P_{cw}(t) = \int_{t-2Z_i/C}^{t-(2Z_i/C-W)} \frac{P_{peak,BGS}(t) \cdot (\Delta v_B/2)^2}{\left(v_0 + \frac{\Delta v_c}{W} \cdot t - v_s - v_B\right)^2 + (\Delta v_B/2)^2} dt. \tag{4.29}$$

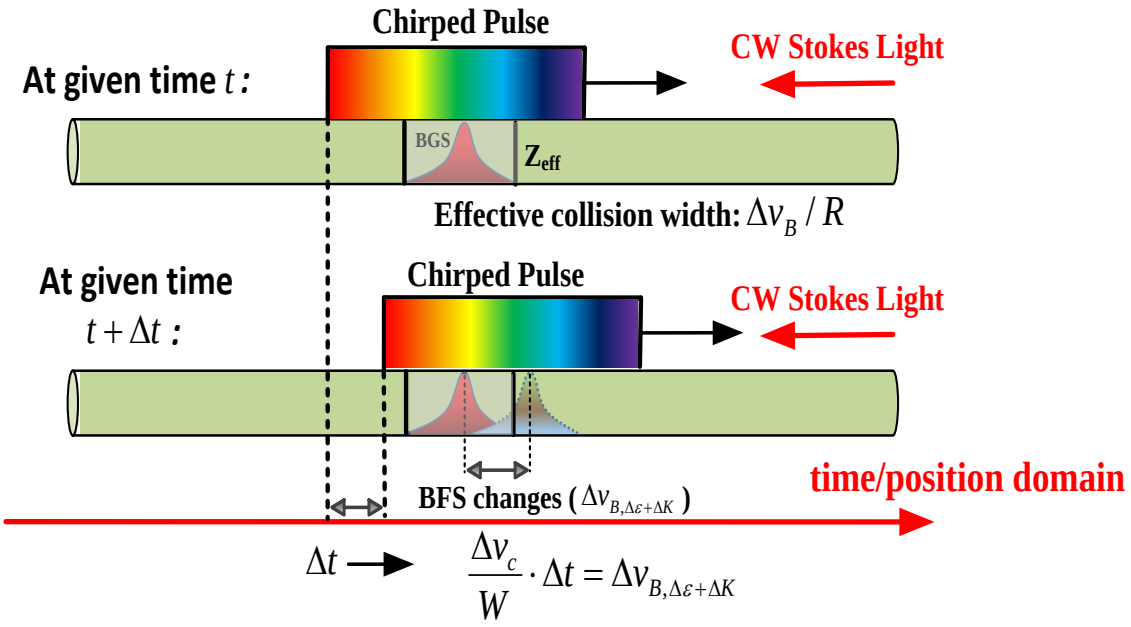

Figure 4.8: Distributed Brillouin frequency shift extraction by local time delays measurement. Δv_B is the temperature/strain induced local Brillouin frequency shifts.

Let us consider there is no strain applied on the fiber at a given time t, as shown in the top figure of the Figure 4.8. According to the Equation (4.29), since the frequency chirping range is larger than the BGS linewidth, the power of Stokes light at a given time t equals:

$$P_{cw}(t,0) = \int_{t-2Z_{\text{eff}}/C}^{t-(2Z_{\text{eff}}/C - W\cdot\Delta v_B/\Delta v_c)} \frac{P_{peak,BGS}\cdot(\Delta v_B/2)^2}{\left(v_0 + \frac{\Delta v_c}{W}\cdot t - v_s - v_B\right)^2 + (\Delta v_B/2)^2} dt, \tag{4.30}$$

where Z_{eff} is the end of the effective collision width, while an applied strain/temperature induced BFS changes of Δv_B is added to v_B at given time $t+\Delta t$, for the same collision section, the power of Stokes light is then given by:

$$P_{cw}(t+\Delta t, \Delta\varepsilon+\Delta K) = \int_{t-2Z_{\text{eff}}/C}^{t-\left(2Z_{\text{eff}}/C - W\cdot\frac{(\Delta v_B}{\Delta v_c}\right)} \frac{P_{peak,BGS}(t)\cdot(\Delta v_B/2)^2}{\left(v_0 + \frac{\Delta v_c}{W}\cdot(t-\Delta t) - v_s - (v_B - \Delta v_{B,\Delta\varepsilon+\Delta K})\right)^2 + (\Delta v_B/2)^2} dt. \tag{4.31}$$

Once the condition of $\Delta v\cdot\Delta t/W = \Delta v_{B,\varepsilon}$ is satisfied. This means that the applied strain-induced power variation could be compensated by the local time delays, given

by:

$$\Delta t = \frac{\Delta v_{B,\varepsilon}}{R}, \quad \text{where} \quad R = \frac{\Delta v_c}{W}. \tag{4.32}$$

In the chirped pulse BOTDA system, the temperature/strain variations induced time delays in the Brillouin traces (amplified Stokes light signal) are linearly proportional to the local Brillouin frequency shifts and inversely proportional to the frequency chirping rate of the chirped pulse, based on the Equation (4.32).

4.3.1 Frequency chirping rate dependent spatial resolution

In the traditional single-frequency pump pulse BOTDA systems in which the spatial resolution is determined by the pulse width and finally limited by the phonon life time (10ns) corresponding to 1 m spatial resolution. The reason is that the backscattered Brillouin signal will show a broader spectral distribution if the spectrum of the pulse signal is wider than the natural Brillouin linewidth, which smears the backscattered signal over a wide spectral range and the measurement contrast vanishes. However, in our chirped pulse BOTDA system, the spatial resolution is limited by the frequency chirping rate (R) and the local non-uniformity.

As shown in Figure 4.8, when the frequency chirping range is larger than the local natural Brillouin gain bandwidth that is determined by the double phonon lifetime around 12 ns, the effective collision section for pump and Stokes signal to generate the SBS effect is not the pulse width, but mainly determined by the frequency chirping rate R (Brillouin gain spectrum bandwidth does not change too much). The effective collision width (W_{eff}) within gray section could be calculated by:

$$W_{\text{eff}} = \Delta v_c / R. \tag{4.33}$$

Figure 4.9 (c) shows the relationship between the frequency chirping rate and the

effective collision width. For a fixed Brillouin gain spectrum width, larger R would give a smaller effective collision width, thus a higher spatial resolution.

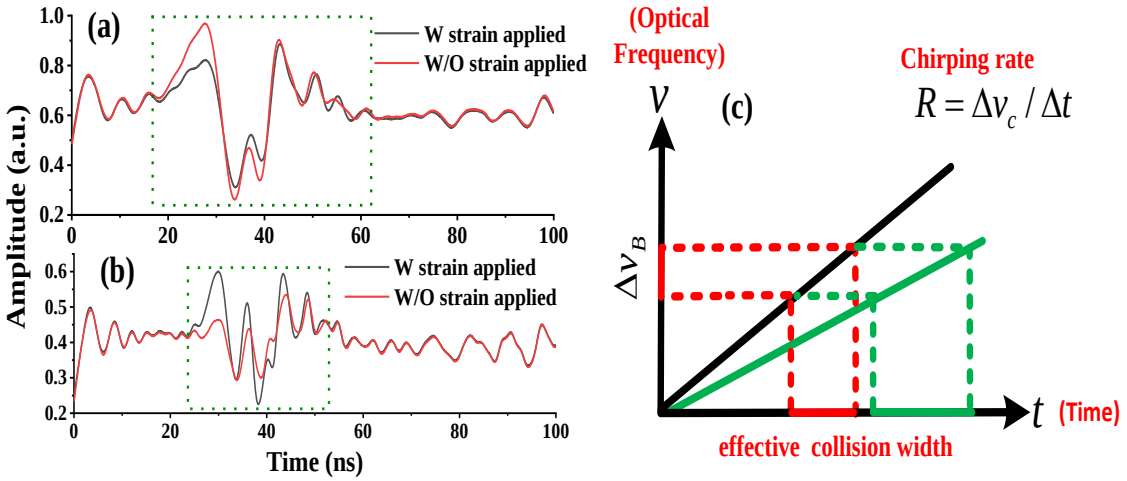

Figure 4.9: Brillouin traces with and without strain applied by using (a) smaller R chirped pulse, (b) larger R chirped pulse; (c) The relationship between frequency chirping rate and the effective collision width.

The Brillouin traces with and without strain applied by using different R are shown in Figure 4.9 (a) and (b). It clearly shows that the period of the intensity fluctuations that represent the non-uniformity of the fiber are getting smaller when a chirped pulse (40ns pulse width) with larger R is used. On the other hand, when the stain is applied to the fiber section with the same length (1m), the longitudinal time shifting section is also getting smaller for the larger R chirped pulse. Both observations show that the relationship between the frequency chirping range and the effective collision width is consistent with our theoretical analysis.

Chapter 5

Chirped pulse φ-OTDR system based on Random fiber grating array

5.1 Contributions of authors

The contributions of the five authors: Yuan Wang (present author), Prof. Xiaoyi Bao, Prof. Liang Chen, Dr. Ping Lu, and Dr. Stephen Mihailov are as follows. The present author built the experimental setup, conducted the data analysis, and produced the graphs. Ping Lu and Dr. Stephen Mihailov from the National Research Council fabricated the Random fiber grating array sample. Prof. Xiaoyi Bao and Prof. Liang Chen provided advice on the presentation of the data as well as comments on the main text of this Chapter. All authors contributed to the final version of all papers in this Chapter.

5.2 High accuracy distributed time delay measurement for temperature sensing

In this section [30], the temperature change-induced time delay in random optical fiber gratings was precisely measured for the first time. This temperature sensor inherently possesses spike-like reflective spectra with high contrast that can be attributed to the enhanced inhomogeneity and reflectivity of random fiber gratings. This property could achieve the interference pattern with a large number of steep peaks in the time domain in a smaller wavelength range compared with single-mode fiber, thus improving the accuracy of the cross-correlation calculation as well as higher power density as required by a smaller wavelength range from the random grating array and hence potentially longer sensing length and higher sensitivity. Because of the larger index change range (10-5) compared to scattering levels from the single-mode fiber, the random grating array (sensor) yields a stable reflected signal. It forms high stability time domain interference patterns, which could significantly improve the sensing precision. The random grating array's time and the spectral domain interference pattern are investigated

in this letter. In addition, high-precision distributed temperature measurement based on chirped pulse phase optical time domain reflectometry is demonstrated. More importantly, this truly distributed temperature measurement provides important guidance to employ distributed random fiber grating in the optical sensing field.

Distributed time delay sensing in random fiber grating array based on chirped pulse φ-OTDR

YUAN WANG,[1] PING LU,[3] STEPHEN MIHAILOV,[3] LIANG CHEN,[2] AND XIAOYI BAO[1,2,*]

[1]School of Electrical Engineering and Computer Science, University of Ottawa, Ontario K1N 6N5, Canada
[2]Department of Physics, University of Ottawa, 25 Templeton Street, Ottawa, Ontario K1N 6N5, Canada
[3]National Research Council Canada, Ottawa, Ontario K1A 0R6, Canada

Received XX Month XXXX; revised XX Month, XXXX; accepted XX Month XXXX; posted XX Month XXXX (Doc. ID XXXXX); published XX Month XXXX

A high precision distributed time delay measurement in a chirped pulse phase optical time domain reflectometry (CP φ-OTDR) system based on Random Fiber Grating Array (RFGA) is proposed and demonstrated, in which temperature induced refractive index and fiber dimension changes associated time delay could be measured for distributed temperature sensing. The random fiber grating array includes many inscribed refractive index change locations at periods of sub-micron. When laser pulses are launched into the fiber grating, the backscattered light possesses many unique localized speckle patterns at different locations. Those patterns change with temperature, and hence the backscattering spectral response will change accordingly. By measuring the localized speckle pattern change due to the change of the temperature over the chirped pulse spectrum and performing cross correlation calculation, we can realize distributed temperature measurements in real time using a MHz bandwidth distributed feedback (DFB) laser. Unlike conventional φ-OTDR sensing system which measures distributed phase change along the fiber using an ultra-narrow linewidth laser, the distributed time delay presented in this work is directly measured in real time. It is shown that the time resolved localized pattern trace is stable with very small fluctuation thanks to the enhanced inhomogeneity and reflectivity. The minimum detectable temperature variation is about 0.028℃at meter order of magnitude spatial resolution.

http://dx.doi.org/10.1364/OL.99.099999

A distributed optical fiber sensor, being the disturbance information provider, is expected to reveal temperature, strain and vibration information from any point along an optical fiber through light scattering, which plays a crucial role in the area of civil engineering for structural health monitoring[1]-[3].

Random fiber gratings have attracted increasing attention because of their unique scattering properties and potential novel applications [4-6]. Because of the ultra-wide reflection spectrum (tens to hundreds of nm or wider), those device have the capacity to perform multi-parameter sensing by introducing a wavelength-division method since temperature, strain and refractive index have different wavelength shift coefficients in different wavelength windows [5]. Recently, a novel random grating has been fabricated with a controllable bandwidth of reflectivity, higher backscattering level and lower insertion loss [6]. These properties are beneficial in order to attain a high accuracy of measurement, a low cost of system and a long distributed sensing distance. Because of the broad reflection spectrum of each random grating, a time-division multiplexing (TDM) approach might be a better choice for grating multiplexing. In order to realize real time measurement, a conversion between wavelength shift and real time delay is required.

One solution for frequency-to-time mapping (FTTM) is to use an ultra-narrow pulse from a mode-locked laser that provides spatial coverage of sub-mm which might lower the stability of time domain traces. In order to get wavelength shift information in the time domain, a dispersion element, such as a chirped FBG, is introduced at the receiver end to convert the wavelength shift of reflected signal into time delay [7-9]. The major limitation of this method is that it is only suitable for quasi-distributed sensing since the reflected pulses would overlap in time domain. This occurs when the spacing of the two reflected pulses is smaller than the minimum spatial interval defined by the spectrum range of pulse and the chirping coefficient of the chirp FBG. In additional, a spectral range that is too broad leads to small time delays, which results in relative low temperature measurement precision. A chirped pulse based phase OTDR has been introduced for normal Rayleigh scattering in fibers to demodulate the refractive index change [10]. Because of the weak Rayleigh scattering in regular optical fibers, long pulse duration of 100 ns is used, which is equivalent to 10 m spatial resolution in order to get stable trace with high signal noise ratio. In addition, the corresponding time delay is larger for the same temperature change for longer pulses with the same frequency content This can reduce the stability requirement for achieving the same minimum detectable temperature variation. However, the backscattering time domain

traces from a random fiber grating array is highly structured with discernable peaks that can be associated with the localized random grating structure (spacing in the range of sub-μm comparing with nm in Rayleigh scattering in single mode fiber). This structure is more stable because of larger index change range associated with it (10^{-5}) as compared to scattering levels from the single mode fiber. The backscattering from random fiber gratings can then be used for distributed temperature measurements with high spatial resolution and high precision.

In this letter, we present and demonstrate a real time distributed temperature sensing system based on chirped pulse interrogation of a RFGA for the first time. The random fiber gratings inherently possess spike-like reflective spectra with high contrast that can be attributed to enhanced inhomogeneity. The contrast could be further enhanced when a random fiber grating array is introduced, where the spectral responses of several single random gratings are covered by the interrogation pulse. The resultant interference patterns with multiple peaks ensure the delay time could be measured with high accuracy. Due to the wide reflection spectrum range, the initial frequency of a DFB laser can be tuned to achieve the interference pattern with a large number of steep peaks in time domain thus improving the accuracy of the cross-correlation calculation. More importantly, the enhanced reflectivity of the random fiber grating array over a broadband wavelength range could significantly increase the signal to noise ratio of the OTDR traces and thus increase the precision of the distributed sensing measurement.

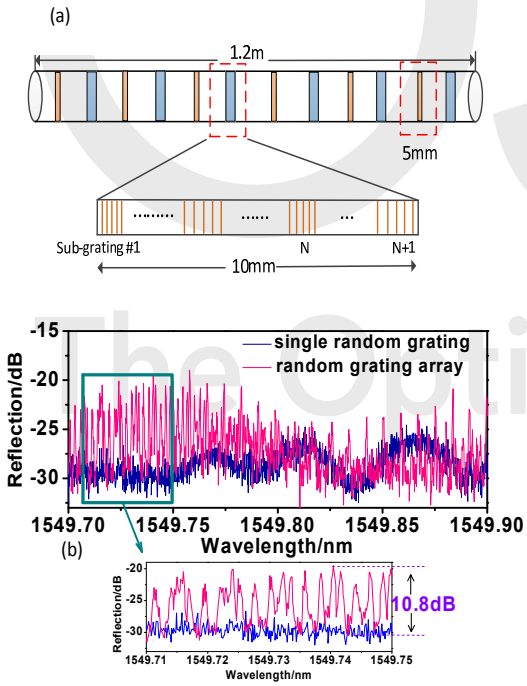

Fig. 1 (a) Schematic of RFGA; (b) Reflection of RFGA and single random grating.

A crucial device in this sensing system is the RFGA, which is fabricated along SMF by the refractive index modulation from the exposure of a femtosecond (fs)-IR pulse laser through the plane-by-plane technique [6], the grating periods of all 12 random gratings are randomly distributed between 0.5180 and 0.5464 μm so that the random gratings have high reflection (-30dB) at the wavelength (around 1550 nm) of the DFB laser used in the experiment as shown in Fig.1(a). And the induced insertion loss by the fs-IR laser during grating fabrication process is minimized. The length of each alternating grating are 10 mm and 5 mm, respectively.

As shown in Fig.1(b),the reflection spectrum (blue) of a 5 mm long single random grating is obtained by sending a ASE profile of an EDFA into the grating. The resultant spectrum possesses an irregular interference pattern with obvious fluctuations. The contrast of the reflective spectrum from random grating (reflection difference between highest point to lowest point as a function of wavelength) is higher than that from single mode fiber because of the larger local refractive index change. In order to further improve the contrast of the reflective spectrum, a RFGA comprising several single gratings as shown in Fig.1(a) was used as a sensor resulting in a contrast more than 10.8 dB. In this case, the irregular interference fringes introduced in the reflection spectra are the result of numerous Fabry-Perot interference (FPI) coupling.

The principle of this FTTM method by using chirped pulse is illustrated in Fig.2 in which a RFGA is used as the sensor. A chirped pulse serving as a probe signal, is sent to the sensor section and then a shaped reflection pattern is detected by a PD. By sending the probe pulse a second time with a certain repetition rate, we obtain two time domain traces (red solid line and blue dashed line) that represent different temperature conditions of the sensor. The real time delay between the two encoded time domain traces is linearly proportional to the frequency shift and is calculated by using trace to trace correlation over a specific time window.

Assume the pulse width and the optical frequency content of the probe pulse are W and Δυ, respectively. t=0 is the moment of the rising edge of chirped pulse. The instantaneous frequency profile of the chirped pulse is then expressed as:

$$\upsilon(t) = \left(\upsilon_0 + \frac{\Delta\upsilon}{W} \cdot t \right) \mathrm{Rect}\left(t/W\right) \quad (1)$$

where the υ_0 is the starting frequency of chirped pulse. Given the fixed receiving time t, the optical power at the input end of the RFGA is given by:

$$I(t) = I_0 \int_{(t-W)c/2n}^{tc/2n} \int_{(t-W)c/2n}^{tc/2n} e^{-2\alpha(Z_i+Z_j)} r(Z_i) \cdot r(Z_j) \cdot e^{i\left[\Delta\varphi_{ij}(t)\right]} dZ_i dZ_j \quad (2)$$

where n is the average value of refractive index and c is the velocity of light in a vacuum. α is the average attenuation of the unit-length RFGA; Z_i and Z_j are the fiber length between the the input end of fiber and i^{th} or j^{th} spot; $\Delta\varphi_{ij}(t)$ is the phase difference of waves from ith and jth scattered spots; I_0 is input power of the light and $r(Z_i)$ and $r(Z_j)$ are the reflection coefficient i^{th} and j^{th} scattered spots, respectively. To simplified the model, we only consider the optical path length difference of any two scattered spots for phase difference calculation. So, the phase difference of any two scattered spots within the pulse width are expressed as

$$\Delta\varphi_{ij}(t) = 2\pi\int_{t-2nZ_j/c}^{t-2nZ_i/c}(\upsilon_0 + \Delta\upsilon\cdot t/W)\,dt$$
$$= 2\pi\left[\left(\frac{2n(Z_i - Z_j)}{c}\right)\left(\upsilon_0 + \frac{\Delta\upsilon}{W}t\right) + \frac{\Delta\upsilon 2n^2}{Wc^2}(Z_j^2 - Z_i^2)\right] \quad (3)$$

As shown in Fig.2, if the delay time of two traces Δt is small (less than 10% pulse width). the optical power at time t_1 moment in the red solid curve and at time $t_1+\Delta t$ moment in the blue dashed curve could be calculated by using the same integration range of the fiber. The same fiber section corresponds to pulse range AB at t_1 and pulse range CD at $t_1+\Delta t$. With this assumption, the two time domain traces $I_1(t)$ and $I_2(t+\Delta t)$ are decided by the phase difference of any two scattered spots within the pulse width.

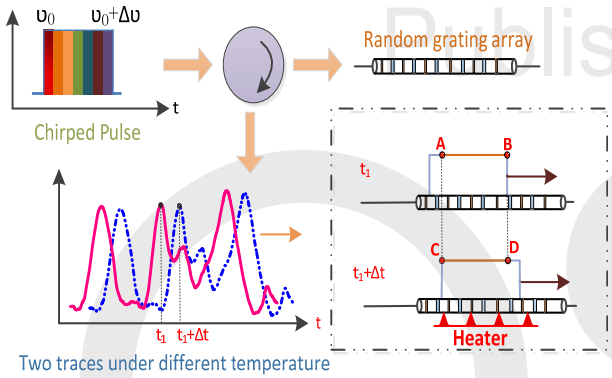

Fig. 2. Principle of proposed real time distributed sensing system based on RFGA (red solid line represents no temperature change applied, blue dashed line represents certain temperature change applied on RFGA).

In Equ.3, the second part on the right hand is very small compared with first term and can be neglected. The two traces (red solid curve and blue dashed curve) have a certain time delay Δt since the the optical path length of two scattered spots has been changed by the temperature change. Therefore $I_1(t)$ equals to $I_2(t+\Delta t)$. The relationship between real time delay Δt and temperature change could be expressed as:

$$\Delta t = \frac{\upsilon_0 \cdot W \cdot \Delta T}{\Delta\upsilon}\cdot k \quad (4)$$

where ΔT is the temperature change and k is the temperature related time delay coefficient. From Equ.(4), the optical path difference change between I(t) and I(t+Δt) will be compensated by a real time delay Δt. In this case, this frequency-to-time mapping method converts the frequency shift into the real time delay of two one-shot measurement traces achieving a high sensing speed.

Fig.3 depicts the experimental setup used for the temperature change measurement: a chirped pulse generator scheme was composed of a DFB laser diode (CQF938/500, JDS Uniphase), a pulse generator (PG) (8130A, Hewlett Packard) and a semiconductor optical amplifier (SOA) (OPB-10-10-N-C-FA, Kamelian) that was driven by an electrical circuit designed in-house. A polarization controller was utilized to vary the state of polarization of the output light from the DFB laser so as to get maximum efficiency of SOA. The DFB laser had a wavelength of 1550.103nm that was modulated by a 20ns electrical sawtooth signal with 10ns rising edge and 10ns falling edge. The pulse generator introduced a continuous linear variation of the optical frequency of output light. Meanwhile, a synchronized trigger signal with a repetition rate of 1 MHz was used to actuate the drive circuit, yielding an optical pulse at the output end of SOA device.The pulse width is about 6ns with frequency content of 3 GHz.

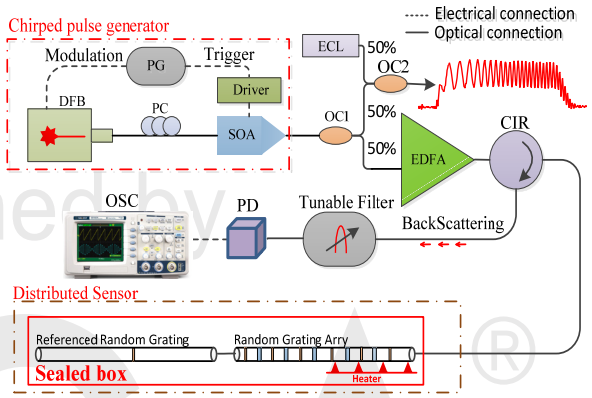

Fig.3. Experimental setup of random grating based distributed sensor for temperature measurement.

It is worth noting that the modulation pulse and trigger pulse were synchronized. The chirped optical pulse signal was split by a 50/50 optical coupler (OC1) and then recombined with a reference narrow linewidth external cavity laser (ECL) that acted as a monitor by another 50/50 optical coupler (OC2). After being boosted by an Erbium doped fiber amplifier (EDFA), the output light from another branch of OC1 was injected into the random grating sensor through an optical circulator (CIR) to explore external disturbance induced by temperature. A tunable optical filter (OSP-9100, Newport) was then deployed to remove the ASE noise from the EDFA that would be present in the distributed backward scattered signal before detecting it by a 40G bandwidth photo detector (PD) (DSCH10H-39-FC, Discovery Semiconductor Inc). Ultimately, the electrical waveform was monitored in real time by an oscilloscope (DSO81204B, Agilent).

In this experiment, the total length of the RFGA is approximately 1.2±0.01m as shown in Fig.1(a). The total length of the random fiber grating is limited by the fabrication setup and could be further improved. A single random grating with length of 2m is used as reference. A static measurement of temperature were performed on the last half section of the RFGA. The temperature varied from 25℃to 38.2℃with a temperature increment of 0.3 ℃ with standard deviation of 0.02 ℃. For each temperature status, it costed about 3-4 minutes to stabilize and collect the traces. In order to avoid the effect of external environment, the sensor was put into a sealed box.

Fig.4 (a) depicts the time domain traces of second half part of RFGA with time window of 6ns when different temperature is applied. In order to verify the ability of distributed sensing, the time domain traces of referenced random grating also be presented when its temperature remains unchanged as shown in

Fig.4 (b). It is obvious that the traces from RFGA have a significant shift with temperature variation, while the traces from referenced grating almost stay same.

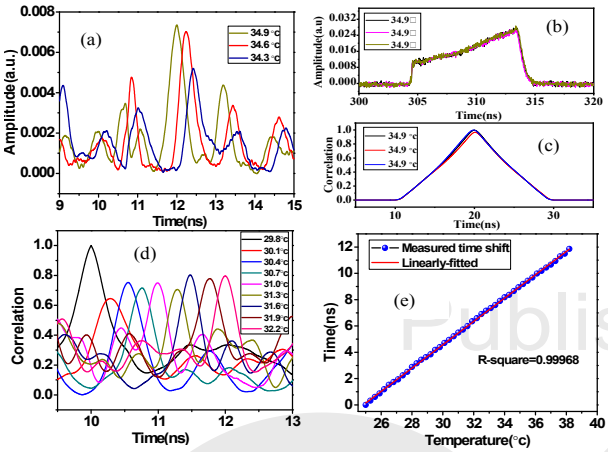

Fig. 4 (a) Real time domain traces of the last half portion of the RFGA at different temperatures ; (b) time domain trace of referenced random grating without temperature variation. (c)normalized cross correlation between traces for the referenced single random grating; (d) normalized cross correlation between traces from the RFGA at different temperature; (e) cross correlation peak of the real time delay.

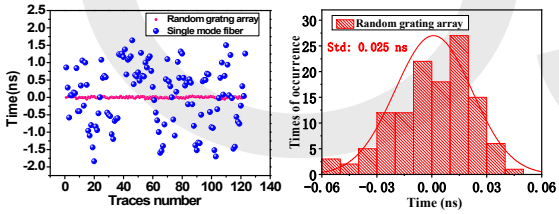

Fig. 5. (a) real time delay fluctuation with 5 samples moving average of RFGA when temperature remains unchanged ; (b) histogram of real time delay fluctuation of RFGA.

In order to investigate the relationship between real time shift of traces and the temperature variation, cross correlation calculation between current trace and the subsequent one is performed. Fig.4 (d) shows cross correlation spectrum between different time domain traces that obtain from different temperature condition. The time difference between any two cross correlation peaks represents the temperature variation induced real time delay. The cross correlation spectrum of the referenced grating is shown in Fig.4 (c), which has a larger line width than the RFGA resulting low demodulation accuracy. The relationship between temperature and real time delay is evaluated using linear fitting as shown in Fig.4 (e). It is evident that good linearity with a R-square value 0.99968 is obtained. The cross correlation peak real time delay-related temperature coefficient is 0.885ns/℃with a standard deviation of 0.03ns. In our demodulation process, the cross correlation calculation is applied within the specific time window of 6ns. Thus, the spatial resolution should be 1.2m. The distributed sensing could be realized by employing demodulation process with different time window. The maximum temperature variation that can be sensed is about 1.2 ℃ in static measurement, which is limited by the frequency content of the chirped pulse.

Ultimately, 128 traces collected by the oscilloscope at the repetition rate of 1 MHz were used to assess the precision of the sensing system when a fixed temperature was applied. The cross correlation peak real time delay results of those 128 traces as shown in Fig.5 (a). In order to reveal the high precision of the random grating sensor, the same evaluation for inherent Rayleigh scattering from a fiber was also measured. The experimental setup was strictly the same, and the only difference was the replacement of the RFGA by a single mode fiber (SMF). Fig.5 (a) shows that the time delay measurement results from a SMF has larger fluctuations than the that of RFGA. The histogram of real time delay fluctuation is shown in Fig.5 (b). The standard division of the fluctuation is calculated by using Gaussian fitting and the precision is 0.025 ns. The corresponding temperature precision is 0.028℃, respectively. This minimum detectable temperature variation is decided by the sampling rate of the oscilloscope and the stability of Rayleigh scattering pattern, which could be improved by further optimizing the system performance.

In conclusion, a novel distributed random grating sensor system based on chirped pulse optical time domain reflectometry is demonstrated for temperature measurement. Compared with normal phase OTDR system, our proposed system could used for static measurement, while it also have a capacity for dynamic measurement up to several kHz which is much higher than OFDR scheme. It is believed that the proposed sensing system based on the random grating sensor array could be potentially applicable in area of engineering because of its low cost and high stability .

Funding. This research has been primarily supported by the Natural Sciences and Engineering Research Council (NSERC) of Canada (STPGP 506628, RGPIN-2015-06071), as well as the Canada Research Chairs (CRC) Program (950231352) and Chinese Scholarship Council (CSC)

Disclosures. The authors declare no conflicts of interest.

References

1. X. Bao and L. Chen, Sensors 12, 8601 (2012).
2. A. Barrias, J. R. Casas, and S. Villalba, Sensors 16, 748 (2016).
3. K. T. V. Grattan and B. T. Meggitt, Optical Fiber Sensor Technology (Chapman & Hall, 1995).
4. Y. Xu, L. Zhang, S. Gao, P. Lu, S. Mihaiov, and X. Bao, Opt. Lett. 42, 1353 (2017).
5. Y. Xu, P. Lu, S. Gao, D. Xiang, P. Lu, S. Mihailov, and X. Bao, Opt. Lett. 40, 5514 (2015).
6. P. Lu, S. Mihailov, D. Coulas, H. Ding and X. Bao, J. Lightwave Technol. 37, 4697 (2019)
7. Bin Wang, Ping Lu, Stephen J. Mihailov, Xinyu Fan, and Jianping Yao, Opt. Lett. 44, 3246 (2019)
8. H. Fu, H. Liu, X. Dong, H. Tam, P. Wai, and C. Lu, Electron. Lett. 44, 618 (2008)
9. L. Ma, C. Ma, Y. Wang, D. Y. Wang, and A. Wang, IEEE Photon. Technol. Lett. 28, 1344 (2016).
10. J. Pastor-Graells, H. F. Martins, A. García-Ruiz, S. Martín-López, and M. González-Herráez, Opt. Express 24, 13121 (2016).

5.3 Distributed static and dynamic strain sensing with enhanced static measurement range

In a conventional chirped pulse φ-OTDR system, the maximum measurable strain or temperature variation is limited by the large time delay estimation (TDE) error due to the distortions of reflected traces from the sensing location. In this section [31], A high-performance distributed sensing system based on a random fiber grating array (RFGA) and multi-frequency database demodulation (MFDD) method for strain-induced delay time measurement is demonstrated for the first time. It enables a wide measurement range for static and dynamic strain sensing since the TDE accuracy is maintained in high value in large strain variation by introducing initial frequency difference compensation. Because of the requirement of high temporal stability and large optical frequency scanning range for database establishment, a random fiber grating array is used as the sensor part to provide stable reflection with a broad spectrum range. Both distributed static and dynamic strain variation sensing is experimentally demonstrated, and the maximum measurable strain variation range is significantly improved compared with the traditional method. More importantly, this performance-enhanced setup provides important guidance to employ chirped pulse phase OTDR in some particular applications, such as the crack detection of large construction and railway tracks, in which large strain variation in long distances is required for the detection of arbitrarily large and unknown perturbation.

Strain measurement range enhanced chirped pulse φ-OTDR for distributed static and dynamic strain measurement based on random fiber grating array

YUAN WANG,[1] PING LU,[3] STEPHEN MIHAILOV,[3] LIANG CHEN,[2] AND XIAOYI BAO[1,2,*]

[1]School of Electrical Engineering and Computer Science, University of Ottawa, Ontario K1N 6N5, Canada
[2]Department of Physics, University of Ottawa, 25 Templeton Street, Ottawa, Ontario K1N 6N5, Canada
[3]National Research Council Canada, Ottawa, Ontario K1A 0R6, Canada

Received XX Month XXXX; revised XX Month, XXXX; accepted XX Month XXXX; posted XX Month XXXX (Doc. ID XXXXX); published XX Month XXXX

A high performance distributed sensing system based on a random fiber grating array (RFGA) and multi-frequency database demodulation (MFDD) method for strain induced delay time measurement is demonstrated. It enables a wide measurement range for both static and dynamic strain sensing. The proposed MFDD method can enlarge the strain measurement range since the large strain variation induced time domain trace distortion could be compensated by laser initial frequency changes. Furthermore, a random fiber grating made with embedded large random refractive index changes along the single mode fiber could provide a stable reflection with a wide reflection spectrum range. Such a structure successfully improve the time delay measurement precision and also achieves a large tuning range as demonstrated by the database that a set of pre-recorded undisturbed reflected Rayleigh traces form RFGA at various laser frequencies. Ultimately, a dynamic strain with peak-to-peak value of 12.5 με at vibration frequency of 50 Hz is accurately reconstructed when the pulse repetition rate is 1 kHz, which was not detected using a conventional chirped pulse φ-OTDR. The maximum measurable strain variation of about 12.5 με represents a factor of 3 improvement. This number is limited by pre-recorded frequency scanning range of RFGA response in the database.

http://dx.doi.org/10.1364/OL.99.099999

Distributed optical fiber sensors (DOFSs) can detect strain or temperature variations along the entire fiber length, which plays an increasingly important role in fields of structural health monitoring and intruder detection. Various DOFSs have been researched and demonstrated for quantitative strain sensing, such as Brillouin optical time domain analysis (BOTDA), phase sensitive optical frequency domain reflectometers (φ-OTDRs) and optical frequency domain reflectometers (OFDRs) [1-4]. The distributed strain measurement is achieved by measuring Brillouin frequency shift (BOTDA), phase shift (φ-OTDR) or wavelength shift (OFDR) at every position in the fiber. Among them, φ-OTDRs have higher strain sensitivity to reach nε levels based on phase demodulation by using ultra narrow line-width lasers (3 kHz) [5]. However, the strain range is limited by the unwrapping algorithm used in φ-OTDR., since the demodulated phase is distorted when the absolute value of the phase jump between two consecutive points is larger than π. To solve the problem, a two-wavelength OTDR is proposed [6]. Such an approach makes the system complex and expensive due to the requirement for two phase locked lasers. Besides, Phase demodulation based on optical interferometry is sensitive to strain and temperature which imposed an environmental dependence. It is important to limit the usage of phase demodulation based phase locked laser and interferometry in order to reduce the overall system cost and environmental sensitivity.

Recently, a novel φ-OTDR sensing system using a distributed feedback (DFB) laser without an optical interferometer-based phase demodulation scheme is proposed [7]. Perturbations (strain or temperature variations) induced optical path length changes are translated into local time delays within the time window of optical trace. The principal advantage of this scheme is that real time high accuracy strain (nε) measurements are achieved by using a low-cost DFB laser (1MHz), where no environmental dependence in demodulation process is observed. However, distortions in OTDR traces appear for large strain or temperature variations. This is due to the position dependence in time delay determination and introduces large error for strain or temperature reconstruction. Therefore, the maximum measurable strain is limited to < 1 με. In some particular applications, such as crack detection on civil structures or railway lines, large strain measurements ranges are required for the detection of arbitrarily large and unknown perturbations. In reference [8], dynamic strain variation of 1190 με at a vibrational frequency of 400 Hz has been successfully reconstructed when high repetition rate of interrogation system was used (200 kHz). However, the total sensing distance which is related to the pulse repetition rate will be

significantly reduced. Another potential method to enhance the measurement range is to increase the chirping slope of the chirped pulse. However this approach reduces the sensitivity of the system (minimum detectable strain variation). There is a trade-off between the strain resolution and sensing range.

In this letter, a novel approach based on the multi-frequency database demodulation (MFDD) method is proposed and demonstrated to improve the strain measurement range for both static and dynamic strain measurements. In order to improve the time delay measurement precision, a random fiber grating array (RFGA) with a larger index change range is utilized as a stable reflected trace provider [9]. The RFGA, with a number of artificial refractive index planes, enables a wide-wavelength reflection [10], which always offers reflection when the initial frequency of the DFB laser experiences a large tuning range in the established database.

Chirped pulse phase OTDR (CP φ-OTDR), which makes use of the Rayleigh backward scattering effect, has been widely used for the measurement of perturbations along an optical fiber. The major difference when compared with traditional phase OTDR is that the optical frequency of integration pulses used here has a linear variation. The instantaneous optical frequency profile of the chirped pulse is then expressed as [7]:

$$\upsilon(t) = \left(\upsilon_0 + \frac{\Delta\upsilon}{W}\cdot t\right) Rect\left(t/W\right) \quad (1)$$

where Rect is the rectangular function,υ_0 is the initial optical frequency of chirped pulse and W and Δυ are the pulse width and the spectral content of the chirped pulse respectively. If this chirped pulse is sent to a section of optical fiber, the optical power at the input end of the optical fiber at given time t is expressed as:

$$I(t)_{AC} = I_0 \int_{(t-W)c/2n}^{tc/2n} \int_{(t-W)c/2n}^{tc/2n} e^{-2\alpha(Z_i+Z_j)} r(Z_i)\cdot r(Z_j) \cdot e^{i\left[\Delta\varphi_{ij}(t)\right]} dz_i dz_j \quad (2)$$

where n is the average value of refractive index and c is the velocity of light in a vacuum. α is the average attenuation of the unit-length random grating array; Z_i and Z_j are the fiber length between the the input end of fiber and scattering center *i* th or *j* th; I_0 is input power of the light and $r(Z_i)$ and $r(Z_j)$ are the reflection coefficient of scattering center *i* th and *j* th, respectively. $\Delta\varphi_{ij}(t)$ is the phase difference between two scattering center *i* th and *j* th, which could be expressed as [7]:

$$\Delta\varphi_{ij}(t) = 2\pi\int_{t-2nZ_j/c}^{t-2nZ_i/c}\left(\upsilon_0 + \Delta\upsilon\cdot t/W\right)dt = 2\pi\left[\left(\frac{2n(Z_i - Z_j)}{c}\right)\left(\upsilon_0 + \frac{\Delta\upsilon}{W}\left(t - \frac{n(Z_i+Z_j)}{c}\right)\right)\right] \quad (3)$$

From Eq. (2) and Eq. (3), we find that the shape of reflected trace from optical fiber is associated with the phase of the reflected electrical field, which is determined by the optical frequency of the laser source and the optical path length between any two scattering centers. Therefore, if a strain or temperature induced variation in the trace shape occurs at one position, the specific time delay between two given times t_0 and t_1 from two time domain traces (before and after strain applied) that could be used to compensate for the strain induced traces distortion [7]. On the other hand, a corresponding optical frequency shift of the laser source also can be applied to reconstruct the changed trace to the previous state [2]. Therefore, the applied strain variation Δε can be extracted based on both the time delay Δt and the initial frequency difference of chirped pulse υ_1-υ_0, such that:

$$\Delta\varepsilon\cdot K = \frac{\Delta nl + n\Delta l}{nl} = -\frac{\frac{\Delta\upsilon}{W}\Delta t + (\upsilon_1 - \upsilon_0)}{\upsilon_0} \quad (4)$$

where K is strain related frequency shift coefficient (equals to -0.59 in RFGA) [7][11]. υ_1 is the initial frequency of the reference trace in the database which has highest similarity with the encoded trace.

Based on the discussion above, we find that the maximum measurable strain variation Δε is significantly improved if we use a database comprised of various traces which are collected from chirped pulses with different initial optical frequencies. The MFDD method is proposed and operated as follows: Firstly, a database including several traces without perturbation is established. These traces are collected when chirped pulses with different initial optical frequency (υ_0 in Eq. 1) are used to interrogate the whole RFGA. Secondly, coded traces are recorded using chirped pulses with known fixed initial optical frequencies when dynamic strain is applied in a period of time. Thirdly, in the demodulation process, the cross correlation calculation between each encoded trace and each reference trace in the database is employed. Finally, the cross correlation calculation result of each coded trace which possesses the highest coefficient will be selected for relative strain change determination.The overall strain variation is reconstructed based on the initial frequency difference υ_1-υ_0 and time delay Δt without integral operation.

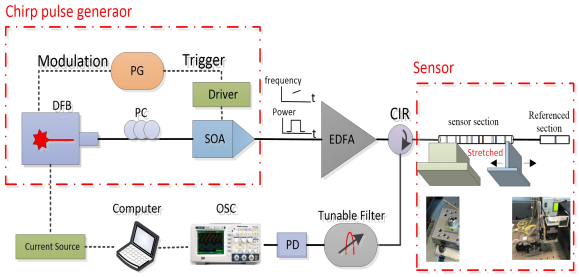

Fig. 1. Experimental setup of RFGA based distributed sensor for static and dynamic strain sensing.

The setup of our proposed system is shown in Fig. 1. A DFB laser diode (CQF938/500, JDS Uniphase) driven by an adjustable DC current source is utilized to generate chirped pulses. The chirped pulse is produced by a pulse generator (PG) (8130A, Hewlett Packard) combined with a semiconductor optical amplifier (SOA) (OPB-10-10-N-C-FA, Kamelian) synchronized through the PG. The pulse generator introduces a frequency sweep of output light by adding an electrical modulation pulse signal with 10 ns rising edge and 10ns falling edge to the DFB laser. The output light of DFB laser is changed into a chirped pulse signal by the SOA that is driven by a home-made electronic circuit board. The chirped pulse signal with 6ns pulse width and 1.375 GHz frequency content is amplified by an Erbium doped fiber amplifier (EDFA) before being sent to the strong RFGA. The one end of the RFGA is fixed on a translation stage, while the other end is glued to the top of

Piezoelectric Transducer (PZT) device (P-6113S, PI). The displacement of the PZT device can be precisely controlled by an electrical signal. The backward scattered signal from the strong RFGA is detected by a 40G bandwidth photo detector (PD) (DSCH10H-39-FC, Discovery Semiconductor Inc). An optical filter (OSP-9100, Newport) is used to remove the ASE noise from the EDFA. Ultimately, the time domain traces are collected by an oscilloscope (DSO81204B, Agilent). For optical frequency sweeping purposes, the computer is employed to change the output of the current source and synchronize the Oscilloscope (OSC) for trace collection.

A crucial factor of the feasibility of the proposed method is the issue of larger time delay measurement uncertainty [11]. In our proposed system, the refractive index changes of the strong RFGA was fabricated along the SMF by the fiber to a femtosecond (fs)-IR pulsed laser through the plane-by-plane technique [12]. The RFGA was 0.8 m in length including 8 alternating sub-gratings that are 10 mm and 5 mm long, respectively. The grating periods of all 8 sub-gratings are randomly distributed between 0.5180 and 0.5464 μm [7]. Because of its larger index change range (10^{-5}) as compared to scattering levels from the single mode fiber, the RFGA reflection could reach -30 dB (SMF is about -70 dB) and thus the (signal to noise ratio) SNR of the trace could be enhanced. More importantly, the cross talk effect induced distortion is negligible when refection of sensor is around -30dB.

A time delay measurement precision evaluation was carried out first. As shown in Fig. 2(a), 1000 traces were collected by OSC using a chirped pulse with a fixed initial optical frequency when no perturbation was applied. The pulse repetition rate was 1 kHz and the total acquisition time was 1 s. In order to distinguish the tiny temporal shift of 1000 traces, a cross correlation calculation between the current and subsequent traces is performed (trace No. 1 with trace No. 2, trace No. 2 with trace No. 3 and .....). The result as shown in the insert figure of Fig. 2(a), indicates the high SNR of the reflected traces from RFGA over the acquisition time. Fig. 2(b) depicts the histogram of the temporal shift fluctuations of the reflected traces with a standard deviation of about 31.8 ps, which indicates that the low SNR induced temporal shift noise is effectively suppressed and the laser frequency drifting could be ignored within 1 second.

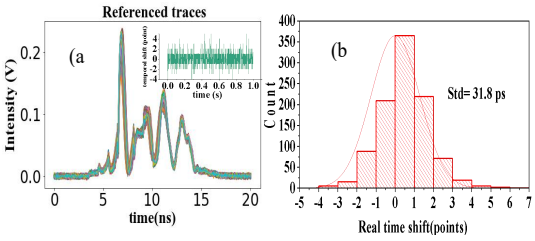

Fig. 2. The evaluation of time delay measurement in CP φ-OTDR based on RFGA. (a) 1000 traces (no average) and (b) the temporal shift standard deviation. (The insert figure shows the temporal shift of traces over acquisition time of 1 s)

Before applying the strain, the database should be established for demodulation under the condition of no applied strain. The current source is precisely controlled by software, and the tuning step is 1 mA (±0.01 mA). As shown in Fig. 3, the 11 collected traces that represent the impulse response from the random fiber grating array are collected when the initial optical frequency of chirped pulses are adjusted from 193536.213 (±0.005) GHz to 193534.838 (±0.005) GHz with tuning step of 0.1375 GHz. One encoded trace collected under certain value of strain is used to calculate the cross correlation with 11 referenced traces in database as shown in Fig. 3 (b). There are 11 pairs of time delays value and coefficient value after the cross correlation calculation. It is obvious that the highest coefficient should be selected for the strain variation calculation since higher coefficients represent a higher similarity between the two traces and thus a higher time delay estimation accuracy. In Fig3. (b), the result of traces sequence of 7 has the highest coefficient (blue solid circle), so its corresponding time delays (green dashed circle) will be selected for strain variation determination. At every measurement, the coefficient will be re-selected and the highest one picked.

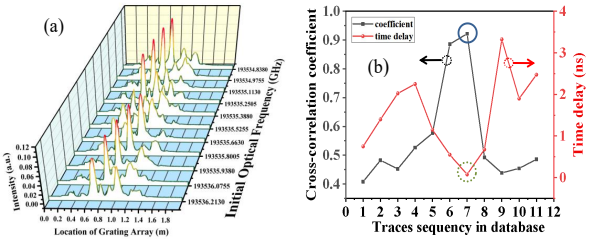

Fig. 3. (a) 11 Reflected traces of random fiber grating array in database when different initial optical frequency of chirped pulses are used; (b) 11 cross correlation results between encoded traces and traces in database.

In order to compare the system performance with and without the MFDD method, static and dynamic strain measurements were performed. In our experiment, the strain was applied on the sensor section (as shown in Fig. 3) through the translation stage and high precision PZT. For static measurements, different strain variation were applied to the RFGA and its corresponding reflected traces were collected. As shown in Eq.(4), the applied strain induced optical path length change is translated into a local time delay within the time window. So the cross-correlation calculation between the two traces is a valid method to extract local time delay information. In the demodulation process, the cross-correlation calculation is performed between the two traces obtained before and after applying the strain variation without using database. Fig.4 (c) illustrates the cross-correlation coefficient variation when different stains are applied. It is obvious that the cross-correlation coefficient decreases significantly with increasing levels of applied stain as shown by the appearance of the distortions of the OTDR traces in Fig.4 (b). Therefore, the similarity of the two traces will obviously decrease, which is embodied through the low cross-correlation coefficient. However, the cross-correlation coefficient maintains a high value under large strain variation when the database is used, since the large strain variation induced optical path length change is compensated by both the initial optical frequency difference and the time delay (Eq.(4)). As depicted in Fig.4 (a), the larger strain variation also gives a high coefficient value when the database is utilized since the initial optical frequency difference compensates a part of the strain variation, resulting in a small time delay. The applied strain variation and its demodulation resulting from the different methods are shown in

Fig.4 (d). The figure clearly shows that the maximum measurable strain variation is significantly enhanced by using the MFDD method. The demodulation result of the reference section (no strain applied) is also obtained at the same time, which proves the capacity for distributed sensing. In our experiment, the selected time window for cross-correlation calculation is 6 ns as shown in Fig. 4 (a), so the spatial resolution is about 1.2 m. The maximum measurable strain variation is about 4.5 με without the MFDD method. While the maximum measurable strain variation for the MFDD method is about 12.5 με with a standard deviation of 66 nε. The minimum detectable strain variation dependent on the time delay measurement precision is about 66 nε.

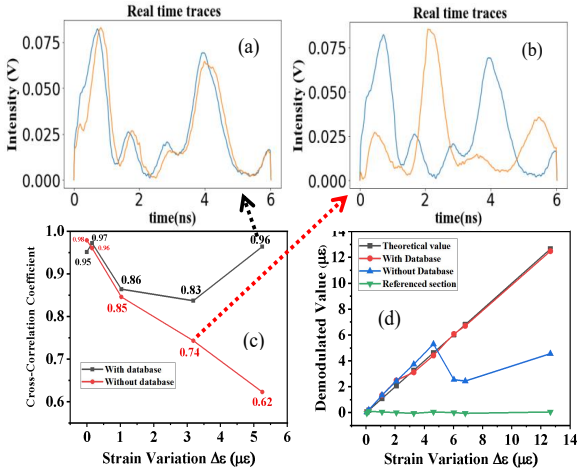

Fig. 4. (a) Reflected trace after applying strain on the RFGA and most similar trace in database; (b) Reflected traces before and after applying strain on the RFGA; (c) the relationship between cross-correlation coefficient and different applied strain; (d) the performance of demodulation with and without database.

Fig. 5 illustrates the result of a dynamic strain measurement in which a fixed peak-to-peak 12.5 με (10 μm length change) strain change and different vibration frequency are applied on the RFGA. The repetition rate of the chirped pulse for all the measurements is fixed at 1 kHz. When the vibration frequency is low, for example 10 Hz, each vibration period has 50 sampling points. In this case, the dynamic strain variation is perfectly revealed by using both methods as shown in Fig.5 (a). In Fig. 5 (c), the frequency response of the demodulated dynamic strain variation indicates a dominant peak precisely locating at 10 Hz with a high SNR up to 43 dB. However, there is a big difference between the two methods when the frequency of applied strain variation is 50 Hz as shown in Fig. 5(b). Because of fewer sampling points (10 samples) within vibration period, the strain variation between some of the two sampling points is close to the maximum value. Thus, the cross-correlation coefficient between the two traces is very low according to Fig. 4 (c). The demodulation results will suffer from a large uncertainty in the delay time estimation, which leads to incorrect reconstructed wave. In comparison, the demodulation process with the MFDD method maintained a good result. In Fig. 5 (d), the zero padding method is used for peak location determination. A dominant peak representing 50 Hz is shown in insert figure. For dynamic strain measurement, the MFDD method significantly improves the maximum detectable vibration frequency. If the size of the database is large enough, the maximum detectable vibration frequency can reach the theoretical limit which is equal to half of the pulse repetition rate.

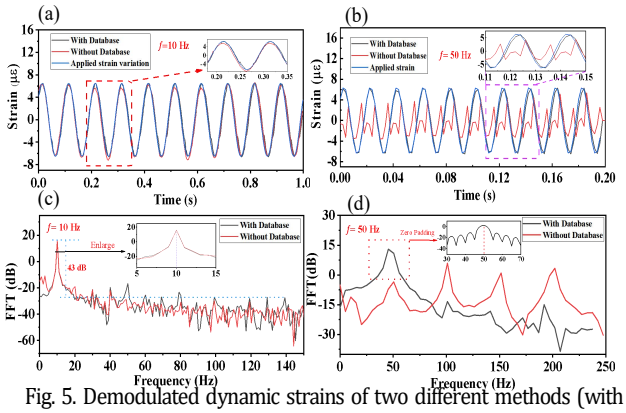

Fig. 5. Demodulated dynamic strains of two different methods (with and without database) (a)10 Hz sinusoidal variation (b) 50 Hz sinusoidal variation and its frequency responses (c) and (d).

To summarize, a high performance CP φ-OTDR based on both the MFDD method and an RFGA is proposed and demonstrated for both static and dynamic strain detection. The RGFA possesses a wide reflection spectrum range and variable widths peaks in time domain , which achieves high time delay sensing accuracy. Experimental results show that the proposed MFDD method could effectively solve the measurement range limitation which is caused by large time delay estimation error, indicating an attractive potential for this approach in the field of structural health monitoring.

Funding. China Scholarship Council (201808330421); Canada Research Chairs (950231352); Natural Sciences and Engineering Research Council of Canada (RGPIN-2015-06071, STPGP 506628).

Disclosures. The authors declare no conflicts of interest.

References

1. Y. Dong, D. Ba, T. Jiang, D. Zhou, H. Zhang, C. Zhu, Z. Lu, H. Li, L. Chen, and X. Bao, IEEE Photonics J. 5(3), 2600407 (2013).
2. Y. Koyamada, M. Imahama, K. Kubota, and K. Hogari, J. Lightwave Technol. 27, 1142 (2009).
3. S. Zhao, J. Cui, L. Suo, Z. Wu, D. Zhou, and J. Tan, J. Lightwave Technol. 37, 3721 (2019) .
4. A. Masoudi and T. Newson, Rev. Sci. Instrum. 87, 011501 (2016).
5. Y. Dong, X. Chen, E. Liu, C. Fu, H. Zhang, and Z. Lu, Appl. Opt. 55, 7810 (2016).
6. H. He, L. Yan, H. Qian, X. Zhang, B. Luo and W. Pan, Opt. Express, 28, 226 (2020).
7. Y. Wang, P. Lu, S. Mihailov, L. Chen, and X. Bao, Opt. Lett. 45, 3423 (2020)
8. H. D. Bhatta, L. Costa, A. Garcia-Ruiz, M. R. Fernandez-Ruiz, H. F. Martins, M. Tur, and M. Gonzalez-Herraez, J. Lightwave Technol. 37, 4888 (2019).
9. Z. Zhou, P. Lu, L. Zhang, S. Mihailov, L. Chen, and X. Bao, Opt. Lett. 44, 4195 (2019).
10. L. Zhang, P. Lu, Z. Zhou, Y. Wang, S. Mihailov, L. Chen, and X. Bao, IEEE Sensors Journal, 20, 5885 (2020).
11. M. R. Fern ´ andez-Ruiz, L. Costa, and H. F. Martins, Sensors, 19, 4368 (2019).
12. P. Lu, S. Mihailov, D. Coulas, H. Ding, and X. Bao, J. Lightwave Technol. 37, 4697 (2019).

5.4 Ultra-low frequency dynamic strain detection with laser frequency drifting compensation

In a conventional chirped pulse φ-OTDR system, the significant laser frequency drifting (LFD) has limited the detection in the ultra-low vibration frequency range (below 1 Hz), where the LFD will introduce a time-dependent noise destroying the dynamic strain reconstruction over long acquisition time. In this section [32], using the referenced random fiber grating with no strain applied, the LFD-induced noise in time delay measurement can be precisely obtained, and then the pure dynamic strain variation will be extracted by performing a simple subtraction operation between referenced portion and the sensor portion. To the best of our knowledge, frequency and amplitude information is obtained for the first time that a 0.01 Hz dynamic strain variation is measured by chirped pulse φ-OTDR system. Since the chirped pulse φ-OTDR system is based on single-shot measurement, the LFD will equally affect all measured sensing points along a random fiber grating array, and the referenced portion could be selected from any part of the sensing fiber for LFD-induced noise compensation. In addition, the SNR-enhanced Rayleigh traces from random fiber grating ensure high accuracy of time delay measurement and laser frequency drifting measurement. More importantly, this performance-enhanced setup provides important guidance to employ chirped pulse phase OTDR in some particular applications, such as monitoring earthquakes and volcanoes, and charting rock and petroleum formations beneath the earth, in which the detection ability for an ultra-low vibration frequency range from 0.01 to 20 Hz is required.

Ultra-low frequency dynamic strain detection with laser frequency drifting compensation based on random fiber grating array

YUAN WANG,[1] PING LU,[3] STEPHEN MIHAILOV,[3] LIANG CHEN,[2] AND XIAOYI BAO[1,2,*]

[1]School of Electrical Engineering and Computer Science, University of Ottawa, Ontario K1N 6N5, Canada
[2]Department of Physics, University of Ottawa, 25 Templeton Street, Ottawa, Ontario K1N 6N5, Canada
[3]National Research Council Canada, Ottawa, Ontario K1A 0R6, Canada

Received XX Month XXXX; revised XX Month, XXXX; accepted XX Month XXXX; posted XX Month XXXX (Doc. ID XXXXX); published XX Month XXXX

Dynamic strain sensing over a frequency range from 0.01 to 20 Hz can be used for monitoring earthquakes and volcanoes, charting rock and petroleum formations beneath the earth. However, significant laser frequency drifting (LFD) has limited the detection in this frequency range, especially for distributed frequency detection with phase OTDR, where the LFD will introduce a time dependent noise destroying the dynamic strain reconstruction. In this study, a simple and effective method that utilizes the referenced random fiber grating to monitor the variation of laser frequency has been both theoretically analyzed and experimentally demonstrated. During the maximum up to 200 seconds data acquisition time, the frequency variation of a DFB laser with MHz linewidth is obtained from the referenced portion of sensing signal, then the 1 Hz and 0.01 Hz dynamic strain variation with amplitude of 30 με is reconstructed with strain measurement standard deviation of 66 nε. Due to SNR enhanced Rayleigh traces from random fiber gratings, a minimum detectable frequency drifting of 7.28 MHz could be achieved over the optical frequency of 2×10^{14} Hz.

http://dx.doi.org/10.1364/OL.99.099999

The phase-sensitive optical time domain reflectometry (φ-OTDR) based on the coherent effect of Rayleigh scattering has been widely used in intrusion monitoring, structural health monitoring and distributed birefringence measurements, because of its cost-effectiveness and larger frequency responding range (sub-kHz to MHz) [1-3]. However, infrasonics, which covers sounds waves beneath 20 Hz down to 0.01 Hz, can be used for monitoring earthquakes and volcanoes, charting rock and petroleum formations inside the earth, and also in ballistocardiography and seismocardiography to study the mechanics of the heart. The low frequency dynamic strain measurement based on φ-OTDRs are difficult to perform [4], because of the phase locked laser frequency and phase changes with time on the ms time scale. Due to the 1/f noise, the received φ-OTDR trace will change accordingly among trace-to-trace detection, and hence it is challenging to capture a low-frequency event. Conventional φ-OTDR normally requires an ultra-narrow linewidth phase locked laser for phase demodulation which is based on coherent detection when the amplitude of the perturbation needed to be quantified [5-6]. Recently, chirped pulse phase-sensitive optical time domain reflectometry (CP-φ-OTDR) that was based on random fiber grating was proposed for strain and temperature measurement [7]. In this technique, the interrogation signal is a train of linearly chirped optical pulses instead of transform-limited pulses. As a result, the linear relationship between the time delay of reflected Rayleigh traces and the perturbation induced wavelength/frequency shift is generated, thus the quantified waveform could be easily obtained by directly performing a cross-correlation calculation between reflected Rayleigh traces without requiring phase unwrapping [7]. More importantly, the laser source used in those schemes is a distributed feedback (DFB) laser with ~1 MHz linewidth. The reason behind this is that a single shot measurement without coherent detection does not require a laser with a long coherent time, as long as the coherence is preserved within the pulse width. Furthermore, because of the usage of random fiber grating array (RFGA), the SNR of reflected Rayleigh traces is enhanced. Thus, the measurement accuracy is significantly improved. Finally, as long as the visibility of the trace is well conditioned, the technique essentially provides a fading free measurement along all points of the fibre[8].

However, the shape of a reflected Rayleigh trace from an optical fiber is associated with the phase difference between any two scattering centers. The phase difference is not only determined by the optical path length between any two scattering centers but also by the optical frequency of the laser source. If the laser frequency drifts, a temporal shift between traces will occur between the neighboring reflected traces, even if the sensing fiber is isolated from the environment. For ultra-low vibration frequency detection, the LFD induced time delay noise becomes more significant during long data acquisition times making it difficult to recover ultra-low frequency dynamic strain variation. To extend this kind of sensor

to further application scenarios, this issue should be addressed urgently and some methods have been proposed [9-12]. In reference [10], an active compensation method for the tracking of LFD is proposed. In this method, LFD is monitored by comparing the current backscattering trace with the "databank' that includes many pre-measured backscattering traces at different optical frequencies. But, the databank may need to rebuild when the environment is changed, which makes this method become complicated and time-consuming. Recently, a simple and effective method based on twice differential has been demonstrated [11]. However, in this coherent detection based φ-OTDR system, the laser frequency drifting will affect fiber locations differently when laser source acts as local oscillator for phase reconstruction and thus laser drifting noise will be added continuously, potentially limiting the feasibility of this method in large frequency drifting or applied stain change. As a result, the referenced section used for compensation should be selected near the sensing section. However, in our proposed method without coherent detection, because the LFD will equally affect all measured sensing points along the RFGA, the referenced section can be easily selected from unperturbed fiber without location limitations.

In this study, a real time dynamic strain sensing system with LFD compensation based on a RFGA is proposed and demonstrated. The LFD induced time delay can be mitigated by a referenced random fiber grating connected to the RFGA that is used for distributed ultra-low frequency dynamic strain detection. In our experiment, 1 Hz and 0.01 Hz dynamic strain signal is successfully reconstructed apart from the LFD induced time delay noise.

The underlying principle of LFD compensation is shown in Fig.1. A referenced random fiber grating (RFG) utilized for monitoring laser frequency drift is connected to a RFGA. If a chirped pulse is used to interrogate the fiber under test, reflected Rayleigh traces comprised of the sensing fiber and the referenced portion will be obtained. The strain and LFD induced time delays between two adjacent Rayleigh traces in the sensor portion could be expressed as[7]:

$$\Delta\varepsilon \cdot K = \frac{\Delta nl + n\Delta l}{nl} = -\frac{\frac{\Delta\upsilon}{W}\Delta t_s + \Delta\upsilon'}{\upsilon_0} \qquad (1)$$

where $\Delta\varepsilon$ is strain variation applied on the RFGA, K is the strain related frequency shift coefficient for RFGA, n is the effective refractive index, Δn and Δl is the applied strain induced refractive index and distance between two scattering centers change, $\Delta\upsilon$ is spectral content, W is the width of chirped pulse, Δt_s is strain and LFD induced time delays. υ_0 and $\Delta\upsilon'$ are the initial optical frequency of laser and the laser frequency drifting, respectively. The stain variation induced time delays Δt_s measured from the sensor portion then is given by:

$$\Delta t_s = -\Delta\varepsilon \cdot K \cdot \upsilon_0 \cdot \frac{W}{\Delta\upsilon} - \Delta\upsilon' \cdot \frac{W}{\Delta\upsilon} = -\frac{\Delta nl + n\Delta l}{nl} \cdot \upsilon_0 \cdot \frac{W}{\Delta\upsilon} - \Delta\upsilon' \cdot \frac{W}{\Delta\upsilon} \qquad (2)$$

Because of the single shot measurement in the chirped pulse φ-OTDR, the LFD will equally affect all measured points along the RFGA[8]. The time delay Δt_R measured from the referenced portion with no strain variation applied can be expressed as:

$$\Delta t_R = -\Delta\upsilon' \cdot \frac{W}{\Delta\upsilon} \qquad (3)$$

The the pure strain variation induced time delays Δt can then be calculated by:

$$\Delta t = \Delta t_s - \Delta t_R = -\Delta\varepsilon \cdot K \cdot \upsilon_0 \cdot \frac{W}{\Delta\upsilon} \qquad (4)$$

In this case, the laser drifting can be effectively compensated without requiring external characterization of the laser. So, the strain variation induced time delays can be extracted and then the applied strain could be reconstructed. As shown in Fig.1(a), the reconstructed dynamic strain waveform from the sensor portion including the LFD induced noise shows an upward and downward fluctuation. On the other hand, if we applied the same data processing procedure for the referenced portion, the LFD induced time delay profile can be obtained for compensation. Then the pure dynamic strain variation will be extracted by performing a simple subtraction operation.

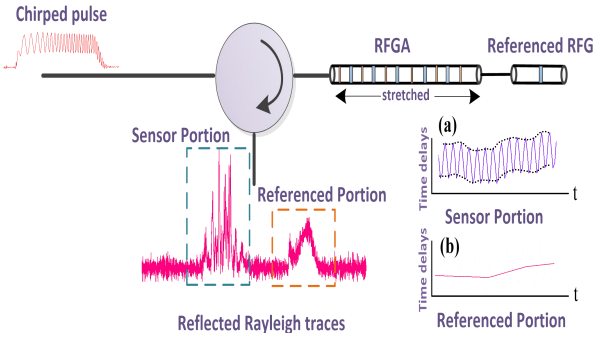

Fig. 1. Underlying principle of the laser frequency drift compensation method that utilizes a referenced random fiber grating (RFG).(time delays variation between two consecutive reflected Rayleigh traces at (a) sensor portion when dynamic strain is applied on RFGA and (b) referenced portion when no strain variation applied.)

The setup of our proposed system is shown in Fig. 1. A DFB laser diode (CQF938/500, JDS Uniphase) driven by an adjustable DC current source is utilized to generate chirped pulses. The chirped pulse is produced by a pulse generator (PG) (8130A, Hewlett Packard) combined with a semiconductor optical amplifier (SOA) (OPB-10-10-N-C-FA, Kamelian) synchronized through the PG. The pulse generator introduces a frequency sweep of output light by adding an electrical modulation pulse signal with 10 ns rising edge and 10ns falling edge to the DFB laser. The continuous light of DFB laser is changed into a chirped pulse signal by the SOA that is driven by a home-made electronic circuit board. Before being sent to the Erbium doped fiber amplifier (EDFA) for amplification, the chirped pulse is separated into two branches. One branch is beat with an external cavity laser (ECL) to monitor the frequency chirping of the pulse signal. The chirped pulse signal has a 6ns pulse width over the 1.375 GHz frequency range. Normally, a larger frequency range could give a bigger strain variation measurement range but with lower resolution, and vice verse.

In the sensor portion, the one end of the RFGA is fixed on a translation stage, while the other end is glued to the top of Piezoelectric Transducer(PZT) device (P-6113S,PI). The whole

setup is put into a home-made sealed box to minimize the impact of temperature fluctuation. The displacement of the PZT device can be precisely controlled by an electrical signal. A RFG is connected with the RFGA, acting as the referenced part. An optical filter (OSP-9100, Newport) is used to remove the ASE noise from the EDFA. After that, the backward scattered signal from the RFGA and referenced RFG is detected by a 40 GHz bandwidth photo-detector(PD) (DSCH10H-39-FC). Ultimately, the time domain traces are collected by an oscilloscope (DSO81204B, Agilent).

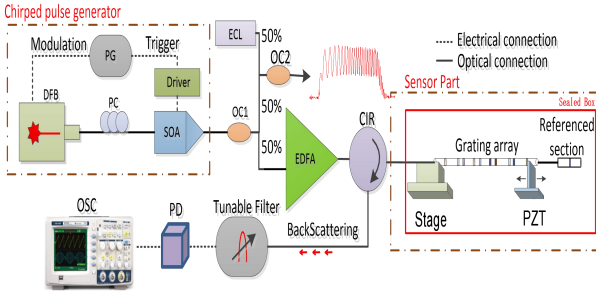

Fig. 2. Schematic of random fiber grating array-based dynamic strain sensing system with laser frequency drifting compensation.

Unlike standard single mode fiber, the RFGA has a strong wavelength-dependent wavelength shift when the same strain variation is applied. It is based on the fact that the spectral response has strong dependence on the dispersion due to grating inscription process in the effective refractive indices of the core mode when the broadband light source is employed[13]. Therefore, strain related wavelength shifts at the wavelength range of chirped pulse should be calibrated before using this grating array for dynamic strain measurement. In the calibration experiments, a broadband light source is employed as the laser source to obtain the reflection spectra of RFGA from the optical spectrum analyzer.

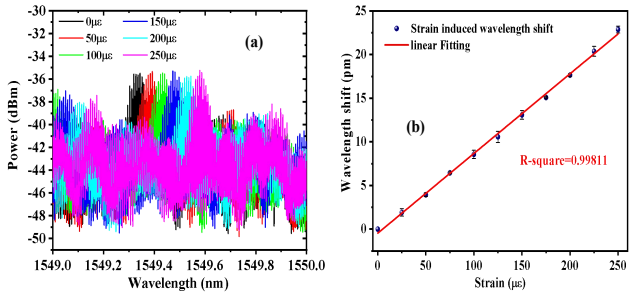

Fig. 3. (a) Reflection spectra of Random fiber grating array under different applied strain; (b) Relationship between applied strain variation and wavelength shift.

As shown in Fig.3 (a), the reflection spectra (1 nm range) from the RFGA with 25000 sampling points and 5 MHz resolution are collected when the applied strain is varied from 0με to 250 με in 50 με increments. It can be seen that the reflection spectra experience a right-ward shift to compensate for the strain variation induced optical path length increase, which satisfies the phase matching condition. In order to obtain the relationship between the applied strain variation and wavelength shift, the cross-correlation calculation between two spectra collected from RFGA under different applied strain is employed. Fig.3 (b) shows linear the relationship between the strain variation and wavelength shift with R-square of 0.99811, and the coefficient is about 0.908 pm/με. According to Equ.(4), the K value equals to 0.586 at wavelength of 1550 nm. After the calibration of the strain induced wavelength shift measurement, dynamic strain variation measurements with different peak-to-peak amplitudes were performed in order to verify the relationship between time delays and applied strain variation. The RFGA is fabricated along the SMF by the refractive index modulation from the exposure of a femtosecond(fs)-IR pulse laser through the plane-by-plane technique[7]. The RFGA is about 0.8m in length including 8 alternating sub-gratings that are 10 mm and 5 mm long, respectively. The grating periods of all 8 sub-gratings are randomly distributed between 0.5180 and 0.5464 μm. the length of the referenced RFG is about 10mm.

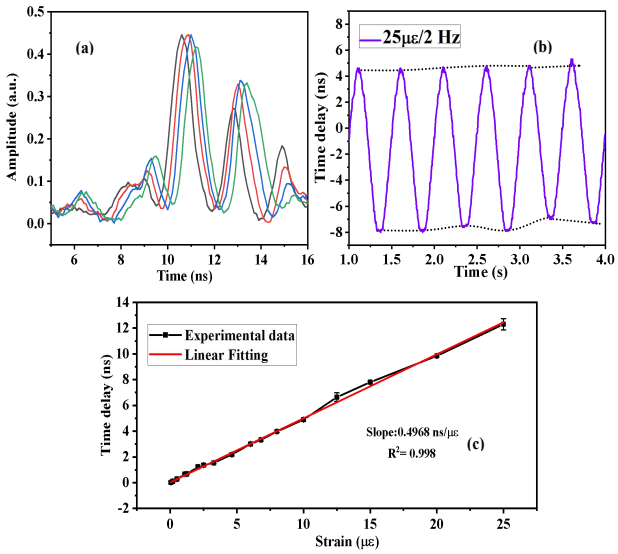

Fig. 4. (a)Reflected Rayleigh traces of RFGA under different strain variation. (b)its reconstructed dynamic strain variation waveform (no average applied); (c)Relationship between peak-to-peak time delays and peak-to-peak dynamic strain variations.

In the experiments, a sinusoidal wave of 2 Hz with amplitude of 1 voltage (equivalent 24 μm peak-to-peak length change) is generated by the function generator to oscillate the PZT, applying a 30 με peak-to-peak dynamic strain variation on the RFGA. The reflected Rayleigh traces from the grating array were continuously recorded with time interval of 4 ms that were determined by the pulse repetition rate. As shown in Fig.4(a), several reflected Rayleigh traces from the RFGA under different strain variations experience a temporal shift due to the photo-elasticity effect and the strain induced grating period changes. Both effects change the effective optical path length of any two scattering centers within the RFGA. For the reconstruction of the dynamic strain, the time delays between two collected traces should be calculated by the cross-correlation calculation. By calculating the time delays between the current trace and the adjacent one, the reconstructed dynamic strain waveform can be reconstructed as shown in Fig.4 (b). Based on the Equ.(4), we could get a linear relation between time delays and applied strain. The strain induced time delays coefficient could be theoretically calculated by using the pulse

width and spectra content of the chirped pulse and wavelength shift coefficient measured above, which are 6 ns, 11pm and 0.908 pm/με. The theoretical strain induced time delays coefficient equals to 0.495 ns/με. To verify this value, 17 measurements of dynamic strains at different amplitudes were performed using the RFGA at a frequency of 1 Hz. It clearly shows that the linear relationship between strain variation and time delay is 0.4968 ns/με with a R-square value of 0.998 and strain variation measurement standard deviation of 66 nε. This is consistent with the theoretical calculation within tolerance error.

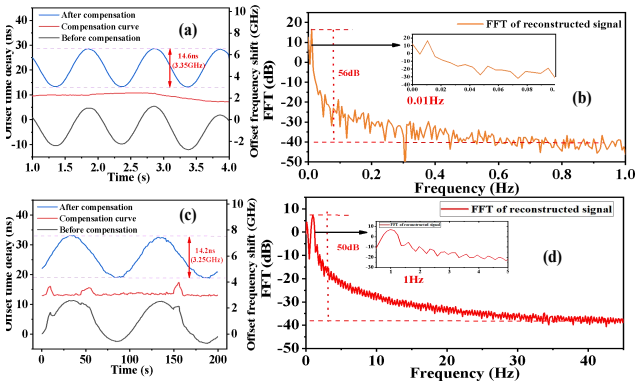

Fig. 5. Dynamic strain measurement with ultra-low vibration frequency of (a)1Hz and (c)0.01 Hz, and its FFT spectra (b) and (d).

Generally speaking, the dynamic strain applied to a RFGA can be detected by monitoring the time delays between the adjacent reflected Rayleigh traces. From the results, the vibration frequency and amplitude of the dynamic strain are precisely obtained. However, we also observed a remarkable fluctuation from the reconstructed waveform as shown in Fig.4 (b), which is mainly caused by the laser source frequency drifting. In order to eliminate the influence of LFD, the time delays of the referenced RFG between adjacent traces are measured to reconstruct the laser frequency fluctuation. These measurements are then used to compensate for the frequency drifting induced noise during the dynamic strain sensing. To demonstrate the capacity of frequency drifting compensation, 1 Hz and 0.01 Hz dynamic strain variation with the same amplitude of 30 με are applied to the RFGA. In Fig.5 (a), the bottom black curve represents 3 periods of the 1 Hz dynamic strain variation, showing a downward shifting. The middle red curve records the frequency drifting during the data acquisition. By applying a subtraction calculation between these two curves, the reconstructed curve without the LFD induced noise is obtained as shown in the upper blue curve. It can be seen that the vibration amplitude of each period in the reconstructed curve remains unchanged with an amplitude of about 30.29 με (14.6 ns time delays) that correlates well with the applied value. The Fast Fourier Transform (FFT) of the reconstructed curve gives a 1 Hz frequency which matched that in the RFGA shown in Fig.5 (b). For 0.01 vibration frequency, 2 periods with a total acquisition time of 200 seconds are collected. As shown in Fig.5 (c), there are several unanticipated peaks on the bottom black reconstructed curve because of the LFD. After employing the subtraction calculation with the compensation curve obtained from the referenced RFG, the reconstructed curve reveals vibration amplitude of 29.46 με (14.2 ns time delays) could be figured out. The small error between the reconstructed amplitude and applied amplitude is caused by the accumulation of time delay measurement error in each cross correlation calculation. In addition, the reconstructed vibration frequency of the dynamic strain variation has signal noise ratio up to 56 dB as shown in Fig.5 (d). In our experiment, the standard deviation of time delay measurement is about 31.8 ps and is determined by the sampling rate of the oscilloscope as well as the signal to noise ratio of the reflected Rayleigh traces. According to the Eq.(3), the minimum detectable frequency drifting is about 7.28 MHz (equivalent wavelength change 58.2 fm) over the optical frequency of 2×10^{14} Hz.

In our experiments, we focus more on the demonstration of LFD compensation, so the sensor portion is treated as a single time window in cross-correlation calculation, that is limited by the short fiber length (0.8 m). It should be noted that the proposed method of LFD compensation can be extended to distributed measurements with the same minimum detectable frequency change, if the RFGA is long enough. Large frequency drifting may cause nonlinear effect of refractive index, but this nonlinear effect induced time delays is far small than what we measured in experiment. So it normally could be neglected.

In summary, a real time dynamic strain sensor based on chirped pulse φ-OTDR with RFGA is experimentally demonstrated. Combined with the laser frequency drift compensation method, it is believed that the random grating sensor array would be applicable to structural health monitoring, especially for quasi-static dynamic strain sensing.

Funding. China Scholarship Council (201808330421); Canada Research Chairs(950231352); Natural Sciences and Engineering Research Council of Canada (RGPIN-2015-06071, STPGP 506628).

Disclosures. The authors declare no conflicts of interest.

References

1. Z. Sha, H. Feng, and Z. Zeng, Opt. Express. 25(5), 4831 – 4844 (2017).
2. A. Masoudi, M. Belaland, T. P. Newson, Meas. Sci. Technol. 24(8), 85204 (2013).
3. X. Zhang, Z. Sun, Y. Shan, Y. Li, F. Wang, J. Zeng, and Y. Zhang, IEEE Photonics J. 9(3), 1 – 12 (2017).
4. X. Bao and L. Chen, Sensors. 12, 8601 (2012).
5. Z. Wang, L. Zhang, S. Wang, N. Xue, F. Peng, M. Fan, W. Sun, X. Qian, J. Rao, and Y. Rao, Opt. Express. 24, 853 (2016).
6. F. Jiang, H. Li, Z. Zhang, Z. Hu, Y. Hu, Y. Zhang, and X. Zhang, Opt. Lett. 44, 911-914 (2019).
7. Y. Wang, P. Lu, S. Mihailov, L. Chen, and X. Bao, Opt. Lett. Opt. Lett. 45, 6110-6113 (2020).
8. M. R. Fernández-Ruiz, L. Costa and H. F. Martins, Sensors. 19(20), 4368-28 (2019).
9. N. Xue, Y. Fu, C. Lu, J. Xiong, L. Yang, and Z. Wang, J. Lightwave Technol. 36(23), 5481 – 5487 (2018).
10. F. Zhu, X. Zhang, L. Xia, Z. Guo, and Y. Zhang, IEEE Photonics Technol. Lett. 27(24), 2523 – 2526 (2015).
11. Q.Yuan, F. Wang, T. Liu, Y. Liu, Y. Zhang, Z. Zhong, and X. Zhang, Opt. Express. 27(3), 3664 – 3671 (2019).
12. M. Wu, X. Fan, Q. Liu, and Z. He, Opt. Lett. 43, 3594 – 3597 (2018).
13. Y. Xu, P. Lu, S. Gao, D. Xiang, P. Lu, S. Mihailov, and X. Bao, Opt. Lett. 40, 5514 (2015).

Chapter 6

Kerr effect enabled Optical frequency chirping range extension

6.1 Contributions of authors

The main results in Section 6.3 and Section 6.4 have been published in Optics Express, titled "Frequency sweep extension using the Kerr effect for static temperature measurement range enhancement in Chirped Pulse φ-OTDR" [187], and "Generation of high performance optical chirped pulse for distributed strain sensing application with high strain accuracy and larger measurement range" [29]. The contributions of the five authors: Yuan Wang (present author), Ole Krarup, Pedro Tovar, Prof.Liang Chen and Prof.Xiaoyi Bao are as follows.

For the [187], the present author (Yuan Wang) and Ole Krarup, whose theoretical work on frequency sideband generation via the Kerr effect, developed the initial idea of using the Kerr effect to enhance the frequency chirping range of the chirped pulse together. The construction of the experimental setup and the data collection was done collaboratively by the present author and Ole Krarup. The present author conducted the data analysis and produced the graphs in a state of continuous discussion and feedback with Ole Krarup. Prof. Liang Chen and Prof. Xiaoyi Bao provided advice on the presentation of the data as well as comments on the main text of the paper.

For [29], the present author developed the initial idea of using both chirped pump and pulse signal to further enhance the frequency chirping range with a high coefficient. The construction of the experimental setup, the data collection, the data analysis, and produce of graphs were done by the present author. Pedro Tovar, the main collaborator, gives many detailed suggestions and comments on the structure and presentation of the manuscript. Prof. Liang Chen and Prof. Xiaoyi Bao provided advice on the presentation of the data as well as comments on the main text of the paper.

6.2 Introduction

In a conventional chirped pulse φ-OTDR system, the maximum measurable strain or temperature variation between two single-shot measurements is limited by the large time delay estimation (TDE) error due to the distortions of reflected traces from the sensing location. Thus, to avoid the trace-to-trace distortion and decorrelation, the largest measurable time delays between two consecutive traces is usually limited to 10% of pulse width [189], as we discussed in Section 4.2.1. The relationship between external disturbance-induced optical path length change, ΔL, and time delay, Δt, is given by [184]:

$$\Delta\varepsilon\ K = \frac{\Delta L}{L} = -\frac{\Delta v_\varepsilon}{v_0} = -\frac{1}{v_0}\frac{\Delta v}{W}\Delta t \tag{6.1}$$

where v_0 is the initial optical frequency of the chirped pulse, Δv_ε is the strain variation induced frequency shift, and K is the strain coefficient. Given the fact that the maximum measurable Δt equals 10% of W, then the maximum detectable strain variation between two consecutive measurements is only limited by the frequency chirping range of the pulses. Hence, high-order Kerr pulses have the potential to increase the maximum detectable strain variation, which is experimentally validated in the following sections.

In this Chapter, we experimentally investigate a method of extending frequency sweeps using the Kerr effect to broaden the frequency chirp range of a nanosecond optical pulse through all-optical signal processing, and the enhancement of temperature/strain measurement range is also demonstrated. Our previous work [189] that requires building a database is time-consuming and easily affected by the change in the status of the fibers. However, the method proposed in this paper utilizes a direct way to extend the measurement range by increasing the range of frequencies swept by each chirped pulse, which is a real-time measurement. More importantly, this performance-enhanced setup provides important guidance to employ chirped pulse phase OTDR in

some particular applications, such as the crack detection of large construction and railway tracks, in which large strain variation in long-distance is required for the detection of arbitrarily large and unknown perturbation. **??** gives the experimental results about Kerr pulses generation and its application in CP φ-OTDR system to improve the static temperature measurable range.

In addition, Section 6.4 shows a novel method to efficiently generate optical chirped pulses with a high chirping rate and lower frequency drifting noise by using a pump and signals with opposite chirping directions. Benefiting from the use of a single laser source, the system exhibits a lower noise performance. More importantly, by combining an up-chirped pulsed signal with a down-chirped pump, we showed that the frequency chirping range of the m^{th} order Kerr chirped pulse is enhanced by a factor of $2m + 1$, which is more efficient than the fixed-frequency pump scheme, which only enhances by a factor m. Compared to other cascaded configurations, our approach shows a high efficiency without requiring multi-stages [190].

6.3 Fixed-frequency pump-based Kerr pulse generation for static temperature measurement range enhancement

In this section, we demonstrate the extension of the frequency range of a chirped laser pulse by all-optical means using evenly spaced frequency sidebands generated via the Kerr effect to improve the Chirped Pulse φ-OTDR measurement range. We report chirp extensions by factors up to 13 and apply the effect to achieve a six-fold increase in the measurement range of a Chirped Pulse φ-OTDR system measuring the temperature of a random fiber grating array.

Research Article | Vol. 29, No. 15 / 19 July 2021 / Optics Express 23202

Optics EXPRESS

Frequency sweep extension using the Kerr effect for static temperature measurement range enhancement in Chirped Pulse φ-OTDR

YUAN WANG,[1,3] OLE KRARUP,[2,3,*] LIANG CHEN,[2] AND XIAOYI BAO[1,2]

[1] School of Electrical Engineering and Computer Science, University of Ottawa, Ontario K1N 6N5, Canada
[2] Department of Physics, University of Ottawa, 25 Templeton Street, Ottawa, Ontario K1N 6N5, Canada
[3] These authors contributed equally to this paper

Abstract: In Chirped Pulse φ-OTDR systems used for sensing temperature or strain along an optical fiber, the largest disturbance between two single-shot measurements that can reliably be detected depends on the range of frequencies swept by the chirped pulse. If electrical modulation is used to generate the laser frequency sweep, the achievable sweeping range is limited by the electrical components, leading to a narrow measurement range for static measurements. In this work, we demonstrate the extension of the frequency range of a chirped laser pulse by all-optical means using evenly spaced frequency sidebands generated via the Kerr effect to improve the Chirped Pulse φ-OTDR measurement range. We report chirp extensions by factors up to 13 and apply the effect to achieve a sixfold increase in the measurement range of a Chirped Pulse φ-OTDR system measuring the temperature of a random fiber grating array. The method described in this paper can be applied to other optical systems utilizing chirped laser pulses and allow for variable extension of their chirping range.

1. Introduction

Compared to devices based on electrical signals, environmental sensors utilizing optical fibers have a number of advantages. Apart from durability and immunity to electromagnetic interference, optical fibers allow for distributed sensing, where information is recorded along their entire length. To measure a quantity of interest, such as local temperature, strain or vibration, a technique referred to as phase sensitive Optical Time Domain Reflectometry (φ-OTDR) is often employed. By launching a monochromatic pulse of light into a fiber and measuring the Rayleigh back-scattered intensity as a function of time, one can determine the state of the fiber along its length in a continuous manner [1]. However, since the relationship between the magnitude of an applied disturbance and the change in the intensity of the back-scattered Rayleigh traces is not linear, conventional amplitude demodulation cannot be used in φ-OTDR to measure the magnitude of the disturbance [2] [3] [4]. Measuring the magnitude of disturbances requires the use of various phase demodulation techniques. These involve comparing the relative phase change of two different segments of fiber [5], utilizing 90° optical hybrid based homodyne detection [6], dual-pulse phase modulation [7], or the phase-generated carrier demodulation algorithm [8]. One drawback of phase demodulation techniques is their reliance on optical interferometers, which are limited by phase recovery range and fringe contrast.

To obtain accurate, single-shot measurements of the magnitudes of applied disturbances based on back-scattered Rayleigh traces, one can instead utilize chirped pulses, where the instantaneous frequency of the pulse is linearly increased or decreased within pulse duration. This technique called Chirped Pulse φ-OTDR (CP φ-OTDR) relies on the interference of a range of frequencies back-scattered by different parts of the fiber due to the Rayleigh effect. By calculating the cross

Optics EXPRESS

correlation between subsequent Rayleigh traces, such sensing systems have achieved resolutions of 1 mK for temperature and 4 $n\varepsilon$ for strain [9]. When using Rayleigh traces from chirped pulses scattered by a random fiber grating array (RFGA), lower pulse powers are required and a spatial resolution of 1.2 m can be achieved [10]. Since CP φ-OTDR with an RFGA is a single-shot system which does not require heterodyne detection, one section of the sensor without disturbance could be utilized for compensating time delay errors induced by laser frequency drifts. This technique enables the detection of ultra-low frequency vibrations [11]. While CP φ-OTDR is highly sensitive because the Rayleigh traces undergo large changes from small applied disturbances, the static measurement range is limited because subsequent traces become decorrelated if the external perturbation is too large. In practice, two Rayleigh traces recorded before and after a disturbance is applied will be approximately identical (with high correlation coefficient) apart from a time delay, Δt, if this delay is smaller than 10% of the pulse duration. To conduct dynamic measurements, large perturbations could be detected by oversampling using a high repetition rate for the pulses. However, in distributed sensing systems, there is a trade off between pulse repetition rate and sensor length. To extend the limited measurement range, one method based on multi-frequency database demodulation has been implemented [12]. By establishing a database consisting of Rayleigh traces collected from chirped pulses with different initial optical frequencies, the time delays Δt due to large strains can be partially compensated by the initial frequency difference of the chirped pulses, thereby extending the static measurement range by a factor of 3. Additional extension of the measurement range using this method requires building a database for a larger number of frequencies, which is time consuming. Another direct way to extend the measurement range is to increase the range of frequencies swept by each chirped pulse.

When two frequencies of light are launched into a fiber with a large nonlinear parameter, γ, the Kerr effect causes frequency sidebands to be generated. Since the output power of these sidebands depends on the input power, the Kerr effect has been used to enhance the extinction ratio of optical pulses for OTDR by all-optical means [13], and to enhance the resolution of fiber optical sensors [14]. Furthermore, changing the frequency spacing between the input lasers causes the central frequencies of the higher order sidebands to shift by integer multiples of this change. When used in Optical Frequency Domain Reflectometry (OFDR), this method can extend the range of a laser frequency sweep taking place on the scale of seconds, thereby improving the resolution of an OFDR measurement [15]. This frequency chirp magnification (FCM) induced by the Kerr effect has also been used for magnifying the wavelength drift of an FBG sensor subject to strain and temperature changes, thereby enhancing its sensitivity [16]. Because the Kerr effect is fundamentally caused by the reaction of bound electrons in the glass fiber to variations in the power of an external optical field, the smallest duration of a sweep extendable using the Kerr effect is determined by the electron response time, which is on the scale of femtoseconds. Therefore, it should be possible to extend frequency sweeps, which are much shorter in duration than ones typically used in OFDR.

In this paper, we apply the method of extending frequency sweeps using the Kerr effect to broaden the chirp range of a nanosecond optical pulse by factors up to 13 through all-optical signal processing. First, the measurement principle behind CP φ-OTDR, its advantages and limitations are discussed. A theoretical model describing sideband generation using the Kerr effect is then presented, showing how the frequency shift of a sideband depends on its order. An experimental setup used for extending the chirping range of a pulse is described, and it is shown how the static temperature measurement range of a system based on an RFGA can be increased by factors up to 6. Finally, the limitations of our model and experiment are discussed along with potential application to other optical techniques relying on chirped pulses.

Optics EXPRESS

2. Theory

2.1. Chirped Pulse φ-OTDR measurement principle

In traditional φ-OTDR, a monochromatic pulse is employed as the interrogation signal to investigate the status of the fiber. The lack of a linear relationship between the applied external disturbance and the intensity of Rayleigh traces means that the magnitude of the disturbance cannot be determined directly. In order to create a linear relationship between applied disturbances and the intensity profile of the Rayleigh traces, a chirped pulse is utilized instead of a monochromatic pulse. The instantaneous optical frequency profile of the chirped pulse is expressed as [12]

$$v(t) = \left(v_0 + \frac{\Delta v}{W} \cdot t\right) \mathrm{Rect}(t/W), \tag{1}$$

where v_0 is the initial laser frequency, Δv is chirping range of the chirped pulse, W is the pulse duration, and Rect is the rectangular function with unit height. When the chirped pulse is sent into the fiber under test, the interference of back-scattered electrical fields occurring in the fiber section corresponding to the half pulse width will form the time domain Rayleigh traces. At the time t, when the interference signal arrives at the detection end, the optical power can be expressed as:

$$I(t)_{AC} = I_0 \int_{(t-W)c/2n}^{tc/2n} \int_{(t-W)c/2n}^{tc/2n} e^{-2\alpha\left(Z_i+Z_j\right)} r\left(Z_i\right) \cdot r\left(Z_j\right) \cdot e^{i\left[\Delta\varphi_{ij}(t)\right]} dZ_i dZ_j, \tag{2}$$

where n is the average value of refractive index, c is the speed of light in vacuum, α is the average attenuation of the fiber, Z_i and Z_j are the positions of the i^{th} and j^{th} scattering centers along the fiber, I_0 is the input intensity of the light and $r(Z_i)$ and $r(Z_j)$ are the reflection coefficient of the i^{th} and j^{th} scattering centers respectively. The exponent, $\Delta\varphi_{ij}(t)$, represents the phase difference between two scattering centers and is given by:

$$\Delta\varphi_{ij}(t) = 2\pi \int_{t-2nZ_j/c}^{t-2nZ_i/c} \left(v_0 + \Delta v \cdot t/W\right) dt = 2\pi \left[\left(\frac{2n\left(Z_i - Z_j\right)}{c}\right)\left(v_0 + \frac{\Delta v}{W}\left(t - \frac{n\left(Z_i + Z_j\right)}{c}\right)\right)\right]. \tag{3}$$

Equation (2) shows that the measured optical power depends on the interference of light from all combinations of two scattering centers, while Eq. (3) shows that the relative phase between two scattering centers depends on their relative optical path lengths, their absolute position along the fiber and the range of the frequency sweep. To understand how CP $\varphi-$OTDR enables environmental sensing, consider a simplified picture with only two scattering centers located at Z_a and Z_b being illuminated by a chirped pulse with a fixed chirping rate, $\Delta v/W$, and a spatial width, which is much greater than $Z_b - Z_a$. At a time, t, after the chirped pulse was launched, a certain signal intensity, $I(t, T_1)$, is detected due to the interference of frequencies scattered by the two centers, when the temperature is T_1. If the temperature of the fiber is increased slightly to T_2 so the optical path length between the centers is increases from L to $L + \Delta L$, the intensity value, $I(t, T_1)$, from before the temperature change will now occur at a different time, $I(t + \Delta t, T_2)$. The reason is that the frequencies that gave rise to $I(t, T_1)$ arrive at the scattering centers slightly later. If ΔT is large enough for the arrival time of the frequencies to be different, but small enough for the way they interfere to be unaltered, one can assume that the intensities $I(t, T_1) = I(t + \Delta t, T_2)$ are actually generated by the same segment of fiber being exposed to two different frequency ranges starting at $v(t)$ and $v(t + \Delta t)$ respectively. The relative change in optical path length must then be related to the change in the frequency range by

$$\frac{\Delta L}{L} = \frac{v(t) - v(t + \Delta t)}{v_0} = -\frac{1}{v_0}\frac{\Delta v}{W}\Delta t. \tag{4}$$

Optics EXPRESS

Considering that a change in temperature causes the optical path length ratio to change by $K_T \cdot \Delta T$, where K_T is the coefficient of linear thermal expansion for the fiber, one can determine that:

$$\mathrm{K}_{\Delta\mathrm{T}} \cdot \Delta\mathrm{T} = -\frac{\frac{\Delta v}{W}\Delta t}{v_0} \Rightarrow \Delta t = -\frac{W \cdot v_0 \cdot \mathrm{K_T}}{\Delta v} \cdot \Delta\mathrm{T} \tag{5}$$

This shows that a small applied temperature change causes a time delay, Δt, which is linearly dependent on the magnitude of the disturbance. The time delay between two traces can be found by calculating the correlation between them. Note that if the chirp range, Δv is small, a small change in temperature will cause a large time shift. In this case, the sensitivity of the CP φ-OTDR will be high while its measurement range will be short. If the chirping range is increased, the same change in temperature will cause a smaller time delay, meaning that the static measurement range is increased at the cost of lower sensitivity. In the demodulation process, the maximum detectable time delay is about 10% of pulse duration, W. If the time delay Δt is too large, the integration range in Eq. (2) for I(t) and I (t+Δt) are significantly different. This means that the interference of back-scattered light occurs in different sections of the RFGA, which makes the two traces decorrelate. Therefore, the maximum measurable temperature change only depends on the frequency chirping range Δv according to Eq. (5), since the duration, W, cancels out on both sides if Δt is replaced with $0.1 \cdot W$. In short, a method that allows the chirping range to be extended can increase the static measurement range.

2.2. Sideband generation using the Kerr effect

The following description of the generation of sidebands in a Kerr medium is based on the approach used in [17]. Sending laser light with two different frequencies, ω_p<ω_c into a Kerr medium consisting of an optical fiber of length, L, with a high nonlinear parameter, γ, the normalized electric field amplitude is initially given by $A_{in} = \left[\sqrt{P_p}\exp(-i0.5\omega_d t) + \sqrt{P_c}\exp(i0.5\omega_d t)\right]$. Here, $P_{p/c}$ referes to the power of the pump field/chirped pulses, $\omega_d = \omega_c - \omega_p$, and the power of the field as a function of time is $P_{in} = \left[P_p + P_c + 2\sqrt{P_p P_c}\cos\omega_d t\right]$. Assuming that dispersion, loss, and polarization effects are negligible, the input field evolves according to the Nonlinear Schrödinger Equation, $dA/dz = i\gamma|A|^2 A$ [18]. Solving this differential equation for the field at the output of the Kerr medium yields $A_{out} = A_{in}\exp\left[i\gamma L(P_p + P_c)\right]\exp\left[i\gamma L 2\sqrt{P_p P_c}\cos\omega_d t\right]$. In the following, the exponential factor, $\exp\left[i\gamma L(P_p + P_c)\right]$, is ignored, as it does not affect the output frequency if the input powers remain constant. Chirps induced by self-phase modulation (SPM) are only present near the pulse edges constituting less than 5% of pulse duration and do not contribute significantly to the scattered signal. The Jacobi-Anger expansion [19], $\exp\left[iM\cos Bt\right] = \sum_{n=-\infty}^{\infty} i^n J_n(M)\exp(inBt)$, where J_n indicates the n^{th} order Bessel function of the first kind is then applied to the output field, thereby expressing it as an infinite sum of frequency sidebands spaced ω_d apart:

$$A_{out} = \sum_{n=-\infty}^{\infty} i^n e^{in\omega_d t}\left[J_n\left(2\gamma L\sqrt{P_p P_c}\right)\sqrt{P_p} + i \cdot J_{n-1}\left(2\gamma L\sqrt{P_p P_c}\right)\sqrt{P_c}\right]. \tag{6}$$

Note that $n = 0$ corresponds to the output sideband located at the frequency of the input pump, ω_p, while $n = 1$ corresponds to the output sideband located at the same frequency as the input chirped pulses. The central frequency of the n^{th} order sideband will be $\omega_n = n\omega_d = n(\omega_c - \omega_p)$ away from ω_p. Assuming that ω_c changes linearly with time at a rate of $\Omega[rad/s^2]$, the frequency of the n^{th} order sideband becomes $\omega_n(t) = n(\omega_c(0) + \Omega t - \omega_p) = n\Omega t + n(\omega_c(0) - \omega_p)$. This shows that if the input pulse is chirped at a rate, Ω, filtering out the n^{th} order sideband will produce a pulse with a chirp rate $n\Omega$. Furthermore, if the condition $0<2\gamma L\sqrt{P_c P_c}<\sqrt{1+|n|}$ is satisfied, the intensity profile of the output pulse will be an integer exponent of the input pulse [20]. If the intensity profile of the input pulse is a square, the potentiation effect for higher order

3. Experimental setup and results

The experimental setup for temperature measurement with chirped pulses is shown in Fig. 1. A distributed feedback laser (DFB) (CQF938/500, JDS Uniphase) with a linewidth of 1MHz emitting at 193506.25 GHz is periodically modulated by a saw-tooth pattern with a rising edge of 20 ns from a signal generator (8130A, Hewlett Packard). The so-called "bias-T structure" converts the applied electrical modulation to a change in the drive current supplied to the DFB. When the saw-tooth signal periodically increases(decreases) the supplied current, the instantaneous frequency emitted by the DFB is increased(decreased). Figure 1(a) depicts the laser signal at the output of the DFB. In the time domain, the laser signal is a continuous wave (CW) and its power is approximately constant because the change in the drive current is small compared to the total current supplied. The spectrum shown in Fig. 2(b) is measured with an optical spectrum analyzer (OSA) (AP201x, APEX) and has a 5dB width of 746 MHz, indicating that the changing drive current causes the central frequency to vary in this range. The signal generator creating the saw-tooth pattern also generates rectangular signals at a rate of 1 MHz activating a custom solid state optical amplifier (SOA) driver circuit board. When activated by a pulse, this circuit board switches on the SOA (SOA-S-OEC-1550, CIP) allowing it to serve as a gate for pulsing the signal from the DFBs with a duration of 6ns. As illustrated in Fig. 1(b), once the modulation of the DFB and the trigger for the SOA are synchronized, a linearly chirped optical pulse is produced.

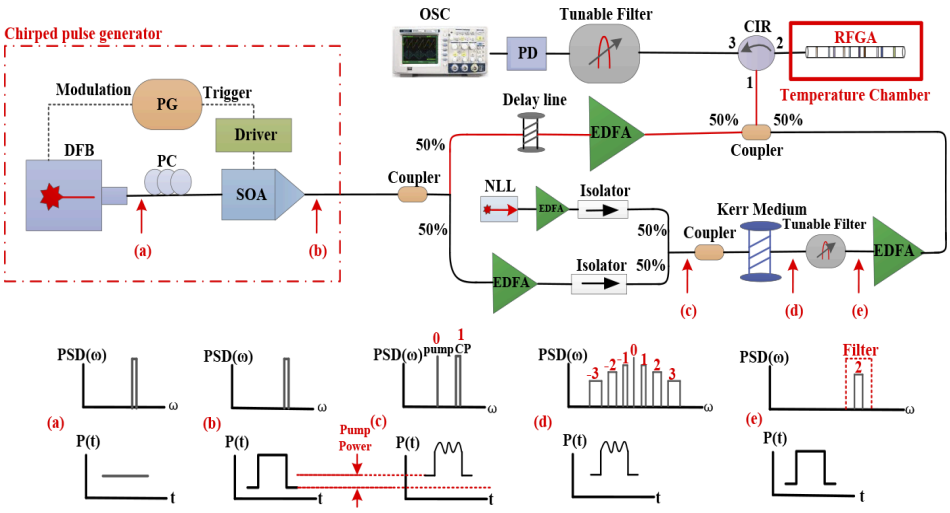

Fig. 1. The experimental setup for applying the Kerr effect to enhance the frequency range of chirped pulses for temperature sensing using CP φ-OTDR. Subfigures (a-e) illustrate the spectrum and signal at successive stages of the setup.

Once generated, the chirped optical pulses are split into two different branches of the setup by a 50:50 coupler. The branch, which sends pulses through a delay line and an erbium doped fiber amplifier (EDFA) (AEDFA-PA-25-B-FA, Amonics) without applying nonlinear chirp extension is marked with a red fiber in Fig. 1. We refer to pulses from this branch as "pure pulses". The delay line ensures that the pure pulses and the pulses generated by the other branch arrive at the RFGA with a 40 ns time delay, allowing for an accurate comparison of their response to changes in temperature.

The pulses in the other branch are first amplified by an EDFA (APEDFA-C-10-B-FA, Amonics) and then sent through an isolator into one input port of a 50:50 coupler. A CW light wave from a

Optics EXPRESS

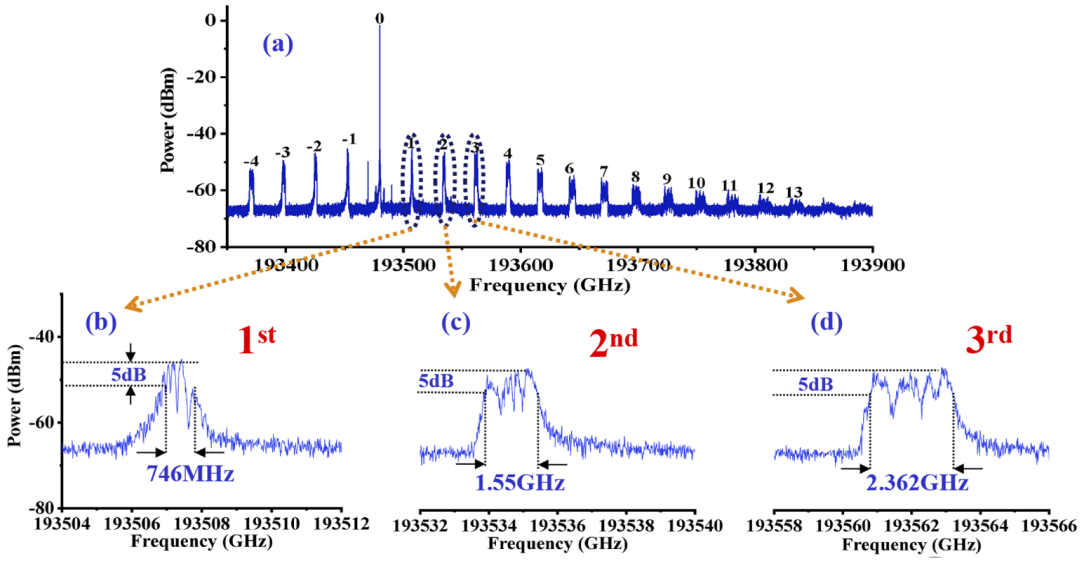

Fig. 2. (a) Measured spectrum after the Kerr medium showing sidebands in the range from $n = -4$ to $n = 13$. Note that $n = 0$ corresponds to the CW pump, while $n = 1$ corresponds to the input chirped pulses. (b-d) Zoom on the first, second and third order sidebands respectively, demonstrating integer scaling of the sweep range.

narrow linewidth laser (NLL) (PS-NLL-1550.12, Teraxion) with a linewidth of 5 kHz emitting at 193480.00 GHz is amplified by an EDFA (AEDFA-33-B-FA, Amonics), passed through an isolator and sent into the other input port of the 50:50 coupler. The chirped pulses and the light from the NLL used as a pump are combined and launched into a highly nonlinear fiber with a non-uniform core referred to as a "Kerr medium" (418SG 04611A, Draka Comteq). The non-uniform core continuously changes the Brillouin frequency of the fiber, which prevents the CW light of the narrow linewidth laser from losing power to Stimulated Brillouin Scattering. The combined spectrum of the chirped pulses and the narrow linewidth laser signal before entering the Kerr medium is visualized in Fig. 1(c). At this stage, the power of the signal in the time domain consists of a constant offset due to CW light from the NLL and a pulse with a sinusoidally varying optical power due to interference. Because of the nonlinear phase modulation caused by the interference of the NLL and the chirped pulses described in Subsection 2.2, frequency sidebands spaced 26.25 GHz apart are generated. Figure 1(d) illustrates three higher order sidebands generated by this process. Figure 2(a) shows a recorded optical spectrum after the Kerr medium with sidebands ranging from -4 to 13. Figures 2(b)-2(d) shows that the chirp range for the n^{th} order sideband is n times the chirp range of the input pulse as predicted in Subsection 2.2. Individual sidebands are extracted using a tunable filter (XTM-50, EXFO). This produces a chirped pulse, referred to as a "Kerr pulse", with a wider chirping range than the pure pulses, but with the same shape and duration.

The extracted Kerr pulses for the n^{th} order sideband are amplified by an EDFA (AEDFA-PA-25-B-FA, Amonics) and recombined with the pure pulses in a 50:50 coupler. They are then launched through a circulator to an RFGA placed inside an insulating, temperature controlled styrofoam box. The RFGA has a reflection coefficient of -30 dB, and a length of 0.8m, which is used to provide a locally enhanced Rayleigh scattering signal. It consists of 8 alternating sub-gratings of lengths 10mm and 5mm respectively. The periods of the sub-gratings are randomly distributed between 0.5180µm and 0.5464µm. The reflected Rayleigh patterns are passed back through the circulator, through a tunable filter (Lambda Commander OSP 9100, Newport) and finally to a

Optics EXPRESS

photodiode (PDB435C, Thorlabs) connected to an oscilloscope (infiniium DSO81204B, Agilent) sampling at 40 GSa/s.

To determine the temperature static measurement range for different Kerr pulses, the heating element inside the styrofoam box is activated, raising the temperature of the RFGA to 40°C. The intensities of the two Rayleigh traces from the pure and Kerr pulses are equalized by adjusting the amplifiers. The heater is then switched off, allowing the RFGA to gradually cool down, causing the Rayleigh traces to shift accordingly. For every 0.1°C step down to 34°C, a Rayleigh trace is recorded. The duration of Rayleigh traces is about 20ns, and the total number of samples for each traces is 800. The oscilloscope is set to average 16 traces to reduce the impact of intensity fluctuation and electrical noise. A custom python script is used to determine the magnitude of the time delays between the traces recorded at different temperatures by numerically calculating the correlation between them. First, pulses for sideband orders from -2 to 6 were used to measure temperature changes in steps of 0.1 °C, demonstrating the feasibility of using higher order sideband pulses. Figure 3 shows the measured time delay as a function of the temperature change for different Kerr pulses in steps of 0.1°C. The slope corresponding to pulses from the n^{th} order sideband is n times smaller than the slope for the pure pulses as predicted in Subsection 2.2. The sign of the slope is negative for sidebands where n<0, corresponding to pulses for which the direction of the chirp is reversed.

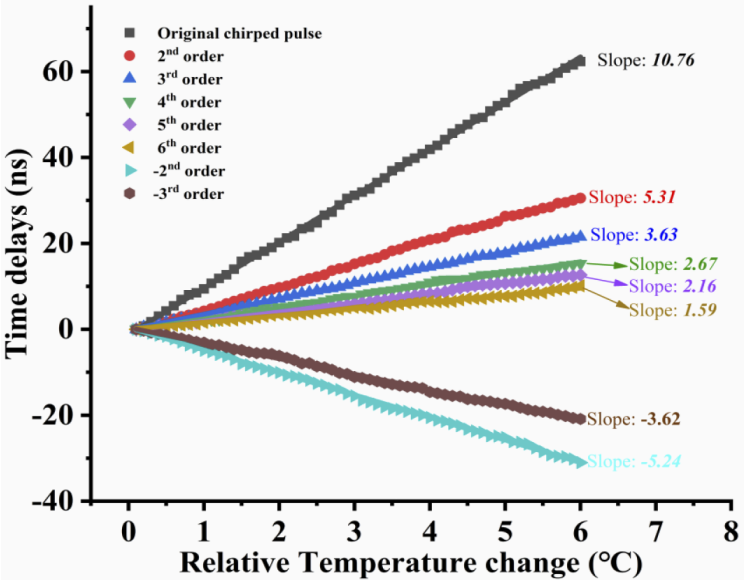

Fig. 3. Time delays of Rayleigh traces corresponding to pure pulses and Kerr pulses for various sideband orders as a function of temperature change. Note that the slope of the n^{th} order sideband is n times smaller than the slope for the pure pulses in agreement with Eq. (5).

Next, the static measurement range of pulses from each sideband order are investigated. Figure 4 depicts the reflected traces from the RFGA before and after the application of a temperature change. For pure pulses with a short chirping range, a temperature change of 0.2°C causes the traces from before and after the change to lose correlation. This is in accordance with Subsection 2.1 where it was predicted, that a short chirping range would imply high sensitivity and low static measurement range. For the 2^{nd} order Kerr pulses, the same temperature change of 0.2°C introduces a smaller time delay due to the extended frequency chirping range. As shown in Fig. 4(f) in which the 6^{th} order Kerr pulses are used, two traces collected before and after a temperature change of 0.6°C remain highly correlated. Recovering the correct time delay between two subsequent traces is not possible for temperature changes that cause the cross correlation

Optics EXPRESS

coefficient to drop below 0.8. For example, when 1^{st} order chirped pulse is used to measure temperature variations of 0.2°C as shown in Fig. 4(b), the coefficient decreases to 0.505. In this case, the demodulation cannot recover the correct time delay, making temperature measurements impossible. Therefore, the largest change in temperature that can be measured between two single shots can be found by determining which temperature shift is required for the traces to decorrelate. The relationship between the cross-correlation coefficient and the temperature variation range for different order Kerr pulses is shown in Fig. 5. Choosing a correlation coefficient of 0.8 as a threshold, it is seen that the static temperature measurement range for the 6^{th} order sideband is improved by a factor 6 compared to the pure pulses.

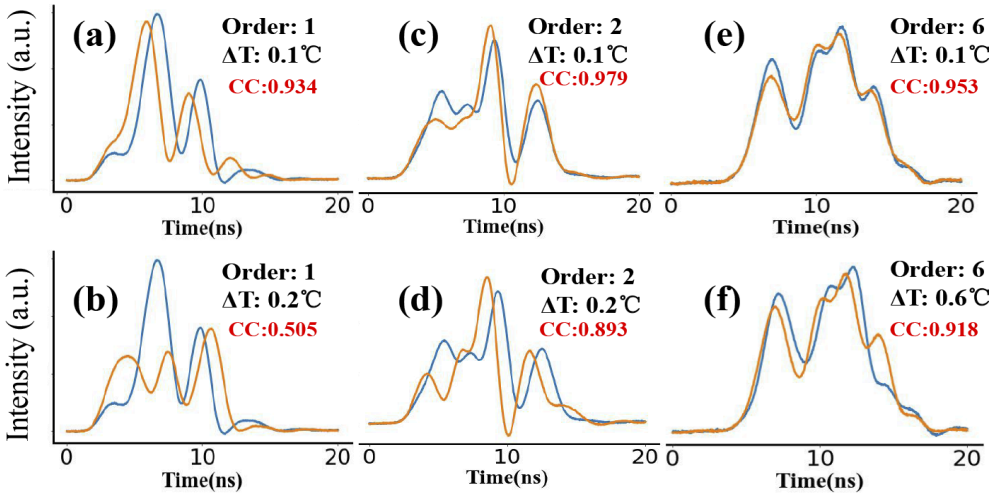

Fig. 4. Measured Rayleigh traces corresponding to various sideband orders before (blue) and after (orange) temperature changes along with their correlation coefficients. (a-b) Traces for pure pulses, (c-d) traces for 2^{nd} order pulses and (e-f) traces for 6^{th} order pulses. CC: Cross-Correlation Coefficient.

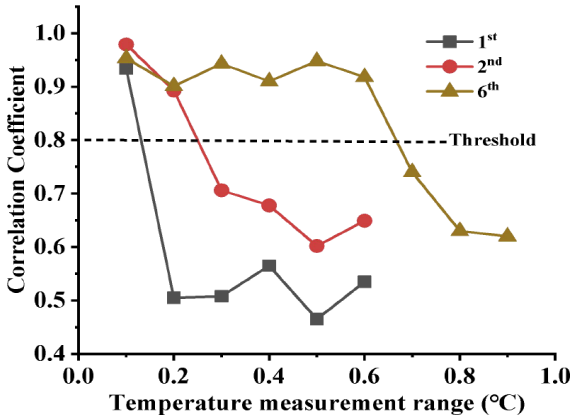

Fig. 5. Cross-Correlation Coefficient of two Rayleigh traces when different temperature changes are applied for sideband orders 1, 2 and 6. Pulses from higher order sidebands remain correlated longer and thus provide enhanced static measurement range.

To investigate how the resolution of the temperature measurements changes when different Kerr pulses are used, 500 Rayleigh traces generated by averaging 16 raw traces are collected at constant room temperature over 0.8s for different orders. Fluctuations in the time delays between

Optics EXPRESS

consecutive pulses are calculated and the equivalent temperature variations are determined using the slopes in Fig. 5. The raw fluctuation data for pure pulses and 6^{th} order Kerr pulses are shown in Fig. 6(a). A histogram of this data is shown in Fig. 6(b). The calculated standard deviation is 2.82 mK for the pure pulses and 25.1 mK for pulses from the 6^{th} order sideband. The temperature measurement precision for different sideband orders is shown in Fig. 6(c). The dashed lines in Fig. 6(c) indicate how the standard deviation of the arrival time and the smallest discernable temperature change should behave in an ideal case. We attribute the discrepancy between the measured resolution and the ideal one to the decreasing Signal to Noise Ratio (SNR) for higher values of n. As mentioned in Subsection 2.2, the power profile of the n^{th} order Kerr pulse will be the power profile of the pure pulse raised to the n^{th} exponent. This potentiation magnifies small power fluctuations and decreases the SNR [21]. Furthermore, the Kerr pulses are affected by power fluctuations for both the input pulses and the amplified NLL used as a pump. The magnified intensity noise causes subsequent traces for higher order sidebands to vary more in shape leading to the larger measured variation in arrival time shown in Fig. 6(c).

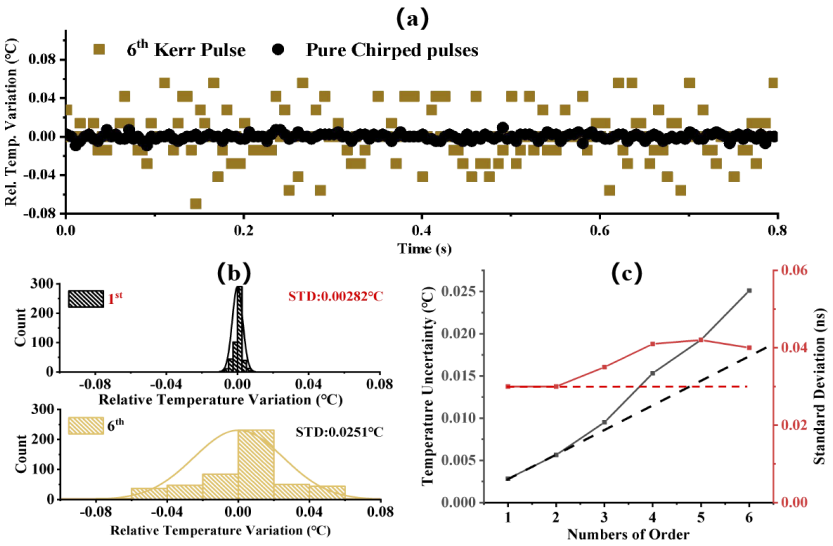

Fig. 6. (a) Temperature measurement uncertainty for pure chirped pulses and 6^{th} order sidebands Kerr pulses within 0.8 seconds when no temperature change is applied.(b) Histogram of the temperature measurement uncertainty for the pure chirped pulses (top) and 6^{th} order Kerr pulses (bottom) and its standard deviation. (c) The standard deviation of measured arrival time and the corresponding uncertainty in measured temperature for sideband orders in the range from 2 to 6. The nonlinear increase in temperature uncertainty for higher orders is attributed to frequency fluctuations in the DFB and NLL being scaled up along with the frequency chirp.

4. Discussion

Several simplifying assumptions are used in modelling the extension of the chirping range. The pure pulses launched into the Kerr medium are assumed to be quasi-CW, which is a valid assumption if the duration of the pulses is much longer than the period of the beat with the CW light from the NLL ($\omega_d \gg 2\pi/W$). In this experiment, the frequency difference of 26.25 GHz implies a beat period of 38 ps, which is much shorter than the pulse duration of 6ns, meaning that the quasi-CW assumption is acceptable. Loss was ignored, and dispersion in the Kerr medium was assumed to be zero. The latter assumption is valid for operation close to the zero-dispersion wavelength, and one can ensure that the sidebands experience similar dispersion

Optics EXPRESS

by making the frequency difference between the input pulses and the CW light from the NLL small. Effects related to the relative polarization of the input pulses and CW light were also ignored. A comprehensive model accounting for all these effects is being researched, but is beyond the scope of this paper.

By calculating the power of each of the sidebands in Eq. (6), and expressing the Bessel functions in terms of their Taylor expansions, it can be shown that their power decreases as $1/(n!)^2$. Thus, utilization of sidebands beyond $n = 6$ is limited by their rapidly decreasing power. Furthermore, because the Kerr effect magnifies power fluctuations, accurately calculating the correlation between traces for sidebands higher than $n = 6$ proved unfeasible. This limitation due to the lasers and amplifiers can be addressed by using more stable devices. To minimize the effect of power fluctuations, one could use a single, highly stable laser to generate both the chirped pulses and the pump. Another way to reduce the impact of intensity fluctuations is to utilize pulse powers that cause the argument of the n^{th} order Bessel function in Eq.(6) to equal its first maximum [22]. In this regime, power fluctuations are attenuated by the Kerr effect. These possibilities will be investigated in future work.

The method described in this paper implies a trade-off between sensitivity and static measurement range for higher order Kerr pulses. However, as the experimental approach demonstrates, it is possible to mitigate this trade-off by using both highly sensitive pure pulses and Kerr pulses with a large static measurement range simultaneously. The extension of chirped pulses described in this work was only applied to a single RFGA, but could be applied to distributed measurements using CP φ-OTDR. More generally, it can be applied to extend the chirping range of pulses in a wide variety of optical systems. For example, the ability to broaden or reverse chirped pulses by all-optical means without altering the pulse duration could be useful in systems relying on Chirped Pulse Amplification [23] or Dispersive Fourier Transforms [24].

5. Conclusion

All-optical chirp extension based on the Kerr effect is demonstrated for sidebands ranging from $n = -3$ to $n = 6$. When applied to a CP φ-OTDR system, the effect allows the measurement range to be scaled up by integer multiples of the sideband number as predicted by theoretical calculations. The chirp extension effect can be applied to existing system relying on chirped pulses to extend their chirping range.

Funding. China Scholarship Council (201808330421); Natural Sciences and Engineering Research Council of Canada (RGPIN-2020-06302, STPGP 506628-17); Canada Research Chairs (950231352).

Disclosures. The authors declare no conflicts of interest.

Data availability. Data underlying the results presented in this paper are not publicly available at this time but may be obtained from the authors upon reasonable request.

References

1. J. P. Dakin, "Distributed optical fiber sensors," in *Distributed and Multiplexed Fiber Optic Sensors II*, vol. 1797 J. P. Dakin and A. D. Kersey, eds., International Society for Optics and Photonics (SPIE, 1993), pp. 76–108.
2. Y. Lu, T. Zhu, L. Chen, and X. Bao, "Distributed vibration sensor based on coherent detection of phase-otdr," J. Lightwave Technol. **28**(22), 3243–3249 (2010).
3. J. C. Juarez, E. W. Maier, K. N. Choi, and H. F. Taylor, "Distributed fiber-optic intrusion sensor system," J. Lightwave Technol. **23**(6), 2081–2087 (2005).
4. S. V. Shatalin, V. N. Treschikov, and A. J. Rogers, "Interferometric optical time-domain reflectometry for distributed optical-fiber sensing," Appl. Opt. **37**(24), 5600–5604 (1998).
5. Y. Dong, X. Chen, E. Liu, C. Fu, H. Zhang, and Z. Lu, "Quantitative measurement of dynamic nanostrain based on a phase-sensitive optical time domain reflectometer," Appl. Opt. **55**(28), 7810–7815 (2016).
6. Z. Wang, L. Zhang, S. Wang, N. Xue, F. Peng, M. Fan, W. Sun, X. Qian, J. Rao, and Y. Rao, "Coherent phase-otdr based on i/q demodulation and homodyne detection," Opt. Express **24**(2), 853–858 (2016).
7. A. E. Alekseev, V. S. Vdovenko, B. G. Gorshkov, V. T. Potapov, and D. E. Simikin, "A phase-sensitive optical time-domain reflectometer with dual-pulse diverse frequency probe signal," Laser Phys. **25**(6), 065101 (2015).

Optics EXPRESS

8. G. Fang, T. Xu, S. Feng, and F. Li, "Phase-sensitive optical time domain reflectometer based on phase-generated carrier algorithm," J. Lightwave Technol. **33**(13), 2811–2816 (2015).
9. J. Pastor-Graells, H. F. Martins, A. Garcia-Ruiz, S. Martin-Lopez, and M. Gonzalez-Herraez, "Single-shot distributed temperature and strain tracking using direct detection phase-sensitive otdr with chirped pulses," Opt. Express **24**(12), 13121–13133 (2016).
10. Y. Wang, P. Lu, S. Mihailov, L. Chen, and X. Bao, "Distributed time delay sensing in a random fiber grating array based on chirped pulse ϕ-otdr," Opt. Lett. **45**(13), 3423–3426 (2020).
11. Y. Wang, P. Lu, S. Mihailov, L. Chen, and X. Bao, "Ultra-low frequency dynamic strain detection with laser frequency drifting compensation based on a random fiber grating array," Opt. Lett. **46**(4), 789–792 (2021).
12. Y. Wang, P. Lu, S. Mihailov, L. Chen, and X. Bao, "Strain measurement range enhanced chirped pulse ϕ-otdr for distributed static and dynamic strain measurement based on random fiber grating array," Opt. Lett. **45**(21), 6110–6113 (2020).
13. B. Vanus, C. Baker, L. Chen, and X. Bao, "High extinction ratio optical pulse characterization method via single-photon counting," Appl. Opt. **60**(1), 20–23 (2021).
14. O. Krarup, C. Baker, L. Chen, and X. Bao, "Nonlinear resolution enhancement of an fbg based temperature sensor using the kerr effect," Opt. Express **28**(26), 39181–39188 (2020).
15. B. Wang, X. Fan, S. Wang, J. Du, and Z. He, "Millimeter-resolution long-range ofdr using ultra-linearly 100 ghz-swept optical source realized by injection-locking technique and cascaded fwm process," Opt. Express **25**(4), 3514–3524 (2017).
16. J. Du and Z. He, "Sensitivity enhanced strain and temperature measurements based on fbg and frequency chirp magnification," Opt. Express **21**(22), 27111–27118 (2013).
17. A. Boskovic, S. V. Chernikov, J. R. Taylor, L. Gruner-Nielsen, and O. A. Levring, "Direct continuous-wave measurement of n2 in various types of telecommunication fiber at 1.55 μm," Opt. Lett. **21**(24), 1966–1968 (1996).
18. G. Agrawal, "Chapter 4 - self-phase modulation," in *Nonlinear Fiber Optics (Fifth Edition)*, G. Agrawal, ed. (Academic Press, Boston, 2013), Optics and Photonics, pp. 87–128, fifth edition ed.
19. "NIST Digital Library of Mathematical Functions," http://dlmf.nist.gov/10.12, Release 1.0.27 of 2020-06-15. F. W. J. Olver, A. B. Olde Daalhuis, D. W. Lozier, B. I. Schneider, R. F. Boisvert, C. W. Clark, B. R. Miller, B. V. Saunders, H. S. Cohl, and M. A. McClain, eds.
20. "NIST Digital Library of Mathematical Functions," http://dlmf.nist.gov/10.7.E3, Release 1.0.27 of 2020-06-15. F. W. J. Olver, A. B. Olde Daalhuis, D. W. Lozier, B. I. Schneider, R. F. Boisvert, C. W. Clark, B. R. Miller, B. V. Saunders, H. S. Cohl, and M. A. McClain, eds.
21. B. Vanus, C. Baker, L. Chen, and X. Bao, "All-optical intensity fluctuation magnification using kerr effect," Opt. Express **28**(3), 3789–3794 (2020).
22. B. Vanus, C. Baker, L. Chen, and X. Bao, "All-optical pulse peak power stabilization and its impact in phase-otdr vibration detection," OSA Continuum **4**(5), 1430–1436 (2021).
23. D. Strickland and G. Mourou, "Compression of amplified chirped optical pulses," Opt. Commun. **56**(3), 219–221 (1985).
24. S. Sanders, "Wavelength-agile fiber laser using group-velocity dispersion of pulsed super-continua and application to broadband absorption spectroscopy," Appl. Phys. B **75**(6-7), 799–802 (2002).

6.4 Chirped pump-based High efficiency chirped pulse generation from single laser source

Research Article | Vol. 30, No. 11 / 23 May 2022 / Optics Express 18518
Optics EXPRESS

Generation of high performance optical chirped pulse for distributed strain sensing application with high strain accuracy and larger measurement range

YUAN WANG,[1] PEDRO TOVAR,[2] LIANG CHEN,[2] AND XIAOYI BAO[1,2]

[1]School of Electrical Engineering and Computer Science, University of Ottawa, Ontario K1N 6N5, Canada
[2]Department of Physics, University of Ottawa, 25 Templeton Street, Ottawa, Ontario K1N 6N5, Canada

Abstract: A photonic approach for generating low frequency drifting noise, arbitrary and large frequency chirping rate (FCR) optical pulses based on the Kerr effect in the nonlinear optical fiber is theoretically analyzed and experimentally demonstrated. Due to the Kerr effect-induced sinusoidal phase modulation in the nonlinear fiber, high order Kerr pulse with a large chirping rate is generated. In the concept-proof experiments, the FCR of the m^{th} Kerr pulse has been significantly improved by a factor of $2m+1$. In addition, dynamic strain measurement along with a random fiber grating array (RFGA) sensor by using different order Kerr pulse is carried out for demonstrating a large strain measurement range with lower uncertainty sensing capability. Benefiting from the use of a single laser source and large FCR Kerr pulse, the system exhibits a 3.9 $\mu\varepsilon$ static strain measurable range, 0.24 $\mu\varepsilon$ measurement uncertainty by using -4^{th} order Kerr pulse that has an FCR up to 0.8 GHz/ns. Note that the FCR of the chirped pulse could be further enhanced by using larger FCR chirped pulse seed or choosing higher order Kerr pulses.

1. Introduction

Chirped pulses, known as frequency-swept pulses have been widely used in radar technologies [1], spread-spectrum communication system [2], chirped pulse microwave computed tomography [3] and also other applications covering military and civilian systems such as communications, surveillance, countermeasures, navigation and imaging equipment [4]. Most radar applications make use of long chirped pulses with wide bandwidth, or pulses with a high time-bandwidth product (TBWP), allowing the detection of targets at long distances with improved range resolution. High TBWP chirped pulses could be generated by many photonic approaches, including space-to-time mapping (STM) [5], frequency-to-time mapping (FTM) [6] and Self-Heterodyne Technique [4,7,8]. FTM methods attract more attention thanks to its simplicity and low cost. Such technique is enabled by sending a short optical pulse with large frequency bandwidth from mode-locked laser with fixed repetition rate through a dispersive element (e.g. chirped fiber Bragg grating), so that the accumulated quadratic spectral phase impresses a large linear chirp on the resulting time-domain waveform.

For distributed optical fiber sensing, optical chirped pulses have increasingly gained the attention of researchers, as they can be used as interrogation signal for quantitatively detecting the environmental disturbance along the sensing fiber, without requiring the frequency sweep process. As a novel technique for distributed sensing, it has been widely used for temperature [9], dynamic strain [10] and seismic [11] sensing, based on chirped pulse ϕ-OTDR (CP-ϕ-OTDR) or chirped pulse BOTDA (CP-BOTDA) [12]. Although long duration chirped microwave pulses are required

Optics EXPRESS

for radar applications, short duration chirped optical pulses are key for fiber-sensing applications. In most chirped pulse based systems, the spatial resolution is limited by the pulse width. An exception is the combination of chirped pulse with non-matched filter [13], but it requires an ultra-high coherent laser source, such that conventional techniques with narrow optical pulses are still of great interest. Therefore, optical chirped pulses with large bandwidth and small pulse width, i.e. with large FCR, are required to achieve large static measurement range with high spatial resolution. Due to limitations of electrical devices, the optical chirped pulses generated by arbitrary waveform generator (AWG) combined with frequency shifter (FS) usually have small chirping range and wide pulse width, resulting in limited chirping rates up to several tens of MHz per nanosecond. An alternative method to generate optical chirped pulses is by direct modulation of the DFB laser current, since the emitted optical frequency of a DFB laser varies with the injected current [9,14]. However, the limited modulation speed and linear variation range increase the complexity to arbitrarily enhance the chirping rate [8]. FTM method, which is usually used for chirped microwave generation, is a good candidate for optical chirped generation by using one dispersive device to stretch the ultra-short pulses. However, the ultra-short pulses usually have a fixed repetition rate and because dispersive devices are passive elements, the FTM method is not suitable for the generation of optical chirped pulses with tunable parameters, such as repetition rate, chirping rate, and center frequency.

In this paper, we propose a novel scheme to generate optical chirped pulses with tunable frequency chirping rate (up to 0.8 GHz/ns), central frequency and repetition rate based on Kerr effect in nonlinear optical fiber. In our approach, high order Kerr pulses were generated from single laser chirp, showing a lower frequency drifting noise and higher frequency chirping range. As a demonstration for the application of our proposed approach, dynamic strain measurement with enhanced static measurement range is achieved in CP-ϕ-OTDR system. Experimental results show low strain measurement uncertainty and larger static measurement range by using the generated high order Kerr pulse with large chirping rate. Beyond that, the proposed method is also a promising alternative for other applications, such as radar [1], ultra-wideband sensing [15], bio-medical imaging [3], and non-contact healthcare monitoring [16].

2. Theory

When optical waves propagate in dielectric media with molecular inversion symmetry such as optical fibers, changes in the effective refractive index are induced and governed by the third-order susceptibility, $\chi^{(3)}$. The higher is the intensity of the optical waves, the greater are the changes in the refractive index, a phenomenon known as Kerr effect. Media with high $\chi^{(3)}$, or high nonlinear parameter, exhibit higher index changes even for low powers, and will be henceforth referred to as Kerr media. As a result of optical Kerr effect, two laser lights with different frequencies undergo self-phase modulation (SPM) and cross-phase modulation (XPM) along a Kerr medium [17]. Assuming that the angular frequencies of two light waves entering a Kerr medium are ω_p and ω_c, with optical electric fields E_p and E_c, respectively, and $\omega_p<\omega_c$, then the total input electric field is $E_{in} = E_p + E_c$, introducing a slowly varying envelope modulation in the intensity profile with modulation frequency $\omega_d = \omega_c - \omega_p$. Therefore the amplitude of the slowly varying electrical field and its optical power at the input end of the Kerr medium are given by:

$$A_{in} = \eta \sqrt{2P} \cos(\omega_d t/2) \tag{1}$$

$$P_{in} = \eta^2 P(1 + \cos(\omega_d t) \tag{2}$$

where P is half of the optical power of the total electric field, and η is the SOP efficiency of the coherent mixing. In the following derivations, we assume η to be 1 for simplicity, indicating that E_p and E_c enter the Kerr medium with polarizations aligned. Due to the Kerr effect, the overall

Optics EXPRESS

effective refractive index is therefore a linear function of the optical intensity, $I = P/A$, which is expressed by [18]:

$$n(I) = n + n_2 I \tag{3}$$

where n_2 (in unit of cm^2/W) is the optical Kerr coefficient of the medium, with $n_2 = \frac{3\eta_0}{n^2\epsilon_0}\chi^{(3)}$, where η_0 is the vacuum impedance, ϵ_0 is vacuum permittivity, n is the refractive index, and A is the cross section of the Kerr medium. So the amplitude of the slowly varying optical field at the output of the Kerr medium is given by [19]:

$$A_{out} = \sqrt{2P}\cos(\omega_d t/2)\exp(i\phi_{\mathrm{NL}}) \tag{4}$$

where $\phi_{NL} = (P + P\cos\omega_d t)n_2 k_0 L/A$ is the sinusoidal phase-modulation as a result of the Kerr effect induced by the field components, and L is the length of the Kerr medium. In the following, the exponential factor $\exp(in_2 k_0 LP/A)$ is neglected as it does not affect the output frequency if the input powers remain constant. Solving this equation for the field at the output of the Kerr medium with the Jacobi-Anger expansion, $\exp[iz\cos Bt] = \sum_{m=-\infty}^{\infty} i^m J_m(z)\exp(imBt)$, thereby expressing the results as an infinite sum of frequency sidebands spaced ω_d apart, the amplitude of the m^{th} order sideband electrical field at the output end of the Kerr medium is expressed by:

$$A_m = \sqrt{2P}\cos(\omega_d t/2)(i)^m J_m(Pn_2 k_0 L/A)\exp(im\omega_d t) \tag{5}$$

where J_m indicates the m^{th} order Bessel function of the first kind. Above analysis mainly focus on the Kerr effect-induced phase modulation.

Equation (5) shows that the m^{th} order sideband generated by the Kerr effect is m times ω_d apart from ω_p. Also, since sidebands are generated at both sides of ω_p but J only assume non-negative orders, we will hereafter refer to lower frequency sidebands as negative orders, but the positive value should be used for the Bessel function calculation, i.e. $J_{|m|}$. By modulating one of the laser lights with chirped pulses, say ω_c, after propagation through the Kerr medium the chirping range of the m^{th} sideband would also be enhanced m times after propagation through the Kerr medium as predicted by Eq. (5). Fig. 1(a) shows a schematic spectral diagram of the fixed-frequency and chirped pulse configuration, where chirped pulses with spectral content $\Delta\nu$ and pulse width $(T_1 - T_0)$ are injected into a highly nonlinear fiber (Kerr medium). Considering the output spectrum at the end of the fiber, the starting frequency component of chirped pulses signal at time T_0 (solid line) will interact with pump signal yielding numerous sidebands that will be $\omega_m = m\omega_d = m(\omega_c - \omega_p)$ away from ω_p, while the ending frequency component at time T_1 (dashed line) of chirped pulses will generate sidebands that will be $\omega_m = m(\omega_d + \Delta\nu) = m(\omega_c + \Delta\nu - \omega_p)$ away from ω_p. Note that $m = 0$ corresponds to the output sideband located at the frequency of the input pump, ω_p, while $m = 1$ corresponds to the output sideband located at the same frequency as the input chirped pulses. In addition, the input pulse intensity profile is square-shaped, higher order sidebands does not alter the intensity profile or duration of the output pulse. Therefore, for the m^{th} order sideband Kerr pluses, the frequency chirping range is improved from $\Delta\nu$ to $m\Delta\nu$, but with same pulse duration W that equals to $(T_1 - T_0)$. It is noted that the generated Kerr chirped pulses in the left side experience a decreased in optical frequency (red shift), while the right side Kerr chirped pulses undergo an increased in optical frequency (blue shift).

In order to further improve the frequency chirping rate $(\Delta\nu/W)$ without changing the pulse width W, an anti-chirped pump signal from the same laser source, i.e. with chirping content $-\Delta\nu$, is utilized to extend the frequency chirping range. This new optimized method is shown in Fig. 1(b). Since the chirped pump and original chirped pulses are synchronized in time domain, the interaction between starting frequency components (at time T_0) of chirped pulse (blue solid line) and chirped pump (red solid pump) generates sidebands with frequency $\omega_m = m\omega_d = m(\omega_c - \omega_p)$ apart from ω_p. On the other hand, the two ending frequency components (at time T_1) from chirped pump and chirped pulse will interact with each other and yield negative sidebands that

Optics EXPRESS

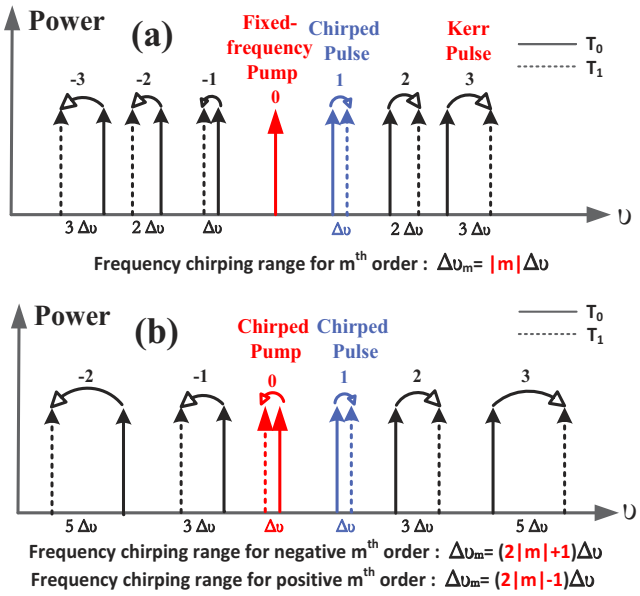

Fig. 1. Schematic diagram of normalized spectrum for generated sidebands from Kerr effect for (a) fixed-frequency pump and (b) chirped pump.

will be $\omega_m = m(\omega_d + 2\Delta v) = m(\omega_c + 2\Delta v - \omega_p)$ apart from $\omega_p - \Delta v$. Note that the ending frequency of negative order Kerr pulse at time T_1 is generated from the chirped pump signal at frequency of $\omega_p - \Delta v$ since the blue shifts occurs within the pulse duration from T_0 to T_1, resulting an additional frequency chirping extension of Δv. The frequency chirping range for negative sidebands is extended from Δv to $(2m + 1)\Delta v$ with same pulse duration. Thus, the chirping rate enhancement factor is $(2m+1)$ for the negative $-m^{\text{th}}$ order sideband Kerr pulses. Similarly, the positive sidebands will experience a chirping rate enhancement factor of $(2m\text{-}1)$, since the first positive sideband is considered as the original chirped pulse, shown in Fig. 1(b).

In the chirped pulse φ-OTDR, to avoid the trace-to-trace distortion and decorrelation, the largest measurable time delays between two consecutive traces is usually limited to 10% of pulse width [20]. The relationship between external disturbance-induced optical path length change, ΔL, and time delay, Δt, is given by [14]:

$$\Delta\varepsilon\, K = \frac{\Delta L}{L} = -\frac{\Delta v_\varepsilon}{v_0} = -\frac{1}{v_0}\frac{\Delta v}{W}\Delta t \tag{6}$$

where v_0 is the initial optical frequency of the chirped pulse, Δv_ε is the strain variation induced frequency shift and K is the strain coefficient. As explained in [9,14], too large strain changes between consecutive traces may result in a cross-correlation that compares traces originating from partially different scatterers. Instead of a unique correlation peak, such cross-correlations may exhibit a few peaks of fairly close magnitudes and the likelihood of producing an anomalous estimate of Δt, called an outlier, becomes too high. In order to reduce the probability of appearance of outliers in our system, the maximum measurable Δt equals to 10% of W, then the maximum detectable strain variation between two consecutive measurements is only limited by frequency chirping range of the pulses [21]. Hence, high order Kerr pulses have the potential to increase the maximum detectable strain variation, which is experimentally validated in the following sections.

Optics EXPRESS

3. Experimental setup

To verify the principle mentioned in section 2 and investigate the noise performance of high order Kerr pulses, a chirped pulse φ-OTDR system with Kerr pulses is implemented for dynamic strain sensing. The experimental setup is depicted in Fig.2. A DFB laser with 1 MHz linewidth is periodically modulated by triangular-shaped current pulses with equal rising and falling edges of 20 ns and at a 1 μ s repetition period from a signal generator (8130A, Hewlett Packard). Thus, the output optical frequency of the DFB experiences a periodic modulation including blue and red shift, as shown in Fig. 2(a). The output modulated signal is divided into two branches, and the optical wave in the upper branch is then chopped by the SOA with 6 ns pulses, acting as a gate device, only allowing the transmission of the blue-shifted portion of the modulated signal. Note that, despite the application of a linearly varied input current, the output frequency change of the DFB laser is not linear across 20 ns. However, within a carefully selected interval of 6 ns, the frequency chirp exhibits high linearity. In the bottom branch, a single-sideband suppressed-carrier (SSB-SC) modulator shifts the optical frequency of the input signal by ω_d = 25 GHz, which is used as the pump signal ω_p. Another way to obtain such frequency difference from the upper branch is to use a second laser as the pump, although this can only be used as a fixed pump as shown in Fig. 1(a). These two methods have different noise performance and will be discussed in next section. Before being combined by the 50/50 coupler and sent to the Kerr medium, the chirped pulse and chirped pump signals are amplified by two EDFAs to enhance the efficiency of Kerr effect. A delay line is employed to align the original chirped pulse signal and the chirped pump signal to make sure they have the same frequency chirping range but with opposite chirp [22]. As shown in Fig. 2(b) and (c), the two optical signals have the same frequency content of 545 MHz and the same chirping period of 6 ns. After propagating along the Kerr medium, numerous Kerr chirped pulses with extended frequency chirping range but same pulse width are generated, as shown in Fig. 2(d). After that, a single high order Kerr pulse can be selected through an optical tunable filter for high performance sensing application. Note that, by filtering one high order Kerr pulse, the intensity beating between pairs of high order pulses is removed, such that the output pulse has the same shape of the original chirped pulse, as shown in Fig. 2(e).

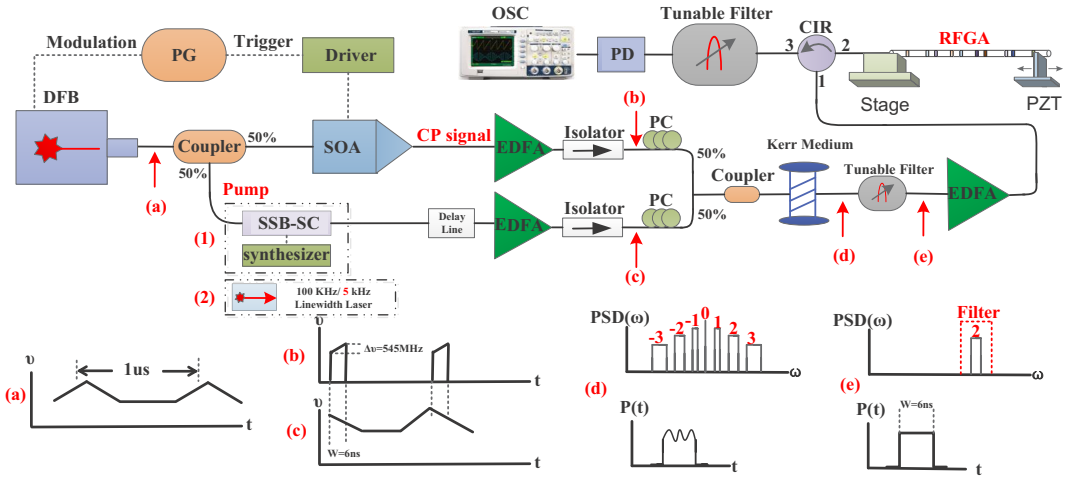

Fig. 2. Experimental setup of chirped pulse φ-OTDR based on Kerr pulses.DFB, distributed feedback laser; SOA, semiconductor optical amplifier; EDFA, Erbium doped fiber amplifier; PC, polarization controller; NLL, narrow linewidth laser; PG, pulse generator; PD photo-detector; OSC, oscilloscope; EM, electrical modulation; CIR, circulator; RFGA, random fiber grating array.

Optics EXPRESS

After being amplified by the EDFA, the high order Kerr chirped pulse is sent through an optical circulator to a random fiber grating array (RFGA) that acts as a strain sensor with enhanced Rayleigh scattering. Before detecting the reflected Rayleigh signal by a photodiode (PDB435C, Thorlabs), the amplified spontaneous emission (ASE) noise is removed by another tunable filter. Finally, the Rayleigh signals are collected by an oscilloscope (infiniium DSO81204B, Agilent) with sampling rate of 40 GSa/s, which corresponds to a sampling period of 25 ps.

4. Experimental results

The measured optical spectra of Kerr chirped pulses are shown in Fig. 3(a) for the two schemes discussed in section 2 – using an opposite chirping pump and a fixed-frequency pump from a second laser with 100 kHz-linewidth. The maximum order of the Kerr chirped pulses is limited by the optical powers of the pump (0^{th}) and the original chirped pulse (1^{st} order). This can be confirmed by analysing Eq. (5), in which the amplitude of the J_m term decays with m, so that higher input powers are required to generate high order sidebands. However, too high powers give rise to other nonlinear effects in the fiber, such as stimulated Brillouin scattering, which could significantly deplete the pump power and prevent the generation of high order Kerr pulses. To optimize the generation of high order Kerr pulses while preventing undesired non-linear effects, the peak power of the chirped pulse signal was tuned to about 13 dBm and that of the pump signal to ~20-23 dBm. Another important aspect that has a significant impact on the number of Kerr chirped pulses is the relative SOP between pump and original chirped pulses, described by the parameter η in Eqs. (1) and (2). The physical reason is that the peak power of the optical beating signal from two optical waves in Eq. (2) is SOP dependent, directly affecting the phase modulation depth. After optimizing the optical power and the SOP of two injection signals, more than 8 order Kerr chirped pulses were well generated. In order to verify the frequency chirping range of high order Kerr pulses, the frequency content of the -1^{st} and -4^{th} orders is measured at 5 dB linewidth, as shown in Figs. 3(b) and (c). In Fig. 3(b), the frequency chirping range of the -1^{st} order by using fixed-frequency pump remains of 545 MHz, which is the same as the original chirped pulse signal, while that of the -1^{st} order by using chirped pump signal is about 1.61 GHz, a 3 times improvement. For the frequency chirping range of the -4^{th} order Kerr pulses from fixed-frequency and chirped pumps, as shown in Fig. 3(c), the former is enhanced by 4 times to about 2.18 GHz, while the latter is increased to 4.84 GHz, which is almost a 9 times enhancement. The frequency chirping range is linearly proportional to the order m, which is consistent with the theoretical analysis in section 2. As predicted, the frequency chirping range of negative $-m^{\text{th}}$ order is improved by $2m+1$ times when using chirped pump, while the enhancement factor is m times when using a fixed-frequency pump.

Compared with fixed-frequency scheme by employing two lasers source, the proposed method with chirped pump not only have higher efficiency in term of frequency chirping range extension, but also have a lower noise performance benefits from the usage of single laser source. Given the fact that low frequency fluctuation of laser central optical frequency is one of the main noise sources that limits the accuracy in distributed sensing systems, we analyzed the optical frequency stability for both pumping schemes. In the experiments, different order of Kerr pulses from the two schemes are used as interrogation pulses in the chirped pulse φ-OTDR. Based on Eq. (6), any central optical frequency drifting of the interrogation pulses will introduce overall time delays in the reflected Rayleigh traces, and this time delay is calculated by the frequency drifting divided by pulse chirping rate, i.e., $t_{\text{delay}} = \frac{f_{\text{drift}}}{\Delta\nu/W}$. By measuring the trace-to-trace time delays, the equivalent frequency jitters of high order Kerr pulses can be obtained. Figures 4(a) and (c) present the equivalent frequency jitters of different orders Kerr pulses for chirped and fixed-frequency pump configurations, respectively. It clearly shows that the unwanted frequency jitters are increasing from lower order to higher order Kerr pulses in both pumping schemes. The reason is that two consecutive Kerr pulses do not share the same central frequency due to

Optics EXPRESS

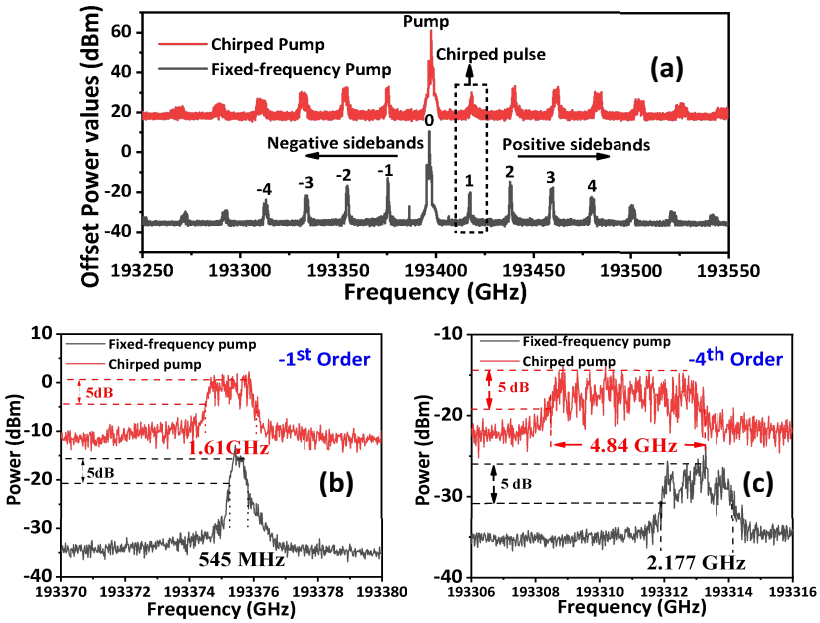

Fig. 3. Spectrum of generated high order Kerr pulses at the output end of the Kerr medium by using fixed-frequency or chirped pump. (a) overview spectrum, and close-up view of the (a) -1^{st} order and (c) -4^{th} order from fixed-frequency and chirped pump, respectively.

laser frequency fluctuation, and this central frequency difference is greater for higher order Kerr pulses. For instance, for the positive m^{th} order Kerr pulses, the instantaneous central frequency is $m(\omega_d + \Delta\omega_{\text{drift}}(t))$, indicating an increase in the frequency drift by a factor m. However, if we compare the frequency jitters from the same -4^{th} order between the fixed-frequency case and chirped pump case, the latter has lower frequency jitter noise, as shown in Fig. 4(b) and (d). Since the central frequency fluctuation of chirped pulses and chirped pump signals come from the same laser, nearly the same central frequency drift is expected in chirped pulses, ω_c, and chirped pump, ω_c, thus resulting in a low central frequency drifting noise. The standard deviations of the frequency jitter for all measured Kerr pulses are shown in Fig. 4(e), revealing that the noise performance of Kerr pulses in the chirped pump scheme using a single 1 MHz-linewidth laser is comparable to the fixed-frequency scheme with 5 kHz-linewidth laser, and much smaller than the fixed-frequency scheme with 100 kHz-linewidth laser.

To verify the capability of frequency chirping range extension, dynamic and static strain measurement experiments are conducted. In the principle-proof experiments, a Rayleigh back-scattering enhanced sensor, RFGA, is used to acquire Rayleigh traces with a high signal-to-noise ratio. The RFGA has an average reflection of about -30 dB and a length of 0.8 m. It consists of 8 alternating sub-gratings of lengths 10 mm and 5 mm. The periods of the sub-gratings are randomly distributed between 0.5180 μm and 0.5464 μm. More details about the fabrication of this sensor can be found in our previous publication [23]. The setup for applying strain variation is shown in Fig. 2, in which one end of the RFGA is glued on the fixed translation stage and another end is fixed on a Piezo Transducer (PZT). The displacement of the PZT could be precisely controlled so that the desired strain variation could be applied on the RFGA accurately. Firstly, a triangle-shaped strain variation with an amplitude of 50 $\mu\epsilon$ and a period of 2 s is applied on the RFGA, and the reflected Rayleigh signal from the RFGA is continuously collected in the oscilloscope over 4 s, resulting in 4000 traces with a duration of 10 ns each. The differential strain was then calculated for each pair of consecutive traces through cross-correlation operation, and by integrating the differential strain over the measurement time we obtained the overall

Optics EXPRESS

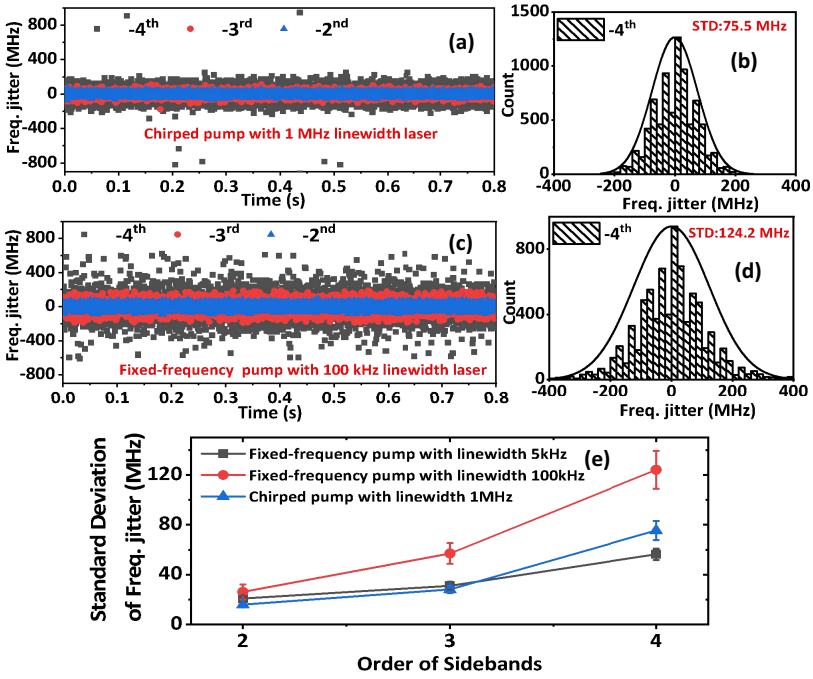

Fig. 4. Frequency jitter noise of different high order Kerr pulses with chirped (a) or fixed-frequency (c) pump, and their respective histograms (b) and (d). (e) shows the comparison of frequency jitter noise from different order Kerr pulses with fixed-frequency (5 kHz/100 kHz linewidth laser source) or chirped pump (1 MHz linewidth laser source).

strain variation as shown in Fig. 5(a). It clearly shows that higher-order Kerr pulses with the same pulse width but larger frequency chirping range introduce smaller time delays. This is consistent with Eq. (6), which shows an inverse proportional relationship between strain-time delays coefficient and frequency chirping rate ($\Delta\omega/W$). Figure 5(b) depicts the relationship between time delays and applied strain variations when different order of Kerr pulse are utilized. According to the ratio between coefficients of the different order of the Kerr pulses, the frequency chirping range enhancement factor could be calculated as shown in Fig. 5 (c). The enhancement factor of Kerr pulses in chirped pump scheme is close to the theoretical values. As a comparison, the enhancement factor of different order Kerr pulses in the fixed-frequency pump scheme is also calculated, and results are consistent with the predictions in section 2.

In chirped pulse φ-OTDR, similarly to other Rayleigh scattering-based dynamic strain measurements, the strain variation is measured by the differential strain measurement from two adjacent Rayleigh traces, and then the whole strain variation is calculated by integration over time. Hence, the maximum measurable strain variation over certain time period is limited by the system acquisition rate (based on pulse repetition rate) and the measurable strain variation between two single-shot measurements, as known as static strain measurement range, which is limited by frequency chirping range of the interrogation pulse based on the analysis in section 2. The maximum pulse repetition rate is limited by the length of the sensor, so the only way to increase the dynamic strain measurement range is to increase the frequency chirping range. Note that, when the applied strain variation between two Rayleigh traces exceeds the static measurement range, then the two traces become decorrelated, which translates into large uncertainty in the measured strain variation. For this reason, the generated Kerr pulses with extended chirping range could give a larger static strain measurement range and a lower uncertainty. In order to demonstrate the static measurement range of each order of Kerr pulses, different static strain

Optics EXPRESS

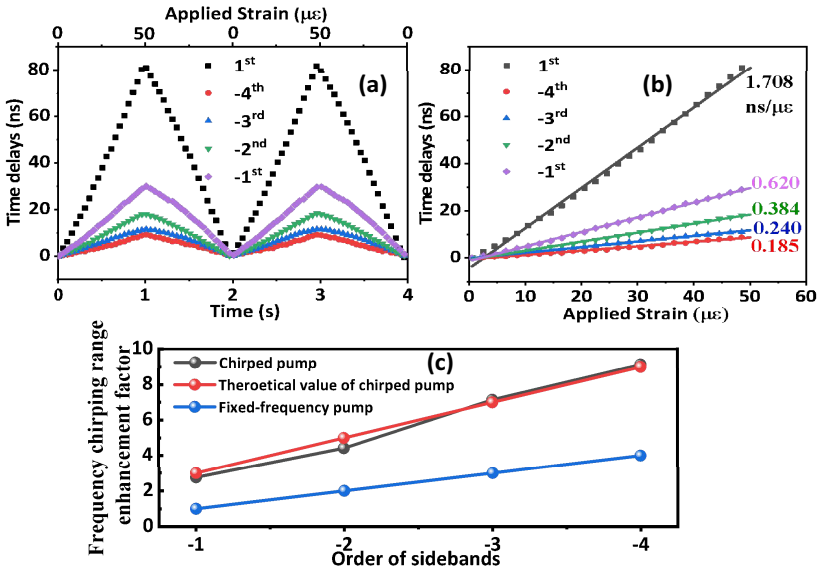

Fig. 5. (a) Dynamic strain measurement of using different order Kerr chirped pulses in chirped pump scheme (10 times averaging); (b) The relationship between applied strain and time delays in chirped pump scheme; (c) Frequency chirping range enhancement factor of fixed-frequency and chirped pump scheme.

variations are applied on the RFGA and the demodulated strain variation results are shown in Fig. 6(a). Each measurement has been repeated 20 times, and the average value of 20 tests used as the final measured strain variation result. For each order sideband, the measured results start to experience a larger uncertainty after a certain value of applied strain variation, which in fact could be potentially used to determine the static measurement range. So a measurement error, β, is introduced, and it is expressed by:

$$\beta = |\Delta\varepsilon_{mea} - \Delta\varepsilon_{app}|/\Delta\varepsilon_{app} \tag{7}$$

where $\Delta\varepsilon_{mea}$ is the measured strain variation and $\Delta\varepsilon_{app}$ is the strain variation applied on the RFGA. So, if β=10% is set as the threshold (tolerance) for the static measurement range determination of each Kerr pulse, we could find that the static measurement range of higher order Kerr pulses is significantly enhanced. The static range for -4^{th} order is up to 4 $\mu\varepsilon$, while that of the original (1^{st} order) chirped pulse is about 0.5 $\mu\varepsilon$. This general analysis confirmed that the static measurement range enhancement by using higher order Kerr pulse is significantly improved. Therefore, instead of improving the repetition rate of the interrogation pulse, our propose method solves the fundamental limitations of improving the strain measurable range without scarifying the sensing distance.

Ultimately, the strain uncertainty was verified for Kerr pulses of different orders in the absence of strain variations. 8000 Rayleigh traces were collected within 8 seconds, and the relative time delays between consecutive pulses were calculated. In order to compare the strain uncertainty of Kerr pulses with the same chirping range for fixed-frequency and chirped pump schemes, we define an enhancement factor α, which represents the chirping range of Kerr pulses over the chirping range of the original chirp pulse, $\alpha = \Delta\nu_{out}/\Delta\nu_{in}$. Note that the fixed-frequency case requires higher order Kerr pulses to obtain the same enhancement factor achieved from the chirped pump configuration, as clearly shown in Fig. 5(c). Figures 7(a) and (b) show the demodulated strain of high order Kerr pulses with enhancement factors 3 and 5, respectively (all results were obtained from negative order sidebands). Based on Figs. 7(a) and (b), the

Optics EXPRESS

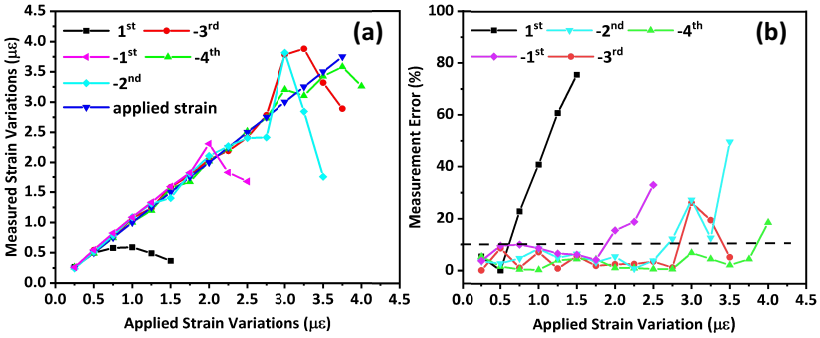

Fig. 6. Static measurement range assessment of Kerr pulses. (a) Static strain measurement and its measurement error (b).

strain measurement uncertainty from chirped pump scheme is always lower than that from the fixed-frequency scheme, which agrees with results from Figs. 4 and 5, as lower order Kerr pulses can always achieve higher enhancement factor in chirped pump scheme, and with a reduced laser drifting noise. The summarized results are shown in Fig. 7(c), in which four negative order Kerr pulses are evaluated. It shows that the measurement uncertainties for Kerr pulses with the same chirping range are lower in the chirped pump scheme. Furthermore, since wider chirping ranges are obtained in the chirped pump scheme for lower order Kerr pulses, the chirped pump case exhibits a significant benefit in terms of SNR, which can be seen in Fig. 3(a). Experimentally, utilization of sidebands beyond m = 6 is limited by their rapidly decreased power due to high order Bessel function. The constant electrical noise from detector and amplifier and lower signal power leads to higher power fluctuations, which will reduce accurately calculation of time delays for the CP-ϕ-OTDR application. There is a trade off in increasing chirp range by higher order Kerr pulses for large strain range at the cost of reducing strain measurement accuracy.

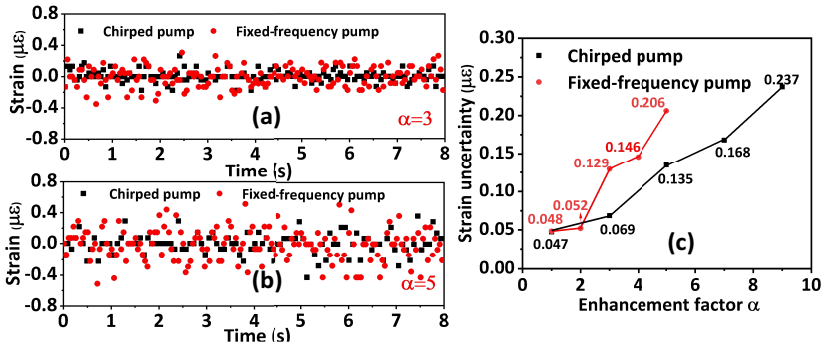

Fig. 7. Comparison of strain measurement uncertainty from fixed-frequency and chirped pump schemes when frequency chirping range enhancement factor is (a) 3 and (b) 5; (c) The strain measurement uncertainty achieved from different enhancement factors α for chirped and fixed-frequency schemes.

5. Discussion and conclusion

It is interesting to note that, although the SOA simply acts as a gating device by chopping a linear frequency chirping region, the abrupt intensity change in the rising and falling edges of the SOA pulse induce an additional SPM to the system. Hence, across the pulse width, the chirp is not purely linear. However, since in the current experiment the pulse edges have a duration of 500

Optics EXPRESS

ps, much smaller than pulse width of 6 ns, this edge effect can be neglected since it contributes minimally to the resulting Rayleigh traces. Furthermore, based on the results in Fig. 5(b), the relationship between relative strain variation and time delays has good linearity for all sideband orders despite non-linear chirp near the pulse edges.

Another relevant point to mention is the trade-off between static strain measurement range and measurement sensitivity. By enhancing the chirping range we showed that the static measurement range can be highly enhanced. However, as shown in Fig. 5, higher chirping ranges result in lower strain sensitivities, such that the minimum detectable strain is higher for high order Kerr pulses. Although most applications for strain measurement are more interested in high static strain measurement range than in high strain sensitivity, the proposed scheme offers a way to combine both features: with the addition of a few extra components, high and low order Kerr pulses could be sent alternately to the fiber sensor, thus generating two different measurement results, one with high static strain measurement range, and another with high sensitivity. Thus, the proposed method is general enough to cover multiple demands in strain measurement applications.

In our cross-correlation calculation based sensing system, a section of Rayleigh trace (time window) is selected for local time delays demodulation. And the fiber section covered by each time window is determined by the duration of time window and pulse width. Therefore, the spatial resolution is the convolution between pulse width and time window duration. In our experiments, the selected time window and pulse width are both 6ns, hence the spatial resolution of our proposed system is 1.2m. In fact, time window can be adjusted to increase or decrease the spatial resolution depending on positioning resolution of events and sampling rate of OSC depending on signal to noise ratio.

In conclusion, we generated high order chirped Kerr pulses with enhanced optical frequency chirping range from a single DFB laser to improve the performance of distributed strain sensing. By combining an up-chirped pulsed signal with a down-chirped pump in a novel configuration, we showed that the frequency chirping range of the m^{th} order Kerr chirped pulse is enhanced by a factor of $2m+1$, which is more efficient than the fixed-frequency pump scheme, which only enhances by a factor m. To experimentally validate the effect of high order chirped Kerr pulses in a strain sensing application, we used the -4^{th} order Kerr pulse from the proposed scheme to interrogate a strain sensor (RFGA) under strain variation induced by a PZT. With the chirped-pump configuration we achieved about 8 times larger static strain measurement range, much higher than that obtained with a fixed-frequency pump. Moreover, the chirped-pump configuration have also shown better performance in terms of measurement uncertainty. This novel scheme with anti-chirped pump exhibits better chirping enhancement factor, lower strain measurement uncertainty and higher SNR than the fixed-frequency configuration. Our proposed all-optic method opens new avenues to generate chirped pulse with higher chirping rate over nano-second pulse widths, without using complicate cascaded scheme and expensive electronic devices.

Funding. Canada Research Chairs (950231352); Natural Sciences and Engineering Research Council of Canada (RGPIN-2020-06302, STPGP 506628-17); China Scholarship Council (201808330421).

Disclosures. The authors declare no conflicts of interest.

Data availability. Data underlying the results presented in this paper are not publicly available at this time but may be obtained from the authors upon reasonable request.

References

1. D. K. Barton, *Radar system analysis and modeling* (Artech House, 2004).
2. R. Skaug and J. F. Hjelmstad, *Spread spectrum in communication*, 12 (IET, 1985).
3. M. Bertero, M. Miyakawa, P. Boccacci, F. Conte, K. Orikasa, and M. Furutani, "Image restoration in chirp-pulse microwave ct (cp-mct)," IEEE Trans. Biomed. Eng. **47**(5), 690–699 (2000).
4. L. E. Y. Herrera, R. M. Ribeiro, V. B. Jabulka, P. Tovar, and J. P. von der Weid, "Photonic generation and transmission of linearly chirped microwave pulses with high tbwp by self-heterodyne technique," J. Lightwave Technol. **36**(19), 4408–4415 (2018).

Optics EXPRESS

5. J. D. McKinney, D. Seo, D. E. Leaird, and A. M. Weiner, "Photonically assisted generation of arbitrary millimeter-wave and microwave electromagnetic waveforms via direct space-to-time optical pulse shaping," J. Lightwave Technol. **21**(12), 3020–3028 (2003).
6. C. Wang and J. Yao, "Photonic generation of chirped microwave pulses using superimposed chirped fiber bragg gratings," IEEE Photonics Technol. Lett. **20**(11), 882–884 (2008).
7. O. L. Coutinho, J. Zhang, and J. Yao, "generation of a linearly chirped microwave waveform with a large time-bandwidth product based on self-heterodyne technique, in *2015 International Topical Meeting on Microwave Photonics (MWP)*, (IEEE, 2015), pp. 1–4.
8. P. Tovar, L. E. Ynóquio Herrera, R. M. Ribeiro, and J. P. von der Weid, "Photonic generation of nlfm microwave pulses from dfb-laser chirp," IEEE Photonics Technol. Lett. **31**(17), 1417–1420 (2019).
9. J. Pastor-Graells, H. F. Martins, A. Garcia-Ruiz, S. Martin-Lopez, and M. Gonzalez-Herraez, "Single-shot distributed temperature and strain tracking using direct detection phase-sensitive otdr with chirped pulses," Opt. Express **24**(12), 13121–13133 (2016).
10. Y. Wang, P. Lu, S. Mihailov, L. Chen, and X. Bao, "Ultra-low frequency dynamic strain detection with laser frequency drifting compensation based on a random fiber grating array," Opt. Lett. **46**(4), 789–792 (2021).
11. E. F. Williams, M. R. Fernández-Ruiz, R. Magalhaes, R. Vanthillo, Z. Zhan, M. González-Herráez, and H. F. Martins, "Distributed sensing of microseisms and teleseisms with submarine dark fibers," Nat. Commun. **10**(1), 5778 (2019).
12. Y. Wang, L. Chen, and X. Bao, "Single-shot chirped pulse botda for static and dynamic strain sensing," Opt. Lett. **46**(22), 5774–5777 (2021).
13. D. Chen, Q. Liu, Y. Wang, H. Li, and Z. He, "Fiber-optic distributed acoustic sensor based on a chirped pulse and a non-matched filter," Opt. Express **27**(20), 29415–29424 (2019).
14. Y. Wang, P. Lu, S. Mihailov, L. Chen, and X. Bao, "Distributed time delay sensing in a random fiber grating array based on chirped pulse ϕ-otdr," Opt. Lett. **45**(13), 3423–3426 (2020).
15. J. Mar, Y.-R. Lin, and Y.-C. Yeh, "Ultra-wide bandwidth in-vehicle channel measurements using chirp pulse sounding signal," IET Sci., Meas. Technol. **3**(4), 271–278 (2009).
16. C. Li, V. M. Lubecke, O. Boric-Lubecke, and J. Lin, "A review on recent advances in doppler radar sensors for noncontact healthcare monitoring," IEEE Trans. Microwave Theory Tech. **61**(5), 2046–2060 (2013).
17. C. Baker, Y. Lu, and X. Bao, "Chromatic-dispersion measurement by modulation phase-shift method using a kerr phase-interrogator," Opt. Express **22**(19), 22314–22319 (2014).
18. B. E. Saleh and M. C. Teich, *Fundamentals of photonics* (john Wiley & sons, 2019).
19. Y. Wang, O. Krarup, L. Chen, and X. Bao, "Frequency sweep extension using the kerr effect for static temperature measurement range enhancement in chirped pulse φ-otdr," Opt. Express **29**(15), 23202–23212 (2021).
20. Y. Wang, P. Lu, S. Mihailov, L. Chen, and X. Bao, "Strain measurement range enhanced chirped pulse ϕ-otdr for distributed static and dynamic strain measurement based on random fiber grating array," Opt. Lett. **45**(21), 6110–6113 (2020).
21. H. D. Bhatta, L. Costa, A. Garcia-Ruiz, M. R. Fernandez-Ruiz, H. F. Martins, M. Tur, and M. Gonzalez-Herraez, "Dynamic measurements of 1000 microstrains using chirped-pulse phase-sensitive optical time-domain reflectometry," J. Lightwave Technol. **37**(18), 4888–4895 (2019).
22. W. Xie, Z. Xia, Q. Zhou, H. Shi, Y. Dong, and W. Hu, "Photonic generation of low phase noise arbitrary chirped microwave waveforms with large time-bandwidth product," Opt. Express **23**(14), 18070–18079 (2015).
23. P. Lu, S. J. Mihailov, D. Coulas, H. Ding, and X. Bao, "Low-loss random fiber gratings made with an fs-ir laser for distributed fiber sensing," J. Lightwave Technol. **37**(18), 4697–4702 (2019).

Chapter 7

Impact waves detection in I-steel Beam based on CP φ-OTDR

7.1 Contributions of authors

The contributions of the five authors: Yuan Wang (present author), Prof. Xiaoyi Bao, Prof. Neil Hoult, Prof. Joshua Woods and Hannah Kassenaar are as follows. Prof. Joshua Woods and Hannah Kassenaar from Queen's University built the impact wave generation setup and installed the Weak FBG array in the I-steel beam structure. The present author built the CP φ-OTDR system, conducted the data analysis, and produced the graphs in a state of continuous discussion and feedback with all co-authors. The OFDR data in Figure 7.4 (c) and Figure 7.5 are from Prof. Joshua Woods. Prof. Neil Hoult and Prof. Xiaoyi Bao provided advice on the presentation of the data as well as comments on the main text of this chapter. The main results in this chapter have been submitted and accepted by OFS 2022 for a poster presentation [33].

7.2 Introduction

Infrastructure, such as buildings, roads, and highways, is critical to the day-to-day lives of people around the world. However, these structures have lifetimes and could deteriorate due to the ageing of materials, overloading, and lack of sufficient maintenance [191]. Therefore, a real-time distributed monitoring system is required to avoid losses for users due to structural failure.

Distributed fiber optic sensor (DOFS) has been widely used in civil engineering as a tool for the health and safety monitoring of structures, benefiting from their geometric (small size, sensor length, flexibility, and lightweight) and metrological advantages (accuracy, high recording frequency, millimetric spatial resolution, and sensitivity) [192]. In addition, the DOFS have been the subject of numerous studies, including their behaviour at the core of reinforced concrete beams [18], their ability to detect internal cracks in concrete structures [193] [194], and the stress transfer mechanisms between the components of optical fibre sensors [195]. However, challenges arise when strain changes rapidly with time depending on the condition of deterioration, determined by peak strains at kHz change rate and high accuracy of $\mu\varepsilon$, both conditions are difficult to achieve due to noisy data [196]. The structural strain change under different loading is in the range of a few $\mu\varepsilon$.

To achieve more complex structural forms such as those required for material optimization, more data about performance in lab and field is required. The current research investigates different techniques to capture distributed dynamic (few Hz to 1kHz) and static (<1 $\mu\varepsilon$) strain. They are important for detecting the early failure sign: small cracks and deformation. With this specific dynamic strain requirement with high-speed response and static strain accuracy requirement, the best candidate is the phase OTDR which is capable of handling dynamic strain with wide frequency response and high strain accuracy. At the same time, OFDR is good for static strain or low-frequency strain measurement. Recently, a novel Chirped pulse φ-OTDR (CP φ-OTDR) sensing

system using a distributed feedback (DFB) laser without an optical interferometer-based phase demodulation scheme is proposed [30]. The external disturbance-induced optical path length changes are translated into local time delays within the time window of reflected Raleigh traces. The direct single-shot time delays measurement without coherent detection offers a capability of real-time high-accuracy strain (nε) and high-frequency measurements (only limited by fiber length) [197], achieved by using a low-cost DFB laser (1 MHz), where no environmental dependence in demodulation process is observed.

In this chapter, the proposed CP φ-OTDR is used for the first time in a civil engineering application to measure the impact load response of a steel I-beam, including acoustic wave, damped harmonic oscillations and static strain measurement. One challenge with this measurement is the high-frequency acoustic wave. For the OFDR technique, the frequency sweep process lowers the highest sampling rate below 100 Hz, and the high-frequency components are difficult to capture. However, the proposed sensor in this chapter uses chirped pulse for tensile/compressive strain measurement with single-shot measurement, which enables a higher sampling rate that is only limited by the sensor length. Another challenge is that the environmental noise and generated sound waves make coherent detection invalid, resulting in no readout data for acoustic wave detection. However, the proposed sensor directly measures the time delays between selected windows for the same location in time domain traces, without using the phase demodulation process. The specific objectives of this chapter are to: (1) measure the dynamic response of the steel beam, including the acoustic wave and low-frequency dynamic strain variations (2) compare the static strain measurement from WFBGA-based φ-OTDR to other traditional strain measurement technologies, including a commercially available OFDR-based DOFS system as well as a traditional electrical resistance strain gauge, and (3) investigate the damping parameters in the low-frequency dynamic strain section and the impact of the drop height on the response of the steel I-beam.

7.3 Experimental principle and setup

In this study, a lumped mass is released from a desired height, which generates an impact force on the top flange of a simply supported beam at midspan. Figure 7.1 shows the differential strain variations of the steel beam structure after the impact force is applied. At the very beginning, surface acoustic waves are initially generated and propagate along the length of the beam. The frequency range of the generated surface acoustic wave is determined by the kinetic energy of the lumped mass. In the second stage, the beam structure experiences a damped free-vibration response, in which the beam exhibits harmonic oscillations. Because the high-frequency acoustic wave has large attenuation, it vanishes quickly. The frequency of the damped harmonic oscillations is usually in the infrasonic range and depends on the parameters of the beam (e.g., length and stiffness). Finally, as the beam comes to rest with the additional applied mass, a static strain is expected when the beam stops oscillating. To quantify the beam behavior, these three states of the beam response need to be monitored and quantified, which can be challenging by only using one sensor.

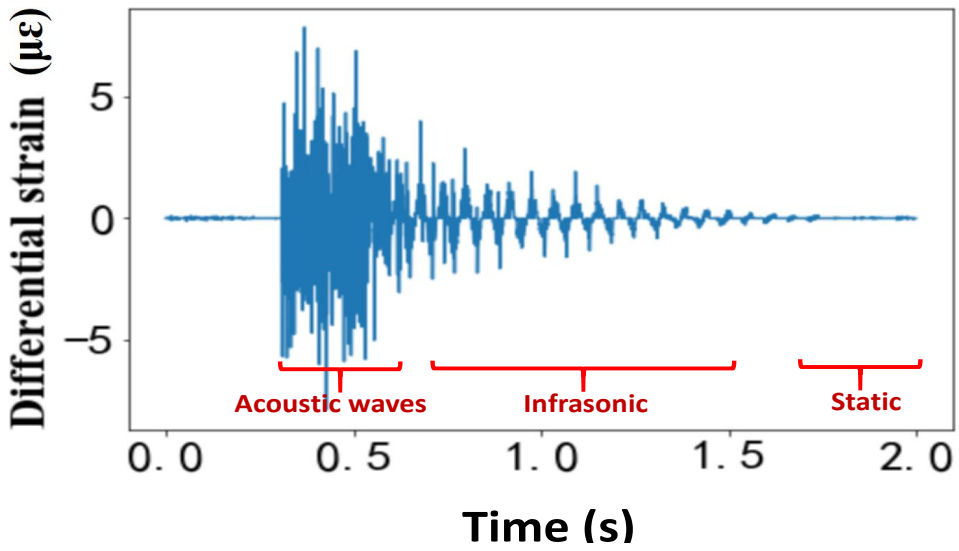

Figure 7.1: Expected responses of I-steel beam structure with impact load applied.

Consider that the damped harmonic oscillator differential equation to describe the

"infrasonic" section of the response is given by:

$$\ddot{x} + 2\gamma\dot{x} + \omega_0^2 x = \delta(t), \tag{7.1}$$

where x is the vertical displacement of the beam structure, γ is the intrinsic damping parameter, and ω_0 is the fundamental frequency for the system. This equation describes the impulse $\delta(t)$ response, it can be solved for the initial condition $x(t) = 0$, and the solution is given by:

$$x(t) = \Theta(t)\frac{\sin\left[\sqrt{\omega_0^2 - \gamma^2}t\right]}{\sqrt{\omega_0^2 - \gamma^2}}e^{-\gamma t}, \tag{7.2}$$

where $\Theta(t)$ is the step function or Heaviside function. By fitting the measured strain data with different impact weights, these two parameters can be determined for structural health monitoring and used to understand the condition of the structure. It should be noted that these two parameters do not depend heavily on the falling weight (or drop height) in these experiments. After the low-frequency oscillations, the beam structure will come to rest with the lumped mass on top. In this state of equilibrium, the beam experiences bending stresses with compression above the neutral axis and tension below.

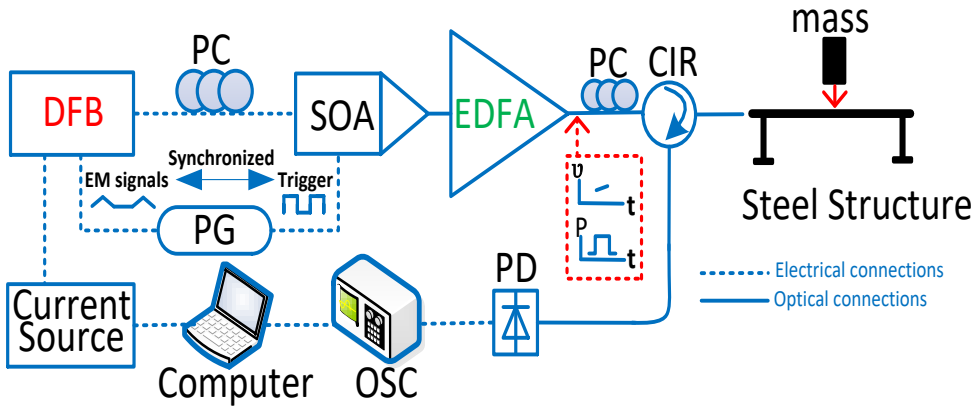

Figure 7.2: Scheme of chirped pulse φ-OTDR sensing system. DFB, distributed feedback laser; SOA, semiconductor optical amplifier; EDFA, Erbium doped fiber amplifier; PC, polarization controller; PG, pulse generator; PD photo-detector; OSC, oscilloscope; EM, electrical modulation; CIR, circulator.

Figure 7.2 depicts the chirped pulse φ-OTDR system used for the distributed impact wave measurements. The key components include: the chirped pulse generator scheme which is composed of a DFB laser diode (CQF938/500, JDS Uniphase), a pulse generator (PG) (8130A, Hewlett Packard) and a semiconductor optical amplifier (SOA) (OPB-10-10-N-C-FA, Kamelian) that is driven by an electrical circuit. A polarization controller is utilized to vary the state of polarization of the output light from the DFB laser so as to get maximum efficiency of SOA. By applying an electrical triangle signal, which is generated by a pulse generator, the output frequency of the DFB laser experiences a continuous variation. Meanwhile, a synchronized trigger signal actuates the SOA, yielding an optical chirped pulse with a pulse width of 8ns and a linear frequency chirping range of 1.25 GHz. After amplifying with a Erbium-doped fiber amplifier (EDFA), the chirped pulse signal is sent to the weak FBG array. The back-scattered Rayleigh signal is transferred from optical signals to electrical signals via a 1G bandwidth photodetector (PD) and then is collected in real-time by a digital oscilloscope (DSO81204B, Agilent) with a sampling rate of 40 GSa/s.

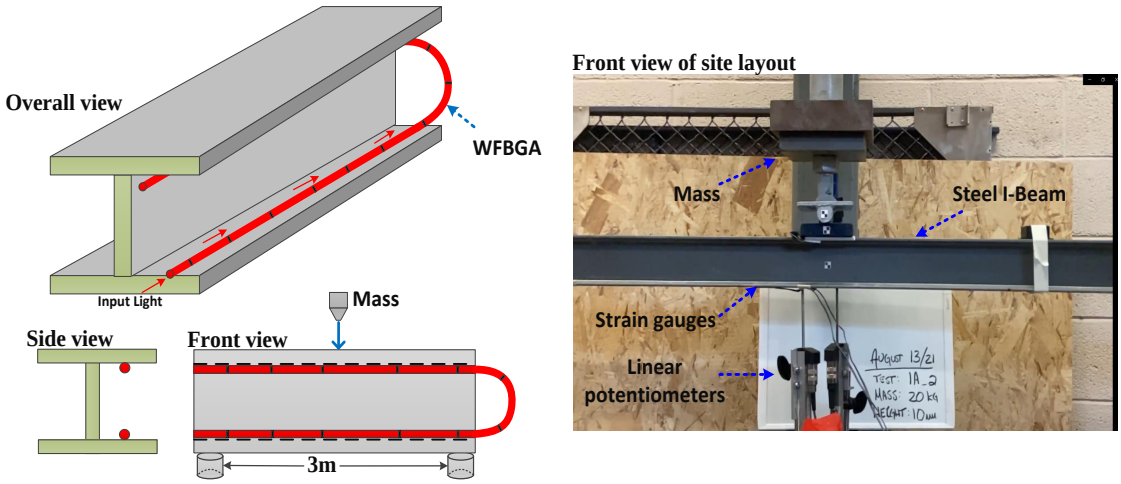

Figure 7.3: Layout of the weak FBG array in the I-Steel beam.

Figure 7.3 shows impact wave generation and installation of the FBG array on the surface of the steel I-beam. The length of the I-beam is about 3 m, and the total length of our WFBGA sensor is about 6 m. The WFBGA has enhanced reflectivity of -30 dB

and a grating period of 10 cm. The WFBGA was manufactured by the fiber sensing lab at Wuhan University of Technology. The array is glued to the beam from the top of the bottom flange to the bottom of the top flange to measure the tension and compression behavior. Two strain gauges and 2 linear potentiometers (LPs) are also used to monitor the generated impact waves. The strain gauges were mounted approximately 160 mm from the centre of the beam, while the 2 LPs were mounted at the midspan of the beam to measure the displacement on either side of the flange. Because a single load was applied in the centre of a simply supported beam in the drop test, it is anticipated that the strain will decrease linearly towards the supports. Thus, linear interpolation is appropriate to compare strain values measured at different locations along the length of the beam.

7.4 Experimental results

To evaluate the capability of the proposed sensing system to measure the dynamic response of the beam, a series of tests were conducted with two loading combinations. A 20 kg mass was dropped onto the beam for each test using an impact mechanism. The impact mechanism consisted of a steel wire and pulley system that was used to raise the mass to 10 mm or 40 mm above the top of the beam. The acquisition rate of WFBGA based CP φ-OTDR is set as 2 or 4 kHz, and the spatial resolution was 0.8 or 1 m. The sampling rate of strain gauges and OFDR systems are 2 kHz and 100 Hz, respectively.

7.4.1 Static strain measurement

Before assessing the dynamic performance of the strain sensing technologies, the ability of the two distributed fiber-optic sensing technologies to measure the static strain response was assessed in the third stage of impact response as shown in Figure 7.1. The

layout of the fiber optic cable installed on the beam is shown in Figure 7.4 (a). The WFBGA is glued using epoxy glued to the inside of the top flange loops around to the bottom left flange of the beam. The total length of the test fiber is about 10 m, of which only a 6 m section was bonded to the test beam. By sending a chirped pulse as the interrogation signal, the reflected Rayleigh traces from weak FBG array can be continuously collected. Since the local differential strain variation is translated into local time delays between two single-shot measured Rayleigh traces, the strain at any given time is the integration of the differential strain variations up to that point in time.

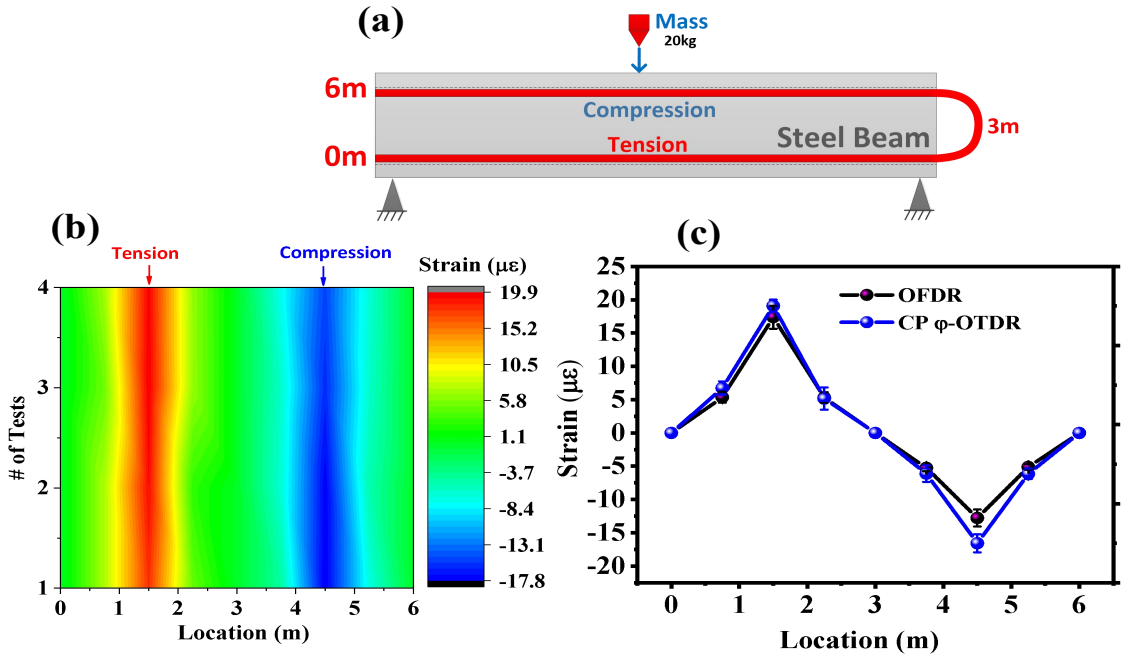

Figure 7.4: (a) layout for static strain measurement; (b) Distributed static strain monitoring along the steel I-beam based on chirped pulse φ-OTDR; (c) Static strain distribution from OFDR and chirped pulse φ-OTDR system (1m spatial resolution).

Note that the first stage in Figure 7.1 contains high-frequency components beyond the maximum measurable frequency of the system, which results in larger measurement uncertainty for strain variation demodulation in the "static" part. Thus, to avoid the impact of the high-frequency acoustic waves, the first reference trace to calculate the strain variation profile of the "infrasonic" and "static" parts is set as the trace from

the beginning of the test, in which there is no strain applied. Figure 7.4 (b) shows the static strain distribution for the steel I-beam, in which the first section would experience tension and the fiber on the bottom of the top flange experiences compressive strains. It is noted that the spatial resolution of OFDR need to be modified to enable a direct comparison since the gauge length and longitudinal locations of the fiber on the beam cross-section are different. With the assumption of linear strain variation along the I-beam from the supports end to the midspan, the theoretical strain value at a different location along the beam could be calculated based on the strain gauge readings. Thus the strain variation profile with different spatial resolutions could be obtained by integrating these values within the spatial resolution range. The static strain measurement comparison between the OFDR system and CP φ-OTDR is shown in Figure 7.4 (c), which shows a good consistency within 2 $\mu\varepsilon$ variation between results. The measurement uncertainty from different tests is shown in the error bar in Figure 7.4 (c) with the average value of about 1.2 $\mu\varepsilon$.

It is noted that there is a strain mismatch near the load points (the supports and where the mass is dropped). So, as a result, when the actual strain is integrated over the middle 1m, the compressive strain is less than the tensile strain. The results show that the tension strain at the top mid (1.5m) are slightly higher than the compressive strain results at the bottom mid (4.5m).

7.4.2 Dynamic measurement

In the dynamic measurement, the lumped mass is released from a height of 40 mm or 10 mm, depending on the test, on the mid-span of the beam. A horizontal cylindrical rod was placed on the bottom of the impact mechanism and perpendicular to the longitudinal axis of the beam to simulate a point load. To prevent the beam from sliding or bouncing during the impact tests, a ratchet strap was placed around the beam at the outer end of each support to not interfere with the behavior of the

beam. The impact load response of the beam structure with a drop height of 10 mm is monitored by the sensor array and strain gauges, and the results are shown in Figure 7.5. As was discussed for the results in Figure 7.1, the beam undergoes three distinct states, including high-frequency vibration, damped oscillation, and static strain, which are captured differently by these two types of sensors. Apart from the difference in distributed and point sensors, they also show a different capacity for high-frequency vibration detection.

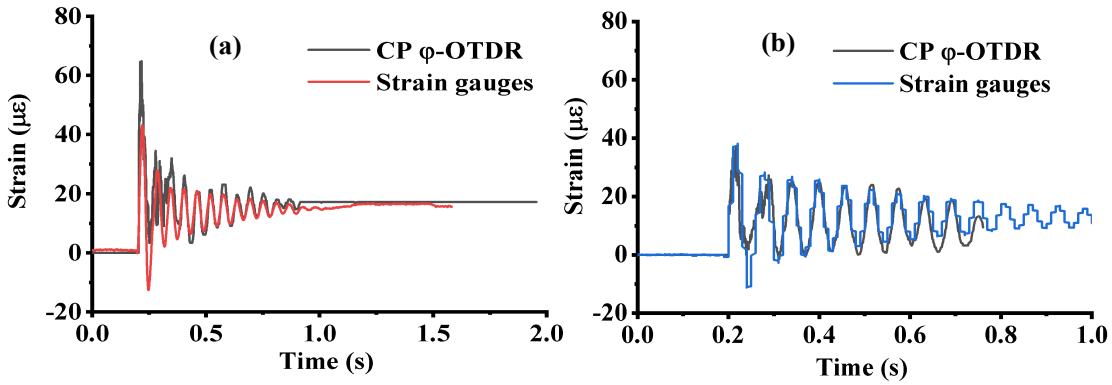

Figure 7.5: Strain-time response comparison between at CP φ-OTDR and strain gauge at midspan with different spatial resolution of (a) 0.8m and (b) 1 m.

In Figure 7.5, the CP φ-OTDR results are compared against the strain gauges results, which were adjusted to have a 1000 mm or 800 mm gauge length. For the damped oscillation and static portions of the response, the CP φ-OTDR measurements and the modified strain gauge results are in good visual agreement, while there is some noise in the CP φ-OTDR measurements in the first part of the response (from approximately t=0.2s- 0.3s). The noise is due to high-frequency vibrations in the beam caused by the impact (which corresponds to the sound of the mass impacting the beam). The sound wave coupled with the WFBGA and generated high-frequency strain variation with a comparable strain amplitude to the minimum detectable value (approximately nε) that decays rapidly. But this sound wave is not detected by the electrical strain gauge due to the limited sensitivity and lower coupling efficiency compared with the WFBGA.

After that, the mass, together with the beam, enters the damped oscillation stage after the first 0.1 s after impact, which can be captured by both CP φ-OTDR and the strain gauges.

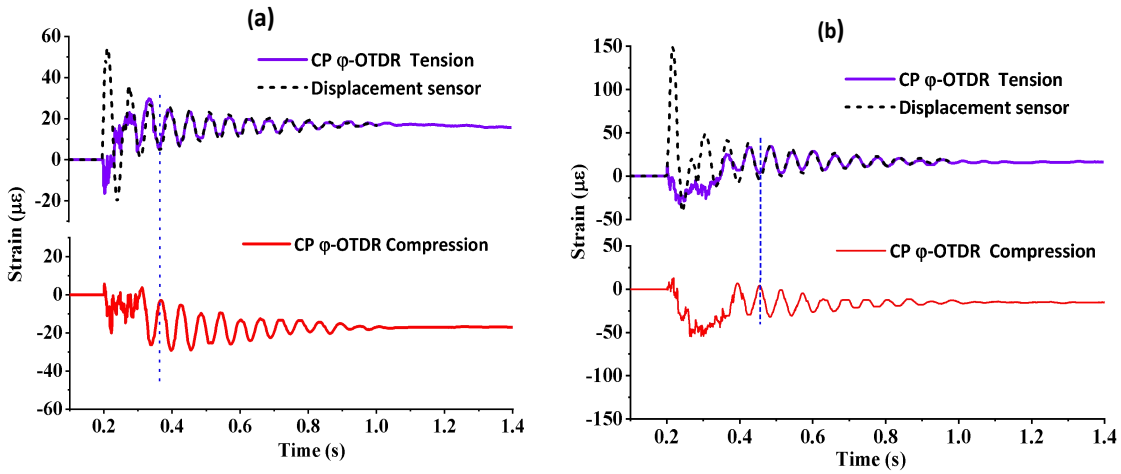

Figure 7.6: Strain-time response comparison between at CP φ-OTDR and Linear Potentiometer (LP) at midspan with different drop height of (a) 10 mm and (b) 40 mm.

The impact force-induced negative strain (compression) and positive strain (tension) can be calculated by the vertical midspan displacement of the beam, which is measured by the Linear Potentiometer (LP) sensor and the displacement-tensile strain coefficient. The displacement-tensile strain coefficient is decided by the beam properties and the integration length, which is 0.8 m for the results in Figure 7.6. The dashed line in Figure 7.6 (a) shows the equivalent strain value based on the displacement sensor by using the displacement-tensile strain coefficient of 35 $\mu\varepsilon/mm$, While the solid line shows the results from CP φ-OTDR. It is noted that local stress concentrations in the vicinity of the point loads introduce a discrepancy between the peak tensile and compressive strain, which means that the displacement-strain coefficient is different for tensile and compressive strain. Here, we only compare the tensile strain results from the CP φ-OTDR and LP sensor to verify the measurement accuracy of the proposed system. The result from the two sensors is largely in good agreement with no variation of more than 2 $\mu\varepsilon$ after the sound vibration induced high-frequency vibration section (about 0.2s-0.3s).

To verify the displacement-strain coefficient, the mass drop height is set as 40mm. The dynamic strain response is obtained by applying the displacement-strain coefficient to convert the displacement to the strain, which is shown in Figure 7.6 (b). The two tests with different drop heights show a different initial impact behavior, with the impact of acoustic wave (noisy profile at the beginning) lasting for a longer time for the 40 mm drop, which is to be expected since more energy is imparted to the beam. For both tests, the vertical dashed line shows that the bottom and top flange have symmetrical responses. More importantly, the dynamic strain measurement from the CP φ-OTDR show good consistency with the result from the LP sensor, except the acoustic wave detection at the beginning of the test. Another interesting point that should be noted is the time duration of the high-frequency section is doubled from about 0.1 s to 0.2 s, since the 40 mm height mass creates a larger impact force that leads to stronger sound waves and more energy transfer from potential energy to kinetic energy, which leads to a longer duration time of decay process for high-frequency acoustic wave. The decay process is related to the γ parameter and the maximum amplitude of the displacement.

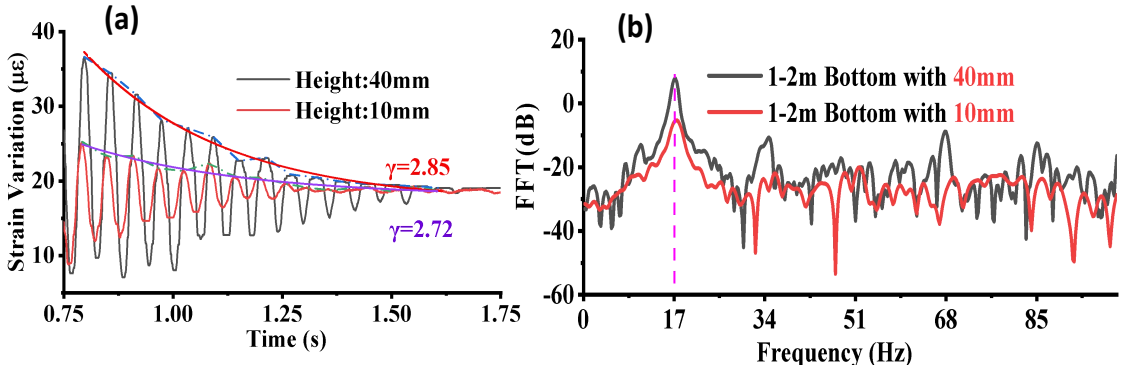

Figure 7.7: (a) The intrinsic damping parameter fitted in the damped oscillation section and (b) the natural frequency with different drop heights.

By selecting the damped harmonics oscillation section of the response, the intrinsic damping parameter is fitted to the peak value of each vibration period, as shown in Figure 7.7 (a). Similar to what was predicted in the theoretical analysis based on Eq.7.1,

the damping parameter does not depend significantly on the drop height (or impulse force). Thus, the different drop heights yield a similar result of 2.85 and 2.72 for the intrinsic damping parameter. The small difference may come from the system noise and fitting errors. In addition to the damping parameter, the fundamental frequency of the system is evaluated from the Fast Fourier Transfer (FFT) analysis, as shown in Figure 7.7 (b). A dominant peak could be found at the same location of 17 Hz in both measurements with different drop heights. With larger impulse force from 40mm drop test as shown in Figure 7.7 (b), higher harmonic components are excited. The high potential energy leads to higher kinetic energy with higher impact wave frequency, as illustrated in Figure 7.7 (b).

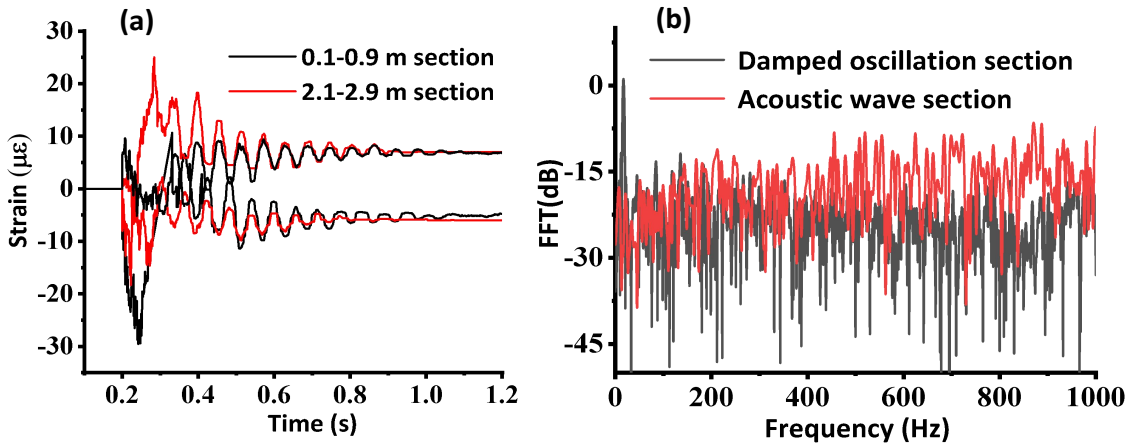

Figure 7.8: (a)Distributed dynamic strain measurement by CP φ-OTDR at left-span and right-span; and (b) FFT analysis of damped oscillation section and acoustic wave section with same drop height of 40 mm.

In the previous discussion, the dynamic measurements taken/averaged about the mid-span of the beam were investigated. It is also important to monitor the dynamic strain distribution along the beam, as damage may occur at other locations. Figure 7.8 (a) presents the strain for the left and right spans. In the 0.1 – 0.9 m range, the CP φ-OTDR provides a higher compression measurement than that in the 2.1 – 2.9 m range in the first 0.1 s after impact, which is an unexpected result from a mechanical strain point

of view. The reason is that the differential strain variation between two adjacent single-shot measurements for the two side-spans is supposed to be a few nano-strain. But for the real measurement, this differential strain could be up to the sub-microstrain range and with the same sign due to the broadband frequency of the acoustic waves exceeding the sampling rate of the proposed system (2 kHz). Thus, the overall strain variations show an irregular strain profile at the beginning when integrating the differential strains over time. To solve this problem, and give a more precise strain variation profile at the beginning of the test, further improvements in sensing accuracy and sampling rate are required.

Finally, the FFT analysis of the acoustic wave section is shown in Figure 7.8 (b). It shows that the broadband acoustic frequency range in the acoustic wave section is excited compared with the damped oscillation section, that only has a dominant peak at the fundamental frequency location. The mass, together with I-beam, vibrates based on the assumption of the rigid body in which the first modal frequency is dominant. On the other hand, lumped mass with higher drop height has larger kinetic energy and will excite more high-frequency components at the beginning of the test. When the drop height is increased, the kinetic energy can not be fully absorbed by the I-beam. The non-absorbed kinetic energy leads to different oscillations of I-beam in a very short time at higher frequency. It is noted that this broadband high-frequency acoustic wave detection is only enabled by the proposed system, which could reveal potential cracks introduced by the external load. The diagnosis of structural damage or cracks based on the FFT analysis of generated acoustic waves illustrates that the rigid body assumption should be used carefully for a high-frequency impact condition.

7.5 Discussion

The spatial resolution limitation is caused by the relatively nonuniform strain across the shorter gauge length, which increases uncertainty. To reduce the spatial resolution for dynamic strain measurement, the trade-off is further averaging the measurements, reducing the frequency range. For impact wave detection, one needs a higher frequency range, which can only be obtained at the cost of spatial resolution. In addition, the shorter pulse with smaller frequency chirping offers a limited measurement range, which introduces large distortions in the two Rayleigh traces with lower cross-correlation coefficient. Thus, a lower accuracy with larger uncertainty is expected.

7.6 Conclusion

This chapter demonstrates a distributed multi-parameter sensor for acoustic wave, dynamic strain and static strain sensing using a weak FBG array fiber. A proof of concept impact test was conducted by dropping a known mass from a fixed height onto a simply supported beam. The time-dependent impact response, including broadband frequency vibration of the I-beam, was successfully detected by the CP φ-OTDR system with a high sampling rate up to 2 kHz in a distributed manner. In the experiments, the sampling rate is limited by the memory size of the oscilloscope. In addition, the results from the CP φ-OTDR system are compared with a commercially available OFDR system (only static strain), strain gauges, and Linear Potentiometer, showing good agreement with errors below 3 $\mu\varepsilon$. The proposed sensor shows the capacity to detect high-frequency acoustic waves, while OFDR has no readout for the beginning section of the impact response. which is not caputred by the strain gauges and LPs are point sensors due to the small coupling coefficient and limited sensitivity.

Chapter 8

Single shot Chirped pulse BOTDA for strain sensing

8.1 Contributions of authors

The contributions of the five authors: Yuan Wang (present author), Prof.Xiaoyi Bao, Prof.Liang Chen are as follows. The present author built the experimental setup used in this Chapter, conducted the data analysis, and produced the graphs in a state of continuous discussion and feedback with all co-authors. Prof. Xiaoyi Bao and Prof. Liang Chen provided advice on the presentation of the data as well as comments on the main text of this Chapter. All authors contributed to the final version of all papers in this Chapter. The results of Section 8.3 has been published in Optics Letters, and the results of Section 8.4 has been presented in OFC 2022.

8.2 Introduction

To the best of our knowledge, Section 8.3 [34] is the first demonstration of a single-shot measurement BOTDA system by using a frequency-chirped pulse as a pump signal for strain-induced BFS changes measurement. Benefiting from the time-varying features of the Brillouin traces from Non-uniform fiber, the time delays between two adjacent Brillouin traces could be precisely determined by cross-correlation calculation. Due to the frequency sweeping free-based technique, the acquisition rate of the proposed system is only limited by the fiber length without averaging. Therefore, this proposed system is a promising tool for highly accurate distributed high-frequency dynamic strain sensing. More importantly, The pump source is a 1 MHz linewidth laser without a phase-locking loop. The laser frequency drifting noise could be compensated by the reference signal from the non-disturbed fiber section. BFS measurement resolution of 0.42 MHz with 4.5m spatial resolution is demonstrated over 5 km non-uniform fiber. The proposed system provides important guidance to employ chirped-pulse BOTDA in some particular applications requiring high frequency and high precision dynamic strain measurement.

In Section 8.4 [198], A real-time simultaneous temperature and strain measurement based on hybrid chirped pulse φ-OTDR and chirped pulse BOTDA is demonstrated for the first time. The high accuracy of 4.3 $\mu\epsilon$ for strain and 0.32 °C for temperature is achieved over 5 km non-uniform fiber.

8.3 Chirped pulse BOTDA

Single-shot chirped pulse BOTDA for static and dynamic strain sensing

YUAN WANG,[1] LIANG CHEN,[2] AND XIAOYI BAO[1,2]

[1]*School of Electrical Engineering and Computer Science, University of Ottawa, Ontario K1N 6N5, Canada*
[2]*Department of Physics, University of Ottawa, 25 Templeton Street, Ottawa, Ontario K1N 6N5, Canada*

Driven by the strong need for distributed high frequency dynamic strain sensing, ultra-fast Brillouin optical time-domain analysis is rapidly becoming a vital technique. Thus, in this letter, we propose and demonstrate a novel method by using chirped pulse as pump signal to extract the relative Brillouin frequency shift (BFS) changes through the real time delays between adjacent Brillouin traces, it enables static and dynamic strain measurement without time-consuming frequency sweeping process. Benefiting from single shot measurement based on Brillouin traces, the system has high acquisition rate that is only limited by sensor length without averaging and also immune to the polarization fading problem thanks to electrical delay time measurement. The pump source is a 1 MHz linewidth laser without a phase-locking loop, the laser frequency drifting noise could be compensated by the signal from the non-disturbed fiber section. In the experiments, BFS measurement resolution of 0.42 MHz with 4.5m spatial resolution are demonstrated over 5 km non-uniform fiber. © 2021 Optical Society of America

http://dx.doi.org/10.1364/OL.441815

Backward stimulated Brillouin scattering (SBS) in fiber, in which the Brillouin frequency shift (BFS) is a linear function of temperature and strain, is widely used for civil structure health monitoring, modern industrial controlling, and national defense security[1,2,3]. Among these Brillouin scattering based distributed sensors, Brillouin optical time-domain analysis (BOTDA) has gained more and more attention in the past few decades, because of its outstanding features, including a high signal-to-noise ratio (SNR), a high sampling rate[4], a long sensing distance[5], a high spatial resolution[6], leading to widespread field applications.

In the traditional BOTDA system, the frequency sweeping process takes usually several seconds to several minutes, which lowers the acquisition rate of the system, leading to a limited measurable frequency range of dynamic strain. Recently, many ultra-fast BOTDA systems have been studied to save the sweeping time for high frequency dynamic strain measurement. In optical frequency comb (OFC) scheme [7], the OFC wave is utilized as the probe signal to obtain the BGS in the frequency domain, in which the Brillouin beating signal will be amplified by the single frequency pump pulse via SBS effect when the frequency deviation span covers the BGS. Then the distributed BGS could be reconstructed by computing the Fast Fourier Transform (FFT) of the Brillouin beating signal. However, the frequency interval of OFC limits the spatial resolution to several tens of meters. In slope-assisted scheme [8], it skips the BGS scanning process by taking the advantage of the linearity at the edge of the BFS to convert the BFS to the amplitude variation, so that a single frequency pump pulse can demodulate the distributed BFS along the fiber. However, the Lorentz shape of BGS has a limited linear range at the slope edge, resulting in limited measurement range. In the fast-frequency sweeping scheme [4], T_{switch}, which is the frequency-switching time of the microwave generator, has been significantly reduced. The high-speed reconstruction of BGS is achieved by fast switching an arbitrary waveform generator (AWG) instead of a synthesizer based electronic sweeping, in which only single-shot measurement is required to obtain the BGS in the temporal (spatial) domain. However, The asymmetrical BGS should be reshaped through an algorithm to reduce the demodulation errors, making the data process more complicated. Recently, the pulse frequency chirping technique has been widely used in distributed Rayleigh sensing systems [9,10,11], and also a frequency-sweep fast BOTDA was implemented to achieve fast dynamic measurement in a 10 km fiber [12]. However, the entire distribution acquisition rate is limited by the number of measurement points along a fiber, due to it needs repeated pulse launching until the whole completed distribution is obtained.

In this letter, a real time chirped pulse Brillouin optical time-domain analysis (CP-BOTDA) sensing system with laser drifting compensation based on a non-uniform fiber is theoretically analyzed and experimentally demonstrated. Since we measure the pulse envelope over the chirped spectrum range of hundreds of MHz at every fiber location, the linewidth of the laser source does not affect the time delays measurement. In our experiment, stepping increased static and dynamic strain measurements are carried out to verify the principle. 4.5m spatial resolution with 0.42 MHz BFS resolution are achieved, and the BFS resolution could be further improved by increasing the pulse width or decreasing the frequency chirping range. More importantly, in our proposed system, the maximum acquisition rate is only limited by the sensor

length and times of averaging, which is a promising technique for ultra-fast dynamic strain sensing.

An emblematic BOTDA system is based on a "pump-probe" configuration in which the CW Stokes light is amplified by the pump pulse signal through the SBS when their frequency deviation matches up with the local BFS of the fiber. However, the reconstruction of BGS always requires a laser frequency sweeping process to extract the external perturbations induced BFS changes.

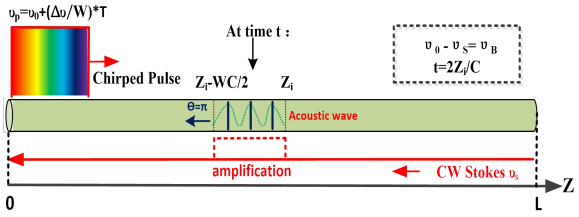

Fig. 1. Underlying principle for the chirped pulse-BOTDA.

Let's consider a chirped pulse with frequency profile of $\upsilon_p=\upsilon_0+(\Delta\upsilon/W)\cdot T$ utilized as pump signal as shown in Fig.1, where υ_0 is initial optical frequency of laser source, $\Delta\upsilon$ is frequency chirping range, υ_s is the frequency of Stokes light, and W is pulse width. Suppose the chirped pulse is lunched at t=0 with energy of $E_p(tC/2)$ and propagates to Z direction, where C is the speed for both pump and Stokes lights. CW Stokes is launched at Z=L with energy of $E_{cw}(tC/2)$ and propagates to L-Z direction. At given time t, Brillouin interaction in the region of $[Z_i\text{-}WC/2, Z_i]$ will arrive at Z=0, here Z_i is the distance between the input end and the front end of interaction range. Thus, the power of the CW Stokes light at that end is given by [13]:

$$P_{cw}(t)=E_{cw}(t)/dt=P_{cw}(L)\exp(-\alpha_{cw}L)+(g/A)\cdot E_p(\frac{tC}{2})\cdot\frac{WC}{2}/dt \cdot P_{cw}(L)\exp(-\alpha_{cw}L) \quad (1)$$

where g is the Brillouin gain coefficient, α_{cw} is the attenuation coefficient and A is the effective cross section of the fiber. Ignoring the contribution of spontaneous Brillouin emission, that pulse energy $E_p(tC/2)$ satisfies the following equation :

$$\frac{dE_p(tC/2)}{d(tC/2)}=-\left[\alpha_p+(g/A)P_{cw}(tC/2)\right]E_p(tC/2)$$
$$P_{cw}(tC/2)=P_{cw}(L)\exp[-\alpha_{cw}(L-tC/2)] \quad (2)$$

where α_p is the attenuation coefficient for a chirped pulse. Usually when z<60km or $P_{cw}(L)$<1mW, the pulse energy could be expressed as $E_p(tC/2)=E_p(0)\cdot exp(-\alpha_p\cdot tC/2)$. So, the optical power of CW Stokes light at fixed receiving time t is given by [13]:

$$P_{cw}(t)=P_{dc}+(g/A)\cdot\frac{WC}{2}\cdot P_p(0,\upsilon_p)\cdot\exp(-\alpha_p\cdot tC/2)\cdot P_{dc} \quad (3)$$

where $P_{dc}=P_{cw}(L)\exp(-\alpha_{cw}L)$ representing CW Stokes light that arrives at Z = 0 without interacting with the pulse and $P_p(0,\upsilon_p)$ is the power of pump pulse with frequency of υ_p at time t=0. Note that the Brillouin gain g depends on the frequency difference υ_p-υ_s, so for chirped pulse pump signal, $(g/A)\cdot WC/2$ in the Equ.3 should be calculated by the integral within the interaction region $[Z_i\text{-}WC/2, Z_i]$. Then, the power of Stokes light $P_{cw}(t)$ could be expressed as:

$$P_{cw}(t)\propto P_{dc}+P_p(0,\upsilon_p)\cdot\exp(-\alpha_p\cdot tC/2)\cdot P_{dc}\cdot \frac{Cg_p}{2A}\int_{t-2Z_i/C}^{t-(2Z_i/C-W)}\frac{(\Delta\upsilon_B/2)^2}{(\upsilon_0+\frac{\Delta\upsilon}{W}t-\upsilon_s-\upsilon_B)^2+(\Delta\upsilon_B/2)^2}dt \quad (4)$$

Where υ_B is the local Brillouin frequency shift of the fiber, g_p is the peak value of the Brillouin gain coefficient occurring at υ_p-υ_s=υ_B, and $\Delta\upsilon_B$ is the Brillouin gain bandwidth. According to Equ.4, the Stokes light power is relating to the frequency difference between υ_p-υ_s and local υ_B. Let's consider there is no strain applied on the fiber at given time t, and the power of Stokes light is $P_{cw}(0, t)$, while an applied strain ($\Delta\varepsilon$) induced BFS changes of $\Delta\upsilon_\varepsilon$ added to υ_B at given time t+Δt, and the power of Stokes light is $P_{cw}(\Delta\varepsilon, t+\Delta t)$. It means that the applied strain induced power variation could be compensated by the time delays Δt, giving by:

$$\frac{\Delta\upsilon}{W}\cdot\Delta t=\Delta\upsilon_\varepsilon \quad (5)$$

Equ.(5) means that the Brillouin traces (Stokes light power) experience a transversely time shift when the strain variation is applied, leading to $P_{cw}(0,t)=P_{cw}(\Delta\varepsilon, t+\Delta t)$.

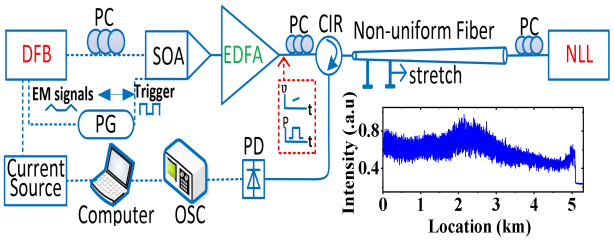

Fig. 2. Experimental setup for the chirped pulse-BOTDA sensing system. DFB, distributed feedback laser; SOA, semiconductor optical amplifier; EDFA, Erbium doped fiber amplifier; PC, polarization controller; NLL, narrow linewidth laser; PG, pulse generator; PD photo-detector; OSC, oscilloscope; EM, electrical modulation; CIR, circulator (The inset shows the Brillouin traces along the 5 km non-uniform fiber.)

The setup of our proposed CP-BOTDA scheme is shown in Fig. 2. A DFB laser diode (CQF938/500, JDS Uniphase) driven by an adjustable DC current is utilized as a pump laser source for chirped pulse generation, in which the output parameters are set at 193441.574 GHz and 20 mW. Before being intensity modulated using a semiconductor optical amplifier (SOA) (OPB-10-10-N-C-FA, Kamelian) into a 40ns chirped pulse, the electrical modulation signal (EM signal) from the pulse generator (PG) (8130A, Hewlett Packard) is applied to the DFB laser to generate frequency modulated light by linearly changing its drive current. Note that the EM signal and the trigger signal for SOA are synchronized, so that the desired frequency chirping range will be selected. The frequency chirping range is tunable and is set at about 675 MHz in our proposed system.

After being amplified by the Erbium doped fiber amplifier (EDFA) (AEDFA-33-B-FA, Amonics), the chirped pulse is injected into non-uniform fiber as pump signal by optical circulator. On the other end of non-uniform fiber, a narrow linewidth laser (PS-NLL-1550.12, TERAXION) with 5 kHz linewidth is utilized as Stokes light source. Hence, both pump pulse and CW Stokes light are launched into the non-uniform fiber with counter-propagate direction. Ultimately, the amplified CW Stokes light, namely Brillouin traces, will be detected by a photo-detector (PD) (PDB435C, Thorlabs) and then be collected by the oscilloscope

(DSO81204B, Agilent). Three polarization controllers (PC) are also used to optimize the optical signals.

As a specially designed sensor, the non-uniform fiber possesses a continuously changed mode field diameter from 5 μm to 7 μm and also a varied dispersion coefficients from 7.7 ps/nm/km to -0.3 ps/ns/km. Along the non-uniform fiber, the local Brillouin frequency shift and peak gain coefficient are varied, and the overall BFS distribution bandwidth is about 350 MHz [14].

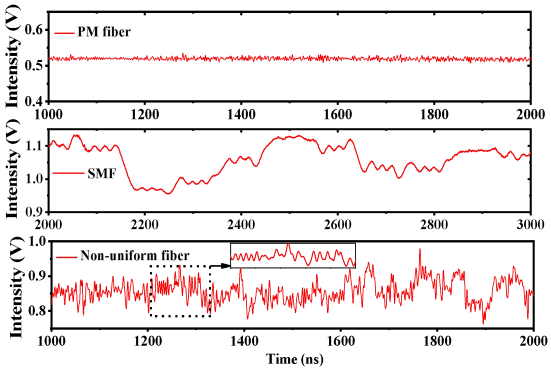

Fig. 3. Detected Brillouin traces for different types of fiber (Polarization maintaining fiber (PMF), Single mode fiber (SMF) and Non-uniform fiber).

Based on Equ.6, the applied strain variation is translated into local time delays between two adjacent temporal traces. So Brillouin traces with distinct peaks are very important for this method. The Brillouin traces from three different types of fiber are measured as shown in Fig.3. We could find that both Brillouin traces from SMF and non-uniform fiber experience significant fluctuations due to the state of polarization (SOP) dependence of the Brillouin gain, while the trace from PM fiber is stable with little fluctuations. The Brillouin signal from PM fiber is hard to used for time delay measurement unless the contrast of the fluctuation could be improved, while the low variation period of that from SMF would give lower spatial resolution and lower accuracy. The inset is a close-up view of Brillouin traces from non-uniform fiber around 120m-130m experiencing faster intensity fluctuations with more distinct peaks, which is more suitable for time delays determination. The main underlying reason for this phenomenon is that continuously increased core diameter is designed along the fiber, leading to an enhanced SOP dependence of Brillouin gain coefficient. Another reason which also contributes to the dense peaks is that the changed BFS and Brillouin gain coefficient along the fiber resulted from the changed local effective refractive index.

A simulation test is carried out before the strain measurement to verify the above theoretical analysis. As shown in Fig.4 (a), a time window of 16ns from Brillouin traces is selected to study the relationship between local time delays (Δt) of Brillouin traces and BFS changes ($\Delta\upsilon_\varepsilon$). In the simulation test, the initial laser frequency (υ_0) is finely tuned by changing the drive current to imitate the equivalent BFS changes. The frequency deviation υ_p-υ_s is firstly set as 10 GHz to match up with local BFS to obtain maximum gain coefficient. Cross-correlation based computation between two adjacent traces shows a result of interest that the local time delays is linearly proportional to the frequency deviation changes with a R-square of 0.998 and a coefficient of 59.2 ps/MHz, which is consistent with Equ.5 when the frequency chirping range and pulse width are set at 675 MHz and 40 ns, respectively.

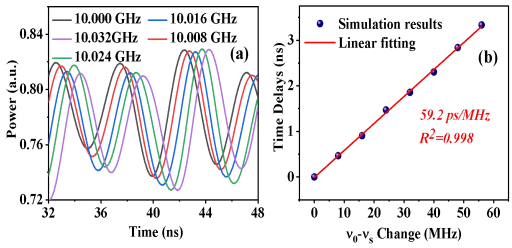

Fig. 4. Simulation results. (a) Time domain Brillouin traces with different frequency deviation between initial frequency of chirped pump pulse (υ_0) and frequency of Stokes light (υ_s). (b) Relationship between relative frequency deviation changes and time delay.

The experiments of the static strain measurement are performed by stretching the end segment of non-uniform fiber with the same strain variation step of 153.8 με. The 2D strain-spatial intensity responses of the non-uniform fiber are shown in Fig.5 (a), where the first 4m segments among the total 10m traces window clearly experiences a right-hand transversal shift. While other regions without stretching shows smaller fluctuations mainly caused by the slow laser frequency drifting [15], as shown in the inset of Fig.5 (b). To precisely determine the time delays that are attributed to the applied stain induced BFS changes, cross-correlation calculation is employed to extract the temporal shifts. In the data processing, a smaller selected time window gives a higher spatial resolution since the spatial resolution is the convolution of pulse width and time window duration. And the time delays results of each peak (A, B and C) have been estimated as shown in Fig.5 (c). Demodulation results with high consistency reveal that any peak in the disturbed section could be selected for time delays measurement to obtain a higher spatial resolution. In addition, the laser frequency drifting could introduce some obvious errors as the error data points shown in Fig.5 (c). In single-shot based measurements, one chirped pump pulse is sent to fiber for distributed Brillouin gain investigation together with CW Stokes light, which means any frequency drifting between two measurements will affect the disturbed and non-disturbed region equally. Fig.5 (d) presents the linear fitting for strain variation induced time delays with and without compensation. By using the compensation data (green dots) from the reference section, the uncertainty of time delays-related strain coefficient has been significantly decreased. To verify the repeatability of coefficient value, a larger stain variation step of 230.8 με is applied. And the demodulation results with and without compensation are illustrated in Fig.5 (e). It clearly shows that the uncertainty of coefficient is smaller than that of without compensation. More importantly, the corrected coefficient is consistent with the previous measurement. The time window of 5 ns is selected in cross-correlation calculation, resulting in an overall 4.5m spatial resolution.

On top of that, the core mode field size dependence of time delays-related strain coefficient is studied. Two same tests are applied to two ends of the non-uniform fiber. From the results in Fig.5 (f), we could find that there is a small difference in coefficient value between two different core diameters. This could be explained by that same strain variation could introduce larger effective refractive index change, leading to a larger BFS changes. However, this little difference could be neglected, considering it is very close to the uncertainly of the system.

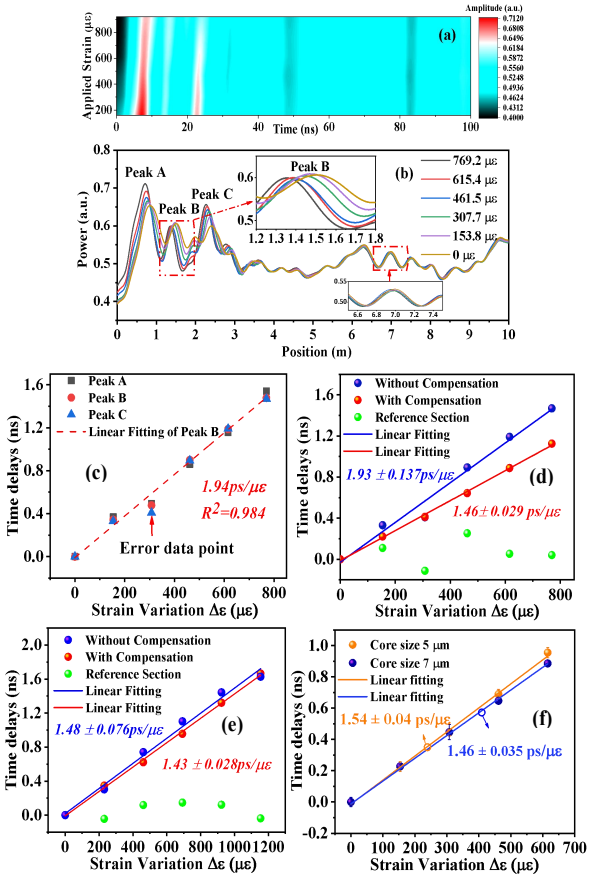

Fig. 5. Experimental results. (a) 2D strain-spatial map of Brillouin traces intensity; (b) Time domain Brillouin traces with different strain (64 time averaging). And its demodulation results. (c) Time delays between two traces under different applied strain for three time windows peak A, Peak B and Peak C; Applied strain induced time delays measurement with and without compensation when applied strain variation is (d) 230 με and (e) 154 με; (f) Relationship between applied strain and time delays in different core diameters section.

To investigate the capacity of dynamic measurement, a trigonal strain variation with frequency of 10 Hz and amplitude of 120 με is applied on the 1m segment of the fiber near the end of the fiber. One end of the section under test is fixed, while another end is fixed on the precise PZT stage (P-6113S, PI). During one variation period, 1000 measurements are achieved and the strain variation with standard deviation ±8.52 με could be monitored as shown in Fig.6 (a). Here the acquisition rate of 10 kHz is set, limited by the fiber length and memory size of OSC. Ultimately, the time delays resolution evaluation is conducted without the applied strain variation. The time delays measurement errors here are mainly attributed to environmental disturbance induced polarization noise and also electrical noises from electrical devices. In Fig.6 (b), the standard deviation of time delays fluctuation is calculated to represent the sensing resolution. Also, the equivalent minimum measurable BFS is computed, as shown in the right y axis of Fig.6 (b). It clearly shows that the time delays resolution highly depends on the times of averaging, and is finally limited by the minimum time interval of OSC which is 25ps corresponding to the sampling rate of 40 GSa/s with 100 times of averaging. The minimum detectable BFS change is about 0.42 MHz (equivalent several micro strain resolution). Therefore, the proposed system is a good candidate for fine dynamic strain measurement. One thing needs to highlight is that this BFS resolution is also decided by the chirping rate of the chirped pulse. In addition, the highest acquisition rate of the system is limited by the times of averaging and the length of the fiber.

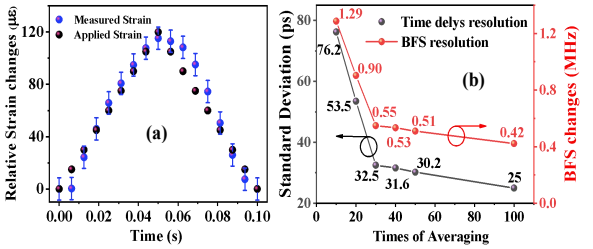

Fig. 6. (a) Dynamic strain measurement with frequency of 10 Hz (50 times averaging). (b) Standard deviation of time delays and BFS changes with different times of averaging.

In summary, a real time distributed strain sensor based on chirped pulse BOTDA with non-uniform fiber is experimentally demonstrated. In the demodulation process, the laser frequency drift compensation method is introduced to improve the sensing accuracy. It is believed that the proposed system in this letter is applicable to structural health monitoring, especially for distributed high frequency dynamic strain sensing.

Funding. China Scholarship Council (201808330421); Canada Research Chairs(950231352); Natural Sciences and Engineering Research Council of Canada (RGPIN/06302-2020, STPGP 506628).

Disclosures. The authors declare no conflicts of interest.

Data Availability. Data underlying the results presented in this paper are not publicly available at this time but may be obtained from the author upon reasonable request.

References

1. Y. Dong, Photonic Sens. 11, 69 - 90 (2021).
2. H. Zhang, D. Zhou, B. Wang, C. Pang, P. Xu, T. Jiang, D. Ba, H. Li, and Y. Dong, Appl. Sci. 8, 1820 (2018).
3. X. Bao and L. Chen, Sensors 11, 36 (2011).
4. D. Zhou, Y. Dong, B. Wang, C. Pang, D. Ba, H. Zhang, Z. Lu, H. Li, and X. Bao, Light Sci. Appl. 7(1), 32 (2018).
5. X. Y. Wang, Z. N. Wang, S. Wang, N. T. Xue, W. Sun, L. Zhang, B. Zhang, and Y. J. Rao, in 6th Proc. European Workshops on Optical Fibre Sensors (EWOFS) (SPIE), paper 99162S (2016).
6. W.Li. X. Bao, Y. Li, and L. Chen, Opt. Express, 16, 21616–21625 (2008).
7. A. Voskoboinik, O. F. Yilmaz, A. W. Willner, and M. Tur, Opt. Express 19, B842 (2011).
8. Y. Peled, A. Motil, L. Yaron, and M. Tur, Opt. Express 19, 19845 (2011).
9. J. Pastor-Graells, H. F. Martins, A. García-Ruiz, S. Martín-López, and M. González-Herráez, Opt. Express 24, 13121 (2016).
10. Y. Wang, P. Lu, S. Mihailov, L. Chen, and X. Bao, Opt. Lett. 45, 6110 (2020).
11. Y. Wang, P. Lu, S. Mihailov, L. Chen, and X. Bao, Opt. Lett. 45, 3423 (2020).
12. C. Kito, H. Takahashi, K. Toge, and T. Manabe, J. Lightwave Technol. 35, 1738 (2017).
13. T. Horiguchi and M. Tateda, J. Lightwave Technol. 7(8), 1170 -1176 (1989).
14. S. Gao, L. Zhang, Y. Xu, L. Chen, and X. Bao, IEEE Photon. Technol. Lett. 29, 1352 (2017).
15. Y. Wang, P. Lu, S. Mihailov, L. Chen, and X. Bao, Opt. Lett. 46(4), 789 -792 (2021).

8.4 Simultaneous distributed temperature/strain sensing

1. Introduction

In the traditional BOTDA system, the frequency sweeping process takes usually several seconds to several minutes, which lowers the acquisition rate of the system, leading to a limited measurable frequency range of dynamic strain. Recently, many ultra-fast BOTDA systems have been studied to save the sweeping time for high frequency dynamic strain measurement, such as optical frequency comb (OFC) scheme [1], slope-assisted scheme [2], and fast-frequency sweeping scheme [3]. However, these proposed schemes have disadvantage on low spatial resolution, small measurement range and complicated post-data process. In [4], the frequency-sweep pulse is used to achieve fast dynamic measurement in a 10 km fiber by converting the temperature or strain-induced Brillouin frequency shift into local time delays . However, the entire distribution acquisition rate is limited by the number of measurement points along a fiber, due to it needs repeated pulse launching until the whole completed distribution is obtained.

However, most of there proposed methods could only used for one parameter measurement. In this paper, a real time and simultaneous temperature and strain sensing system is proposed by combining the chirped pulse Brillouin optical time-domain analysis (CP-BOTDA) technique and chirped pulse φ-OTDR technique. The proposed system is an good candidate for dynamic sensing and the acquisition rate is only limited by fiber length and averaging time. In the proof-of-principle experiment, 4.5m spatial resolution with strain uncertainty of 4.3 με and temperature uncertainty of 0.32℃ is achieved in a 5 km non-uniform fiber.

2. Experiment setup and principle

In Fig.1, a frequency chirped pulse ($\upsilon_p=\upsilon_0+(\Delta\upsilon/W)*T$) with pulse width of W=40ns and frequency chirping range of $\Delta\upsilon$=575MHz is utilized as pump signal, and another single frequency Stokes lights (υ_s) is counter-propagating along the fiber. When the frequency deviation range between chirped pump pulses and probe signals covers the local Brillouin gain spectrum (BGS), the amplified Stokes lights could be calculated the integral of the amplified Stokes light within the effective width corresponding to the local Brillouin gain spectrum convoluted with chirped pulse spectrum. And the power of Stokes light $P_{cw}(t)$ at given time t could be expressed as:

$$P_{cw}(t) \propto P_{dc} + P_p(0,\upsilon_p)\cdot\exp(-\alpha_p\cdot tC/2)\cdot P_{dc}\cdot\frac{Cg_p}{2A}\int_{t-2Z_{eff}/C}^{t-(2Z_{eff}/C-W\cdot\frac{\Delta\upsilon_B}{\Delta\upsilon})}\frac{(\Delta\upsilon_B/2)^2}{(\upsilon_0+\frac{\Delta\upsilon}{W}t-\upsilon_s-\upsilon_B)^2+(\Delta\upsilon_B/2)^2}dt \quad (1)$$

where υ_B is the local Brillouin frequency shift of the fiber, g_p is the peak value of the Brillouin gain coefficient occurring at υ_p-υ_s=υ_B, and $\Delta\upsilon_B$ is the Brillouin gain bandwidth. P_{dc}=$P_{cw}(L)$exp(-$\alpha_{cw}L$) representing CW Stokes light that arrives at Z = 0 without interacting with the pulse and $P_p(0,\upsilon_p)$ is the power of pump pulse with frequency of υ_p at time t=0. C is the speed of the lights in the fiber. α_p is the attenuation coefficient for a chirped pulse and A is the effective cross section of the fiber. Z_{eff} represents the distance between the input end and the front end of the interaction range.

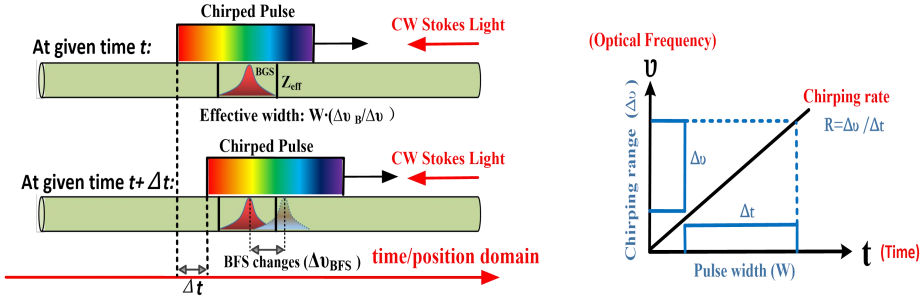

Fig.1 Principle of Chirped pulse BOTDA.

For two measurements with and without strain/temperature applied, the same interested fiber section (within in effect width) is corresponding to different parts of the chirped pulse, since a BGS shift is introduced by local strain variation. The different parts of a chirped pulse (covers BGS range) have different arrival time, t_0 and $t_0+\Delta t$, thus the strain variation induced-BGS shifts is translated into local time delays when a frequency chirped pulse is used. The value of the time delays is determined by the chirping rate of the pulse and the local BFS changes as shown in right figure in Fig.1. Since the local BFS changes are measured from the local time delays within a selected time window from Brillouin traces, the intensity of the Brillouin signal within selected time window includes convolution of the chirped spectrum and Brillouin spectrum, and we measure the delay pulse envelope, which has little sensitivity to the polarization matching required pump and probe signal for maximum Brillouin gain, and thus the time delays measurement is immune to the polarization fading problems. On the other hand, the principle of chirped pulse φ-OTDR by using Rayleigh traces for temperature/strain measurement could be found in references [5].

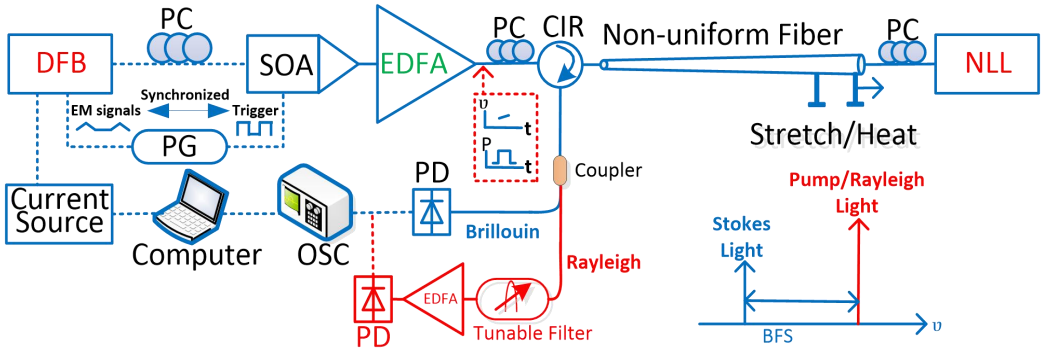

Fig.2 The proposed hybrid system for simultaneous temperature and dynamic strain measurement

The setup of our proposed system is shown in Fig.1. A DFB laser diode (CQF938/500, JDS Uniphase) is driven by an linearly modulated current source to generated a frequency chirped output optical signal, which is further reshaped by the semiconductor optical amplifier (SOA) into a rectangular chirped optical pulse signal. After being boosted by Erbium doped fiber amplifier (EDFA), the chirped pulse signal (pump) is launched into a non-uniform fiber, while probe lights operated at Stokes frequency is sent into the fiber from another end. The reflected optical signal includes amplified Stokes lights from SBS effect and Rayleigh signals from Rayleigh scattering, which are accompanied with frequency deviation about 10 GHz, determined by the local Brillouin frequency shifts. Due to the intense amplified Stokes lights in the mixed signals, Rayleigh signal should be filtered out by a optical tunable band-pass filter before sending it to EDFA to avoid the gain competition. After that, the amplified Stokes lights, namely Brillouin traces, and Rayleigh traces could be detected by photodetector and then displayed on the Oscillatorscope (OSC).

3. Demodulation method and experimental results

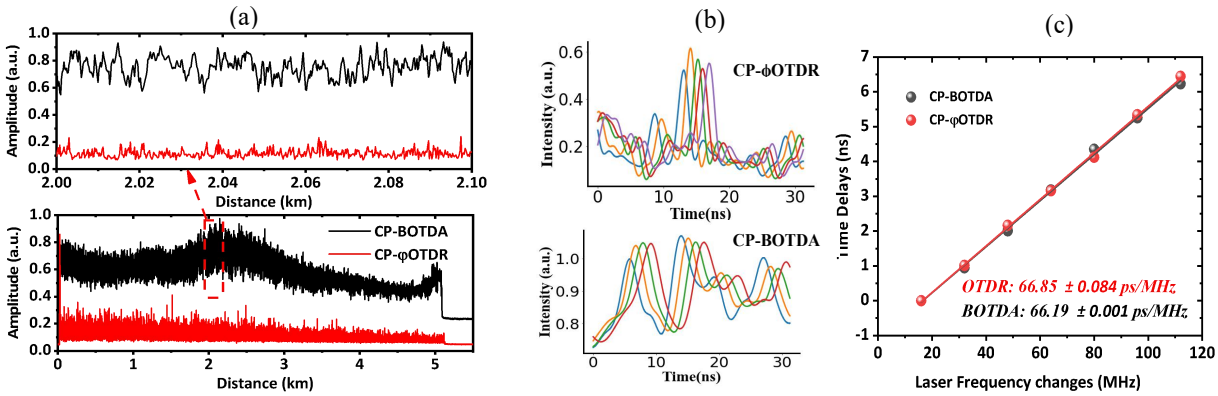

Fig. 3. (a) Time domain traces from stimulated Brillouin scattering (SBS) effect and Rayleigh scattering effect; (b) Time shifts of Brillouin traces and Rayleigh traces when the frequency deviation between pump and probe lights is changed with step of 16 MHz (blue traces is corresponding to frequency deviation of 10 GHz); (c) Relationship between relative frequency deviation changes and time delays.

The time domain Brillouin and Rayleigh traces are shown in Fig.3 (a). The high accuracy time delay measurement requires that the Brillouin traces have steep peaks in the intensity variation profile, which allows small change in BFS changes being measured due to small temperature or strain change. Based on Fig.3, a non-uniform fiber with steep peaks could give various sharp fluctuations, which is a good candidate for small strain or temperature measurement. The simulation results between time delays in Brillouin traces/Rayleigh traces and frequency deviation changes are shown in Fig.3 (b). It clearly shows that the time domain traces experience longitudinal temporal shifts when the frequency deviation between pump and probe is changing by tuning the initial frequency v_0 of the chirped pulse. The relationship between time delays and frequency deviation changes in Brillouin traces and Rayleigh traces are plotted in Fig.3 (c), and they have almost the same coefficient since it is only determined by the chirping rate of the chirped pulse signal.

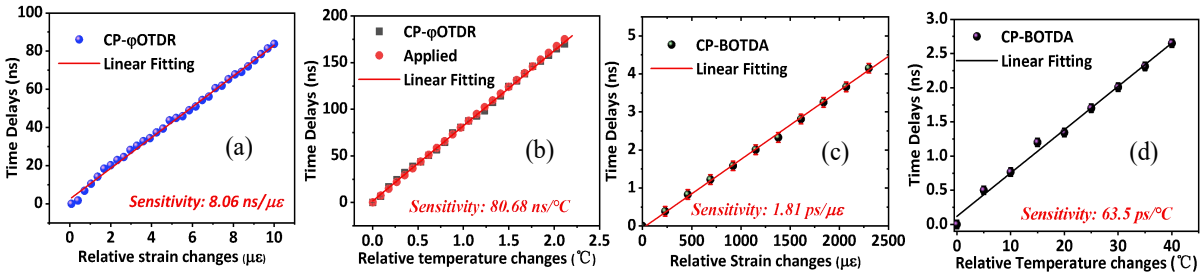

Fig. 4 Time delays-strain coefficient (a) (c) and time delays-temperature coefficient (b) (d) in CP-φOTDR and CP-BOTDA respectively.

In order to obtained the time delays related temperature and strain coefficient for dynamic distributed temperature and strain measurement , static strain and temperature measurement with acquisition rate of 10 kHz is carried out at the end of the fiber. Four different coefficients are obtained as shown in Fig.4. The temperature and strain could be then demodulated separately by linear equation with two unknowns as following:

$$\begin{bmatrix}\Delta t_{CP-\varphi OTDR}\\ \Delta t_{CP-BOTDA}\end{bmatrix}=\begin{bmatrix}C_{\varepsilon-OTDR} & C_{T-OTDR}\\ C_{\varepsilon-BOTDA} & C_{T-BOTDA}\end{bmatrix}\begin{bmatrix}\Delta\varepsilon\\ \Delta T\end{bmatrix} \quad (2)$$

where $C_{\varepsilon\text{-}OTDR}$ and $C_{T\text{-}OTDR}$ are respectively the strain-time delays coefficient (Fig.4 (a)) and temperature-time delays coefficient (Fig.4 (b)) on the Rayleigh traces. $C_{\varepsilon\text{-}BOTDA}$ and $C_{T\text{-}BOTDA}$ are the strain-time delays coefficient (Fig.4 (c)) and temperature-time delays coefficient (Fig.4 (d)) on the Brillouin traces, respectively. Then the measurement uncertainties of the temperature and strain are respectively

$$\delta T=\frac{\sqrt{(C_{\varepsilon-OTDR}\cdot\delta t_{CP-BOTDA})^2+(C_{\varepsilon-BOTDA}\cdot\delta t_{CP-\varphi OTDR})^2}}{|C_{\varepsilon-OTDR}C_{T-BOTDA}-C_{\varepsilon-BOTDA}C_{T-OTDR}|}=0.32℃ \quad \text{and} \quad \delta\varepsilon=\frac{\sqrt{(C_{T-OTDR}\cdot\delta t_{CP-BOTDA})^2+(C_{T-BOTDA}\cdot\delta t_{CP-\varphi OTDR})^2}}{|C_{\varepsilon-OTDR}C_{T-BOTDA}-C_{\varepsilon-BOTDA}C_{T-OTDR}|}=4.3\ \mu\varepsilon.$$

Note that large difference between strain and temperature coefficient in Brillouin and Rayleigh signals would give a much smaller measurement uncertainties.

3. Conclusion

The distributed temperature and strain measurement could be achieved simultaneously in our proposed system, providing a method to solve cross sensitive problems with high accuracy. This proposed system with compact configuration and simple data processing could become an good tool for distributed temperature/ strain sensing.

4. References

[1] A. Voskoboinik, O. F. Yilmaz, A. W. Willner, and M. Tur, Opt. Express 19, "Sweep-free distributed Brillouin time-domain analyzer (SF-BOTDA), B842 (2011).

[2] Y. Peled, A. Motil, L. Yaron, and M. Tur, " Slope-assisted fast distributed sensing in optical fibers with arbitrary Brillouin profile, Opt. Express 19,19845 (2011).

[3] D. Zhou, Y. Dong, B. Wang, C. Pang, D. Ba, H. Zhang, Z. Lu, H. Li, and X. Bao, "Single-shot BOTDA based on an optical chirp chain probe wave for distributed ultrafast measurement", Light Sci. Appl. 7(1), 32 (2018).

[4] C. Kito, H. Takahashi, K. Toge, and T. Manabe, "Dynamic strain measurement of 10-km fiber with frequency-swept pulsed BOTDA"J. Lightwave Technol. 35, 1738 (2017).

[5] Y. Wang, P. Lu, S. Mihailov, L. Chen, and X. Bao, "Distributed time delay sensing in a random fiber grating array based on chirped pulse Φ-OTDR, Opt. Lett. 45, 3423 (2020).

Chapter 9

Fast and high spatial resolution distributed temperature and strain sensor based on birefringence measurement in PM fiber via Brillouin dynamic grating

9.1 Introduction

The permanent refractive index changes in the fiber core could be achieved by many fabrication methods, and gives a strong backward reflection when the wavelength of the incident beam satisfies the Bragg conditions. Recently, an all-optical way to generate Brillouin dynamic grating (BDG) in PM fiber has attracted extensive attention in recent years [10] [11]. The refractive index of the PM fiber core will be altered temporarily due to the acoustic wave during the SBS effect when two optical waves are counter-propagating along the same axis of the PM fiber with a frequency deviation of Brillouin frequency shift. The strong interaction between two waves generates the acoustic wave through electrostriction.

Since the first proof-of-concept experiment on all optical dynamic grating by SBS [10] where the reflectance of 4% was obtained by the acoustic waves in a 30 m panda-type PM fiber, the BDG has been intensively studied, including the theoretical model analysis [199] [200] and the demonstration of BDG operation in a different medium: single mode fiber [201] [202], elliptical-core two-mode fibers [203], few-mode fiber [204] and dispersion-shifted fiber [205]. In addition, there has been considerable attention to the applications of the BDG for distributed sensing since the temperature/strain-induced BDG spectrum sensitivity is much larger than that in the Brillouin gain spectrum [206]. In theory, the BDG reflection could be described by the interaction among the four waves, and the intensity of the idler (readout) signal is related to the frequency offset of the pump and probe signal based on the FWM phase-matching condition. And the frequency offset is determined by the effective refractive index difference between two axes, which could measure the birefringence of the PM fiber [207] [208]. The first strain/temperature-induced birefringence variations measurement based on the BDG spectrum recovery is demonstrated in [209]. More importantly, Brillouin frequency shift and the birefringence change have the same signs as the strain-dependence, but opposite signs for temperature-dependence, which could be used for discriminating the

temperature and strain variations with high accuracy [210] [211] [212]. Different from the spatial resolution limited by 1 m owing to the finite phonon lifetime in conventional Brillouin scattering-based sensors, the spatial resolution using BDG spectrum recovery sensing mechanism was soon identified as physically limited only by the motion of the acoustic wave that is much lesser than a millimetre. FWM-enhanced SBS can improve the sensitivity of the Brillouin spectrum peak changes induced by the fiber birefringence variation, which is different from pump-probe approach in BOTDA technique where the Brillouin spectrum is measured by SBS amplification. Phase matching of FWM-SBS measures upper and down-conversion of the SBS spectrum. The time constant is phase matching of FWM-SBS, which has a much smaller dependence on phonon lifetime. This special feature opened a new feasibility for the fast and dynamic measurement of distributed BDG sensing. Thus it could be used to achieve high-spatial-resolution distributed sensing up to centre-meters range or even less [11] [213] [214].

However, there is not much work studying the fast demodulation method for BDG spectrum shift measurement to extend BDG-based sensing to the dynamic regime. One method [215] is demonstrated based on a slope-assisted technique to convert the BDG spectrum shift to the optical power measurement, leading to a dynamic strain measurement with vibration frequency up to kHz. But, in this work, only the vibration frequency is obtained without the strain amplitude demodulation. In this chapter, we have proposed a novel BDG-based sensing system, i.e., chirped pulse BDG-OTDR, for the first time to the best of our knowledge. It enables the measurement of the dynamic strain value and vibration frequency to achieve simultaneously. In contrast to the conventional method of precisely tuning the frequency difference between pump and probe in the orthogonal axis, our method with direct measurement of birefringence variation introduced by external perturbations based on local time delays saves the spectrum scanning required interrogation time so that the acquisition rate is significantly improved. As a result, 1 Hz dynamic strain with peak-to-peak amplitude of 2 $\mu\varepsilon$

is reconstructed in both frequency and amplitude accurately. It is noted that the highest measurable vibration frequency is only limited by the fiber length and average time. On the other hand, a high spatial resolution of 10 cm is achieved by sending a 40ns pulse with a frequency chirping rate of 93.5 MHz/ns. The improved spatial resolution is enabled by the phase matching of FWM-related birefringence change between fiber sections, so that small time window (new spatial resolution) can be used to calculate the cross-correlation to extract the shifts of FWM-SBS spectrum in PMF since PMF has beat length of mm-to-cm.

9.2 Theoretical analysis

The principle of BDG generation and detection involve four waves interacting through material density variations among two axes in PM fiber is shown in Figure 9.1 (a). The BDG is generated by injecting two optical waves (CW pump v_p and CW Stokes v_S) into the slow axis of PM fiber from two ends. Once the frequency difference between the pump and Stokes wave is carefully tuned to match the Brillouin frequency shift of that axis, the BDG (acoustic field) will be well excited through the SBS effect. The propagation direction of the BDG is the same as the pump wave. To detect the BDG, a probe wave is sent to the PM fiber from the same end as the pump signal but on a different axis (fast-axis). Due to the strict phase-matching condition requirements, the frequency separation between the probe wave and pump wave needs to be carefully selected to generate the idler wave (v_i). The diffracted idler wave has a lower frequency compared with the probe wave with a difference of BFS due to the Doppler effect. It propagates along the same direction as the Stoke wave but in the fast-axis, which is ready for distributed birefringence measurement. It is crucial to mention that although pump and probe pulses propagate in the same direction, their group velocity is different due to the different refractive indexes in the fast and slow axis of PMF,

which leads to a severe walk-off over long PMF. For example, the time delay between two pulses launched into the orthogonal axis of a 10km-long PMF with birefringence of 6×10^4 is about 20 ns [208]. To avoid this problem, the pump wave is CW in our experiments. The frequency deviation of the four-wave and its propagation axis are shown in Figure 9.1 (c).

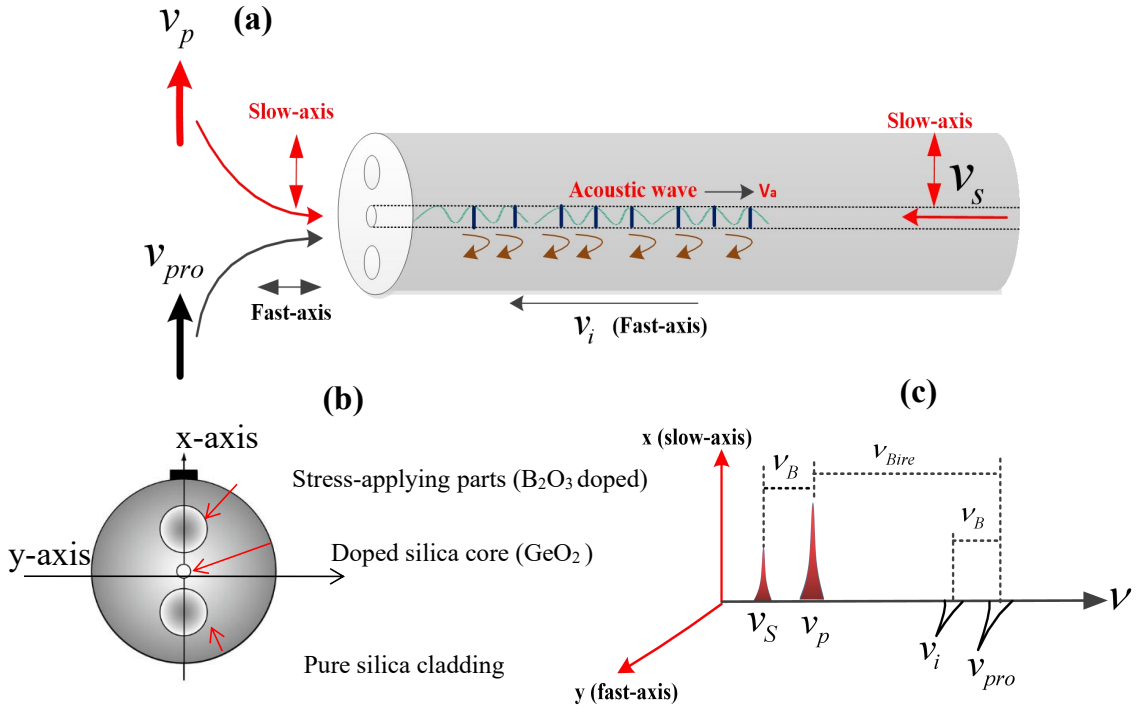

Figure 9.1: (a) Principle of distributed Brillouin dynamic grating detection in PM fiber; (b) Illustration of birefringence property in PM fiber; (c) frequency of different optical waves in BDG detection. v_p: pump wave; v_{pro}: probe wave; v_i: idler wave; v_S: Stokes wave; v_B: Brillouin frequency shift; v_{Bire}: birefringence-induced frequency separation and V_a: velocity of acoustic wave.

The interaction between the four waves inside the PM fiber could be regarded as the four-wave mixing (FWM) process. When the frequency difference between the pump and Stokes wave is locked at the Brillouin frequency of the slow-axis, this FWM process could be described by the four coupled equations under a steady state with

slowly varying envelope approximation, which is given by [200]:

$$\begin{aligned}
\frac{\partial A_p}{\partial z} &= -\eta \left[A_p \left| A_S \right|^2 + A_S A_{\text{pro}} A_i^* \exp(i\Delta k z) \right], \\
\frac{\partial A_S}{\partial z} &= -\eta \left[A_S \left| A_p \right|^2 + A_p A_i A_{\text{pro}}^* \exp(-i\Delta k z) \right], \\
\frac{\partial A_{\text{pro}}}{\partial z} &= -\eta \left[A_{\text{pro}} \left| A_i \right|^2 + A_p A_i A_S^* \exp(-i\Delta k z) \right], \\
\frac{\partial A_i}{\partial z} &= -\eta \left[A_i \left| A_{\text{pro}} \right|^2 + A_S A_{\text{pro}} A_p^* \exp(i\Delta k z) \right],
\end{aligned} \tag{9.1}$$

where the coupling constant is

$$\eta = \frac{8\pi^3 \gamma_e^2}{\rho_0 c \lambda_p^3 \Omega_B \Gamma_B A_{\text{eff}}^{\text{a}}}, \tag{9.2}$$

with the acousto-optic effective area of

$$A_{\text{eff}}^{\text{ao}} = \left[\frac{\langle F^2(x,y) \rangle}{\langle F^2(x,y) F_A(x,y) \rangle} \right] \left\langle F_A^2(x,y) \right\rangle, \tag{9.3}$$

where $F(x,y)$ is the dimensionless fundamental mode profile for the four interacting waves, $F_A(x,y)$ is the dimensionless mode profile of the acoustic wave, and angular brackets denote averaging over the transverse cross-section of the fiber, A_P, A_i, A_S and A_{pro} are the slowly varying fields; Δk is the phase mismatch related to the frequency difference between pump and probe wave, as well as birefringence of the fiber, γ_e is the electrostrictive constant, ρ_0 is the average density; c is the velocity of light in vacuum; λ_p is the operation wavelength of the pump wave; Γ_B is the Brillouin linewidth.

9.2.1 Birefringence-related frequency deviation between pump and probe

Birefringence, as a crucial property of polarization maintaining fiber, is introduced by the difference in thermal contraction between B_2O_3-doped silica and pure silica, as shown in Figure 9.1 (b). The two-dimensional stress is raised and stored in the core during the drawing process in fiber fabrication. And the residual stress makes the refractive index of two axes different: x-axis (n_x) >y-axis (n_y). The Birefringence

value is defined by the refractive index difference between two axes (i.e., birefringence $B = \Delta n = n_x - n_y$). This value in PM fiber is very small, about $B = \ 7.4 \times 10^{-4}$, but large enough to ensure less coupling between two orthogonal modes so that the linearly-polarized lightwaves along either x- or y-axis could maintain their polarization states.

The stimulated acoustic wave generated in the slow axis gives a spatially varied refractive index, which is common to both polarization in two axes. However, the birefringence converts this common spatial frequency to a different optical frequency for two axes (v_p and v_{pro}). The SBS effect in the slow axis between pump (v_p) and Stokes wave (v_S) will reach the maximum efficiency when the conservation of the energy and momentum are satisfied [206]:

$$\begin{aligned} v_B &= v_p - v_S, \\ \frac{v_B}{V_a} &= \frac{n_x\left(v_p\right) \cdot v_p}{c} + \frac{n_x\left(v_S\right) \cdot v_s}{c}, \end{aligned} \tag{9.4}$$

where $n_x(v_p)$ is the effective refractive index in the x-axis at v_p frequency and the phase-matching condition for the maximum reflectance from the BDG is obtained by the simultaneous conservation of the momentum for both slow (x)- and fast(y)-axis waves, which is described as follows:

$$\begin{aligned} \frac{v_B}{V_a} &= \frac{n_x\left(v_p\right) \cdot v_p}{c} + \frac{n_x\left(v_p - v_B\right) \cdot \left(v_p - v_B\right)}{c} \\ &= \frac{n_y\left(v_p + v_{\text{Bire}}\right) \cdot \left(v_p + v_{\text{Bire}}\right)}{c} + \frac{n_y\left(v_p + v_{\text{Bire}} - v_B\right) \cdot \left(v_p + v_{\text{Bire}} - v_B\right)}{c}, \end{aligned} \tag{9.5}$$

by applying the Taylor expansion to n_x and n_y around v_p and simplification, we could obtain:

$$2\left(n_x\left(v_p\right) - n_y\left(v_p\right)\right) \cdot v_p - \left(n_{gx} - n_{gy}\right) \cdot v_B = 2 n_{gy} v_{\text{Bire}}, \tag{9.6}$$

where n_{gx} and n_{gy} are the group refractive index in two axes. Since v_p is much larger than Brillouin frequency, the term with v_B could be ignored, leading to:

$$v_{\text{Bire}} = \frac{\Delta n \cdot v_p}{n_{gy}}. \tag{9.7}$$

9.2.2 Birefringence sensitivities to Temperature/strain

In a high-birefringence fiber, such as Panda-type PMF as shown in Figure 9.1 (b), the birefringence scale is determined by the residual tensile stress (σ_{xy}) with the ambient temperature (T_a):

$$B \propto \sigma_{xy} = k \cdot (\alpha_3 - \alpha_2) \cdot (T_{fic} - T_i)\,, \tag{9.8}$$

where T_{fic} denotes the fictive temperature (e.g., 850 °C of silica glass, $\alpha_3(\alpha_2)$ is the thermal coefficient of stress-applying parts (pure-silica cladding), and k is a constant determined by the geometrical location of stress-applying parts in the fiber. When temperature increases (ΔT >0), the residual stress is released and thus, the birefringence decreases. Thus, the temperature changes will introduce a birefringence change (ΔB_T), given by:

$$\Delta B_T = -B_0 \cdot \frac{\Delta T}{T_{fic} - 25}, \tag{9.9}$$

where B_0 is the birefringence value of the PM fiber at 25 °C. So, the birefringence sensitivity to temperature could be expressed by:

$$C_B^T = \frac{\Delta B_T}{\Delta T} = \frac{-B_0}{T_{fic} - 25} = -8.97 \times 10^{-7}/°\mathrm{C}, \tag{9.10}$$

where $B_0 = 7.4 \times 10^4$. According to the Equation (9.7), the frequency offset sensitivities to temperature is about 118.6 MHz/°C when n_{gy}=1.46 and v_P is around 193 THz (λ=1550 nm).

In contrast, when an axial strain variation, $\Delta\varepsilon$, is applied upon the fiber, additional stress is generated because the stress applying parts and the cladding contract in the lateral direction differently due to their different Poisson's ratios (γ_3 >γ_2). The strain variation induced birefringence change could be expressed by:

$$\Delta B_\varepsilon = +B_0 \cdot \frac{(\gamma_3 - \gamma_2) \cdot \Delta\varepsilon}{(\alpha_3 - \alpha_2)\,(T_{fic} - 25)}, \tag{9.11}$$

thus the birefringence sensitivity to strain is given by:

$$C_B^\varepsilon = \frac{\Delta B_\varepsilon}{\Delta\varepsilon} = +B_0 \cdot \frac{(\gamma_3 - \gamma_2)}{(\alpha_3 - \alpha_2)\,(T_{fic} - 25)} = 8.99 \times 10^{-9}/\mu\varepsilon, \tag{9.12}$$

where $\frac{(\gamma_3-\gamma_2)}{(\alpha_3-\alpha_2)(T_{fic}-25)} = 12.2 \times 10^{-6}/\mu\varepsilon$. And the frequency offset sensitivities to strain is about 1.13 MHz/ $\mu\varepsilon$ when the v_{Bire}=92.8 GHz in our PM fiber.

9.2.3 Birefringence variation induced time delay measurement analysis

The principle of time delay measurement in PM fiber for temperature/strain sensing is illustrated in Figure 9.2. Assume the probe signal for BDG detection in the y-axis has a linearly chirped frequency profile with an instantaneous frequency of

$$\begin{aligned} v_{\text{probe}} &= v_0 + R \cdot t, \\ R &= (\Delta v_c / W), \end{aligned} \tag{9.13}$$

where v_0 is the initial optical frequency and R is the frequency chirping rate. Let's consider the chirped probe pulse position at two different given time, t_0 and $t_0 + \Delta t$, in two independent single-shot measurements, as shown in Figure 9.2.

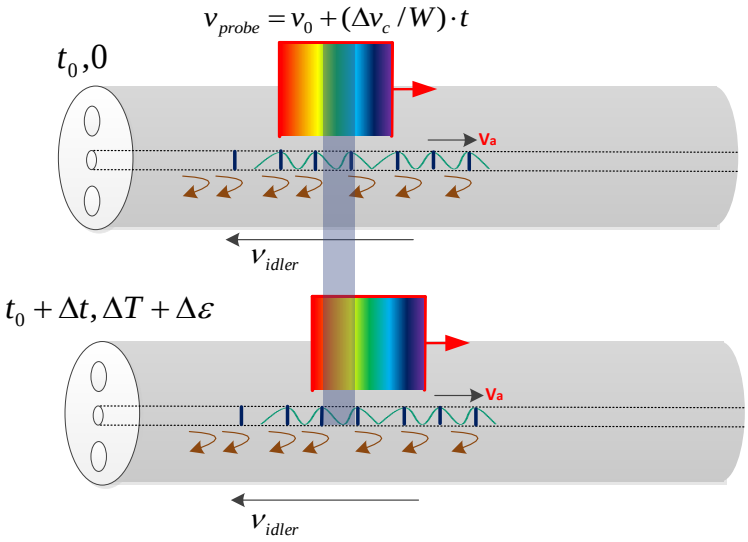

Figure 9.2: Principle of distributed birefringence variation-induced time delays measurement in Brillouin dynamic grating.

At the given time t_0, the frequency components within the blue band are satisfied the local birefringence-induced frequency offset between the pump and probe waves

and are located within the BDG gain spectrum. Thus they will be reflected by the BDG and gives a specific power intensity which is the sum of the interaction between each frequency component and the BDG. If there are temperature or strain variations $(\Delta T + \Delta\varepsilon)$ in the interaction section of the fiber in the subsequent measurement, the frequency offset between pump and probe that is used to satisfy the phase-matching condition will change accordingly and thus make the power intensity at the detection end change. However, if we consider a different given time $t_0 + \Delta t$ in the subsequent measurement with temperature/strain changes, the frequency components covered by the interest section of fiber experience a frequency shift since the optical frequency is linearly varied within the chirped probe pulse. Therefore, The frequency change of each component at a different given time will compensate for the temperature/strain changes-induced frequency offset (v_{Bire}) variation to give an equal power intensity. Here, we assume the power intensity of each frequency component within the chirped pulse is similar. Finally, the temperature/strain-induced birefringence change could be directly measured by the local time delay within the selected time window in two adjacent time domain reflected traces from the BDG. Based on Equation (9.7), Equation (9.13), Equation (9.12) and Equation (9.10), the time delays related temperature and strain coefficient (C_t^{ε} and C_t^{ε}) are given by:

$$\begin{aligned} C_t^{\varepsilon} &= \frac{C_B^{\varepsilon} \cdot v_p}{n_{gy} R} = 1.13/R(ns/\mu\varepsilon), \\ C_t^{T} &= \frac{C_B^{T} \cdot v_p}{n_{gy} R} = -118.6/R(ns/^{\circ}\text{C}). \end{aligned} \tag{9.14}$$

9.3 Experimental setup and results

The experimental setup based on Brillouin dynamic gratings-assisted distributed birefringence variations measurement for temperature and strain sensing is shown in Figure 9.3. The chirped pulse generation section is the same as that used in previous experiments, in which the distributed feedback (DFB) laser source is directly modulated by an electrical modulation (EM) signal that is generated by the pulse generator

(PG). Before being amplified by the Erbium-doped optical fiber amplifier (EDFA), the modulated signal from the DFB laser pulse-modulated served as the probe signal. It is noted that only the blue or red frequency shift section will be selected by carefully adjusting the time delays between the EM signals and the trigger signal so that the optical frequency is linearly varied within the pulse duration. After that, a polarization controller (PC), which is connected after an optical circulator, aligns the polarization to the fast-axis before sending the probe pulses to the PMF under test through a polarization beam combiner (PBC).

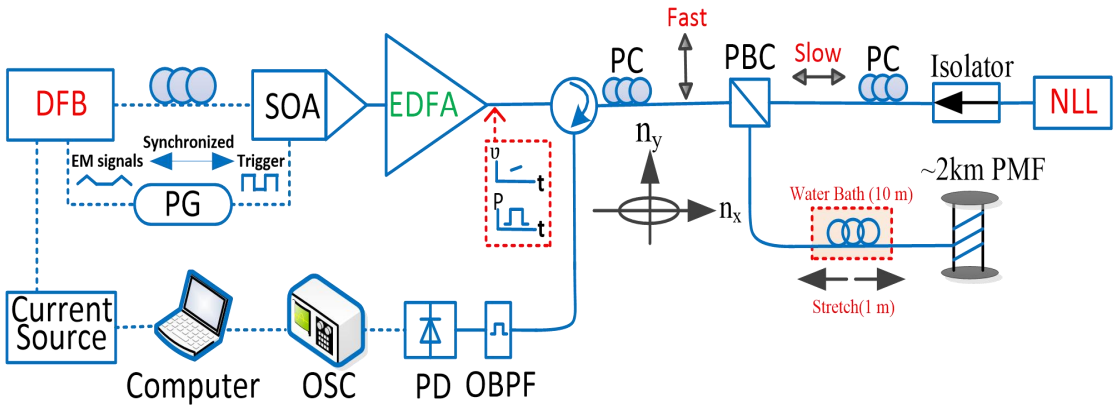

Figure 9.3: Experimental setup for distributed temperature and strain sensing based on BDG detection in PM fiber. DFB laser: distributed feedback laser; SOA: semiconductor optical amplifier; EDFA: Erbium-doped optical fiber amplifier; PC: polarization controller; PBC: polarization beam combiner; NLL: narrow linewidth laser; PG: pulse generator; OBPF: optical band-pass filter; PD: photo-detector; OSC: oscilloscope.

In another branch of the PBC, CW light from a narrow linewidth laser (NLL) source is aligned to the slow-axis polarization and then is sent to the PMF under test, acting as the pump signal to excite the BDG in the slow-axis. For the idler signal (probe signal reflection from the BDG) detection, an optical band-pass filter is used to filter out the other three waves in a fast-polarized backscattered signal, such that only the idler wave is detected at a Photo-detector (PD). Finally, the time domain could be collected by the oscilloscope (OSC), and the drive current of DFB laser is controlled by

the computer to change the initial optical frequency for simulation purposes.

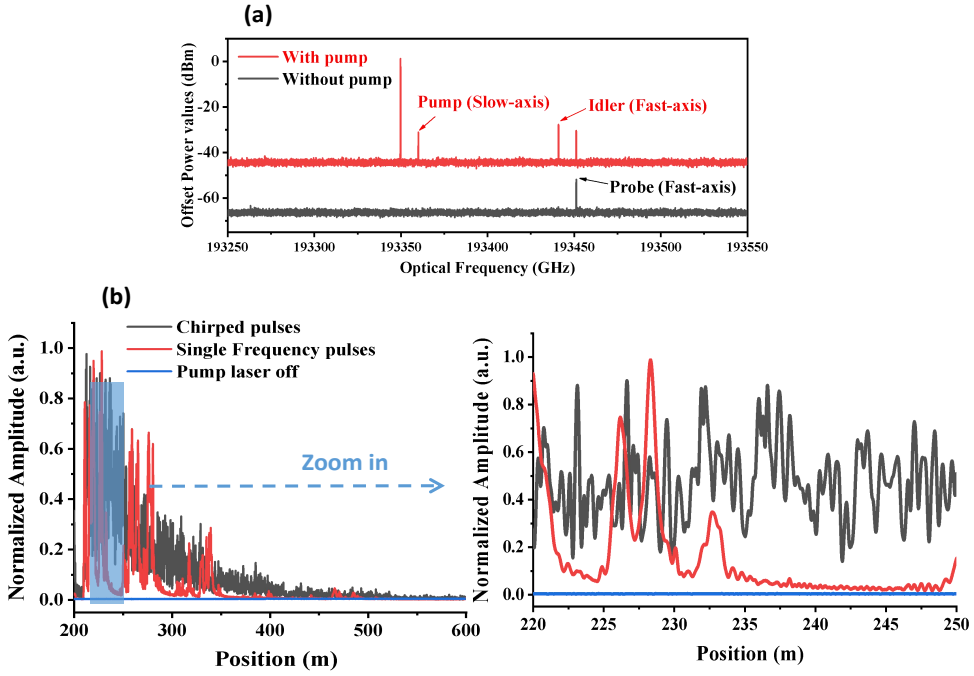

Figure 9.4: The backscattering signal of probe wave from BDG in spectral (a) and time domain (b). (b) also includes the comparison of time domain signal with and without frequency chirping.

The output signal in the fast-axis is firstly measured in the Optical Spectrum Analyzer (OSA) to verify that only the idler signal will be detected at the PD end. As shown in Figure 9.4 (a), the power of the probe signal is set at a low level to avoid the SBS effect so that there is no Stoke light which is supposed to locate at the same frequency with idler signal when the pump light is off. Due to the intense BDG generation, when a strong pump signal is sent to the slow-axis, a reflection signal shows up with v_B frequency apart from the probe signal in the fast axis. The time domain traces from both single frequency pulse and chirped pulse are shown in Figure 9.4 (b). Both traces experience a significant decrease in intensity due to pump depletion. It is noted that the idler signal from single frequency pulses has some intensity fading section in which the power intensity is reduced to zero, as shown in the position range of 240 m-250 m in the "zoom in" inset. The reason is that the continuously changed bire-

fringence along the PM fiber due to the imhomogeneity requires different pump-probe frequency differences to satisfy the local phase-matching conditions. A general solution is to sweep the frequency of the interrogation pulse to get the frequency response at each given position, and the birefringence profile could be spatially resolved by selecting the peak of the local BDG reflection spectrum.

This solution usually takes a long time to reconstruct the birefringence profile, which lowers the sensing speed (system sampling rate) in distributed sensing applications. However, the BDG reflection could be fully spatial obtained by sending a chirped pulse, and the time domain trace is shown in the black curve of the inset without an intensity fading problem. Compared with single-frequency pulse of the same pulse width, the different optical frequency components in chirped pulse are taking much smaller time section among the entire pulse width, which allows precise spectrum scanning in a smaller time window than the pulse width. The linearly chirped pulse frequency can tune the birefringence change associated phase matching condition of FWM accurately in the spatial domain. This is the key to achieving a higher spatial resolution than the optical pulse. In addition, the intensity idler signal shows a time-varied feature, which is attributed to the fast birefringence variation along the fiber due to the imhomogeneity. At different given time t (different pulse locations), each frequency component within the chirped pulse interacts with the corresponding fibre section. Still, only some of them by the phase-matching condition could be reflected by BDG. The reflected frequency components keep changing when the pulse propagation along the fiber because of the local birefringence variations, resulting in a jagged time domain pattern.

9.3.1 Distributed temperature sensing

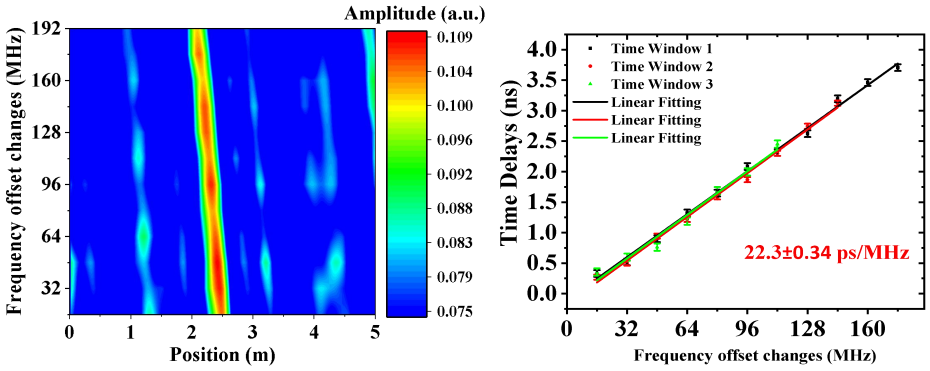

Figure 9.5: Simulation results of changing the pump-probe frequency offset (v_{Bire}) without temperature/strain variations applied.

Before demonstrating the distributed temperature/strain measurement, a simulation is carried out to verify the linear relationship between time delays and pump-probe frequency offset v_{Bire}. As shown in Figure 9.5 (a), the idler traces within 1 m window are collected when the v_{Bire} (frequency offset) is changed around 92.8 GHz with a range of 0-192 MHz by adjusting the frequency of DFB laser. It clearly shows that the idler traces experience a longitudinal time shift from right to left, and the shifting direction depends on the sign of both v_{Bire} and the frequency chirping rate. To obtain the linear relationship between the time delays and the v_{Bire} changes, a time window with 5ns is selected around the intensity peaks from two adjacent idler traces for cross-correlation calculation. The result is shown in Figure 9.5 (b), and the sensitivity of the frequency offset changes-induced time delays is about 22.3 ps/MHz. In our experiments, the pulse width and frequency chirping range are set to 40ns and 1.8 GHz leading to a sensitivity of 22.22 ps/MHz, consistent with the simulation results.

In distributed temperature/strain measurement, the frequency of the DFB laser is adjusted to set the pump-probe frequency v_{Bire} as a proper value around 92.8 GHz, such that the frequency chirping range could cover the birefringence variations along the fiber. As shown in Figure 9.6 (a), the idler signal shows a time-varied profile due

to the fast local birefringence changes and no fading problem. The time domain trace of the idler signal with temperature variations shows a longitudinal shift as shown in Figure 9.6 (b), while the time domain traces maintain unchanged as shown in Figure 9.6 (c).

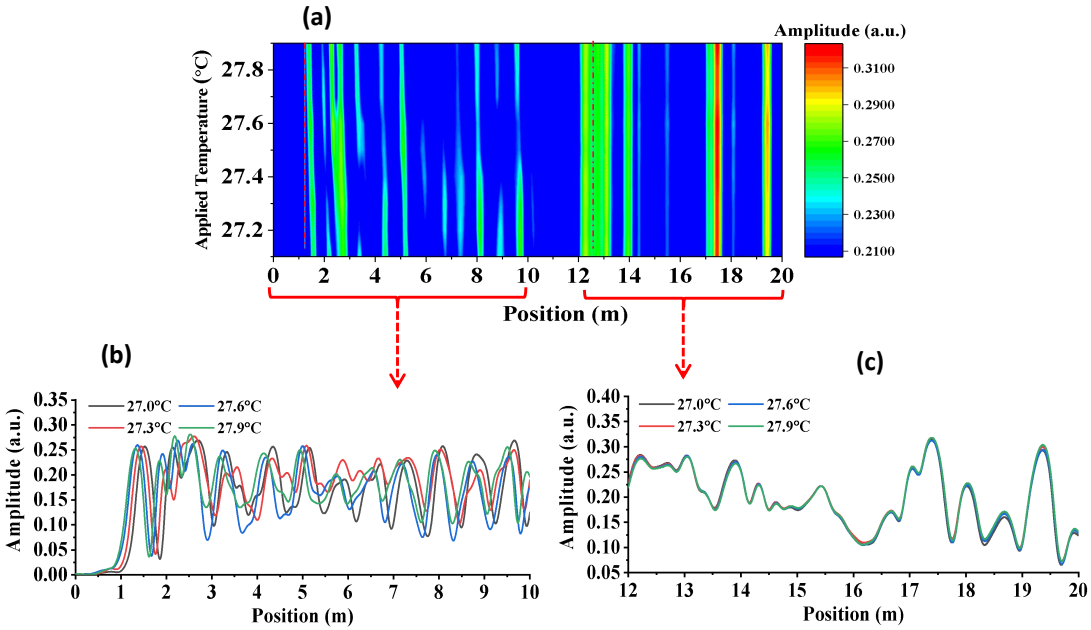

Figure 9.6: 2D intensity map of the time domain idler traces with a temperature change from 27.2-27.8 °C.

The distributed temperature distribution is reconstructed by selecting a time window with 5 ns duration and then calculating the cross-correlation, as shown in Figure 9.7. The fiber section from 2 m to 12 that is put into the water bath experiences a temperature increase from 27 to 27.6 °C, and the temperature variation is resolved by the local time delays (frequency offset changes). And the error band is also added to show the measured temperature uncertainty at each location. The relationship between temperature and time delays at the 2 m locations is also calculated, giving a coefficient of -2.46 ns/°C (-110.3 MHz/°C), which is close to the theoretical value based on Equation (9.10). The error is attributed to the measurement uncertainty and the parameter difference of the PM fiber samples. The uncertainty of the measurement is evaluated

by comparing the measured temperature variations at one location of the fiber when the same temperature variations between each measurement are applied. The standard deviation of temperature uncertainty is about 0.038 °C.

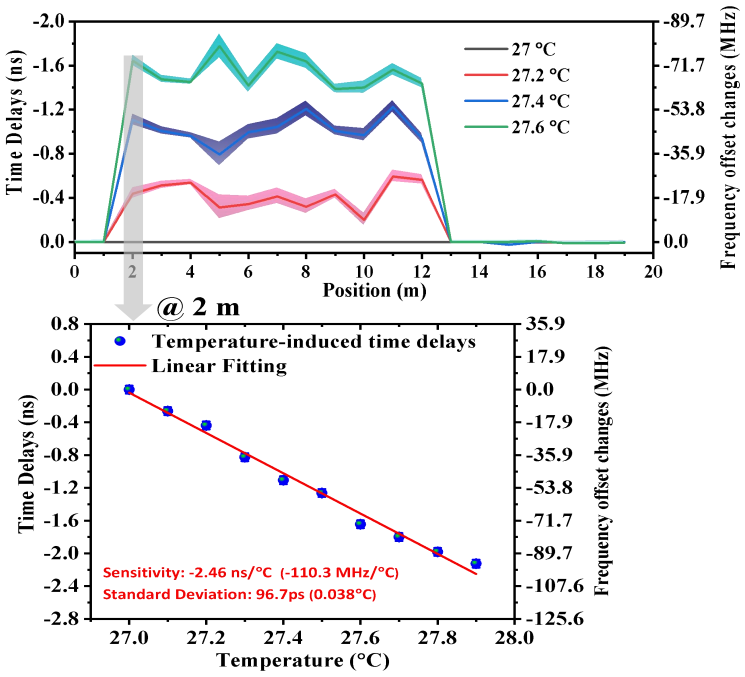

Figure 9.7: Temperature distribution along the fiber and the temperature-induce time delays coefficient at 2 m location.

9.3.2 Distributed strain sensing

The distributed strain sensing is also demonstrated by stretching the 1 m section of the PM fiber. One end of the stretched section is glued on the fixed translation stage, while another end is fixed on the highly precise PZT that could stretch the fiber section both in a static or dynamic manner. Firstly, the static strain measurement is carried out, and the 2D intensity map of idler traces with different static strain applied is shown in the Figure 9.8 (a). A close-up version is given as shown in Figure 9.8 (b), which clearly shows the idler traces experience longitudinal time delays when different static strain variations are applied. Similar to the temperature distribution recovery, a 5 ns time window that corresponds to the 0.5 m fiber length is selected for time delay

determination by cross-correlation calculation. The time window is moved from the beginning to the end, and thus the strain distribution is reconstructed. As shown in Figure 9.8 (c), only the fiber sections centred at 4.5 and 5.0 m show strain variations. In contrast, other location shows a very low strain value which is the time delay measurement uncertainty. The spatial resolution here is about 0.5 m, limited by the width of the selected time windows. Finally, the strain-induce time delays coefficient is also explored as shown in the Figure 9.8 (d), giving a sensitivity of 28.2 ps/$\mu\varepsilon$ (0.852 MHz/$\mu\varepsilon$). It is noted that the frequency chirping rate is increased to 33.1 ps/MHz (1.2 GHz frequency chirping range and 40 ns pulse width) to obtain a larger strain variations-induced time delays coefficient. The difference between the experimental and theoretical coefficient value comes from the in-determination of thermal contraction coefficient α and Poisson's ratios γ.

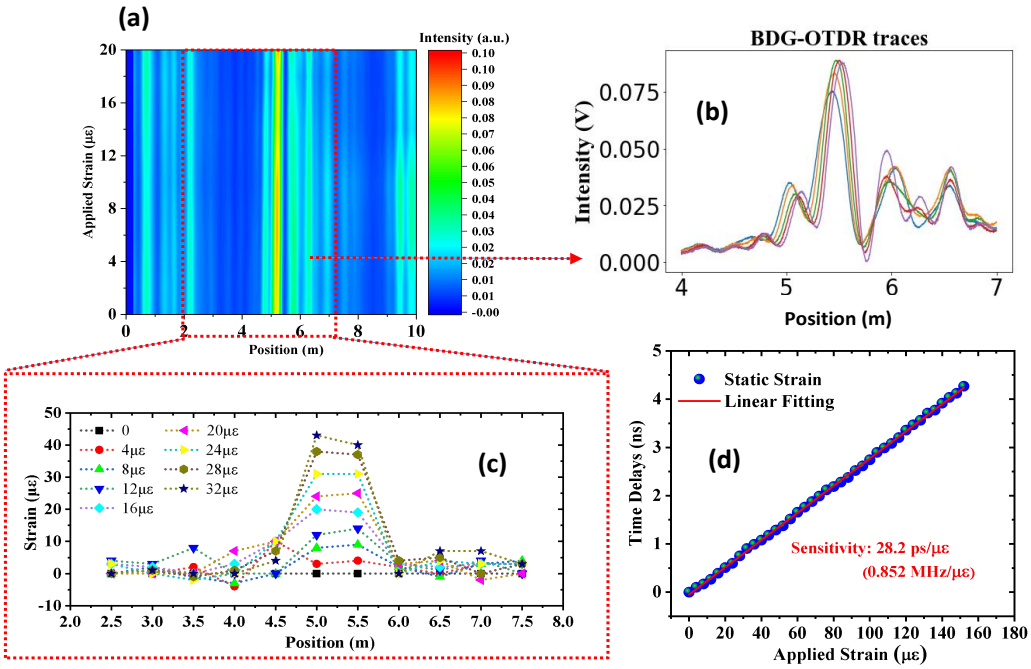

Figure 9.8: (a) 2D intensity map of the idler traces in the time domain with a strain change from 0-20 $\mu\varepsilon$; (b) The idler traces with different strain variation applied; (c) Strain distribution along the PM fiber, and (d) Strain-induced time delays coefficient.

In the dynamic strain measurement, three sinusoidal strain variations with an am-

plitude of 5/10/20 $\mu\epsilon$ and a frequency of 1 Hz are applied on the 1m section of PM fiber. The measured idler traces intensity change with time and position is collected and shown in the Figure 9.9 (a).

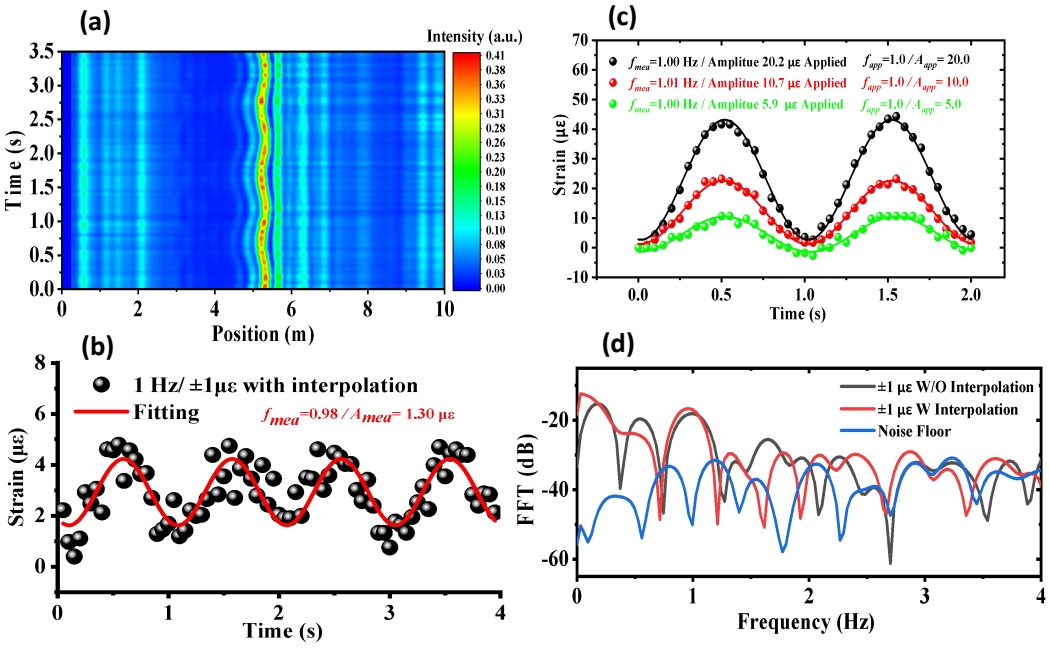

Figure 9.9: (a) 2D intensity map of idler traces with dynamic strain variations applied; (b) Dynamic strain variations measurement with peak-to-peak amplitude of 2 $\mu\varepsilon$ and its FFT analysis (d); (c) Demodulated dynamic strain variations profile at the location near 5 m.

The colour clearly shows the peak of idler traces within the 5-6 m section experiencing sinusoidal time shifts, while the intensity of the traces in other region keeps almost unchanged. The strain variations near 5 m location with different amplitude applied is shown in Figure 9.9 (c), which is calculated from the local time delays between each updated traces and the adjacent reference traces through the cross-correlation calculation with time window of 5 ns (0.5m spatial resolution). The demodulated peak-to-peak strain amplitude agrees with the applied value with relatively small uncertainty. To verify the minimum detectable strain variations, a 1 Hz sinusoidal strain variation with peak-to-peak amplitude of 2 $\mu\varepsilon$ is applied on the fiber, and the reconstructed signal

with interpolation in idler traces is shown in Figure 9.9 (b). Due to the amplitude of the applied strain is very close to the measurement uncertainty of the system, so the amplitude of the demodulated signal shows a relative larger error compared to the applied signal. The interpolation algorithm achieves more data points for each idler trace. Thus a better time delay measurement resolution is obtained, which gives a better stain measurement accuracy. Based on the FFT analysis as shown in Figure 9.9 (d), we know that the demodulated signal with interpolation algorithm has a better SNR, in which the noise peak around 0.6 and 1.7 Hz is significantly suppressed.

9.4 Discussion

In conventional BOTDA or Brillouin scattering-based sensing techniques, the spatial resolution is usually limited by the phonon lifetime (∼10 ns), which usually gives a spatial resolution of 1 m. However, for our proposed technique in this chapter, the spatial resolution is improved up to 0.5 m by using a chirped pulse as a probe signal for BDG detection. Due to the mapping of pump-probe frequency offset to time delays, the temperature/strain-induced birefringence changes will be translated into local time delays in reflected idler traces. Since there is no BDG spectrum recovery process, the phonon lifetime limitation is released, as chirped pulse measured phase matching condition of down-conversion of SBS instead of SBS gain spectrum itself, which is limited by the phonon lifetime related decay process. While in FWM conversion, we are measuring the rise time triggering the process of FWM conversion due to birefringence change in PMF, which is in the cm range.

On the other hand, the spatial resolution in our technique is determined by the birefringence variation and the frequency chirping rate. There is an effective pulse width based on these two parameters, which gives the final spatial resolution. The physical reason is that the reflection probe signal is pump-probe frequency offset dependent.

Unlike Rayleigh scattering, which has responses for any incident frequency, there is a phase matching condition (FWM) for the BDG reflection. Therefore, only some of the frequency components within the chirped pulse meet that condition and could be reflected by BDG. Depending on the birefringence variation, the effective pulse width that covers these satisfied frequency components could be much smaller than the pulse width of the chirped pulse. The range of the frequency band within the chirped pulse that satisfies the FWM condition is determined by the local birefringence variations. Overall, the spatial resolution is determined by both non-uniformity of fiber birefringence and the frequency chirping rate of the interrogation pulses. A higher frequency chirping rate would give a high spatial resolution.

To investigate the impact of the frequency chirping rate on the spatial resolution, we have generated chirped pulse with different frequency chirping rates used as probe signals for birefringence variation measurement. As shown in Figure 9.10 (a), all time domain idler traces show a time-varied profile but with a different number of peaks and contrast. With the increased chirping rate, the same BDG gain bandwidth occupies a narrower time duration, giving a high spatial resolution. Thus, a faster time-varied profile with more peaks will be obtained. The peak number is counted within the 3 dB grey band for each trace, and the result is shown in Figure 9.10 (b). It is noted that the BDG gain bandwidth is also length dependent, which means a shorter interaction time duration will broaden the gain bandwidth. Therefore, when the chirping rate increases from 93.5 to 188 MHz/ns, the occupation time duration is also extended and gives a similar spatial resolution. In addition, the short interaction time duration will also lower the contrast of the idler traces since the total input of the probe signal is decreased with the increase of the chirping rate. The relationship between chirping rate and contrast is shown in the black line of Figure 9.10 (b). Finally, the spatial resolution is verified by using the 93.5 MHz/ns with good spatial resolution and contrast. A 10 cm (rising and falling edge) spatial resolution is obtained, and the result is shown in Figure 9.10

(c). This indicates the phase matching condition associated with FWM-SBS occurs at a much faster speed than phonon lifetime imposed limitation on spatial resolution, which is the reason why higher spatial resolution than pulse width is achieved in our proposed system.

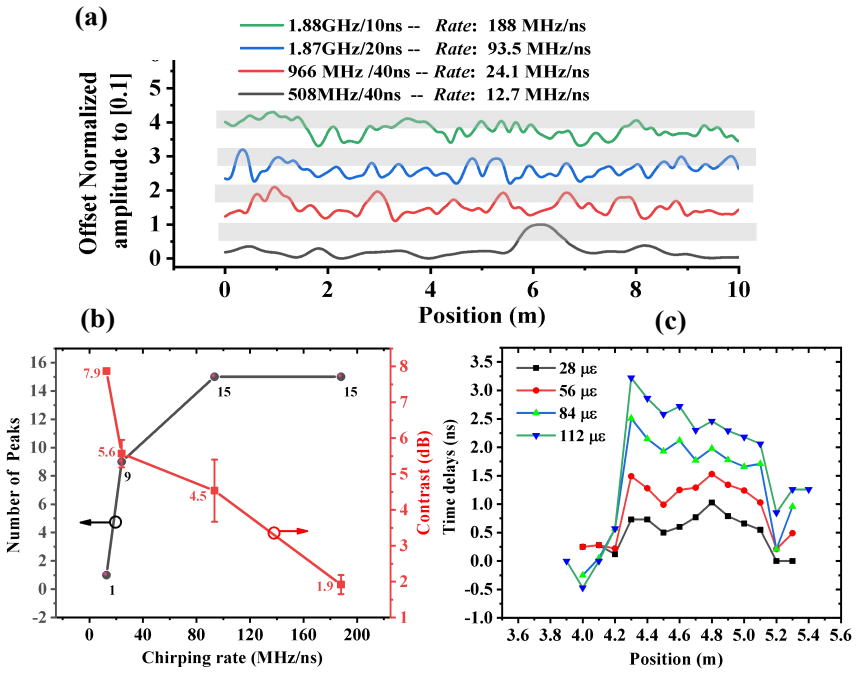

Figure 9.10: (a) BDG reflection signal with different chirping rate; (b) The relationship between number of peaks/signal contrast and chirping rate; (c) The static strain distribution along with the fiber.

9.5 Conclusion

This chapter demonstrates the temperature and static/dynamic strain-induced distributed birefringence variations measurement enabled by the Brillouin dynamic grating along the PM fiber in chirped pulse BDG-OTDR. In the proposed sensing system, the birefringence variation could directly translate into local time delays in the idler traces. A simulation is firstly carried out, in which the frequency offset between the probe and pump signal is varied and gives a linear relationship due to the usage of linear frequency chirped pulse. After that, the distributed temperature and dynamic strain

measurement are demonstrated on a section of PM fiber. The result shows a good linearity of temperature/strain-related time delay coefficient, which is about -2.46 ns/°C and 28.2 ps/$\mu\varepsilon$. The dynamic strain measurement is also demonstrated by applying a 1 Hz sinusoidal variation profile, and the peak-to-peak amplitude of 2 $\mu\varepsilon$ is successfully reconstructed. Finally, the spatial resolution is analyzed, and we conclude that the spatial resolution is determined by both the local birefringence profile and the frequency chirping rate of the probe pulse signal. A high spatial resolution with a rising and falling edge of 10 cm is obtained by using a 93.5 MHz frequency chirping rate.

Chapter 10

Summary and Future work

10.1 Summary

This thesis focuses on the high chirping rate pulse generation and its applications on the distributed optical fiber sensors, including CP-φ-OTDR, CP BOTDR, and CP BDG-OTDR. We developed the theoretical model for analyzing the working principle of the optimized scheme, in which chirped pulse is sent as the interrogation signal. The limitation of the existing technology is also discussed in order to draw the performance optimization guidelines of the system. Various sensing schemes utilizing chirped pulse as probe signal based on φ-OTDR and BOTDA have been proposed. The summarized results are as follows.

A novel distributed random grating sensor system based on chirped pulse optical time domain reflectometry is demonstrated for temperature measurement. Compared with a normal phase OTDR system, our proposed system could be used for static measurement and has a capacity for dynamic measurement up to several kilohertz, which is much higher than the OFDR scheme. It is believed that the proposed sensing system based on the random grating sensor array could be potentially applicable in areas of engineering because of its low cost and high stability. In addition, a real-time dynamic strain sensor based on the laser frequency drift compensation method is

also demonstrated; it is believed that the random grating sensor array would apply to structural health monitoring, especially for quasi-static dynamic strain sensing.

A high-performance CP φ-OTDR based on both the MFDD method and an random fiber grating array (RFGA) is proposed and demonstrated for both static and dynamic strain detection. The RFGA possesses a wide reflection spectrum range and variable width peaks in time domain, which achieves high time delay sensing accuracy. The experimental results show that the proposed MFDD method could effectively solve the measurement range limitation which is caused by a large time delay estimation error, indicating an attractive potential for this approach in the field of structural health monitoring.

We generated high-order chirped Kerr pulses with enhanced optical frequency chirping range from a single DFB laser to improve the performance of distributed strain sensing. By combining an up-chirped pulsed signal with a down-chirped pump in a novel configuration, we showed that the frequency chirping range of the m^{th} order Kerr chirped pulse is enhanced by a factor of $2m+1$, which is more efficient than the fixed-frequency pump scheme, which only enhances by a factor m. To experimentally validate the effect of high-order chirped Kerr pulses in a strain sensing application, we used the -4^{th} order Kerr pulse from the proposed scheme to interrogate a strain sensor (RFGA) under strain variation induced by a PZT. We achieved about 8 times larger static strain measurement range with the chirped-pump configuration with -4^{th} order Kerr pulses, much higher than that obtained with a fixed-frequency pump. Moreover, the chirped-pump configuration has also shown better performance in terms of measurement uncertainty. Our proposed all-optic method opens new avenues to generate a chirped pulse with a higher chirping rate over nano-second pulse widths without using a complicated cascaded scheme and expensive electronic devices.

A real-time distributed strain sensor based on a chirped pulse BOTDA with a non-uniform fiber is experimentally demonstrated. Without the frequency sweep process,

the Brillouin frequency shift variations could be directly obtained by the local time delays in Brillouin traces. In the demodulation process, the laser frequency drift compensation method is introduced to improve the sensing accuracy. The proposed system is believed to be applicable to structural health monitoring, especially for distributed high-frequency dynamic strain sensing.

Last, a distributed birefringence measurement via Brillouin dynamic grating for strain and temperature sensing is experimentally demonstrated. The result shows a good linearity of temperature/strain-related time delay coefficient, which is about -2.46 ns/°C and 28.2 ps/$\mu\varepsilon$. A high spatial resolution with a rising and falling edge of 10 cm is obtained using a 93.5 MHz frequency chirping rate.

10.2 Future work

In this thesis, several novel sensing schemes have been proposed and demonstrated for distributed temperature/strain measurement. The capacity of large static measurement range, low measurement uncertainty, and frequency drifting noise compensation in chirped pulse φ-OTDR and high acquisition rate for dynamic sensing in both chirped pulse BOTDA and chirped pulse BDG-OTDR are achieved. However, there are still many challenges to solve in these proposed systems. The more interesting thing is to extend the proposed system's application to other fields, which brings more added value to our research. Possible directions for future works are as follows.

(1) In section Section 9.4, we have discussed that the spatial resolution of the chirped pulse BDG-OTDR is not determined by the probe pulse width but by the frequency chirping rate with a given PM fiber as a sensor. So it is interesting to investigate the limitation of the spatial resolution by further increasing the frequency chirping rate. To generate the larger frequency chirping rate pulse, the method mentioned in Chapter 6 could be used. As shown in Figure 9.10 (b), the contrast decreases with the increase

of frequency chirping rate, lowering the SNR of the idler traces. Thus, the first thing that needs to deal with before sending a higher chirping rate pulse is to increase the strength of the DBG.

(2) The sign of temperature- and strain-dependent BDG frequency shifts are opposite, which provides a potential solution for high-accuracy temperature/strain discrimination in the distributed sensor. To achieve that, we not only need to collect the reflected idler signal from the BDG but also the Rayleigh signal from the same axis. Those two signals with different optical carrier frequencies are easy to distinguish by the optical band-pass filter. Compared to other proposed methods, such as the combination of BOTDA and BDG-OTDR, the proposed method has a better accuracy due to the higher temperature and strain coefficient in Rayleigh scattering. In addition, the chirped pulse as a probe signal could bring this simultaneous temperature/strain sensing system to the dynamics measurement domain.

(3) Brillouin random fiber laser (BRFL), a new type of fiber laser, has shown excellent advantages in generating highly coherent photons and in sensing applications. However, current RFLs based on Brillouin gain still suffer from the laser frequency drifting noise due to the longitudinal mode hopping or jumping. Once the lasing frequency within the Brillouin gain spectrum is changed, the high gain regime in the spatial domain will change accordingly due to the non-uniformity of the Brillouin frequency shift, which will change the local birefringence of the PM fiber based on Kramers–Kronig relations [216]. This Behavior could be monitored by measuring the local birefringence variations in the gain medium. Thus, the high accuracy and spatial resolution birefringence variation measurement system proposed in Chapter 9 is a good tool to measure the local birefringence change in the gain medium, to further reveal the character and the internal working states of the BRFL.

References

[1] Arthur H Hartog. *An introduction to distributed optical fibre sensors*. CRC press, 2017.

[2] Henry F Taylor and Chung E Lee. Apparatus and method for fiber optic intrusion sensing, March 16 1993. US Patent 5,194,847.

[3] R Posey Jr, GA Johnson, and ST Vohra. Strain sensing based on coherent rayleigh scattering in an optical fibre. *Electronics Letters*, 36(20):1, 2000.

[4] Yuelan Lu, Tao Zhu, Liang Chen, and Xiaoyi Bao. Distributed vibration sensor based on coherent detection of phase-otdr. *Journal of lightwave Technology*, 28(22):3243–3249, 2010.

[5] WF Eickhoff and RJAPL Ulrich. Optical frequency domain reflectometry in single-mode fiber. *Applied Physics Letters*, 39(9):693–695, 1981.

[6] Toshio Kurashima, Tsuneo Horiguchi, Hisashi Izumita, Shin-ichi Furukawa, and Yahei Koyamada. Brillouin optical-fiber time domain reflectometry. *IEICE transactions on communications*, 76(4):382–390, 1993.

[7] Kaoru Shimizu, Tsuneo Horiguchi, Yahei Koyamada, and Toshio Kurashima. Coherent self-heterodyne detection of spontaneously brillouin-scattered light waves in a single-mode fiber. *Optics letters*, 18(3):185–187, 1993.

[8] Tsuneo Horiguchi and Mitsuhiro Tateda. Botda-nondestructive measurement of single-mode optical fiber attenuation characteristics using brillouin interaction: theory. *Journal of lightwave technology*, 7(8):1170–1176, 1989.

[9] Tsuneo Horiguchi and Mitsuhiro Tateda. Optical-fiber-attenuation investigation using stimulated brillouin scattering between a pulse and a continuous wave. *Optics letters*, 14(8):408–410, 1989.

[10] Kwang Yong Song, Weiwen Zou, Zuyuan He, and Kazuo Hotate. All-optical dynamic grating generation based on brillouin scattering in polarization-maintaining fiber. *Optics letters*, 33(9):926–928, 2008.

[11] Yongkang Dong, Xiaoyi Bao, and Liang Chen. Distributed temperature sensing based on birefringence effect on transient brillouin grating in a polarization-maintaining photonic crystal fiber. *Optics letters*, 34(17):2590–2592, 2009.

[12] JP Dakin, DJ Pratt, GW Bibby, and JN Ross. Distributed optical fibre raman temperature sensor using a semiconductor light source and detector. *Electronics letters*, 13(21):569–570, 1985.

[13] George A Brown and Arthur Hartog. Optical fiber sensors in upstream oil & gas. *Journal of petroleum technology*, 54(11):63–65, 2002.

[14] E Hurtig. Borehole temperature measurements using distributed fibre optic sensing. *Scientific Drilling*, 3:283–286, 1993.

[15] A. Hartog. Distributed fibre-optic temperature sensors: Technology and applications in the power industry. *Power Engineering Journal*, 9(3):114–120, 1995.

[16] Zhe-Wen Ding, Xu-Ping Zhang, Ning-Mu Zou, Fei Xiong, Jin-Yu Song, Xing Fang, Feng Wang, and Yi-Xin Zhang. Phi-otdr based on-line monitoring of overhead power transmission line. *Journal of Lightwave Technology*, 39(15):5163–5169, 2021.

[17] Christopher KY Leung, Kai Tai Wan, Daniele Inaudi, Xiaoyi Bao, Wolfgang Habel, Zhi Zhou, Jinping Ou, Masoud Ghandehari, Hwai Chung Wu, and Michio Imai. Optical fiber sensors for civil engineering applications. *Materials and Structures*, 48(4):871–906, 2015.

[18] Xiaoyi Bao, Chunshu Zhang, Wenhai Li, M Eisa, S El-Gamal, and B Benmokrane. Monitoring the distributed impact wave on a concrete slab due to the traffic based on polarization dependence on stimulated brillouin scattering. *Smart materials and structures*, 17(1):015003, 2007.

[19] Hyuk-Jin Yoon, Kwang-Yong Song, Jung-Seok Kim, and Dae-Sang Kim. Longitudinal strain monitoring of rail using a distributed fiber sensor based on brillouin optical correlation domain analysis. *NDT & E International*, 44(7):637–644, 2011.

[20] Cong Du, Susom Dutta, Pradeep Kurup, Tzuyang Yu, and Xingwei Wang. A review of railway infrastructure monitoring using fiber optic sensors. *Sensors and Actuators A: Physical*, 303:111728, 2020.

[21] U Glombitza and Henrik Hoff. Fibre optic radar system for fire detection in cable trays. In *Proc. 13th Int. Conf. Automatic Fire Detection*, pages 1–23, 2004.

[22] Xiaoyi Bao and Liang Chen. Recent progress in distributed fiber optic sensors. *Sensors*, 12(7):8601–8639, 2012.

[23] Giuseppe Marra, Cecilia Clivati, Richard Luckett, Anna Tampellini, Jochen Kronjäger, Louise Wright, Alberto Mura, Filippo Levi, Stephen Robinson, André Xuereb, Brian Baptie, and Davide Calonico. Ultrastable laser interferometry for earthquake detection with terrestrial and submarine cables. *Science*, 361(6401):486–490, 2018.

[24] María R. Fernández-Ruiz, Hugo F. Martins, Ethan F. Williams, Carlos Becerril, Regina Magalh aes, Luis Costa, Sonia Martin-Lopez, Zhensheng Jia, Zhongwen

Zhan, and Miguel González-Herráez. Seismic monitoring with distributed acoustic sensing from the near-surface to the deep oceans. *J. Lightwave Technol.*, 40(5):1453–1463, Mar 2022.

[25] David K Barton. *Radar system analysis and modeling*. Artech House, 2004.

[26] J Mar, Y-R Lin, and Y-C Yeh. Ultra-wide bandwidth in-vehicle channel measurements using chirp pulse sounding signal. *IET science, measurement & technology*, 3(4):271–278, 2009.

[27] Mario Bertero, Michio Miyakawa, Patrizia Boccacci, Franco Conte, Kentaroh Orikasa, and Masatoshi Furutani. Image restoration in chirp-pulse microwave ct (cp-mct). *IEEE transactions on biomedical engineering*, 47(5):690–699, 2000.

[28] Changzhi Li, Victor M. Lubecke, Olga Boric-Lubecke, and Jenshan Lin. A review on recent advances in doppler radar sensors for noncontact healthcare monitoring. *IEEE Transactions on Microwave Theory and Techniques*, 61(5):2046–2060, 2013.

[29] Yuan Wang, Pedro Tovar, Liang Chen, and Xiaoyi Bao. Generation of high performance optical chirped pulse for distributed strain sensing application with high strain accuracy and larger measurement range. *Optics Express*, 30(11):18518–18529, 2022.

[30] Yuan Wang, Ping Lu, Stephen Mihailov, Liang Chen, and Xiaoyi Bao. Distributed time delay sensing in a random fiber grating array based on chirped pulse φ-otdr. *Optics Letters*, 45(13):3423–3426, 2020.

[31] Yuan Wang, Ping Lu, Stephen Mihailov, Liang Chen, and Xiaoyi Bao. Strain measurement range enhanced chirped pulse φ-otdr for distributed static and dynamic strain measurement based on random fiber grating array. *Optics Letters*, 45(21):6110–6113, 2020.

[32] Yuan Wang, Ping Lu, Stephen Mihailov, Liang Chen, and Xiaoyi Bao. Ultra-low frequency dynamic strain detection with laser frequency drifting compensation based on a random fiber grating array. *Optics Letters*, 46(4):789–792, 2021.

[33] Yuan Wang, Gerard Tatel, Pedro Tovar, Chen Chen, and Xiaoyi Bao. Distributed multi-parameter sensor for impact wave detection in i-steel beam structure. In *Optical Fiber Sensors*, pages W4–44. Optica Publishing Group, 2022.

[34] Yuan Wang, Liang Chen, and Xiaoyi Bao. Single-shot chirped pulse botda for static and dynamic strain sensing. *Optics Letters*, 46(22):5774–5777, 2021.

[35] Robert W Boyd. *Nonlinear optics*. Academic press, 2020.

[36] Govind P Agrawal. Nonlinear fiber optics. In *Nonlinear Science at the Dawn of the 21st Century*, pages 195–211. Springer, 2000.

[37] Yonas Muanenda, Claudio J Oton, and Fabrizio Di Pasquale. Application of raman and brillouin scattering phenomena in distributed optical fiber sensing. *Frontiers in Physics*, 7:155, 2019.

[38] D Heiman, DS Hamilton, and RW Hellwarth. Brillouin scattering measurements on optical glasses. *Physical Review B*, 19(12):6583, 1979.

[39] RY Chiao, CH Townes, and BP Stoicheff. Stimulated brillouin scattering and coherent generation of intense hypersonic waves. *Physical Review Letters*, 12(21):592, 1964.

[40] Charles W Ballmann, Jonathan V Thompson, Andrew J Traverso, Zhaokai Meng, Marlan O Scully, and Vladislav V Yakovlev. Stimulated brillouin scattering microscopic imaging. *Scientific reports*, 5(1):1–7, 2015.

[41] Bahaa EA Saleh and Malvin Carl Teich. *Fundamentals of photonics*. john Wiley & sons, 2019.

[42] Luc Thevenaz. *Advanced fiber optics: concepts and technology*. EPFL press, 2011.

[43] Carlos Augusto Galindez-Jamioy and Jose M Lopez-Higuera. Brillouin distributed fiber sensors: an overview and applications. *Journal of Sensors*, 2012, 2012.

[44] RW Tkach, AR Chraplyvy, and RM Derosier. Spontaneous brillouin scattering for single-mode optical-fibre characterisation. *Electronics Letters*, 22(19):1011–1013, 1986.

[45] Valeri I Kovalev and Robert G Harrison. Waveguide-induced inhomogeneous spectral broadening of stimulated brillouin scattering in optical fiber. *Optics letters*, 27(22):2022–2024, 2002.

[46] Eugene Hecht. *Optics*. Pearson Education India, 2012.

[47] Benjamin Chu. *Laser light scattering: basic principles and practice*. Courier Corporation, 2007.

[48] Immanuil L Fabelinskii. *Molecular scattering of light*. Springer Science & Business Media, 2012.

[49] Lev Davidovich Landau and Evgenii Mikhailovich Lifshitz. *Física teórica. Física estadística*, volume 5. Reverté, 1969.

[50] Masataka Nakazawa. Rayleigh backscattering theory for single-mode optical fibers. *JOSA*, 73(9):1175–1180, 1983.

[51] MK Barnoski and SM Jensen. Fiber waveguides: a novel technique for investigating attenuation characteristics. *Applied optics*, 15(9):2112–2115, 1976.

[52] Dietrich Marcuse. Curvature loss formula for optical fibers. *JOSA*, 66(3):216–220, 1976.

[53] CK Asawa, SK Yao, RC Stearns, NL Mota, and JW Downs. High-sensitivity fibre-optic strain sensors for measuring structural distortion. *Electronics letters*, 9(18):362–364, 1982.

[54] SK Yao and CK Asawa. Microbending fiber optic sensing. In *Fiber Optic and Laser Sensors I*, volume 412, pages 9–13. SPIE, 1983.

[55] Gordon Oscroft. Intrinsic fibre optic sensors. In *Fibre Optics' 87*, volume 734, pages 207–213. SPIE, 1987.

[56] Alistair MacLean, Chris Moran, Walter Johnstone, Brian Culshaw, Dan Marsh, and Geoff Andrews. Distributed fiber optic sensor for liquid hydrocarbon detection. In *Smart Structures and Materials 2001: Sensory Phenomena and Measurement Instrumentation for Smart Structures and Materials*, volume 4328, pages 47–53. SPIE, 2001.

[57] A Hartog. A distributed temperature sensor based on liquid-core optical fibers. *Journal of lightwave Technology*, 1(3):498–509, 1983.

[58] AJ Rogers. Polarisation optical time domain reflectometry. *Electronics Letters*, 13(16):489–490, 1980.

[59] Fabrizio Corsi. Polarization mode dispersion characterization of single-mode optical fiber using backscattering technique. *Journal of lightwave technology*, 16(10):1832, 1998.

[60] Byoung Kim, Dann Park, and Sang Choi. Use of polarization-optical time domain reflectometry for observation of the faraday effect in single-mode fibers. *IEEE Journal of Quantum Electronics*, 18(4):455–456, 1982.

[61] Paul A Williams, AH Rose, Gordon W Day, TE Milner, and MN Deeter. Temperature dependence of the verdet constant in several diamagnetic glasses. *Applied Optics*, 30(10):1176–1178, 1991.

[62] J Neil Ross. Birefringence measurement in optical fibers by polarization-optical time-domain reflectometry. *Applied optics*, 21(19):3489–3495, 1982.

[63] Michael V Dashkov. Localization of optical fiber sections under stress using potdr. In *Optical Technologies for Telecommunications 2007*, volume 7026, pages 181–186. SPIE, 2008.

[64] AH Hartog, DN Payne, and AJ Conduit. Polarisation measurements on monomode fibres using optical time-domain reflectometry. In *IEE Proceedings H. Microwaves, Optics and Antennas*, volume 128, pages 168–170, 1981.

[65] Yoshinori Namihira. Opto-elastic constant in single mode optical fibers. *Journal of lightwave technology*, 3(5):1078–1083, 1985.

[66] Feng Wang, Yuancheng Zhang, Wei Wang, Rongrong Dou, Jianlun Lu, Weihong Xu, and Xuping Zhang. Development of a multiperimeter sensing system based on potdr. *IEEE Photonics Journal*, 10(3):1–7, 2018.

[67] Huijuan Wu, Jun Liu, Lidong Lu, Xiaoyan Sun, David Atubga, and Yunjiang Rao. Multi-point disturbance detection and high-precision positioning of polarization-sensitive optical time-domain reflectometry. *Journal of Lightwave Technology*, 34(23):5371–5377, 2016.

[68] Ziyi Zhang and Xiaoyi Bao. Distributed optical fiber vibration sensor based on spectrum analysis of polarization-otdr system. *Optics express*, 16(14):10240–10247, 2008.

[69] Sergey V Shatalin, Vladimir N Treschikov, and Alan J Rogers. Interferometric optical time-domain reflectometry for distributed optical-fiber sensing. *Applied optics*, 37(24):5600–5604, 1998.

[70] Yahei Koyamada, Mutsumi Imahama, Kenya Kubota, and Kazuo Hogari. Fiber-optic distributed strain and temperature sensing with very high measurand resolution over long range using coherent otdr. *Journal of Lightwave Technology*, 27(9):1142–1146, 2009.

[71] Juan C Juarez, Eric W Maier, Kyoo Nam Choi, and Henry F Taylor. Distributed fiber-optic intrusion sensor system. *Journal of lightwave technology*, 23(6):2081–2087, 2005.

[72] Tao Zhu, Qian He, Xianghui Xiao, and Xiaoyi Bao. Modulated pulses based distributed vibration sensing with high frequency response and spatial resolution. *Optics express*, 21(3):2953–2963, 2013.

[73] JP Dakin. Distributed fibre optic sensor system. *UK patent, GB2222247A*, 1990.

[74] Roger Ian Crickmore and David John Hill. Traffic sensing and monitoring apparatus, January 26 2010. US Patent 7,652,245.

[75] AE Alekseev, Viktor Sergeevich Vdovenko, Boris Georgievich Gorshkov, Vladimir Timofeevich Potapov, Il'ya Aleksandrovich Sergachev, and Denis Evgen'evich Simikin. Phase-sensitive optical coherence reflectometer with differential phase-shift keying of probe pulses. *Quantum Electronics*, 44(10):965, 2014.

[76] Alli Masoudi, Mohammad Belal, and TP Newson. A distributed optical fibre dynamic strain sensor based on phase-otdr. *Measurement Science and Technology*, 24(8):085204, 2013.

[77] Richard G Priest. Analysis of fiber interferometer utilizing 3 x 3 fiber coupler. *IEEE Transactions on Microwave Theory and Techniques*, 30(10):1589–1591, 1982.

[78] Chang Wang, Chen Wang, Ying Shang, Xiaohui Liu, and Gangding Peng. Distributed acoustic mapping based on interferometry of phase optical time-domain reflectometry. *Optics Communications*, 346:172–177, 2015.

[79] Mario Martinelli. Time reversal for the polarization state in optical systems. 1992.

[80] Gaosheng Fang, Tuanwei Xu, Shengwen Feng, and Fang Li. Phase-sensitive optical time domain reflectometer based on phase-generated carrier algorithm. *Journal of lightwave technology*, 33(13):2811–2816, 2015.

[81] Miguel Gonzalez-Herraez, Maria R. Fernandez-Ruiz, Hugo F. Martins, and Sonia Martin-Lopez. Phase-sensitive optical time-domain reflectometry: concept and applications. *2022 27th OptoElectronics and Communications Conference (OECC) and 2022 International Conference on Photonics in Switching and Computing (PSC)*, pages 1–3, 2022.

[82] Dany-Sebastien Ly-Gagnon, Satoshi Tsukamoto, Kazuhiro Katoh, and Kazuro Kikuchi. Coherent detection of optical quadrature phase-shift keying signals with carrier phase estimation. *Journal of lightwave technology*, 24(1):12, 2006.

[83] Zhengqing Pan, Kezhen Liang, Qing Ye, Haiwen Cai, Ronghui Qu, and Zujie Fang. Phase-sensitive otdr system based on digital coherent detection. In *2011 Asia Communications and Photonics Conference and Exhibition (ACP)*, pages 1–6. IEEE, 2011.

[84] Juan José Mompó, Lihi Shiloh, Nadav Arbel, Nadav Levanon, Alayn Loayssa, and Avishay Eyal. Distributed dynamic strain sensing via perfect periodic coherent codes and a polarization diversity receiver. *Journal of Lightwave Technology*, 37(18):4597–4602, 2019.

[85] Zinan Wang, Li Zhang, Song Wang, Naitian Xue, Fei Peng, Mengqiu Fan, Wei Sun, Xianyang Qian, Jiarui Rao, and Yunjiang Rao. Coherent ϕ-otdr based on i/q demodulation and homodyne detection. *Optics express*, 24(2):853–858, 2016.

[86] Guojie Tu, Xuping Zhang, Yixin Zhang, Fan Zhu, Lan Xia, and Bikash Nakarmi. The development of an ϕ-otdr system for quantitative vibration measurement. *IEEE Photonics Technology Letters*, 27(12):1349–1352, 2015.

[87] Guangyao Yang, Xinyu Fan, Shuai Wang, Bin Wang, Qingwen Liu, and Zuyuan He. Long-range distributed vibration sensing based on phase extraction from phase-sensitive otdr. *IEEE Photonics Journal*, 8(3):1–12, 2016.

[88] Haijun He, Lianshan Yan, Heng Qian, Xinpu Zhang, Bin Luo, and Wei Pan. Enhanced range of the dynamic strain measurement in phase-sensitive otdr with tunable sensitivity. *Optics express*, 28(1):226–237, 2020.

[89] Yongkang Dong, Xi Chen, Erhu Liu, Cheng Fu, Hongying Zhang, and Zhiwei Lu. Quantitative measurement of dynamic nanostrain based on a phase-sensitive optical time domain reflectometer. *Applied Optics*, 55(28):7810–7815, 2016.

[90] Jialin Jiang, Zi-nan Wang, Zi-tan Wang, Yue Wu, Shengtao Lin, Ji Xiong, Yongxiang Chen, and Yunjiang Rao. Coherent kramers-kronig receiver for *phi*-otdr. *Journal of Lightwave Technology*, 37(18):4799–4807, 2019.

[91] Xiaonan Hui, Shilie Zheng, Jinhai Zhou, Hao Chi, Xiaofeng Jin, and Xianmin Zhang. Hilbert–huang transform time-frequency analysis in φ-otdr distributed sensor. *IEEE Photonics Technology Letters*, 26(23):2403–2406, 2014.

[92] Arthur Hartog and Kamal Kader. Distributed fiber optic sensor system with improved linearity, October 27 2015. US Patent 9,170,149.

[93] Jun Zhou, Zhengqing Pan, Qing Ye, Haiwen Cai, Ronghui Qu, and Zujie Fang. Characteristics and explanations of interference fading of a ϕ-otdr with a multi-frequency source. *Journal of lightwave technology*, 31(17):2947–2954, 2013.

[94] Mohammadmasoud Zabihi, Yusheng Chen, Tong Zhou, Jingxiao Liu, Yuanyuan Shan, Zhen Meng, Feng Wang, Yixin Zhang, Xuping Zhang, and Mengmeng Chen. Continuous fading suppression method for ϕ-otdr systems using optimum tracking over multiple probe frequencies. *Journal of Lightwave Technology*, 37(14):3602–3610, 2019.

[95] Meiqi Ren, Ping Lu, Liang Chen, and Xiaoyi Bao. Theoretical and experimental analysis of ϕ-otdr based on polarization diversity detection. *IEEE Photonics Technology Letters*, 28(6):697–700, 2015.

[96] Ali Masoudi and Trevor P Newson. Contributed review: Distributed optical fibre dynamic strain sensing. *Review of scientific instruments*, 87(1):011501, 2016.

[97] Mutsumi Imahama, Yahei Koyamada, and Kazuo Hogari. Restorability of rayleigh backscatter traces measured by coherent otdr with precisely frequency-controlled light source. *IEICE transactions on communications*, 91(4):1243–1246, 2008.

[98] Liqiang Qiu, Dexin Ba, Dengwang Zhou, Qi Chu, Zongda Zhu, and Yongkang Dong. High-sensitivity dynamic distributed pressure sensing with frequency-scanning φ-otdr. *Optics Letters*, 47(4):965–968, 2022.

[99] Li Zhang, Zhisheng Yang, Łukasz Szostkiewicz, Krzysztof Markiewicz, Sergei Mikhailov, Thomas Geernaert, Etienne Rochat, and Luc Thévenaz. Long-distance distributed pressure sensing based on frequency-scanned phase-sensitive optical time-domain reflectometry. *Optics Express*, 29(13):20487–20497, 2021.

[100] Yuyao Wang, Hua Zheng, and Chao Lu. High-sensitivity distributed relative salinity sensor based on frequency-scanning φ-otdr. *Optics Express*, 30(13):22860–22870, 2022.

[101] Juan Pastor-Graells, HF Martins, Andrés Garcia-Ruiz, Sonia Martin-Lopez, and Miguel Gonzalez-Herraez. Single-shot distributed temperature and strain tracking using direct detection phase-sensitive otdr with chirped pulses. *Optics express*, 24(12):13121–13133, 2016.

[102] Ji Xiong, Jialin Jiang, Yue Wu, Yongxiang Chen, Lianlian Xie, Yun Fu, and Zinan Wang. Chirped-pulse coherent-otdr with predistortion. *Journal of Optics*, 20(3):034001, 2018.

[103] Luis Costa, Regina Magalhães, Luca Palmieri, Hugo Martins, Sonia Martin-Lopez, María R Fernández-Ruiz, and Miguel Gonzalez-Herraez. Fast and direct measurement of the linear birefringence profile in standard single-mode optical fibers. *Optics Letters*, 45(3):623–626, 2020.

[104] Yuan Wang, Liang Chen, and Xiaoyi Bao. A novel method for distributed phase birefringence measurement based on chirped pulse φ-otdr. In *Optical Fiber Communication Conference*, pages Th1A–42. Optical Society of America, 2021.

[105] María R Fernández-Ruiz, Hugo F Martins, Ethan F Williams, Carlos Becerril, Regina Magalhães, Luis Costa, Sonia Martin-Lopez, Zhensheng Jia, Zhongwen Zhan, and Miguel González-Herráez. Seismic monitoring with distributed acoustic sensing from the near-surface to the deep oceans. *Journal of Lightwave Technology*, 40(5):1453–1463, 2022.

[106] Luis Costa, Luca Schenato, Hugo F Martins, Luca Palmieri, Sonia Martin-Lopez, Maria R Fernández-Ruiz, and Miguel González-Herráez. Pressure transducing

plane cable structure for fully distributed sound measurements. In *Optical Fiber Sensors*, pages W2A–2. Optica Publishing Group, 2020.

[107] Xiaoyi Bao, Zichao Zhou, and Yuan Wang. distributed time-domain sensors based on brillouin scattering and fwm enhanced sbs for temperature, strain and acoustic wave detection. *PhotoniX*, 2(1):1–29, 2021.

[108] Feng Wang, Xuping Zhang, Xiangchuan Wang, and Haisheng Chen. Distributed fiber strain and vibration sensor based on brillouin optical time-domain reflectometry and polarization optical time-domain reflectometry. *Optics letters*, 38(14):2437–2439, 2013.

[109] Yongkang Dong, Liang Chen, and Xiaoyi Bao. System optimization of a long-range brillouin-loss-based distributed fiber sensor. *Applied Optics*, 49(27):5020–5025, 2010.

[110] Luc Thévenaz, Stella Foaleng Mafang, and Jie Lin. Effect of pulse depletion in a brillouin optical time-domain analysis system. *Optics express*, 21(12):14017–14035, 2013.

[111] Alejandro Dominguez-Lopez, Xabier Angulo-Vinuesa, Alexia Lopez-Gil, Sonia Martin-Lopez, and Miguel Gonzalez-Herraez. Non-local effects in dual-probe-sideband brillouin optical time domain analysis. *Optics Express*, 23(8):10341–10352, 2015.

[112] Xiaoyi Bao, David J Webb, and David A Jackson. 32-km distributed temperature sensor based on brillouin loss in an optical fiber. *Optics letters*, 18(18):1561–1563, 1993.

[113] Xiaoyi Bao and Liang Chen. Recent progress in distributed fiber optic sensors. *sensors*, 12(7):8601–8639, 2012.

[114] Agnese Coscetta, Aldo Minardo, and Luigi Zeni. Distributed dynamic strain sensing based on brillouin scattering in optical fibers. *Sensors*, 20(19):5629, 2020.

[115] Tsuneo Horiguchi, Toshio Kurashima, and Mitsuhiro Tateda. Tensile strain dependence of brillouin frequency shift in silica optical fibers. *IEEE Photonics Technology Letters*, 1(5):107–108, 1989.

[116] Toshio Kurashima, Tsuneo Horiguchi, and Mitsuhiro Tateda. Distributed-temperature sensing using stimulated brillouin scattering in optical silica fibers. *Optics letters*, 15(18):1038–1040, 1990.

[117] Fabien Ravet, Xiaoyi Bao, Lufan Zou, Qinrong Yu, Yun Li, Vladimir Kalosha, and Liang Chen. Accurate strain detection and localisation with the distributed brillouin sensor based on phenomenological signal processing approach. In *Nondestructive Evaluation and Health Monitoring of Aerospace Materials, Composites, and Civil Infrastructure V*, volume 6176, pages 284–292. SPIE, 2006.

[118] Yun Li, Xiaoyi Bao, Fabien Ravet, and Evgueni Ponomarev. Distributed brillouin sensor system based on offset locking of two distributed feedback lasers. *Applied Optics*, 47(2):99–102, 2008.

[119] Marc Nikles, Luc Thévenaz, and Philippe A Robert. Simple distributed fiber sensor based on brillouin gain spectrum analysis. *Optics letters*, 21(10):758–760, 1996.

[120] Yun-Jiang Rao, Jun Luo, Zeng-Ling Ran, Jian-Feng Yue, Xiao-Dong Luo, and Zhi Zhou. Long-distance fiber-optic ϕ-otdr intrusion sensing system. In *20th international conference on optical fibre sensors*, volume 7503, pages 250–253. SPIE, 2009.

[121] Bruno Bristiel, Shifeng Jiang, Philippe Gallion, and Erwan Pincemin. New model of noise figure and rin transfer in fiber raman amplifiers. *ieee photonics technology letters*, 18(8):980–982, 2006.

[122] Hugo F Martins, Sonia Martin-Lopez, Pedro Corredera, Juan Diego Ania-Castañon, Orlando Frazão, and Miguel Gonzalez-Herraez. Distributed vibration sensing over 125 km with enhanced snr using phi-otdr over a urfl cavity. *journal of Lightwave Technology*, 33(12):2628–2632, 2015.

[123] ZN Wang, J Li, MQ Fan, L Zhang, F Peng, H Wu, JJ Zeng, Y Zhou, and YJ Rao. Phase-sensitive optical time-domain reflectometry with brillouin amplification. *Optics letters*, 39(15):4313–4316, 2014.

[124] ZN Wang, JJ Zeng, J Li, MQ Fan, H Wu, F Peng, L Zhang, Y Zhou, and YJ Rao. Ultra-long phase-sensitive otdr with hybrid distributed amplification. *Optics letters*, 39(20):5866–5869, 2014.

[125] Chams Baker, Benoit Vanus, Marc Wuilpart, Liang Chen, and Xiaoyi Bao. Enhancement of optical pulse extinction-ratio using the nonlinear kerr effect for phase-otdr. *Optics Express*, 24(17):19424–19434, 2016.

[126] Xiaozhong Tian, Rui Dang, Dongjie Tan, Lu Liu, and Haiming Wang. 123 km ϕ-otdr system based on bidirectional erbium-doped fiber amplifier. In *Optical Communication, Optical Fiber Sensors, and Optical Memories for Big Data Storage*, volume 10158, pages 191–194. SPIE, 2016.

[127] Muping Song, Weiji Zhu, Qiaolan Xia, Cong Yin, Yan Lu, Ying Wu, and Shouwang Zhuang. 151-km single-end phase-sensitive optical time-domain reflectometer assisted by optical repeater. *Optical Engineering*, 57(2):027104, 2018.

[128] Faruk Uyar, Talha Onat, Canberk Unal, Tolga Kartaloglu, Ibrahim Ozdur, and Ekmel Ozbay. 94.8 km-range direct detection fiber optic distributed acoustic

sensor. In *2019 Conference on Lasers and Electro-Optics (CLEO)*, pages 1–2. IEEE, 2019.

[129] Zhengqing Pan, Kezhen Liang, Jun Zhou, Qing Ye, Haiwen Cai, and Ronghui Qu. Interference-fading-free phase-demodulated otdr system. In *OFS2012 22nd International Conference on Optical Fiber Sensors*, volume 8421, pages 418–421. SPIE, 2012.

[130] Yonas Muanenda, Claudio J Oton, Stefano Faralli, Tiziano Nannipieri, Alessandro Signorini, and Fabrizio Di Pasquale. Hybrid distributed acoustic and temperature sensor using a commercial off-the-shelf dfb laser and direct detection. *Optics Letters*, 41(3):587–590, 2016.

[131] Da-Peng Zhou, Wei Peng, Liang Chen, and Xiaoyi Bao. Computational distributed fiber-optic sensing. *Optics Express*, 27(12):17069–17079, 2019.

[132] Bin Lu, Zhengqing Pan, Zhaoyong Wang, Hanrong Zheng, Qing Ye, Ronghui Qu, and Haiwen Cai. High spatial resolution phase-sensitive optical time domain reflectometer with a frequency-swept pulse. *Optics letters*, 42(3):391–394, 2017.

[133] Mengshi Wu, Chi Li, Xinyu Fan, Changrui Liao, and Zuyaun He. Large-scale multiplexed weak reflector array fabricated with a femtosecond laser for a fiber-optic quasi-distributed acoustic sensing system. *Optics Letters*, 45(13):3685–3688, 2020.

[134] Gregor Cedilnik, Gareth Lees, Poul Erik Schmidt, Søren Herstrøm, and Tommy Geisler. Pushing the reach of fiber distributed acoustic sensing to 125 km without the use of amplification. *IEEE Sensors Letters*, 3(3):1–4, 2019.

[135] Zengguang Qin, Tao Zhu, Liang Chen, and Xiaoyi Bao. High sensitivity distributed vibration sensor based on polarization-maintaining configurations of phase-otdr. *IEEE Photonics Technology Letters*, 23(15):1091–1093, 2011.

[136] Yongkang Dong, Hongying Zhang, Zhiwei Lu, Liang Chen, and Xiaoyi Bao. Impacts of kerr effect and fiber dispersion on long-range brillouin optical time-domain analysis systems. In *OFS2012 22nd International Conference on Optical Fiber Sensors*, volume 8421, pages 1533–1536. SPIE, 2012.

[137] Mehdi Alem, Marcelo A Soto, and Luc Thévenaz. Analytical model and experimental verification of the critical power for modulation instability in optical fibers. *Optics express*, 23(23):29514–29532, 2015.

[138] Luc Thévenaz, Stella Foaleng Mafang, and Jie Lin. Impact of pump depletion on the determination of the brillouin gain frequency in distributed fiber sensors. In *21st International Conference on Optical Fiber Sensors*, volume 7753, pages 332–335. SPIE, 2011.

[139] Yongkang Dong. High-performance distributed brillouin optical fiber sensing. *Photonic Sensors*, 11(1):69–90, 2021.

[140] Yongkang Dong, Liang Chen, and Xiaoyi Bao. Time-division multiplexing-based botda over 100km sensing length. *Optics Letters*, 36(2):277–279, 2011.

[141] Yongkang Dong, Liang Chen, and Xiaoyi Bao. Extending the sensing range of brillouin optical time-domain analysis combining frequency-division multiplexing and in-line edfas. *Journal of Lightwave Technology*, 30(8):1161–1167, 2011.

[142] Xabier Angulo-Vinuesa, Sonia Martin-Lopez, Pedro Corredera, and Miguel Gonzalez-Herraez. Raman-assisted brillouin optical time-domain analysis with sub-meter resolution over 100 km. *Optics Express*, 20(11):12147–12154, 2012.

[143] Javier Urricelqui, Mikel Sagues, and Alayn Loayssa. Brillouin optical time-domain analysis sensor assisted by brillouin distributed amplification of pump pulses. *Optics express*, 23(23):30448–30458, 2015.

[144] Marcelo A Soto, Gabriele Bolognini, Fabrizio Di Pasquale, and Luc Thévenaz. Simplex-coded botda fiber sensor with 1 m spatial resolution over a 50 km range. *Optics letters*, 35(2):259–261, 2010.

[145] Marcelo A Soto, Jaime A Ramírez, and Luc Thévenaz. Optimizing image denoising for long-range brillouin distributed fiber sensing. *Journal of Lightwave Technology*, 36(4):1168–1177, 2018.

[146] Tao Zhu, Xianghui Xiao, Qian He, and Dongmei Diao. Enhancement of snr and spatial resolution in φ-otdr system by using two-dimensional edge detection method. *Journal of Lightwave Technology*, 31(17):2851–2856, 2013.

[147] Qingwen Liu, Xinyu Fan, and Zuyuan He. Time-gated digital optical frequency domain reflectometry with 1.6-m spatial resolution over entire 110-km range. *Optics Express*, 23(20):25988–25995, 2015.

[148] Dian Chen, Qingwen Liu, and Zuyuan He. High-fidelity distributed fiber-optic acoustic sensor with fading noise suppressed and sub-meter spatial resolution. *Optics Express*, 26(13):16138–16146, 2018.

[149] Weiwen Zou, Shuo Yang, Xin Long, and Jianping Chen. Optical pulse compression reflectometry: proposal and proof-of-concept experiment. *Optics express*, 23(1):512–522, 2015.

[150] Bin Lu, Hanrong Zheng, Zhaoyong Wang, Qing Ye, Fang Wei, Ronghun Qu, and Haiwen Cai. High spatial resolution ϕ-otdr with long sensing distance. In *Optical Fiber Sensors*, page ThE25. Optical Society of America, 2018.

[151] Benzhang Wang, Yongkang Dong, Dexin Ba, and Xiaoyi Bao. High spatial resolution: an integrative review of its developments on the brillouin optical time-and correlation-domain analysis. *Measurement Science and Technology*, 31(5):052001, 2020.

[152] Anthony W Brown, Bruce G Colpitts, and Kellie Brown. Distributed sensor based on dark-pulse brillouin scattering. *IEEE Photonics Technology Letters*, 17(7):1501–1503, 2005.

[153] X Bao, A Brown, M DeMerchant, and J Smith. Characterization of the brillouin-loss spectrum of single-mode fibers by use of very short (¡ 10-ns) pulses. *Optics letters*, 24(8):510–512, 1999.

[154] Kinzo Kishida, Che-Hien Li, and Ken'ichi Nishiguchi. Pulse pre-pump method for cm-order spatial resolution of botda. In *17th International conference on optical fibre sensors*, volume 5855, pages 559–562. SPIE, 2005.

[155] Wenhai Li, Xiaoyi Bao, Yun Li, and Liang Chen. Differential pulse-width pair botda for high spatial resolution sensing. *Optics express*, 16(26):21616–21625, 2008.

[156] Alejandro Dominguez-Lopez, Marcelo A Soto, Sonia Martin-Lopez, Luc Thevenaz, and Miguel Gonzalez-Herraez. Resolving 1 million sensing points in an optimized differential time-domain brillouin sensor. *Optics Letters*, 42(10):1903–1906, 2017.

[157] Luc Thévenaz and Stella Foaleng Mafang. Distributed fiber sensing using brillouin echoes. In *19th International Conference on Optical Fibre Sensors*, volume 7004, pages 522–525. SPIE, 2008.

[158] Stella M Foaleng, Moshe Tur, Jean-Charles Beugnot, and Luc Thévenaz. High spatial and spectral resolution long-range sensing using brillouin echoes. *Journal of Lightwave Technology*, 28(20):2993–3003, 2010.

[159] Anthony W Brown, Michael D DeMerchant, Xiaoyi Bao, and Theodore W Bremner. Advances in distributed sensing using brillouin scattering. In *Smart Struc-*

tures and Materials 1998: Sensory Phenomena and Measurement Instrumentation for Smart Structures and Materials, volume 3330, pages 294–300. SPIE, 1998.

[160] Young Hoon Kim and Kwang Yong Song. Tailored pump compensation for brillouin optical time-domain analysis with distributed brillouin amplification. *Optics Express*, 25(13):14098–14105, 2017.

[161] Qian He, Tao Zhu, Xianghui Xiao, Baomei Zhang, Dongmei Diao, and Xiaoyi Bao. All fiber distributed vibration sensing using modulated time-difference pulses. *IEEE Photonics Technology Letters*, 25(20):1955–1957, 2013.

[162] Haijun He, Li-Yang Shao, Bin Luo, Zonglei Li, Xihua Zou, Zhiyong Zhang, Wei Pan, and Lianshan Yan. Multiple vibrations measurement using phase-sensitive otdr merged with mach-zehnder interferometer based on frequency division multiplexing. *Optics express*, 24(5):4842–4855, 2016.

[163] Sheng Liang, Xinzhi Sheng, Shuqin Lou, Yan Feng, and Kangning Zhang. Combination of phase-sensitive otdr and michelson interferometer for nuisance alarm rate reducing and event identification. *IEEE Photonics Journal*, 8(2):1–12, 2016.

[164] Pengfei Ma, Zhenshi Sun, Kun Liu, Junfeng Jiang, Shuang Wang, Liwang Zhang, Lingfeng Weng, Zhongyuan Xu, and Tiegen Liu. Distributed fiber optic vibration sensing with wide dynamic range, high frequency response, and multi-points accurate location. *Optics & Laser Technology*, 124:105966, 2020.

[165] Qian He, Tao Zhu, Jin Zhou, Dongmei Diao, and Xiaoyi Bao. Frequency response enhancement by periodical nonuniform sampling in distributed sensing. *IEEE Photonics Technology Letters*, 27(20):2158–2161, 2015.

[166] Daisuke Iida, Kunihiro Toge, and Tetsuya Manabe. Distributed measurement of acoustic vibration location with frequency multiplexed phase-otdr. *Optical Fiber Technology*, 36:19–25, 2017.

[167] Mengshi Wu, Xinyu Fan, Xinpu Zhang, Lianshan Yan, and Zuyuan He. Frequency response enhancement of phase-sensitive otdr for interrogating weak reflector array by using ofdm and vernier effect. *Journal of Lightwave Technology*, 38(17):4874–4882, 2020.

[168] Asher Voskoboinik, Omer F Yilmaz, Alan W Willner, and Moshe Tur. Sweep-free distributed brillouin time-domain analyzer (sf-botda). *Optics express*, 19(26):B842–B847, 2011.

[169] Yair Peled, Avi Motil, Lior Yaron, and Moshe Tur. Slope-assisted fast distributed sensing in optical fibers with arbitrary brillouin profile. *Optics express*, 19(21):19845–19854, 2011.

[170] Dengwang Zhou, Yongkang Dong, Benzhang Wang, Chao Pang, Dexin Ba, Hongying Zhang, Zhiwei Lu, Hui Li, and Xiaoyi Bao. Single-shot botda based on an optical chirp chain probe wave for distributed ultrafast measurement. *Light: Science & Applications*, 7(1):1–11, 2018.

[171] Yair Peled, Avi Motil, and Moshe Tur. Fast brillouin optical time domain analysis for dynamic sensing. *Optics express*, 20(8):8584–8591, 2012.

[172] Chihiro Kito, Hiroshi Takahashi, Kunihiro Toge, and Tetsuya Manabe. Dynamic strain measurement of 10-km fiber with frequency-swept pulsed botda. *Journal of Lightwave Technology*, 35(9):1738–1743, 2017.

[173] Reidar Skaug and Jens F Hjelmstad. *Spread spectrum in communication*. Number 12. IET, 1985.

[174] Luis Ernesto Ynoquio Herrera, Ricardo M Ribeiro, Vladimir B Jabulka, Pedro Tovar, and Jean Pierre von der Weid. Photonic generation and transmission of linearly chirped microwave pulses with high tbwp by self-heterodyne technique. *Journal of Lightwave Technology*, 36(19):4408–4415, 2018.

[175] Jason D McKinney, Dongsun Seo, Daniel E Leaird, and Andrew M Weiner. Photonically assisted generation of arbitrary millimeter-wave and microwave electromagnetic waveforms via direct space-to-time optical pulse shaping. *Journal of lightwave technology*, 21(12):3020, 2003.

[176] Chao Wang and Jianping Yao. Photonic generation of chirped microwave pulses using superimposed chirped fiber bragg gratings. *IEEE photonics technology letters*, 20(11):882–884, 2008.

[177] Olympio L Coutinho, Jiejun Zhang, and Jianping Yao. Photonic generation of a linearly chirped microwave waveform with a large time-bandwidth product based on self-heterodyne technique. In *2015 International Topical Meeting on Microwave Photonics (MWP)*, pages 1–4. IEEE, 2015.

[178] Pedro Tovar, Luis E. Ynóquio Herrera, Ricardo M. Ribeiro, and Jean Pierre von der Weid. Photonic generation of nlfm microwave pulses from dfb-laser chirp. *IEEE Photonics Technology Letters*, 31(17):1417–1420, 2019.

[179] J. Pastor-Graells, H. F. Martins, A. Garcia-Ruiz, S. Martin-Lopez, and M. Gonzalez-Herraez. Single-shot distributed temperature and strain tracking using direct detection phase-sensitive otdr with chirped pulses. *Opt. Express.*, 24(12):13121–13133, Jun 2016.

[180] Yuan Wang, Ping Lu, Stephen Mihailov, Liang Chen, and Xiaoyi Bao. Ultra-low frequency dynamic strain detection with laser frequency drifting compensation based on a random fiber grating array. *Opt. Lett.*, 46(4):789–792, Feb 2021.

[181] Ethan F Williams, María R Fernández-Ruiz, Regina Magalhaes, Roel Vanthillo, Zhongwen Zhan, Miguel González-Herráez, and Hugo F Martins. Distributed sensing of microseisms and teleseisms with submarine dark fibers. *Nature communications*, 10(1):1–11, 2019.

[182] Yuan Wang, Liang Chen, and Xiaoyi Bao. Single-shot chirped pulse botda for static and dynamic strain sensing. *Opt. Lett.*, 46(22):5774–5777, Nov 2021.

[183] Dian Chen, Qingwen Liu, Yifan Wang, He Li, and Zuyuan He. Fiber-optic distributed acoustic sensor based on a chirped pulse and a non-matched filter. *Optics express*, 27(20):29415–29424, 2019.

[184] Yuan Wang, Ping Lu, Stephen Mihailov, Liang Chen, and Xiaoyi Bao. Distributed time delay sensing in a random fiber grating array based on chirped pulse ϕ-otdr. *Opt. Lett.*, 45(13):3423–3426, Jul 2020.

[185] Soichi Kobayashi, Yoshihisa Yamamoto, Minoru Ito, and Tatsuya Kimura. Direct frequency modulation in algaas semiconductor lasers. *IEEE Transactions on Microwave Theory and Techniques*, 30(4):428–441, 1982.

[186] Chams Baker, Yang Lu, and Xiaoyi Bao. Chromatic-dispersion measurement by modulation phase-shift method using a kerr phase-interrogator. *Opt. Express*, 22(19):22314–22319, Sep 2014.

[187] Yuan Wang, Ole Krarup, Liang Chen, and Xiaoyi Bao. Frequency sweep extension using the kerr effect for static temperature measurement range enhancement in chirped pulse φ-otdr. *Optics Express*, 29(15):23202–23212, 2021.

[188] María R. Fernández-Ruiz, Luis Costa, and Hugo F. Martins. Distributed acoustic sensing using chirped-pulse phase-sensitive otdr technology. *Sensors*, 19(20):4368, 2019.

[189] Yuan Wang, Ping Lu, Stephen Mihailov, Liang Chen, and Xiaoyi Bao. Strain measurement range enhanced chirped pulse ϕ-otdr for distributed static and dynamic strain measurement based on random fiber grating array. *Opt. Lett.*, 45(21):6110–6113, Nov 2020.

[190] Jiangbing Du, Xinyu Fan, Qingwen Liu, and Zuyuan He. Strain sensitivity enhancement for fbg sensors by all-optical frequency chirp magnification with high-order cascaded fwm. In *23rd International Conference on Optical Fibre Sensors*, volume 9157, pages 401–404. SPIE, 2014.

[191] Xiaoyi Bao and Yuan Wang. Recent advancements in rayleigh scattering-based distributed fiber sensors. *Advanced devices & instrumentation*, 2021, 2021.

[192] Mohamed Saidi and Aron Gabor. Experimental analysis of the tensile behaviour of textile reinforced cementitious matrix composites using distributed fibre optic sensing (dfos) technology. *Construction and Building Materials*, 230:117027, 2020.

[193] Dewei Meng, Farhad Ansari, and Xin Feng. Detection and monitoring of surface micro-cracks by ppp-botda. *Applied optics*, 54(16):4972–4978, 2015.

[194] António Barrias, Joan R Casas, and Sergi Villalba. A review of distributed optical fiber sensors for civil engineering applications. *Sensors*, 16(5):748, 2016.

[195] Dongsheng Li, Liang Ren, and Hongnan Li. Mechanical property and strain transferring mechanism in optical fiber sensors. In *Fiber optic sensors*. IntechOpen, 2012.

[196] Kyle Van Der Kooi, Neil A Hoult, and Hoat Le. Monitoring an in-service railway bridge with a distributed fiber optic strain sensing system. *Journal of Bridge Engineering*, 23(10):05018007, 2018.

[197] Yuan Wang, Ping Lu, Stephen Mihailov, and Xiaoyi Bao. Distributed nano-strain sensing based on random fiber grating array. In *Optical Fiber Sensors*, pages T3–31. Optica Publishing Group, 2020.

[198] Yuan Wang and Xiaoyi Bao. Single-shot hybrid cp-φ otdr / cp-botda system for simultaneous distributed temperature/strain sensing. In *2022 Optical Fiber Communications Conference and Exhibition (OFC)*, pages 1–3. IEEE, 2022.

[199] VP Kalosha, Wenhai Li, Feng Wang, Liang Chen, and Xiaoyi Bao. Frequency-shifted light storage via stimulated brillouin scattering in optical fibers. *Optics letters*, 33(23):2848–2850, 2008.

[200] Da-Peng Zhou, Yongkang Dong, Liang Chen, and Xiaoyi Bao. Four-wave mixing analysis of brillouin dynamic grating in a polarization-maintaining fiber: theory and experiment. *Optics express*, 19(21):20785–20798, 2011.

[201] Kwang Yong Song. Effects of induced birefringence on brillouin dynamic gratings in single-mode optical fibers. *Optics letters*, 37(12):2229–2231, 2012.

[202] Kwang Yong Song. Operation of brillouin dynamic grating in single-mode optical fibers. *Optics letters*, 36(23):4686–4688, 2011.

[203] Yong Hyun Kim and Kwang Yong Song. Mapping of intermodal beat length distribution in an elliptical-core two-mode fiber based on brillouin dynamic grating. *Optics express*, 22(14):17292–17302, 2014.

[204] Shenping Li, Ming-Jun Li, and Richard S Vodhanel. All-optical brillouin dynamic grating generation in few-mode optical fiber. *Optics letters*, 37(22):4660–4662, 2012.

[205] Weiwen Zou and Jianping Chen. All-optical generation of brillouin dynamic grating based on multiple acoustic modes in a single-mode dispersion-shifted fiber. *Optics express*, 21(12):14771–14779, 2013.

[206] Kwang Yong Song, Kazuo Hotate, Weiwen Zou, and Zuyuan He. Applications of brillouin dynamic grating to distributed fiber sensors. *Journal of Lightwave Technology*, 35(16):3268–3280, 2016.

[207] Yongkang Dong, Liang Chen, and Xiaoyi Bao. Truly distributed birefringence measurement of polarization-maintaining fibers based on transient brillouin grating. *Optics letters*, 35(2):193–195, 2010.

[208] Pedro Tovar, Yuan Wang, Liang Chen, and Xiaoyi Bao. Distributed birefringence sensing at 10- 9 accuracy over ultra-long pmf by optical frequency comb and distributed brillouin amplifier. *Optics Express*, 30(18):33156–33169, 2022.

[209] Weiwen Zou, Zuyuan He, and Kazuo Hotate. Complete discrimination of strain and temperature using brillouin frequency shift and birefringence in a polarization-maintaining fiber. *Optics express*, 17(3):1248–1255, 2009.

[210] Weiwen Zou, Zuyuan He, and Kazuo Hotate. Demonstration of brillouin distributed discrimination of strain and temperature using a polarization-maintaining optical fiber. *IEEE Photonics Technology Letters*, 22(8):526–528, 2010.

[211] Yongkang Dong, Liang Chen, and Xiaoyi Bao. High-spatial-resolution time-domain simultaneous strain and temperature sensor using brillouin scattering and birefringence in a polarization-maintaining fiber. *IEEE Photonics Technology Letters*, 22(18):1364–1366, 2010.

[212] Youhei Okawa, Rodrigo Kendy Yamashita, Masato Kishi, and Kazuo Hotate. Distributed measurement of brillouin dynamic grating spectrum localized by an intensity-modulated correlation-domain technique. *Optics Express*, 28(14):21310–21317, 2020.

[213] Kwang Yong Song, Sanghoon Chin, Nikolay Primerov, and Luc Thévenaz. Time-domain distributed fiber sensor with 1 cm spatial resolution based on brillouin dynamic grating. *Journal of Lightwave Technology*, 28(14):2062–2067, 2010.

[214] Sanghoon Chin, Nikolay Primerov, and Luc Thevenaz. Sub-centimeter spatial resolution in distributed fiber sensing based on dynamic brillouin grating in optical fibers. *IEEE Sensors Journal*, 12(1):189–194, 2011.

[215] A Bergman, L Yaron, T Langer, and M Tur. Brillouin dynamic grating time-domain slope-assisted fast and distributed strain sensing. In *23rd International Conference on Optical Fibre Sensors*, volume 9157, pages 997–1000. SPIE, 2014.

[216] Govind P Agrawal. *Applications of nonlinear fiber optics*. Elsevier, 2001.

[217] Chandrasekhara Venkata Raman and Kariamanikkam Srinivasa Krishnan. A new type of secondary radiation. *Nature*, 121(3048):501–502, 1928.

[218] RS Krishnan. Temperature variations of the raman frequencies in diamond. In *Proceedings of the Indian Academy of Sciences-Section A*, volume 24, pages 45–57. Springer, 1946.

[219] IM Robinson, M Zakikhani, RJ Day, RJ Young, and C Galiotis. Strain dependence of the raman frequencies for different types of carbon fibres. *Journal of materials science letters*, 6(10):1212–1214, 1987.

[220] Rolf Brueckner. Properties and structure of vitreous silica. i. *Journal of non-crystalline solids*, 5(2):123–175, 1970.

[221] Camille Sabatier. *Toward the temperature and strain discrimination by Brillouin based distributed fiber sensor*. PhD thesis, Université de Lyon, 2019.

[222] Andreas Othonos. Fiber bragg gratings. *Review of scientific instruments*, 68(12):4309–4341, 1997.

[223] Yahei Koyamada, Mutsumi Imahama, Kenya Kubota, and Kazuo Hogari. Fiber-optic distributed strain and temperature sensing with very high measurand resolution over long range using coherent otdr. *Journal of Lightwave Technology*, 27(9):1142–1146, 2009.

[224] Andreas Othonos, Kyriacos Kalli, and Glenn E Kohnke. Fiber bragg gratings: Fundamentals and applications in telecommunications and sensing. *Physics Today*, 53(5):61, 2000.

[225] Raman Kashyap. *Fiber bragg gratings*. Academic press, 2009.

[226] Kenneth O Hill, Y Fujii, Derwyn C Johnson, and Brian S Kawasaki. Photosensitivity in optical fiber waveguides: Application to reflection filter fabrication. *Applied physics letters*, 32(10):647–649, 1978.

[227] Kenneth O Hill and Gerald Meltz. Fiber bragg grating technology fundamentals and overview. *Journal of lightwave technology*, 15(8):1263–1276, 1997.

[228] I Bennion, JAR Williams, Lin Zhang, K Sugden, and NJ Doran. Uv-written in-fibre bragg gratings. *Optical and Quantum Electronics*, 28(2):93–135, 1996.

[229] DP Hand and P St J Russell. Photoinduced refractive-index changes in germanosilicate fibers. *Optics letters*, 15(2):102–104, 1990.

[230] Paul J Lemaire, RM Atkins, V Mizrahi, and WA Reed. High pressure h/sub 2/loading as a technique for achieving ultrahigh uv photosensitivity and thermal sensitivity in geo/sub 2/doped optical fibres. *Electronics Letters*, 13(29):1191–1193, 1993.

[231] F Bilodeau, Bernard Malo, Jacques Albert, Derwyn C Johnson, Kenneth O Hill, Yoshinori Hibino, M Abe, and Masao Kawachi. Photosensitization of optical fiber and silica-on-silicon/silica waveguides. *Optics Letters*, 18(12):953–955, 1993.

[232] Gerald Meltz, William W Morey, and William H Glenn. Formation of bragg gratings in optical fibers by a transverse holographic method. *Optics letters*, 14(15):823–825, 1989.

[233] Kenneth O Hill, B Malo, F Bilodeau, DC Johnson, and Jacques Albert. Bragg gratings fabricated in monomode photosensitive optical fiber by uv exposure through a phase mask. *Applied Physics Letters*, 62(10):1035–1037, 1993.

[234] Jacques Albert, B Malo, KO Hill, F Bilodeau, and DC Johnson. Point-by-point fabrication of micro-bragg gratings in photosensitive fibre using single excimer pulse refractive index modification techniques. *Electronics Letters*, 1993.

[235] Robert J Campbell and Raman Kashyap. Spectral profile and multiplexing of bragg gratings in photosensitive fiber. *Optics letters*, 16(12):898–900, 1991.

[236] Qin Zhang, DA Brown, L Reinhart, TF Morse, JQ Wang, and Gang Xiao. Tuning bragg wavelength by writing gratings on prestrained fibers. *IEEE photonics technology letters*, 6(7):839–841, 1994.

[237] Song Gao, Chams Baker, Liang Chen, and Xiaoyi Bao. Fabrication of chirped fiber bragg gratings in a non-uniform single-core as 2 se 3-pmma tapered fiber. *Journal of Lightwave Technology*, 38(15):4108–4113, 2020.

[238] J Martin and F Ouellette. Novel writing technique of long and highly reflective in-fibre gratings. *Electronics Letters*, 30(10):811–812, 1994.

[239] HN Rourke, SR Baker, KC Byron, RS Baulcomb, SM Ojha, and S Clements. Fabrication and characterization of long, narrowband fibre gratings by phase mask scanning. *Electronics Letters*, 30(16):1341–1342, 1994.

[240] Damien Kinet, Patrice Mégret, Keith W Goossen, Liang Qiu, Dirk Heider, and Christophe Caucheteur. Fiber bragg grating sensors toward structural health monitoring in composite materials: Challenges and solutions. *Sensors*, 14(4):7394–7419, 2014.

[241] LCS Nunes, LCG Valente, and AMB Braga. Analysis of a demodulation system for fiber bragg grating sensors using two fixed filters. *Optics and Lasers in Engineering*, 42(5):529–542, 2004.

[242] Ping Han, Zhengying Li, Liang Chen, and Xiaoyi Bao. A high-speed distributed ultra-weak fbg sensing system with high resolution. *IEEE Photonics Technology Letters*, 29(15):1249–1252, 2017.

[243] Alan D Kersey, TA Berkoff, and WW Morey. Multiplexed fiber bragg grating strain-sensor system with a fiber fabry–perot wavelength filter. *Optics letters*, 18(16):1370–1372, 1993.

[244] Long Jin, Weigang Zhang, Hao Zhang, Bo Liu, Jian Zhao, Qinchang Tu, Guiyun Kai, and Xiaoyi Dong. An embedded fbg sensor for simultaneous measurement of stress and temperature. *IEEE Photonics Technology Letters*, 18(1):154–156, 2005.

[245] Benjamin Torres, Ignacio Payá-Zaforteza, Pedro A Calderón, and Jose M Adam. Analysis of the strain transfer in a new fbg sensor for structural health monitoring. *Engineering Structures*, 33(2):539–548, 2011.

[246] Cheng-Yu Hong, Yi-Fan Zhang, Meng-Xi Zhang, Lai Ming Gordon Leung, and Li-Qiang Liu. Application of fbg sensors for geotechnical health monitoring, a review of sensor design, implementation methods and packaging techniques. *Sensors and Actuators A: Physical*, 244:184–197, 2016.

[247] George T Kanellos, George Papaioannou, Dimitris Tsiokos, Christos Mitrogiannis, George Nianios, and Nikos Pleros. Two dimensional polymer-embedded quasi-distributed fbg pressure sensor for biomedical applications. *Optics express*, 18(1):179–186, 2010.

[248] Muhammad Arif Riza, Yun Ii Go, Sulaiman Wadi Harun, and Robert RJ Maier. Fbg sensors for environmental and biochemical applications—a review. *IEEE Sensors Journal*, 20(14):7614–7627, 2020.

[249] Hojoon Lee and Govind P Agrawal. Nonlinear switching of optical pulses in fiber bragg gratings. *IEEE journal of quantum electronics*, 39(3):508–515, 2003.

[250] Periklis Petropoulos, Morten Ibsen, AD Ellis, and David J Richardson. Rectangular pulse generation based on pulse reshaping using a superstructuredfiber bragg grating. *Journal of Lightwave Technology*, 19(5):746, 2001.

[251] Robert W Boyd. Material slow light and structural slow light: similarities and differences for nonlinear optics. *JOSA B*, 28(12):A38–A44, 2011.

[252] Jinjie Chen, Bo Liu, and Hao Zhang. Review of fiber bragg grating sensor technology. *Frontiers of Optoelectronics in China*, 4(2):204–212, 2011.

[253] Yunmiao Wang, Jianmin Gong, Dorothy Y Wang, Bo Dong, Weihong Bi, and Anbo Wang. A quasi-distributed sensing network with time-division-multiplexed fiber bragg gratings. *IEEE Photonics Technology Letters*, 23(2):70–72, 2010.

[254] Li Li, Hong He, and Yuchi Lin. Study on the spatial division multiplexing technique of fiber bragg grating sensors. In *2009 Symposium on Photonics and Optoelectronics*, pages 1–3. IEEE, 2009.

[255] Steffen Abbenseth and SI Lochmann. Distinct enlargement of network size or measurement speed for serial fbg sensor networks utilizing sik-ds-cdma. In *Journal of Physics: Conference Series*, volume 15, page 025. IOP Publishing, 2005.

[256] YH Huang, Chao Lu, Ping Kong Alexander Wai, and Hwa Yaw Tam. Large-scale fbg sensors utilizing code division multiplexing. In *2008 Conference on Lasers and Electro-Optics and 2008 Conference on Quantum Electronics and Laser Science*, pages 1–2. IEEE, 2008.

[257] L Dong, J-L Archambault, L Reekie, Russell St PJ, and DN Payne. Single pulse bragg gratings written during fibre drawing. *Electronics Letters*, 17(29):1577–1578, 1993.

[258] MA Putnam, CG Askins, GM Williams, EJ Friebele, M Baskansky, and J Reintjes. Single pulse fabrication of fibre bragg gratings using a phase-conjugated krf excimer laser. *Electronics Letters*, 31(11):885–886, 1995.

[259] Minghong Yang, Wei Bai, Huiyong Guo, Hongqiao Wen, Haihu Yu, and Desheng Jiang. Huge capacity fiber-optic sensing network based on ultra-weak draw tower gratings. *Photonic Sensors*, 6(1):26–41, 2016.

[260] Chengli Li, Jianguan Tang, Cheng Cheng, Longbao Cai, and Minghong Yang. Fbg arrays for quasi-distributed sensing: A review. *Photonic Sensors*, 11(1):91–108, 2021.

[261] CC Chan, Wei Jin, DN Wang, and MS Demokan. Intrinsic crosstalk analysis of a serial tdm fgb sensor array by using a tunable laser. *Microwave and optical technology letters*, 36(1):2–4, 2003.

[262] Yunmiao Wang, Jianmin Gong, Bo Dong, Dorothy Y Wang, Tyler J Shillig, and Anbo Wang. A large serial time-division multiplexed fiber bragg grating sensor network. *Journal of Lightwave Technology*, 30(17):2751–2756, 2012.

[263] Huiyong Guo, Jianguan Tang, Xiaofu Li, Yu Zheng, Hua Yu, and Haihu Yu. Online writing identical and weak fiber bragg grating arrays. *Chinese Optics Letters*, 11(3):030602, 2013.

[264] Brandon Redding, Matthew J. Murray, Andrei Donko, Martynas Beresna, Ali Masoudi, and Gilberto Brambilla. Low-noise distributed acoustic sensing using enhanced backscattering fiber with ultra-low-loss point reflectors. *Opt. Express*, 28(10):14638–14647, May 2020.

[265] Xin Gui, Zhengying Li, Xuelei Fu, Changjia Wang, Honghai Wang, Fan Wang, and Xiaoyi Bao. Large-scale multiplexing of a fbg array with randomly varied characteristic parameters for distributed sensing. *Optics Letters*, 43(21):5259–5262, 2018.

[266] Frédéric Monet, Sébastien Loranger, Victor Lambin-Iezzi, Antoine Drouin, Samuel Kadoury, and Raman Kashyap. The rogue: a novel, noise-generated random grating. *Opt. Express*, 27(10):13895–13909, May 2019.

[267] Changjia Wang, Zhengying Li, Xin Gui, Xuelei Fu, Fan Wang, Honghai Wang, Jiaqi Wang, and Xiaoyi Bao. Micro-cavity array with high accuracy for fully distributed optical fiber sensing. *Journal of Lightwave Technology*, 37(3):927–932, 2018.

[268] Ping Han, Zhengying Li, Liang Chen, and Xiaoyi Bao. A high-speed distributed ultra-weak fbg sensing system with high resolution. *IEEE Photonics Technology Letters*, 29(15):1249–1252, 2017.

[269] Zhengying Li, Yuheng Tong, Xuelei Fu, Jiaqi Wang, Qingqing Guo, Haihu Yu, and Xiaoyi Bao. Simultaneous distributed static and dynamic sensing based on ultra-short fiber bragg gratings. *Optics Express*, 26(13):17437–17446, 2018.

[270] D Du, X Liu, G Korn, Jeff Squier, and G Mourou. Laser-induced breakdown by impact ionization in sio2 with pulse widths from 7 ns to 150 fs. *Applied physics letters*, 64(23):3071–3073, 1994.

[271] PP Pronko, SK Dutta, J Squier, JV Rudd, D Du, and G Mourou. Machining of sub-micron holes using a femtosecond laser at 800 nm. *Optics communications*, 114(1-2):106–110, 1995.

[272] K Miura Davis, Kiyotaka Miura, Naoki Sugimoto, and Kazuyuki Hirao. Writing waveguides in glass with a femtosecond laser. *Optics letters*, 21(21):1729–1731, 1996.

[273] Rafael R Gattass and Eric Mazur. Femtosecond laser micromachining in transparent materials. *Nature photonics*, 2(4):219–225, 2008.

[274] Stephen J Mihailov, Dan Grobnic, Cyril Hnatovsky, Robert B Walker, Ping Lu, David Coulas, and Huimin Ding. Extreme environment sensing using femtosecond laser-inscribed fiber bragg gratings. *Sensors*, 17(12):2909, 2017.

[275] Brent C Stuart, Michael D Feit, Steve Herman, Aleksandr Markovich Rubenchik, Bruce W Shore, and Michael D Perry. Optical ablation by high-power short-pulse lasers. *JOSA B*, 13(2):459–468, 1996.

[276] Chris B Schaffer, Andre Brodeur, and Eric Mazur. Laser-induced breakdown and damage in bulk transparent materials induced by tightly focused femtosecond laser pulses. *Measurement Science and Technology*, 12(11):1784, 2001.

[277] Nemanja Jovanovic, Mattias Åslund, Alexander Fuerbach, Stuart D Jackson, Graham D Marshall, and Michael J Withford. 100 w cw yb3+-doped silica fiber laser utilizing an active-core inscribed point-by-point bragg grating. In *Bragg Gratings, Photosensitivity, and Poling in Glass Waveguides*, page BWB7. Optica Publishing Group, 2007.

[278] Dan Grobnic, Stephen J Mihailov, Christopher W Smelser, and Huimin Ding. Sapphire fiber bragg grating sensor made using femtosecond laser radiation for ultrahigh temperature applications. *IEEE Photonics Technology Letters*, 16(11):2505–2507, 2004.

[279] CR Liao and DN Wang. Review of femtosecond laser fabricated fiber bragg gratings for high temperature sensing. *Photonic Sensors*, 3(2):97–101, 2013.

[280] Yanping Xu, Ping Lu, Song Gao, Dao Xiang, Stephen Mihailov, and Xiaoyi Bao. Optical fiber random grating-based multiparameter sensor. *Optics letters*, 40(23):5514–5517, 2015.

[281] Yanping Xu, Liang Zhang, Song Gao, Ping Lu, Stephen Mihailov, and Xiaoyi Bao. Highly sensitive fiber random-grating-based random laser sensor for ultrasound detection. *Optics letters*, 42(7):1353–1356, 2017.

[282] Liang Zhang, Ping Lu, Zichao Zhou, Yuan Wang, Stephen Mihailov, Liang Chen, and Xiaoyi Bao. High-efficiency random fiber laser based on strong random fiber grating for mhz ultrasonic sensing. *IEEE Sensors Journal*, 20(11):5885–5892, 2020.

[283] Yajun Jiang, Chi Liu, Wending Zhang, Dong Mao, Dexing Yang, and Jianlin Zhao. Multi-parameter sensing using a fiber bragg grating inscribed in dual-mode fiber. *IEEE Photonics Technology Letters*, 29(19):1607–1610, 2017.

[284] Amos Martinez, Igor Y Khrushchev, and Ian Bennion. Direct inscription of bragg gratings in coated fibers by an infrared femtosecond laser. *Optics letters*, 31(11):1603–1605, 2006.

[285] Tingting Yang, Xueguang Qiao, Qiangzhou Rong, and Weijia Bao. Fiber bragg gratings inscriptions in multimode fiber using 800 nm femtosecond laser for high-temperature strain measurement. *Optics & Laser Technology*, 93:138–142, 2017.

[286] Cyril Hnatovsky, RS Taylor, PP Rajeev, Eli Simova, VR Bhardwaj, DM Rayner, and PB Corkum. Pulse duration dependence of femtosecond-laser-fabricated nanogratings in fused silica. *Applied Physics Letters*, 87(1):014104, 2005.

[287] Rod Taylor, Cyril Hnatovsky, and Eli Simova. Applications of femtosecond laser induced self-organized planar nanocracks inside fused silica glass. *Laser & Photonics Reviews*, 2(1-2):26–46, 2008.

[288] Bertrand Poumellec, Matthieu Lancry, Abdelouahed Chahid-Erraji, and Peter G Kazansky. Modification thresholds in femtosecond laser processing of pure silica: review of dependencies on laser parameters. *Optical Materials Express*, 1(4):766–782, 2011.

[289] Christopher W Smelser, Stephen J Mihailov, and Dan Grobnic. Formation of type i-ir and type ii-ir gratings with an ultrafast ir laser and a phase mask. *Optics express*, 13(14):5377–5386, 2005.

[290] Lionel Sudrie, Michel Franco, Bernard Prade, and André Mysyrowicz. Study of damage in fused silica induced by ultra-short ir laser pulses. *Optics Communications*, 191(3-6):333–339, 2001.

[291] Stephen J Mihailov, Christopher W Smelser, Ping Lu, Robert B Walker, Dan Grobnic, Huimin Ding, George Henderson, and James Unruh. Fiber bragg gratings made with a phase mask and 800-nm femtosecond radiation. *Optics letters*, 28(12):995–997, 2003.

[292] J Thomas, E Wikszak, T Clausnitzer, U Fuchs, U Zeitner, S Nolte, and A Tünnermann. Inscription of fiber bragg gratings with femtosecond pulses using a phase mask scanning technique. *Applied Physics A*, 86(2):153–157, 2007.

[293] Ams Martinez, Mykhaylo Dubov, Igor Khrushchev, and Ian Bennion. Direct writing of fibre bragg gratings by femtosecond laser. *Electronics Letters*, 40(19):1, 2004.

[294] Graham D Marshall, Martin Ams, and Michael J Withford. Direct laser written waveguide-bragg gratings in bulk fused silica. *Optics Letters*, 31(18):2690–2691, 2006.

[295] Ping Lu, Stephen J Mihailov, David Coulas, Huimin Ding, and Xiaoyi Bao. Low-loss random fiber gratings made with an fs-ir laser for distributed fiber sensing. *Journal of Lightwave Technology*, 37(18):4697–4702, 2019.

[296] Zichao Zhou, Chen Chen, Ping Lu, Stephen Mihailov, Liang Chen, and Xiaoyi Bao. Random fiber grating characterization based on ofdr and transfer matrix method. *Sensors*, 20(21):6071, 2020.

[297] Yanping Xu. *Fiber Random Grating and Its Applications*. PhD thesis, Université d'Ottawa/University of Ottawa, 2017.

[298] Yang Li, Ping Lu, Xiaoyi Bao, and Zhonghua Ou. Random spaced index modulation for a narrow linewidth tunable fiber laser with low intensity noise. *Optics letters*, 39(8):2294–2297, 2014.

[299] Sébastien Loranger, Mathieu Gagné, Victor Lambin-Iezzi, and Raman Kashyap. Rayleigh scatter based order of magnitude increase in distributed temperature and strain sensing by simple uv exposure of optical fibre. *Scientific reports*, 5(1):1–7, 2015.

[300] Paul S Westbrook, Tristan Kremp, Kenneth S Feder, Wing Ko, Eric M Monberg, Hongchao Wu, Debra A Simoff, Thierry F Taunay, and Roy M Ortiz. Continuous multicore optical fiber grating arrays for distributed sensing applications. *Journal of Lightwave Technology*, 35(6):1248–1252, 2017.

[301] Paul S Westbrook, Kenneth S Feder, Tristan Kremp, Eric M Monberg, Hongchao Wu, Benyuan Zhu, Lei Huang, Debra A Simoff, Scott Shenk, Vincent A Handerek, et al. Enhanced optical fiber for distributed acoustic sensing beyond the limits of rayleigh backscattering. *IScience*, 23(6):101137, 2020.

APPENDICES

Spontaneous Raman scattering

Spontaneous Raman scattering (SpRS) is another inelastic scattering process that is contributed by the interaction between incident pump lightwaves and thermally excited molecular vibrations, such as stretching, bending or rotation of inter-atomic bonds. This phenomenon was first observed by Raman in 1928 [217]. As shown in **??**, SpRS also have two processes to create two spectral bands in the scattering spectrum with about 13.2 THz shift relative to that of incident photons. In the Stokes Raman scattering, the incident photon excites a molecule from the ground energy level to a higher energy level E_1, and sheds energy to generate scattered photons (Stokes light) with reduced energy and, thus, lower frequency. While in the Anti-Stokes Raman scattering, the energy is transferred from material to scattered photons. The process starts with a molecule at energy level E_1 absorbing incident photons. Optical phonons must be available in the process so that their energy, combined with that absorbed from incident photons, is transferred to higher-frequency photons, which are referred to as scattered an-ti Stoked photons.

Different from Brillouin scattering that has narrow spectrum linewidth, due to the strict phase-matching condition, Raman scattering shows up with wide bandwidths. The frequency deviation between scattered Stokes/Anti-Stokes lightwaves and incident lightwave in Raman scattering is defined by the multiple vibrational modes of molecules that are associated with the various possible extensional, bending and rotational modes

of the molecule. As a result, Raman spectrum in the optical fiber is more akin to a combination of several bands rather than a distinct line.

It is noted that the frequency shift in Raman scattering process is the incident wavelength (λ_0) independent since there is only energy conservation with no moment conservation. Thus the wavelength of Stokes (λ_s) and Anti-Stoke ($\lambda_a s$) lightwaves are expressed by:

$$\lambda_{as} = \frac{1}{\frac{1}{\lambda_0} + \nu_R/c}, \quad \lambda_s = \frac{1}{\frac{1}{\lambda_0} - \nu_R/c} \tag{10.1}$$

where ν_R is the Raman frequency shift of about 13.2 THz in standard, and the wavelength shift related to this ν_R=13.2 THz is about 100 nm when the incident wavelength is 1550 nm.

Temperature sensitivity

Raman strain-dependent frequency shift is only readily detected in crystalline [218], or reasonably ordered solid materials such as polymer fibres with aligned molecular chains [219]. As we discussed above, in glasses, the breadth of the Raman line precludes its use in the measurement of the frequency shift, depriving us of the information that it yields in crystals. However, in the thermally-excited Spontaneous process, the strength of Raman scattering is temperature-dependent, which is used for distributed spontaneous Raman temperature sensing.

In the spontaneous inelastic scattering process, only a very small portion of light (approximately 1 in 10 million photons) is scattered and generates photons having optical frequencies shifts from incident photons [22]. More precisely, the number of optical phonons varies statistically according to frequency and ambient temperature. The average number $\bar{n}$ of thermally-activated phonons in each possible independent material wave (vibration mode) at frequency Ω and at temperature T is governed by

the Bose-Einstein statistical distribution:

$$\bar{n} = \frac{1}{e^{\frac{\hbar\Omega}{k_B T}} - 1} \tag{10.2}$$

where k_B is the Boltzmann constant, $\hbar$=$h/2\pi$ with h being the Plank constant. At the wavelength of 1550 nm, the average number of phonons for two inelastic scattering processes at room temperature is given by the following table [42]. This table shows that

Table 10.1: Typical average phonon number for 2 inelastic scatterings

	Frequency shifts	Average phonon number ($\bar{n}$)
Brillouin	11 GHz	570
Raman	13.2 THz	0.14

the intensity of the Brillouin scattering is much stronger than Raman scattering since the number of thermally-activated acoustic phonons at the GHz range is much higher than that of molecular vibrations of optical phonons at THz range. The intensity of Stokes lightwave is proportional to $(\bar{n}+1)$ since one incident photon is annihilated, and thus a Stokes photon and a phonon pair are generated. In contrast, the strength of Anti-Stokes is proportional to $\bar{n}$, given that an incident photon absorbs one phonon, and then a new photon is created. Consider the average phonon number in the Table 10.1, the intensity of Stokes and Anti-Stokes lightwave in Brillouin scattering are fairly equivalent. In contrast, the Stokes lightwave in Raman scattering is about 8 times more intense than the anti-Stokes lightwave, at ambient temperature (T=293 K). For a single line in the Raman spectrum, the intensity of Anti-Stokes (I_{as}) is given by [22]:

$$I_{AS} = I_0 \left(\frac{\ell}{\lambda_{AS}}\right)^4 \frac{1}{\exp\left(\frac{\hbar\Omega_R}{k_B T}\right) - 1} \tag{10.3}$$

where ℓ is the interaction length, $\Omega_R/2\pi$ is the Raman frequency shift and I_0 is the intensity of the incident lightwave. The intensity of Stokes is expressed as:

$$I_S = I_0 \left(\frac{\ell}{\lambda_S}\right)^4 \left(\frac{1}{\exp\left(\frac{\hbar\Omega_R}{k_B T}\right) - 1} + 1\right) \tag{10.4}$$

from these two equations, we could obtain the temperature dependant intensity ratio between Anti-Stokes and Stokes lightwaves, leading to the following:

$$R(T) = \frac{I_{AS}}{I_S} = \left(\frac{\lambda_S}{\lambda_{AS}}\right)^4 \exp\left(-\frac{\hbar\Omega_R}{k_B T}\right) \tag{10.5}$$

At room temperature of 293 K, the sensitivity of Stokes and Anti-Stokes Raman signals are 0.096 $\%K^{-1}$ and 0.83 $\%K^{-1}$. The sensitivity of their ratio is about 0.74 $\%K^{-1}$. Since the intensity of Stokes and anti-Stokes signals converge to the same value, the sensitivity decreases.

Stimulated Raman scattering

Similar to the SBS process, the Raman scattering also can also be a stimulated process called Stimulated Raman scattering (SRS). So, when the beat frequency between the forward-propagating Pump and backwards-propagating Stokes signal occurs at the exact resonance frequency of the molecular vibration mode, the material permittivity (ϵ) will be resonantly modulated at that frequency, giving rise to a sustained coupling between the two waves. The following set of two equations governs this process [36]:

$$\begin{aligned} \frac{dI_s}{dz} &= g_R I_p I_s - \alpha_s I_s, \\ \frac{dI_p}{dz} &= -\frac{\omega_p}{\omega_s} g_R I_p I_s - \alpha_p I_p, \end{aligned} \tag{10.6}$$

where I_s and I_p are the intensity of pump and Stokes signals, respectively. α_s and α_p represent the transmission loss of the Stokes and Pump lightwaves. g_R is the Raman gain coefficient associated with the cross-section of the SpBS. If losses are ignored, a simplified equation can be used to couple incident and scattered photons:

$$\frac{d}{dz}\left(\frac{I_s}{\omega_s} + \frac{I_p}{\omega_p}\right) = 0 \tag{10.7}$$

For the small intensity the Stokes signal, the depletion of the pump signal can be ignored. After propagating along with the fiber, the Stokes lightwave experiences amplification, which is expressed as:

$$I_{\mathrm{s}}(L) = I_s(0)\mathrm{e}^{g_R I_p(0) L_{\mathrm{cff}} - \alpha_{\mathrm{S}} L} \quad \text{where} \quad L_{\mathrm{eff}} = \left(1 - \mathrm{e}^{-\alpha_p L}\right)/\alpha_p \tag{10.8}$$

where L_{eff} is the nonlinear effective length.

Raman scattering has been widely used in many amplification applications. Due to the loose phase-matching condition with broad gain spectrum bandwidth, the pump and Stokes signals can propagate in the same or opposite directions, being an amplification solution compatible with broadband bi-direction transmission systems. Raman amplification gives a lower gain per unit length with low noise, but it works well over a long distance. Therefore, it is a good alternative for compensating fiber transmission losses in the distributed fibre-optic sensor system.

Strain and Temperature sensitivities in Brillouin scattering

Brillouin scattering is widely used in DOFS since the BFS is sensitive to the external disturbances (strain or temperature) applied to the fiber. Thus, the ability to precisely measure the frequency shift of the Brillouin scattering has allowed distributed sensing technology to provide strain and temperature data. As described in (2.8), the Brillouin frequency shift is related to the velocity of acoustic wave (V_A) and the effective refractive index (n_{eff}). In solid materials, the acoustic velocity is given by [115]:

$$V_A = \sqrt{\frac{E_Y\left(1-v_p\right)}{\left(1+v_p\right)\left(1-2v_p\right)\rho}} \tag{10.9}$$

where E_Y is the Young's modulus, v_p is Poisson's ratio and ρ is the material density. Both V_A in Equation (10.9) and n_{eff} in Equation (2.8) are sensitive to strain or temperature changes, while the former is due to the acousto-elastic effect and photo-elasticity effect induced mechanical deformations and the latter is introduced by the thermo-optic effect and thermo-expansion effect, respectively. Therefore, the strain/temperature-related BFS coefficient, $C_{\nu_B\varepsilon,T}$, is expressed by:

$$C_{\nu_B\varepsilon,T} = C_{\epsilon-} = \frac{1}{n_{\text{eff}}}\frac{\partial n_{\text{eff}}}{\partial(\varepsilon,T)} + \frac{1}{V_A}\frac{\partial V_A}{\partial(\varepsilon,T)} \tag{10.10}$$

The strain sensitivity is expressed by:

$$C_{\nu_B,\varepsilon} = C_{a-e} + C_{p-e} \tag{10.11}$$

where C_{a-e} is the acousto-elastic effect coefficient, and C_{p-e} is the photo-elastic effect coefficient. The C_{a-e} is related to Young's modulus, Poisson's ratio, and material density, leading to:

$$C_{a-e} = \frac{1}{V_A}\frac{\partial V_A}{\partial \varepsilon} = \frac{1}{2E_Y}\frac{\partial E_Y}{\partial \varepsilon} + \frac{v_p\left(2-v_p\right)}{\left(1-v_p^2\right)\left(1-2v_p\right)}\frac{\partial v_p}{\partial \varepsilon} - \frac{1}{2\rho}\frac{\partial \rho}{\partial \varepsilon}. \tag{10.12}$$

Based on the experimental results reported in [220], the $\frac{1}{E_Y}\frac{\partial E_Y}{\partial \varepsilon}$ is about 5.75 and $\frac{\partial v_p}{\partial \varepsilon}$ is about 3.07. The generally accepted value of E_Y and v_p are 73.3 GPa and 0.17. Besides, the sensitivity of refractive index to applied strain is determined by two photo-elastic constants p_{11} and p_{12}:

$$C_{p-e} = \frac{1}{n_{\text{eff}}}\frac{\partial n_{\text{eff}}}{\partial \varepsilon} = -\frac{n_{\text{eff}}^2}{2}\left[p_{12} - v_p\left(p_{11}+p_{12}\right)\right] \tag{10.13}$$

By substituting (10.12) and (10.13) in (10.10), combining $\nu_B \approx 11GHz$. We can estimate the BFS-related strain sensitivities in silica fibers around 1550 nm wavelength by:

$$\frac{\Delta v_B}{\Delta\varepsilon \times 10^{-6}} \approx 0.056\text{MHz}/\mu\varepsilon \tag{10.14}$$

On the other hand, due to the thermo-expansion and thermo-optic effects, both effective refractive index and acoustic wave velocity are temperature dependant. Hence, the temperature change induced BFS coefficient, $C_{\nu_B T}$, is expressed by:

$$C_{\nu_B,T} = C_{T-o} + C_{T-e} = \frac{1}{n_{\text{eff}}}\frac{\partial n_{\text{eff}}}{\partial (T)} + \frac{1}{V_A}\frac{\partial V_A}{\partial (T)} \tag{10.15}$$

in the equation above, the first term is defined by the thermo-optic effect:

$$C_{T-o} = \frac{\mathrm{d}n}{\mathrm{d}T} = \frac{\partial n}{\partial T} + \frac{\partial n}{\partial \rho}\frac{\partial \rho}{\partial T} = \frac{\partial n}{\partial T} - 3\alpha\rho\frac{\partial n}{\partial \rho}, \tag{10.16}$$

where α is the thermo-expansion coefficient and $\alpha = 5.6 \times 10^{-7}/^{\circ}\text{C}$ for the silica. So, the total thermo-optic coefficient is positive and about $C_{t-o} = 10.72 \times 10^{-6}/^{\circ}\text{C}$. While the second term corresponds to the thermo-expansion (thermo-acoustic) effect, and it is expressed by [221]:

$$C_{T-e} = \frac{\partial V_A}{\partial T} = \frac{\partial V_A}{2}\left(\frac{1}{E_Y}\frac{\partial E_Y}{\partial T} + \alpha\right) \tag{10.17}$$

where the thermo-expansion coefficient $\alpha = -\frac{1}{\rho}\frac{\partial \rho}{\partial T}$.

It is noted that the acoustic wave velocity changes mainly come from the temperature dependence of Young's modulus. Concerning the widely used SMF28 fiber, its experimentally-measured temperature-related BFS sensitivity is about:

$$\frac{\Delta v_B}{\Delta T} \approx 1.05\text{MHz}/^{\circ}\text{C} \tag{10.18}$$

Strain and Temperature sensitivities in Rayleigh scattering

When the lightwave from a narrow linewidth laser propagates along with the fiber within the coherent length, the lightwave is continuously scattered. The scattering waves from different fiber locations will counter-propagate towards a backward direction and meet together at the input end. Let us consider the phase difference between two lightwaves that are scattered from two scattering centres at the position of Z_i and Z_j along the fiber. The phase difference is related to the optical path length between two scattering centers, including the effective refractive index (n_{eff}) and the distance (l), leading to:

$$\Delta\varphi_{ij} = \frac{2\pi n_{\text{eff}} l_{ij}}{\lambda} = \frac{2\pi n_{\text{eff}} l_{ij} f}{c} \tag{10.19}$$

When a strain variation is applied, n_{eff} and l_{ij} are hereby changed due to the Poisson and photo-elastic effects. On the other hand, the phase difference ($\Delta\varphi_{ij}$) also relates to the optical frequency (wavelength) of the incident light according to the Equation (10.19). Therefore, within the uniform range of 0-1 $\mu\varepsilon$ [96], any strain variations-induced phase different change could be compensated by a certain frequency (wavelength) shits, which is given by:

$$\begin{aligned} &\Delta\varphi_{ij}(f_0, 0) = \Delta\varphi_{ij}(f_0 + \Delta f_\varepsilon, \Delta\varepsilon) \\ &(f_0 + \Delta f_\varepsilon)[(n_{\text{eff}} + \Delta n)(l_{ij} + \Delta l)] = f_0 n_{\text{eff}} l_{ij} \end{aligned} \tag{10.20}$$

where $\Delta\varepsilon$ is the strain variation applied on the fiber and f_0 is the frequency of the

incident lightwave. We could find that:

$$\frac{\Delta f_\varepsilon}{f_0 \Delta\varepsilon} = -(\frac{\Delta l}{l_{ij}\Delta\varepsilon} + \frac{\Delta n}{n_{\text{eff}}\Delta\varepsilon}) = -(1 + C_{p-e}) \tag{10.21}$$

where $C_{p-e} \approx -0.22\,\varepsilon^{-1}$ is the photo-elastic coefficient as described in Equation (10.13). Thus, the applied strain could be obtained by modulating the frequency of incident light to find the strain variations-induced frequency shifts, Δf_ε, by comparing the frequency response with and without applied strain.

On the other hand, temperature variations will also introduce the change of local effective refractive index (n_{eff}) and the distance between two scattering centers (l_{ij}) due to the thermo-optic and thermo-expansion effects as shown in Equation (10.16) and Equation (10.17), leading to :

$$\frac{\Delta f_T}{f_0 \Delta T} = -(\frac{\Delta l}{l_{ij}\Delta T} + \frac{\Delta n}{n_{\text{eff}}\Delta T}) = -(\alpha + C_{t-o}) \tag{10.22}$$

where $\alpha = 5.6 \times 10^{-7}/^{\circ}\text{C}$ and the overall thermo-optic effect coefficient is about $C_{t-o} = 10.72 \times 10^{-6}/^{\circ}\text{C}$ for $n_{\text{eff}} = 1.46$.

Overall, the optical frequency change of incident light used to compensate for the strain and temperature variations is given approximately by [222] [97]:

$$\begin{aligned} \frac{\Delta f_T}{f_0} &= -0.78 \times \Delta\varepsilon \\ \frac{\Delta f_\varepsilon}{f_0} &= -(6.92 \times 10^{-6}) \times \Delta T \end{aligned} \tag{10.23}$$

The strain or temperature change value is estimated by converting the measured laser frequency/wavelength change to the corresponding values based on Equation (10.23) [223].

Strain and Temperature sensitivities in FBG sensors

As shown in Equation (10.26), the Bragg wavelength is relevant to the effective refractive index and the grating period, which is thus sensitive to external temperature or strain variations. The sensitivity of the strain/temperature-induced wavelength shift

is similar with what we have discussed in the Rayleigh scattering section, leading to:

$$\frac{\mathrm{d}\lambda_{\mathrm{B}}}{\mathrm{d}T} = 2\frac{\partial n_{\mathrm{eff}}}{\partial T}\Lambda + 2\frac{\partial \Lambda}{\partial T}n_{\mathrm{eff}} = \lambda_{\mathrm{B}}\left(\frac{1}{n_{\mathrm{eff}}}\frac{\partial n_{\mathrm{eff}}}{\partial T} + \frac{1}{\Lambda}\frac{\partial \Lambda}{\partial T}\right) = \lambda_{\mathrm{B}}(\alpha + C_{t-o}) \tag{10.24}$$

according to Equation (10.22), the $\alpha = 5.6 \times 10^{-7}/^{\circ}\mathrm{C}$ and $C_{t-o} = 10.72 \times 10^{-6}/^{\circ}\mathrm{C}$ when $n_{\mathrm{eff}} = 1.46$. So the temperature-induced wavelength shifts are about $10.8pm/^{\circ}\mathrm{C}$.

The dominant peak in the FBG's reflection spectrum is also sensitive to the axial strain (ε):

$$\frac{d\lambda_{\mathrm{B}}}{\varepsilon} = \lambda_{\mathrm{B}}\left(\frac{1}{n_{\mathrm{eff}}}\frac{\partial n_{\mathrm{eff}}}{\varepsilon} + 1\right) = \lambda_B\left\{1 - \frac{n_{\mathrm{eff}}^2}{2}\left[p_{12} - \nu\left(p_{11} + p_{12}\right)\right]\right\} = \lambda_{\mathrm{B}}\left(1 + C_{p-e}\right) \tag{10.25}$$

where $p_{11} = 0.113$ and $p_{12} = 0.252$, and the photo-elastic coefficient $C_{p-e} = -0.22\varepsilon^{-1}$. So, the strain-induced Bragg wavelength shifts is about $1.21pm/\mu\varepsilon$.

Fiber Bragg Gratngs (FBGs)

At first glance, Rayleigh scattering in optical fibers can be considered as a detrimental phenomenon since it significantly contributes to fiber losses. However, it can be used to develop fiber characterization techniques and, in particular, to perform distributed measurements. However, the ultra-weak Rayleigh scattering (-100dB/mm) that was originally designed for long-haul communications with minimized scattering loss limits the performance of the distributed sensors in terms of sensing distance, spatial resolution and measurement accuracy. To enhance the reflection of the fiber, one can inscribe the grating in the fiber, in which the refractive index change induced by fs laser or UV light is modulated periodically along the core axis of the fibre over a few millimeters or centimeters long [224] [225].

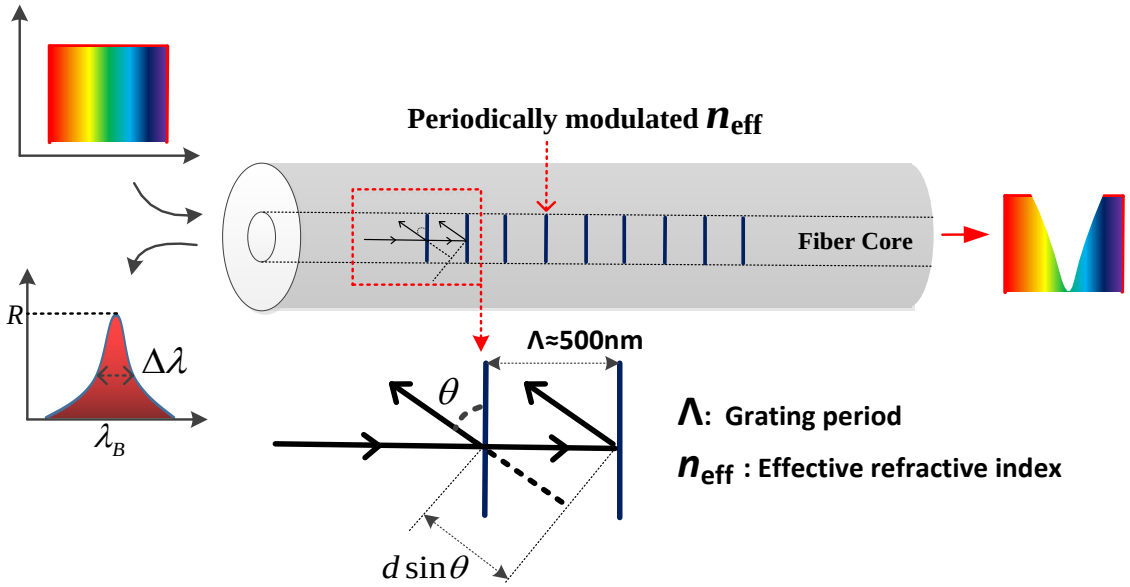

Figure 10.1: Fiber Bragg grating working principle. In an optical fiber, usually only (mostly) consider the forward and backward propagation direction. So for backward reflected waves, the sin θ=1,i.e., θ=$\pi/2$.

In FBGs, the lightwave is refracted by a periodic modulation of the effective refractive index (in range of 10^{-5} to 10^{-2}) in an optical fiber, and then a Bragg peak will be produced if their reflections off the various planes interfered constructively. The working principle of FBGs is first explained by William Henry Bragg through the theory of Bragg refraction, which is originally used for X-ray diffraction by crystalline solids. As shown in Figure 10.1, The reflected waves will interfere constructively if their optical path length difference equals the integer number of the incident light wavelength, which has the effect of reflecting a narrow wavelength range that matches the pitch of the grating, leading to the Bragg condition given by:

$$m\lambda_{\mathrm{B}} = 2n_{\mathrm{eff}}\Lambda \tag{10.26}$$

where λ_B is the Bragg wavelength, Λ is the grating period and m is the positive integer number. The linewidth of the reflection peak in the reflection spectrum is related to

the incident wavelength, and the length (L) of the grating, which is expressed as [225]:

$$\Delta\lambda \approx \frac{\lambda^2}{2n_{\text{eff}}L} \tag{10.27}$$

The FBG is first reported by Hill in 1978 [226], in which the formation of refractive-index gratings in germanosilicate fiber by sustained exposure of the core to the interference pattern of oppositely propagating modes of 488- or 514.5- nm argon-ion laser radiation is reported. The reflectivity of the FBG is about 90% with a reflection spectrum linewidth of 200 MHz, indicating 1m grating length [227]. The behind mechanism responsible for the "Hill" gratings was two-photon absorption into the 240 nm band, with the energy transferred from photos to the glass [228]. The fundamental principle of FBG fabrication relies on the photo-sensitivity of the glass with which the optical fiber is fabricated. This photo-induced refractive index change effect was explained by Hand and Russell in 1990 [229] that attributes the induced refractive index change to photo-ionization of a Geo defect associated with an absorption band at 240 nm in the ultraviolet, and the subsequent trapping of the electron so released, forming Ge(1) and Ge(2) color centers with absorption bands at 281 and 213 nm and the resultant color centres are responsible for changes in the UV absorption spectrum of the glass, and the refractive index change follows from the Kramers-Kronig relationship. The magnitude of the refractive index change (Δn) obtained depends on several different factors, such as the irradiation conditions (wavelength, intensity, and total dosage of irradiating light), the composition of glassy material forming the fiber core and any processing of the fiber before irradiation [227]. Some techniques such as "hydrogen loading" [230] and "flame brushing" [231] are available used to process the fiber before irradiation in order to enhance photo-sensitization, giving larger refractive index changes up to $\Delta n = 10^{-2}$. Drive by the development of the Ultraviolet (UV) side-writing technique and the great potential applications, the fabrication of FBG device attached more attention. There are three main methods for FBG fabrication, including two beams interferometric exposure [232], phase mask UV exposure [233] and point-to-point fs laser writing [234].

As shown in Figure 10.2, by exposing the photosensitive fiber core under the periodical interference pattern of two beams over a sufficient length and with a high optical power intensity when the exposure time, a corresponding periodic index grating in the core of the optical fiber will be inscribed permanently. This transverse holographic technique allows more control over the Bragg wavelength since the period of the inscribed gratings (Λ) is determined by the wavelength of incident UV beams: $\Lambda = \lambda_{\mathrm{UV}}/2sin\theta$, leading to the Bragg wavelength of the grating:

$$\lambda_B = \frac{\lambda_{\mathrm{UV}} n_{\mathrm{eff}}}{sin\theta} \tag{10.28}$$

Therefore even the light beam at UV is used for FBGs fabrication, Bragg gratings with other longer wavelengths in a spectra region of interest for optical devices with applications in optical communication and optical sensors [227]. However, this technique usually requires the laser to be highly coherent and sufficiently stable during fabrication. In 1993, Hill propose an FBG inscription method by using phase mask, which becomes the method of choice with many for reproducible grating fabrication. This benefits from the more mechanically stable configuration because of the proximity of the fiber to the phase mask, which also lowers the requirement of coherence of the laser source.

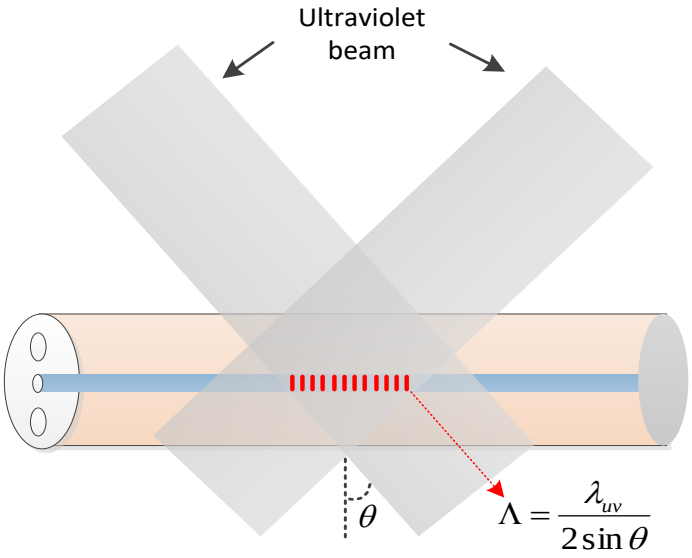

Figure 10.2: Fibre grating inscription through two UV beams interferometric exposure.

As shown in Figure 10.3, the UV beam is almost entirely diffracted without transmission light in the zero-order beam between +1 and -1 order when the depth of the corrugations satisfies: $d = \lambda_{\mathrm{UV}}/2(n_{\mathrm{UV}} - 1)$. The interference between +1 and -1 order beams produces a periodic pattern to change the local refractive index due to the photo-sensitivity. Thus, the Bragg wavelength of the formed gratings corresponds to the period of the phase mask (Λ_{pm}):

$$\lambda_B = n_{\mathrm{eff}}\Lambda_{pm} \tag{10.29}$$

However, various phase masks with different periods are needed for fabricating FBGs with different Bragg wavelengths. This problem could be solved if external strain is applied on the fiber core before being irradiated by the UV beam [235] [236]. Inspired by this idea, A chirped FBG device is fabricated using a non-uniform tapered fiber. Along the non-uniform fiber, a strain gradient is formed when the pre-stretch is applied during the fabrication process, which produces a varying shift in the Bragg spacing at a different position along the taper leading to a tunable chirped grating [237].

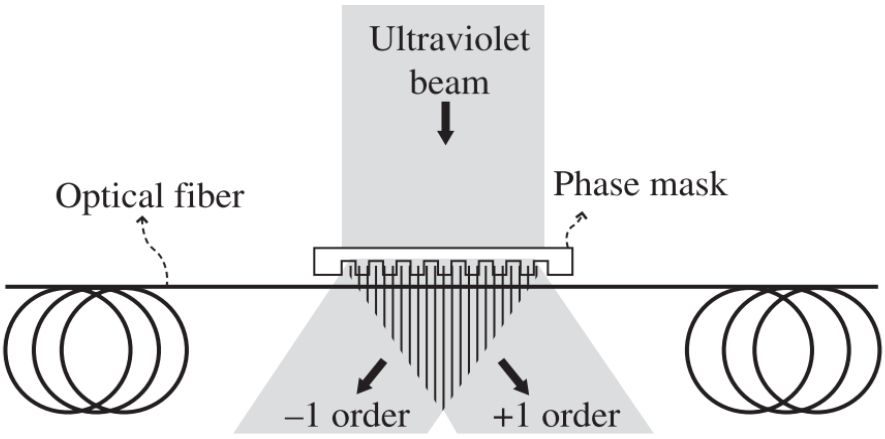

Figure 10.3: Fibre grating inscription by UV exposure through a phase mask [42].

It is noted that the grating length is limited by the size of the interference pattern in this interferometric exposure-based method. Translating a UV beam along the fibre through a phase mask, resulting the insensitivity of the phase of the fringe pattern since the phase mask and fiber are held together. And fiber gratings up to 1.5cm [238] and 5cm long [239] are fabricated. Another FBG fabrication method that has more flexibility in the choice of Bragg wavelength and grating length is the point-to-point method, which was first proposed by Albert in 1993. In this method, each grating is written by using a single laser pulse from an excimer laser to irradiate the photosensitive fiber core at normal incidence and a 360 μm long FBG with a period of 1 and 1.5 μm is obtained [234]. The Bragg wavelength of the FBG is calculated by the pulse repetition rate (f_{rep}) and the speed of the translation stage (ν_{stage}) that is used to fix fiber, giving by:

$$\lambda_B = 2n_{\text{eff}}\frac{\nu_{stage}}{f_{\text{rep}}} \tag{10.30}$$

during the fabrication process, the photo-induced refractive index changes only occur in the region where the focused light beam is applied. And the refractive index modified region could be smaller than the size of the focused light beam. One difficulty of this method is that the fiber core needs to be precisely aligned through the image plane of the slit.

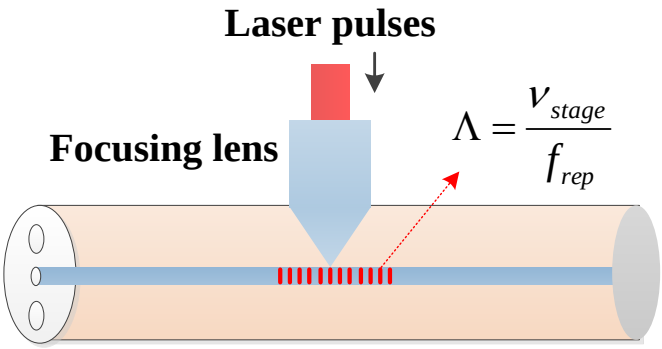

Figure 10.4: Fibre grating inscription by point-to-point method.

FBG has been widely used in optical fiber sensor applications with the advantages of high sensitivity, compact structure, immunity to electromagnetic interference, narrow linewidth ranging from sub-nm to nm in wavelength, resistance to corrosion, and large-scale multiplexing capacity, which can be multiplexed in wavelength domain to make quasi-distributed fiber sensor in wavelength domain using a broadband source [240] [241] [242]. The FBG has wide applications in temperature measurement [243] [244], strain detection [245], geotechnical health monitoring [246], and environmental and biomedical applications [247] [248]. They also can be viewed as nonlinear devices that can be used for pulse switching [249], pulse-shaping [250], and slow light [251]

Weak Fiber Bragg grating array (weak-FBGs)

In the practical application, some tested objects contain more than one measurement point and sometimes possess a continuous distribution such as temperature field, stress field, etc., in order to obtain complete information on tested objects; using distributed sensing technology to build up the sensor networks is indispensably required [252]. FBGs can be multiplexed to make quasi-distributed fiber sensors through different multiplexing methods, including wavelength division multiplexing [240] [246], time division multiplexing [253], spatial division multiplexing [254], and code division multiplexing techniques [255] [256]. Driving by the high demand for distributed sensing application

through FBG multiplexing, several solutions to fabricate FBGs array for long-distance and long-range measurement has been proposed. In 1993, Dong *etal* first reported an inscription method of weak FBGs array by writing the grating after the fiber fabrication process but before applying the coating, so-called on-line writing technique [257], in which two beam interferometry method was used, and the reflectivity of the FBG is about 2%. In 1995, Askins improved this method to inscribe the grating array through Online writing based on the holographic interferometer method, and the reflectivity of the FBG is about 3% [258].

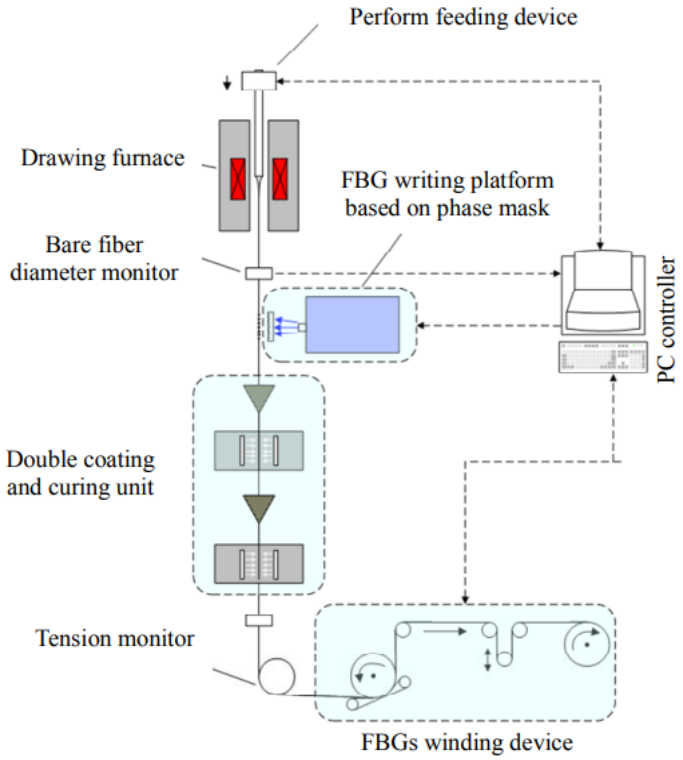

Figure 10.5: Setup of on-line writing weak FBGs array system [259].

By increasing the light intensity of writing setup below than damage threshold of the fiber, the reflectivity of FBG could be significantly improved [260]. It then could be used for high-temperature sensing applications. However, the reflectivity of each FBG affects the multiplexing capacity of a DOFS system. High reflectivity results in strong spectral-shadowing cross-talk and multiple reflection cross-talks [261], which will affect the strain or temperature resolution, as well as set a limit for multiplexing capacity.

Thus, there is a trade-off between grating reflection and the total number of gratings that can be deployed which is limited by the power and bandwidth of the light source. It has been proved that the reflectivity of -40 dB allows suppression of the cross-talk and yet maintains the signal-to-noise ratio to deploy temperature and strain resolution comparable to the distributed sensor with signal mode fiber for nearly 1000 weak FBGs with neighboring grating distance as 1-2 m [253].

To increase the multiplexing capacity and suppress the cross-talk effect, lots of solutions for ultra-weak FBG fabrication have been proposed. In 2012, Wang *etal*. [262] proposed an automated FBG fabrication system based on ultraviolet (UV) photosensitivity of the fiber, including coating removal part and FBG writing part. The phase mask is used in the FBG writing to produce a periodic interference pattern, further introducing a refractive index change. Then the FBGs array including 1000 ultra-weak FBGs are fabricated with typical reflectivity of -37 to -50 dB. In this system, the coating removal process introduces a central wavelength fluctuation duo to the mechanical stability, limiting the multiplexing capacity of the FBGs array. To overcome this problem and improve the multiplexing capacity, a weak FBGs array with good wavelength uniformity has been deployed which enables 1000s of identical weak FBGs fabricated in an optical fiber with reflectivity of -35 to -40 dB for each weak grating fabricated during fiber drawing at one peak wavelength in 2013 [263]. The online writing-based FBG writing platform was mounted on the draw tower near the first coating to weaken fiber vibrating, as shown in Figure 10.5. By using this method, the overlapping spectrum of the FBG array was almost similar to that of its single FBG [259].

In addition to an automated writing system and on-line writing system, Femtosecond (fs) laser with point-to-point method is also unitized for ultra-weak FBGs array fabrication. Most recently, Redding *etal*. [264] inscribed a series of localized weak point reflectors with reflectivity of -53dB along the Standard SMF based on a fully automated

Table 10.2: Different weak FBGs array

Name	method	reflectivity/number of gratings
Dong *etal*. (1993)	On-line writing (two beams interference)	2%
Askins *etal*. (1995)	On-line writing (holographic interferometer)	3%
Guo *etal*. (2012)	On-line writing (draw tower)	-35 to -40 dB/ 1000 gratings
Wang *etal*. (2013)	Automated system	-37 to -50 dB/ 1000 gratings
Gui *etal*. (2018)	On-line writing	-45 dB / 10000 gratings
Redding *etal*. (2020)	Femtosecond laser (point-to-point)	-53 dB/300 reflectors
Wu *etal*. (2020)	Femtosecond laser (point-to-point)	-42 dB/ 980 reflectors

fiber inscription setup. The added weak reflector will introduce very little attenuation, about 0.01 dB/100m. Wu *etal*. also proposed a large-scale multiplexed weak reflector array fabrication method by using a femtosecond laser in 2020. The weak reflector array with relatively high reflectivity (-42 dB) and low transmission loss (0.34/km) shows a 15.8 dB SNR enhancement compared with SMF as the sensing fiber [133]. To further suppress the spectral-shadowing and multiple reflection cross-talk effects, a novel FBGs array with randomly varied characteristic parameters (RVCPs) based on on-line writing technique is proposed in 2018 [265]. This proposed RVCP-FBGs arrays with the center wavelengths and grating spacing randomized within a controlled range, showing a good multiple reflection cross-talk suppression thus improving the accuracy, sensing range, and spatial resolution. Large scale multiplexing of 10000 FBGs with typical reflectivity of -45 dB along a 10m long fiber is demonstrated.

Weak FBGs array gives an increased reflectivity at a series of discrete locations along with the fiber. Thus, a longer sensing distance is still possible as long as the reflectance

is sufficiently low. However, these are not continuously distributed sensing techniques, and can only perform sensing where the gratings are inscribed in the fiber [266]. In order to solve quasi-distributed FBG due to the spatial spacing between weak FBGs, one approach is to use micro-cavity array [267], each pair of adjacent FBGs can form a micro-cavity to make a truly distributed sensor. Besides, Weak FBGs array can also be used for distributed vibration and acoustic sensing, which requires a high acquisition rate and high sensing resolution because of the fact that the acoustic signal often has sub-micro-strain amplitude. One demonstration for fast dynamic strain measurement [268] is to use a narrow optical band-pass filter to translate the strain variation induced wavelength shift to the intensity variation. In the experimental results, strain measurement resolution up to 222 $n\varepsilon$ and dynamic frequency of 2 kHz is achieved. Moreover, combined static and dynamic sensing can be realized by two sets of laser pulses with wavelengths matching the two edges of the FBG reflection spectrum. By using the spectral edges of the gratings, the wavelength shift is converted to the change of intensities at the two wavelengths. A short distance of hundreds of micrometers between two FBGs results in a broad spectral width up to tens of nm, which enables a larger temperature range up to 50°C. And dynamic sensing of $n\varepsilon$ scale vibration and 12.5 kHz acoustic wave are demonstrated at a sampling rate of 50 kHz [269].

Femtosecond laser micromachining method

The first demonstration of using fs laser for micromachining was in 1994 when laser pulses with 150 fs -7 ns pulse width and 780 nm wavelength were used to ablate micrometre sized features on silica and silver surfaces based on laser-induced optical breakdown [270] [271]. This technique has become useful technique either to modify and remove materials or to change the properties of a material and can be applied to transparent and absorptive substances. The advantages of this technique compared with other photonic-device fabrication devices include: (1) the nonlinear absorption-

induced material properties change is spatially confined to focal volume, which makes it possible to micromachine material with more complex structures in three dimensions; (2) the nonlinear absorption independent of materials; (3) all interconnects in the "motherboard" could be fabricated independently.

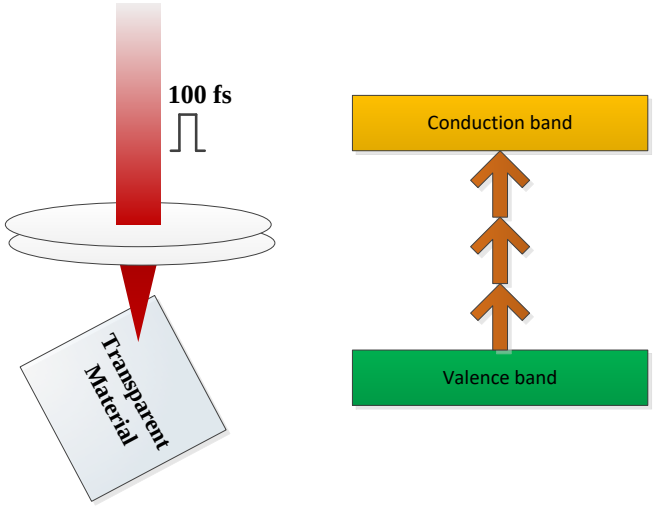

Figure 10.6: The diagram of the fs laser incident on transparent material and diagram of the excitation of electrons to the conduction band.

Fs laser has been utilized to fabricate embedded waveguides in bulk glass in which the refractive index of the material is changed [272]. The fundamental reason for localized permanent refractive index change in transparent material introduced by fs laser is the laser-induced optical breakdown. The absorption of light in a transparent material should be nonlinear since the lower energy of the incident photo is insufficient for electron transitions and be linearly absorbed by the dielectric material. This nonlinear absorption process will easily occur for transparent materials when the intensities of the fs laser pulse are approximately equal to the electric field that binds the valence electrons in the atoms (intensity about $5 \times 10^{20} W/m^{-2}$) [273], which is illustrated by Figure 10.6. When the high-power fs laser pulse is focused on the surface of a transparent material, this absorption results in a highly localized deposition of energy into an electron plasma through nonlinear photoionization that is formed within the focal

volume. A large number of laser-excited electrons then transfer the energy to the lattice of the bulk material after several picoseconds, which then leads to a material modification that is permanent. In the absence of impurities, carriers are generated initially by multiphoton absorption, promoting electrons from the valence to the conduction band.

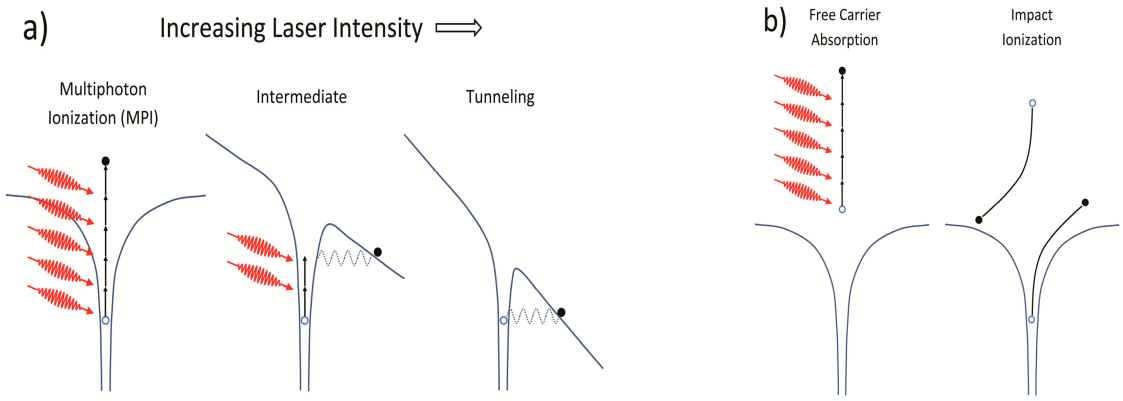

Figure 10.7: Schematic of free electron plasma formation with high intensity pulses where (a) multiphoton and tunneling ionization generates free electrons that (b) absorb radiation and impact-ionize surrounding material resulting in avalanche ionization [274].

Specifically, the fs laser pulse's different frequencies and intensity make the photoionization operate in a different regime, including multiphoton ionization and tunneling ionization with an intermediate regime in between. When a larger frequency incident light below the requirement of the single photo absorption is used, several photons must be incident on an electron at the same time for the process of nonlinear ionization to occur with a high probability since the electron need to absorb enough energy that equals to the band-gap of the material from the incident photos, as shown in the left-hand of the Figure 10.7. In the tunneling ionization, as described in the right-hand of Figure 10.7, the potential barrier (Coulomb well) that binds a valence electron to its parent atom and the band-gap will be significantly suppressed or distorted due to the high intensity of fs lase pulse induced strong electrical field [275] [276]. Then the electron tunnels through the Coulomb well and becomes free, which dominates the strong electric field and lower fs laser pulse frequency. By absorbing several laser photos

sequentially through free-carrier absorption, the free electron at the conduction band moves to higher energy states, then impact-ionize the bound electrons to create more free electrons. the accelerated free electrons create even more free electrons that undergo free-carrier absorption and impact-ionize even more bound electrons, resulting in the generation of an electron avalanche [274]. In the intermediate regime, the photoionization is a mix between tunneling and multiphoton ionization as depicted in the middle panel of Figure 10.7. Depending on the intensity of the fs laser pulse, different degrees of modification should be expected in the form of material compaction, the creation of defects, localized melting, nanograting or microvoid formation. In addition, different pulse energy, pulse width and the focusing numerical aperture would give different micromachined feature sizes.

Fiber Bragg gratings inscribed by the femtosecond laser technology are exploited. They are of great interest in applications, including high-powered fibre lasers [277], sensing in harsh environments [278] [274], High temperature [279], multi-parameters optic-fiber sensing [280], and ultrasound sensing [281] [282]. Traditional FBG fabrication method is based on UV-photosensitive fibers, and the refractive index change is the result of a process where a single UV photon is absorbed by the glass and excites oxygen deficiency defect centers, giving the absorption bands of defect centers at 244 nm [232]. Unlike UV-light induced FBG in the photo-sensitive optical fiber core, femtosecond laser interacts with a dielectric material via nonlinear photoionization mechanisms such as multiphoton and tunneling ionization [273], give the fs-FBG writing process certain advantages over conventional UV-laser FBG inscription, namely the removal of the necessity to use silica-based UV-photosensitive fibers at the wavelength of the writing laser. Compared with ultraviolet laser sources, the advantages of the inscription method by femtosecond pulses are wider machining materials [283], flexible inscription methods [284], and high-temperature resistance [285].

Fs-laser induced FBGs could be divided into two main categories: Type I-IR and

Type I-IR. To achieve these two different type of modification, which depends on pulse duration [286], pulse energy, pulse polarization, pulse repetition rate, the number of pulses deposited in one spot, laser beam focusing conditions and laser wavelength [287] [288].FBG inscription in Ge-doped telecommunication optical fibers with a phase mask and multiple pulses of 800 nm fs-IR laser radiation can generate smooth or Type I-IR refractive index change in the fibers. The magnitude of the index change varies with the fifth power of the laser intensity that was used to write the gratings, indicating a 5-photon absorption process [289]. The refractive index variations in Type I-IR FBG originate from modifications below the damage threshold of the fiber material. This type of smooth refractive index change is completely erasable by annealing at temperatures exceeding 900 °C [290], showing poor thermal stability, which is similar with the UV gratings in photosensitive fiber. However, the type II-IR gratings are usually made with high laser intensity, and self-assembled nanostructures with subwavelength periods can be introduced at the laser focal spot, known as nanograting. It has a refractive index variation up to 10^{-3}, which is characterized by its anisotropy, higher loss, and showing impressive temperature durability at temperature excess of 1000 °C. The further increase of the laser intensity would bring an irreversible optical breakdown.

Two main techniques to fabricate the FBGs by using the fs laser are phase mask scanning method [291] and point-to-point (PbP) writing technique. The fabrication setup for fs-laser inscription of FBGs is similar to the UV light irradiation method based regular FBGs as shown in Figure 10.3 and Figure 10.4, but with the high intensity fs laser pulse as incident light. The first successful demonstration for FBG fabrication using a phase mask approach with fs radiation was in 2003 [291]. A specialty phase mask was precision etched to maximize coupling of the incident fs laser radiation with 800nm wavelength and 120 fs pulse width into the ± 1 orders. The phase mask automatically matched path lengths of the generated orders when aligned at normal incidence to the inscription beam within the dimensions of the spatial envelope of the fs pulses.

To avoid the narrow pulse being broadly dispersed when it passes through the phase mask, the pitches that are much larger than the wavelength of incident radiation are employed. The reflectivity of the FBG is about -44.5 dB with a refractive index change of 1.9×10^{-3}. The FBG fabricated by this phase method shows good thermal stability and did not erase after two weeks at 300 °C. By moving the phase mask and the fiber concerning the fs laser beam, the refract index modification range could be extended up to as long as phase mask [292]. However, the limitation of this method is that only one uniform period FBGs could be fabricated with one mask. Thus the complex grating structure is hard to achieve. In 2004, a direct point-by-point FBGs fabrication method by using fs laser is proposed [293] without the requirement of phase mask and offers good flexibility. Each high-intensity fs laser pulse creates a highly localized refractive index change, and the grating is inscribed sequentially in a step-and-repeat fashion by translating the beam or optical fiber using a high-resolution mechanical stage [294].

RFGs fabrication

Most recently, our group worked with National Research Council of Canada proposed a Random fiber grating array (RFGA) by employing direct writing method [295] [280], as shown in Figure 10.8. An fs-IR beam from a Ti: sapphire regenerative amplifier (Spitfire, Spectra-Physics) was focused onto the core of optical fiber through an objective lens. In order to increase the overlap of the laser-induced index change and the modal field in the fiber core, a cylindrical lens with a focal length of 0.5 m was introduced into the exposure setup before the final microscope objective. The cylindrical shape of the focal volume normally produced by the microscope objective alone is instead transformed into a planar strip or plane. The fiber was clamped onto a precision air-bearing stage (Aerotech) with ±10 nm position accuracy. The fs-IR laser operates at a wavelength of 800 nm with a repetition rate of up to 1 kHz and with a pulse duration of 120 fs. The microscope objective was mounted on a translation stage

(driven by a piezo actuator) that can move the objective back and forth along the fiber up to 20 micrometers. The fiber jacket was removed so that the laser beam could be easily focused on the fiber core. The fiber was free-standing; no index-matching fluid was used between the fiber and the objective.

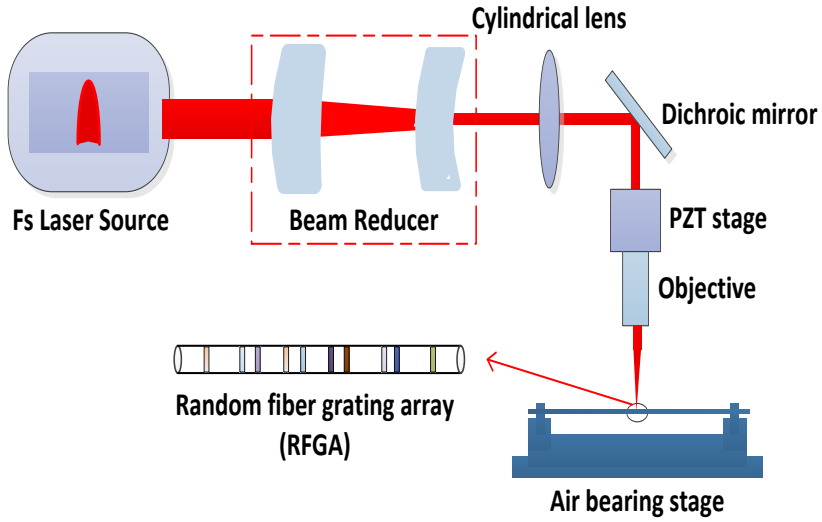

Figure 10.8: Experimental setup of the plane-to-plane fs laser micromachining for Random fiber grating array (RFGA) fabrication.

For RFGA fabrication, there are two main methods to inscribe the refractive index modification plane independently along the fiber core: (1) The repetition rate of the fs laser pulse is fixed at 1000 Hz and the moving speeding of the air-bearing stage is also unchanged at 0.5 mm/s, but the piezo-driven stage dithers along the fiber's axis with a random displacement from 0 to 2.5 μm. (2) The piezo-driven stage is fixed and the moving speeding of the air-bearing stage is also unchanged near 0.5 mm/s, but the repetition rate of the laser pulse rate is varied from 990 Hz to 1100 Hz (2%). As shown in the left-hand of Figure 10.8, the repetition rate of the fs laser pulse is changed every 50 ms. So, the period within the sub-grating is constant depending on the given repetition rate during the 50 ms.

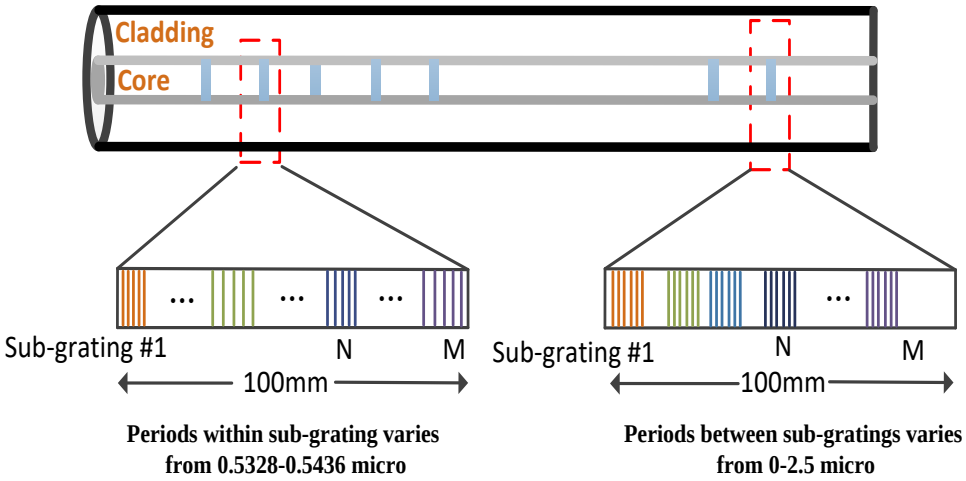

Figure 10.9: Schematic of Random fiber grating array structure based on two different fabrication method: Fs laser pulse repetition rate random variation (left) and piezo-stage dithering (Right). Left: Constant piezo-driven stage, but fs laser pulse repetition rate changes from 900 Hz to 1000 Hz. Right: Fixed pulse repetition rate, but the piezo-driven stage dithers from 0 to 2.5 μm between sub-gratings.

But the periodicity of different sub-grating is not the same, resulting a wider reflection spectrum. The central wavelength (λ_0) could be calculated based on Equation (10.30) and the width ($\Delta\lambda$) are expressed as:

$$\Delta\lambda_B = 2n_{\text{eff}}\nu_{stage}\frac{\Delta f}{f_{\text{rep}}^2} \tag{10.31}$$

where Δf is the repetition variation range. While in the right-hand of Figure 10.8, the Piezo-driven stage dithers from 0 to 2.5 μm every 50ms. It makes the periodicity within different sub-gratings the same, but the periods (distance) between different sub-gratings are randomly changed. The spacing randomness of the RFG from these two methods are predetermined by the random number generated by a computer and stored for repeatable uses afterward.

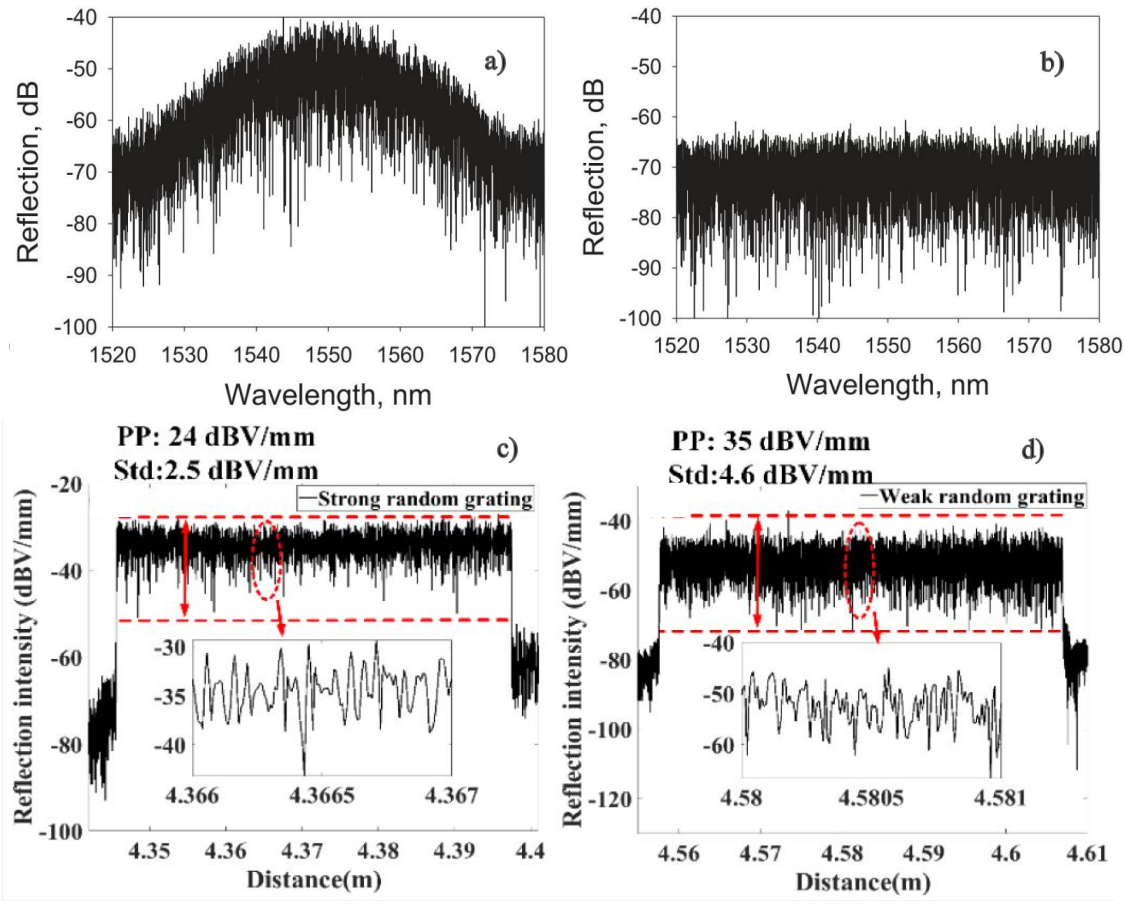

Figure 10.10: Simulated reflection spectrum of the random fiber grating and its measured reflectivity versus distance: (a)(c) pulse repetition rate variation method (Strong RFG) and (b)(d) piezo-stage dithering method (Weak RFG).PP: peak-to-peak, Std: standard deviation [296].

The simulated reflection spectrum of the RFG from two proposed methods by using the coupled mode theory is shown in Figure 10.10 (a) and (b). The RFG fabricated by both those two methods are showing a significantly unique refractive index variation profile in a spatial domain without constant periodicity, resulting in a totally different reflection spectrum without a dominant peak. The randomly varied grating periods highly suppress the phase correlation between the adjacent reflectors, giving noisy multiple interference reflection spectra with wider bandwidth than regular FBG. It is noted that the spectrum bandwidth and peak reflectivity of two types of RFG is different, even the same fs laser pulse induced refractive index variation of 10^{-6} and

grating length of 100 mm are set. The RFG that is inscribed by varying the repetition rate of fs-IR pulse laser has larger reflectivity with narrow reflection spectrum width, which ensures the nanometer-grating spacing change (<10.8 nm). While the RFG with smaller reflectivity that is fabricated by the piezo-stage dithering method has a large grating spacing of 0-2.5 micrometers for a much broader reflection spectrum. The reason behind this is that with a lower degree of randomness and smaller sub-gratings period variation in the lower reflection RFG, the random phase change of the backscattered light in a local region is less stochastic than that in the high disordered RFG (weak FBG) with larger grating period fluctuation (<2.5 micrometers which are larger than optical wavelength around 1.5 micrometers). This leads to partially correlated phase superposition in the low disordered RFG (strong FBG) and uncorrelated phase superposition in high disordered RFG [296]. Besides, the average backscattering strength per unit of two types of RFG are shown in Figure 10.10 (c) and (d). in which weak RFG is -34 dbV/mm and strong RFG is -54 dBV/mm. From the reflection intensity distribution along the RFG, we could know that the index modification depth varies from plane to plane since each plane is inscribed by an fs laser pulse independently with different laser power. Hence such a fiber random grating with random periods and random index modulations loses the general spectral characteristic of FBG and displays a noisy multiple-interference reflection spectrum resulting from the superposition of many low-finesse FPIs and MZIs [297].

RFGA-based Distributed optical fiber sensing

When telecom fiber is used for distributed fiber optical sensors, the low Rayleigh backscattering signal level limits the sensitivity and spatial resolution of distributed temperature or stain measurements by OTDR or OFDR techniques. In recent years, ultraviolet (UV) lasers have been used to increase the backscattering in optical fibers for distributed temperature and strain measurements resulting in higher spatial resolution

and high signal-to-noise ratio (SNR) [298] [299] [300] [301]. Using 10.6µm absorption line in SMF 28, the Rayleigh scattering was enhanced by randomly spaced index modulation using CO_2 laser for inscription [298]. With 100 points of CO2-laser-irradiation with randomly changed distance along the SMF-28 over a 10 cm fiber, the random feedback fiber is formed as Rayleigh scattering enhancement. The 10cm scattering strength is equivalent to a few km SMF lengths. Loranger et al. showed the enhancement of Rayleigh scattering by simple UV exposure to optical fiber. They used H2 loading on SMF-28 fiber and specialty fiber with high Ge-dopant to increase UV photosensitivity [299]. Enhancement of Rayleigh scattering with ultralow loss in SMF-28 fiber was demonstrated using specific phase mask [300], the wavelength range where the backscattering was enhanced was restricted by the specific chirped phase mask used in the experiment. When optical fibers are exposed to high-power laser radiation, it would generate broadband loss due to the formation of color centers and/or micrometers voids that are produced by laser radiation. Using Rayleigh scattering enhanced fiber, the distributed temperature sensor is achieved at accuracy of over 10mm spatial resolution using optical frequency domain reflectometry (OFDR) [295]. For a random grating array-based OTDR system, in order to cover the broad wavelength response of the random grating, a chirped pulse is introduced with a MHz bandwidth DFB laser. The random fiber gratings spectrum has spike-like reflective spectra with high contrast that can be attributed to enhanced in-homogeneity. The contrast could be further enhanced when a random fiber grating array is introduced due to the superposition of a few random grating of sub-cm in length. The resultant interference patterns with multiple peaks ensure high accuracy in delay time measurement. Unlike a conventional phase OTDR sensing system which measures a distributed phase change along the fiber using an ultra-narrow linewidth laser, the distributed time delay is directly measured in real-time. This allowed 0.028^{o}C accuracy for temperature measurement [30].